High-resolution 3D printing enabled, minimally invasive fibre optic sensing and imaging probes

Richard David Robert Caulfield

Thesis submitted as part

of the requirements for the degree of

Doctor of Philosophy

of

University College London.

Supervisor 1: **Prof. Manish K. Tiwari**

Supervisor 2: **Prof. Adrien E. Desjardins**

Clinical Supervisor: **Prof. Anna L. David**

Department of Medical Physics and Biomedical Engineering

University College London

Date of Submission, July 2020

Declaration

I, Richard David Robert Caulfield confirm that the work presented in this thesis is my own. Where information has been derived from other sources, I confirm that this has been indicated in the work.

Abstract

Minimally invasive surgical procedures have become more favourable to their traditional surgical counterparts due to their reduced risks, faster recovery times and decreased trauma. Despite this, there are still some limitations involved with these procedures, such as the spatial confinement of operating through small incisions and the intrinsic lack of visual or tactile feedback. Specialised tools and imaging equipment are required to overcome these issues. Providing better feedback to surgeons is a key area of research to enhance the outcomes and safety profiles of minimally invasive procedures.

This thesis is centred on the development of new microfabrication methods to create novel fibre optic imaging and sensing probes that could ultimately be used for improving the guidance of minimally invasive surgeries. Several themes emerged in this process. The first theme involved the use and optimisation of high-resolution 3D injection of polymers as sacrificial layers onto which parylene-C was deposited. One outcome from this theme was a series of miniaturised parylene-C based membranes to create fibre optic pressure sensors for physiological pressure measurements and for ultrasound reception. The pressure sensor sensitivity was found to vary from 0.02 to 0.14 radians/mmHg, as the thickness of parylene was decreased from 2 to 0.5 µm. The ultrasound receivers were characterised and exhibited a noise equivalent pressure (NEP) value of ~100 Pa (an order of magnitude improvement compared to similarly sized piezoelectric hydrophones).

A second theme employed high-resolution 3D printing to create microstructures of polydimethylsiloxane (PDMS) and subsequently formed nanocomposites, to create microscale acoustic hologram structures. This theme included the development of innovative manufacturing processes such as printing directly onto optical fibres, micro moulding and precise deposition which enabled the creation of such devices. These microstructures were investigated for reducing the divergence of photoacoustically-generated ultrasound beams.

Taken together, the developments in this thesis pave the way for 3D microfabricated polymer-based fibre optic sensors that could find broad clinical utility in minimally invasive procedures.

Impact Statement

Minimally invasive surgical procedures have greatly enhanced the medical field through reduced trauma, improved safety profiles and faster recovery times. However, miniaturised imaging and sensing probes are critical for providing feedback to surgeons during these procedures.

In this work novel micro-manufacturing techniques and processes based on high-resolution 3D printing were developed to overcome the limitations of traditional multi-step, complex fabrication procedures. Photoacoustic materials were investigated and printed at high-resolution (< 10 µm). A novel method of structuring soft materials (e.g. silicone) that are unable to support themselves mechanically was also exploited through the use of high-resolution 3D printed micro moulds. This enabled previously unusable materials to be utilised. A method of printing microstructures directly onto the tip of optical fibres was also achieved. Combining these printing technologies allows a wider range of materials to be used and enables high-resolution printing directly on the tip of optical fibres. Such advances will aid in the future development and integration of photonic devices directly onto optical fibres for many different imaging and sensing applications. These printing techniques could also be used to create silicone structures for a range of other applications, such as microfluidic devices.

Utilising these developed manufacturing techniques several devices were created for use in minimally invasive procedures, all while outside a cleanroom environment. The ability of these techniques to batch produce devices has a large potential for commercialisation.

Firstly, miniaturised polymer-based Fabry-Pérot fibre optic pressure sensors were fabricated to measure physiological arterial pressures during minimally invasive cardiovascular procedures. This microfabrication technique enabled thin parylene-C membranes to be used as the pressure sensing diaphragm, and overcame the complexities associated with fabricating thin membranes using lithographic techniques. This work paves the way for such polymer-based, air backed sensors to be used to monitor arterial pressure during minimally invasive procedures or as a diagnostic measure. By establishing a relationship between the average sensor sensitivity and the thickness of the parylene-C membrane, future sensor designs can

be tuned to achieve a specific sensitivity range. Outside of the medical field these sensors could also be used to monitor fluid pressure during industrial processes.

As well as this, fibre optic hydrophones (FOH) for ultrasound detection were created following a similar microfabrication technique, and their ultrasound reception was characterised. The use of parylene-C membranes for ultrasound detection demonstrates how relatively simple fabrication techniques can be utilised to create highly sensitive fibre optic hydrophones. Even with low finesse cavities, the parylene-C membranes showed excellent acoustic phase sensitivity. Building on this high acoustic sensitivity, future FOH designs with improved optical phase sensitivity could be created. By optimising the optical sensitivity, exceptionally sensitive FOH with noise equivalent pressure values lower than those currently reported in literature could be produced. Apart from medicine, all-optical ultrasound devices could also be used in industry for non-destructing testing applications.

Taken together, the developments outlined in this work could ultimately be combined to produce highly sensitive, miniaturised, multi-capability, imaging and sensing probes for use in minimally invasive surgeries.

Acknowledgements

Firstly, I would like to thank my supervisors Prof. Manish Tiwari, Prof. Adrien Desjardins and Prof. Anna David for their continual support throughout my PhD. They have shared a wealth of wisdom with me that has been invaluable over the course of my research. Their mentorship and advice has been indispensable and helped me reach the culmination of my PhD. The enthusiasm and energy they exude has been truly motivational. I have thoroughly enjoyed working with them and cannot thank them enough.

I would also like to thank all those who I have worked and collaborated with during the course of my research, including Dr. Feihuang Fang for his help with the 3D printers, Dr. Edward Zhang for his expertise in parylene deposition, Dr. Saja Aabith for his support with ink design, Dr. Jo Coote for her guidance in interferometric systems, Dr. Sunish Matthews for his insights in fibre optic hydrophones, Dr. Sacha Noimark for her chemistry expertise, Dr. Richard Colchester for his guidance on all optical ultrasound, Dr. Radhika Poduval and Dr. Callum Little for their rewarding collaboration on miniature imaging phantoms, Dr. Charles Mosse for his practical insights and Dr. Tom Gregory for his training and guidance in SEM imaging.

I am grateful for the opportunities to work with such amazing teams and research groups particularly the Nanoengineered Systems group, the Interventional Devices group and the WEISS centre. The friendly faces and chats have made the PhD experience a truly enjoyable one. Special mentions go to Dr. Zhuyang Chen, Sherif Hamed, Mike Grizen and Nick Salaris who provided endless entertainment and insightful discussions while working in the labs over the years.

I would also like to express my thanks to my friends for their support, humour and encouragement. They have always been there to offer advice and have been more than willing to accompany me to the pub when needed.

In addition, I would like to thank the UCL EPSRC Centre for Doctoral Training in Medical Imaging and the UCL Wellcome/EPSRC Centre for Interventional Surgical Sciences (WEISS) for providing funding for this research.

Finally, I would like to thank my family for their unwavering support and encouragement throughout my studies. They have always inspired me to achieve my goals and I would not be the person I am today without them.

Publications

Journal publications

- Callum D. Little, Radhika K. Poduval, **Richard Caulfield**, Sacha Noimark, Richard J. Colchester, Chris D. Loder, Manish K. Tiwari, Roby D. Rakhit, Ioannis Papakonstantinou, and Adrien E. Desjardins, "Micron resolution, high-fidelity three-dimensional vascular optical imaging phantoms", *Journal of Biomedical Optics* 24(2), 020502 (15 February 2019). https://doi.org/10.1117/1.JBO.24.2.020502

Peer reviewed book chapter

- **Caulfield R.**, Fang F. and Tiwari M.K. (2018) "Drops, Jets and High-Resolution 3D Printing: Fundamentals and Applications". In: Basu S., Agarwal A., Mukhopadhyay A., Patel C. (eds) Droplet and Spray Transport: Paradigms and Applications. Energy, Environment, and Sustainability. Springer, Singapore. https://doi.org/10.1007/978-981-10-7233-8_6.

Selected conference presentations

- **R. Caulfield**; S. Aabith; R. Colchester; S. Noimark; A. David; I. Papakonstantinou; A. Desjardins and M. Tiwari, "3D printed probes with optically-generated ultrasound for high-resolution imaging during minimally invasive procedures", *Photonex London, Advances in Biophotonics*, London, UK, 18th April 2018.
- **R. Caulfield**, S. Aabith, R. Colchester, S. Noimark, A.L. David, I. Papakonstantinou, A. Desjardins and M.K. Tiwari, "3D printed probes with optically-generated ultrasound for high-resolution imaging during minimally invasive procedures", *Biomedical Engineering Conference 2018 (BioMedEng18)*, London, UK, 6-7th September 2018. ISBN 978-1-9996465-0-9.
- **Richard Caulfield**, Saja Aabith, Richard Colchester, Sacha Noimark, Anna David, Ioannis Papakonstantinou, Adrien Desjardins and Manish Tiwari, "High-resolution 3D printing at the tip of optical fibres", *Printing for Fabrication 2018 materials, applications, and processes (34th International Conference on Digital Printing Technologies)*, Dresden, Germany, 23-27th September 2018.

- **Richard Caulfield**, Saja Aabith, Richard Colchester, Sacha Noimark, Anna L. David, Ioannis Papakonstantinou, Adrien Desjardins and Manish K. Tiwari, “Miniaturised 3D printed probes for high-resolution all-optical ultrasound imaging”, *9th International Conference on Advanced Materials and Nanotechnology (AMN9)*, Wellington, New Zealand, 10-14th February 2019.
- Callum Little, Radhika Poduval, **Richard Caulfield**, Sacha Noimark, Richard J. Colchester, Chris D. Loder, Manish K. Tiwari, Roby D. Rakhit, Ioannis Papakonstantinou, and Adrien E. Desjardins, “A hybrid approach of two-photon polymerization scaffold printing and microinjection of optically heterogenous material for the fabrication of vascular imaging phantoms”, *SPIE BiOS Diagnostic and Therapeutic Applications of Light in Cardiology 2019*, San Francisco, California, United States, 7th March 2019.
- **R. Caulfield**, J. Coote, C.A. Mosse, A.L David, A.E. Desjardins and M.K. Tiwari, “Free-standing parylene membranes for optical pressure sensing”, *Biomedical Engineering Conference 2019 (BioMedEng19)*, London, UK, 5-6th September 2019.

Further publications under review

- Saja Aabith, **Richard Caulfield**, Anastasia Papadopoulou, Shervanthi Homer-Vanniasinkam and Manish K. Tiwari, “3D direct-write printing of safe, water soluble micro moulds for precision rapid prototyping”, *Additive Manufacturing*.

Contents

List of Figures

List of Tables

Glossary

2D: two dimensional

3D: three dimensional

AFM: atomic force microscopy

AuNP: gold nanoparticles

CAGR: compound annual growth rates

CB: carbon black

CDH: congenital diaphragmatic hernia

CNT: carbon nanotubes

CTAB: cetyltrimethylammonium bromide

CVD: cardiovascular disease

DI: deionised

DMF: dimethylformamide

DRL: dynamic release layer

DW: direct-write

EHD: electrohydrodynamic

EMI: electromagnetic interference

EUS: endoscopic ultrasound

FBG: fibre Bragg grating

FDA: Food and Drug Administration

FDM: fused deposition modelling

FETO: fetoscopic endoluminal tracheal occlusion

FFR: fractional flow reserve

FIB: focused ion beam

FOH: fibre optic hydrophones

F-P: Fabry-Pérot

GLY: glycerol

HCB: hydroxide catalysis bonding

HIFU: high intensity focussed ultrasound

IABP: intra-aortic balloon pumps

IPA: isopropyl alcohol

iPPROM: iatrogenic preterm premature rupture of membranes

ISO: International Organization for Standards

ITF: interferometer transfer function

ITO: indium tin oxide

IUPAC: International Union of Pure and Applied Chemistry

IVUS: intravascular ultrasound

LCI: low coherence interferometry

LED: light emitting diode

LIFT: laser-induced forward transfer

LUTO: lower urinary track obstruction

MEK: methyl ethyl ketone

MEMS: microelectromechanical system

MMC: myelomeningocele

MOMS: micro opto mechanical systems

MRI: magnetic resonance imaging

MWCNT: multiwalled carbon nanotubes

NDT: non-destructive testing

NEP: noise equivalent pressure

NIR: near infrared

NIRF: near infrared fluorescence

NP: nanoparticles

OCT: optical coherence tomography

OR-PAM: optical-resolution photoacoustic microscopy

PAC: pulmonary artery catheter

PAT: photoacoustic tomography

PCI: percutaneous coronary intervention

PDMS: polydimethylsiloxane

PEI: polyethylenimine

PET: polyethylene terephthalate

PFOTS: perflurooctyl-trichlorosilane

PGMEA: propylene-glycol monomethyl-ether-acetate

PLUTO: percutaneous shunting in lower urinary tract obstruction

PMMA: polymethyl methacrylate

PTFE: polytetrafluoroethylene

PVA: polyvinyl alcohol

PVDF: polyvinylidene

PVP: polyvinylpyrrolidone

RGO: reduced graphene oxide

SD: spectral domain

SEM: scanning electron microscope

SL: stereolithography

SLED: superluminescent light emitting diode

SLS: selective laser sintering

SNR: signal to noise ratio

TAPS: twin anaemia-polycythaemia sequence

TD: time domain

TTTS: twin-twin transfusion syndrome

WHO: World Health Organisation

Chapter 1 – Introduction

This thesis discusses the work undertaken during my doctoral degree. The research presented here centres around utilising high-resolution 3D printing to create imaging and sensing devices to aid with minimally invasive surgeries.

1.1 Motivation

Minimally invasive “keyhole” surgeries are at the forefront of recent medical advancements. They have become more favourable than their traditional open surgical procedure counterparts as they can provide the same surgical outcomes but are carried out through small incisions and have less associated risks (Hernández-Vaquero et al. 2012; Van Mieghem et al. 2012). A benefit of performing procedures through small incisions is that small incisions heal faster than larger cuts. More rapid healing times are obviously preferred for patients as it means less recovery time is required but this is also advantageous to health service providers as shorter recovery times can allow greater patient throughput (Dankelman, Van Den Dobbelsteen, and Breedveld 2011). Not only are recovery times improved but minimally invasive surgeries are also less traumatic, which in turn aids recovery (Dankelman et al. 2011). Traumatic procedures are those that cause unwanted side-effects to the body such as bruising and loss of blood. By reducing these side-effects minimally invasive procedures boost recovery (Marescaux and Diana 2015). Infections are also a major problem in delaying recovery and a main issue being faced by health service providers worldwide. Infection is an increasing problem, especially in a world where antibiotic resistance is constantly on the rise. Globally, an estimated 700,000 people die each year due to antibiotic resistant infections (O’Neill 2016). Minimally invasive surgery can reduce a patients chance of infection by up to 10-fold, since smaller wounds present less surface area for infections to easily enter the body (O’Toole, Eichholz, and Fessler 2009).

Despite the improved healing, recovery times and the associated benefits for both patients and healthcare providers, there are still some drawbacks to minimally invasive procedures. Operating in such a confined environment presents certain challenges to surgeons. The operating tools need to be altered to allow for precise control and manoeuvrability as they perform procedures through the small incisions (Matern and Waller 1999). During traditional surgery, the surgeons view is unobstructed, and they get visual feedback of how the procedure is progressing and

can quickly act to correct problems that arise. In minimally invasive surgery however, the surgeon's view is obstructed by the patient's body. Specialised imaging equipment is required to provide real time visualisation of the procedure while still conforming to the requirements of the confined environment. As well as specialised imaging techniques, advanced sensing equipment is also used to help guide minimally invasive procedures. These sensors are used to monitor and provide feedback of certain physiological measurements to the surgeon such as pressure, temperature, oxygen level etc. To make the most effective use of space in such a restrictive environment, these sensors can be integrated into the surgical tools and imaging equipment. The fabrication of these imaging and sensing probes requires complex procedures. This work seeks to create microfabrication techniques based on high-resolution 3D printing technology to alleviate these limitations.

1.1.1 High-resolution 3D printing technology

3D printing is an additive manufacturing technique that excels in rapid prototyping and production. Additive manufacturing techniques (adding material to create desired structures) have many advantages over more traditional subtractive manufacturing techniques (removing material to create desired structures). These include less wastage, making them more economical, and rapid processing, thus more time efficient (Wong and Hernandez 2012).

In this work high-resolution 3D printing technologies are utilised to manufacture imaging and sensing devices to be integrated with optical fibres for use in the medical field. These technologies enable specifically designed microstructures to be created on a variety of substrate materials, including directly onto optical fibre tips, without the need for specialist manufacturing environments such as cleanrooms and avoiding complex lithographic procedures.

1.1.2 Optical fibre imaging and sensing

Optical fibres have been used for imaging and illumination in the medical field for endoscopy and urology applications since the early 1960's (Hett and Curtis 1961; Marshall 1964). With the advent of low loss fibres in the 1970's research into optical fibre sensing began (Rajan 2015). By the early 1980's optical fibres were being used in medicine to illuminate for colour photography, for pressure sensing and for *in vivo* oximetry measurements (Epstein 1982).

Fibre optic sensors are well suited for biomedical applications due to their inertness and biocompatibility (Roriz et al. 2013). Their small size and flexibility enable them to

be easily integrated with catheters, guidewires and other medical equipment. Due to their optical nature, fibre optic sensors can overcome limitations in miniaturisation faced by electronics-based sensors as wired connections are no longer required. Another advantage of using fibre optics for imaging and sensing is that they are immune to electromagnetic interference. This makes fibre optics compatible with magnetic resonance imaging (MRI) machines and could allow imaging and monitoring of specific physiological parameters during MRI scans and procedures.

Since their advent in the medical field, fibre optic imaging and sensing techniques have been used in many complex procedures in areas such as cardiology, urology, gastroenterology, ophthalmology and neurology (Ansari et al. 2017; Li et al. 2014; Liu et al. 2012; Marshall 1964; Martínez-Mañas et al. 2000; van Soest, Regar, and van der Steen 2015).

In this work the main areas of interest for developing fibre optic imaging and sensing probes are cardiovascular and fetal medicine applications.

1.1.3 Cardiovascular

Heart and Circulatory Diseases (Cardiovascular Disease; CVD) is a term that includes all diseases of the heart and circulation, both inherited and developed. Cardiovascular disease accounts for more than a quarter (28%) of all deaths in the UK annually (British Heart Foundation 2019). The World Health Organization (WHO) has named cardiovascular diseases as the number one cause of death globally, estimating that 17.9 million people died from CVDs in 2016 and of which 85% were due to heart attack or stroke (World Health Organization 2019). Heart attacks and strokes are both due to a blockage in the blood vessels supplying blood to the heart (heart attack) or the brain (stroke) (National Health Service 2018). These blockages are usually caused by atherosclerosis, which is a build-up of fatty deposits, cholesterol and calcium that harden over time to restrict the blood flow to the organs. Atherosclerosis can remain relatively symptomless for a long time until the blood flow reduces so much so that a life-threatening heart attack or stroke is induced. This silent progression of atherosclerosis makes it difficult to diagnose. Trying to image non-invasively from outside the body to spot blockages forming is challenging due to overlying structures obstructing the view and the limited resolution and contrast of these techniques (Tarkin et al. 2016). One solution is to image inside the blood vessels to get a clearer view of the atherosclerosis. Imaging inside the blood vessels requires highly miniaturised imaging and sensing devices which can provide the clinicians with extremely useful structural and function information, thus improving the

outcomes for patients. Fibre optic imaging and sensing devices are well suited for this due to their small dimensions, flexibility and biocompatibility.

Abnormal beating of the heart can also increase the risk of heart attack or stroke, this is called arrhythmia. The beating of the heart muscle is controlled by electrical impulses. In some cases, arrhythmia is treated surgically by treating the regions that are creating the misfiring electrical impulses with radio frequency to ablate them and restore normal beating rhythm. Surgical interventions like this are performed minimally invasively by inserting a catheter into a vein in the patient's leg and navigating to the left atrium of the heart to directly ablate the misfiring tissue. Entry to the left atrium is usually performed via a transseptal puncture (Earley 2009). Imaging and pressure monitoring are critical for tracking the position of the catheter during the procedure. Currently, X-ray fluoroscopic imaging is commonly used with contrast agents. Again, highly miniaturised fibre optic imaging and sensing probes could be utilised in this procedure. Fibre optic devices could be inserted along the inner lumen of the catheter and needle to provide additional positional information and used to provide highly sensitive feedback on physiological pressure measurements throughout the procedure.

These are only two highlighted examples of how highly miniaturised fibre optic imaging and sensing devices could be used to help in the guidance and monitoring of minimally invasive cardiovascular procedures and hopefully lead to greater safety profiles.

1.1.4 Fetal medicine

The use of ultrasound as a diagnostic screening technique has been widely adopted and routinely used in fetal medicine thanks to its relatively cheap cost, ease of use and good safety profile. Thanks to this many fetal problems can be detected early, but what happens when these problems are detected? Therapies are increasingly being delivered to the fetus before birth in an attempt to improve neonatal outcome. Pharmacological treatments are the preferred form of fetal therapy as they are the least invasive but sometimes surgical interventions are unavoidable (Phithakwatchara et al. 2017). Minimally invasive interventions cover all treatments which are performed through incisions or needles. These can include ultrasound-guided needle intervention and fetoscopic surgeries (Phithakwatchara et al. 2017). Open fetal surgery is the most invasive procedure, which carries a higher risk to the fetus, pregnancy and mother (Fowler et al. 2002). It involves a hysterotomy open incision in the uterus (between 3-8 cm long) and direct surgery to the fetus before the

uterine incision is closed. As the amniotic membrane has poor healing properties, frequently post-surgery the amniotic fluid leaks out of the gestation sac and becomes trapped between the overlying uterine muscle, which increases the risk of the amniotic membrane rupturing (iatrogenic preterm premature rupture of membranes, iPPROM). The build-up of trapped fluid leads to contractions and preterm birth in approximately 60% of cases (Nakayama et al. 1984). Though minimally invasive procedures greatly reduce the risk of iPPROM they still have an associated risk (Beck et al. 2012). Beck *et al.* found that the frequency of iPPROM could be predicted by the maximum diameter of the instruments used. The maximum diameter was also significantly related to the gestational age at birth and thus linked to the fetal survival (Beck et al., 2012). Some other surgical characteristics thought to influence iPPROM are the number of operating ports and the duration of the procedure, these links are summarised schematically in Figure 1.1.

Fetal therapies strive to be as non-invasive as possible but, in some cases, interventional fetal surgeries are unavoidable. One such case is twin-twin transfusion syndrome (TTTS). TTTS occurs in pregnancies of twins that share a placenta. The condition is an imbalance of circulating blood between the twins where one receives too little and one receives too much blood. This imbalance results in adverse effects for both twins. If left untreated the overall mortality rate is 73-100% (Slaghekke et al. 2014). The condition is treated by using lasers to coagulate the inter-twin vasculature anastomoses (connecting vessels) on the surface of the placenta to restore equal circulation. Unfortunately, it is difficult to identify and coagulate all of the anastomoses so fine vessels remain in up to 33% of cases which can lead to complications (Dhillon et al. 2015). An improved imaging technique could aid in the identification of these finer anastomoses on the placenta. A multi-capability imaging and laser therapy probe would also be beneficial. Further discussions on minimally invasive fetal interventions and the key needs required for future developments are discussed in Appendix C.

It is theorised that a miniaturised fibre optic high-resolution imaging/sensing probe could further reduce the risk of iPPROM during minimally invasive procedures. Due to the small dimensions of fibre optic devices, the size and number of operating ports could be decreased and through increased visualisation/sensor feedback procedure times could be cut. Thus, improving neonatal outcomes.

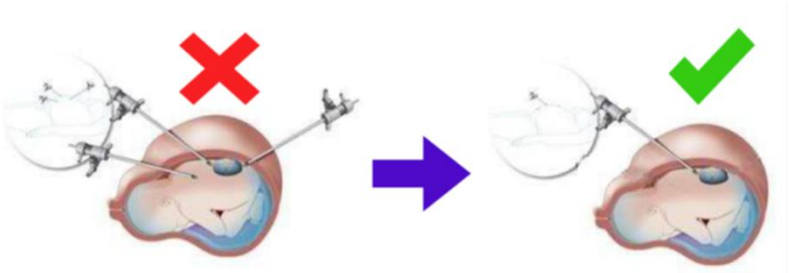

Figure 1.1 - Illustration depicting how the risk of iPPROM can be reduced. Reproduced and adapted from "The Clinical Challenge - GIFT-Surg." Retrieved July 14, 2020 (https://www.gift-surg.ac.uk/project/medical-conditions/).

1.1.5 Physiological pressure measurements

A key physiological parameter to monitor in the medical field is pressure. Knowledge of the pressure in vivo is an important physiological measurement. It can be used during the diagnostic process, for feedback during surgery or for the monitoring of conditions. With this in mind, there is a great need for stable sensors which provide accurate pressure measurements in healthcare. Across the body there is a large range of different pressures with each area/organ of the body having its own ideal pressure range. In a typical human body, the different pressures are normally categorised as Low pressure – approximately between 0 and 10 mmHg (e.g. capillaries, brain and bladder), Medium pressure – approximately between 15 and 115 mmHg (e.g. heart and lungs) and High pressure – approximately above 120 and up to a maximum normal pressure of 150 mmHg (e.g. hips and knees) (Clausen and Glott 2014; Correia et al. 2018; Poeggel, Tosi, et al. 2015). Away from normal physiological states the pressure range can vary drastically. Certain diseases can cause pressure drops as low as -75 mmHg (intra-alveolar and intra-tracheal measurements) and as high as 300 mmHg (aortic and left ventricular measurements) (Correia et al. 2018). When the pressure in an organ deviates from its normal values damage or reduced function can occur with varying degrees of detrimental outcomes (Clausen and Glott 2014). Due to the large range of pressures across the body pressure sensors are usually designed with a specific range and application in mind.

During minimally invasive intravascular procedures pressure measurements are made using disposable pressure transducers. These miniature transducers are inserted percutaneously (needle puncture through the skin) into the vasculature system (veins and arteries). The pressure measurements made can be used to assess the severity of coronary stenoses and determine if percutaneous coronary intervention (PCI) is required (Iwasaki and Kusachi 2010; Pijls et al. 1996). From these pressure measurements the fractional flow reserve (FFR) can be calculated. The FFR is defined as:

$$FFR = \frac{Q}{Q_N}$$

(1.1)

where Q_N is the normal myocardial flow without a stenosis and Q is the myocardial flow with a stenosis (Spaan et al. 2006). The FFR gives a ratio value of the flow through the stenosis with respect to the expected flow if there was no stenosis. The myocardial flows can be defined as:

$$Q = \frac{P_d - P_v}{R}, \quad Q_N = \frac{P_a - P_v}{R}$$

(1.2)

where P_d is the distal coronary pressure (after the stenosis), P_v is the coronary venous pressure, P_a is the proximal coronary pressure (before the stenosis), also known as the aortic pressure. R is myocardial resistance at maximum vasodilation (Iwasaki and Kusachi 2010; Spaan et al. 2006). To ensure the measurements are made at maximum vasodilation, patients are administered with a vasodilator called Adenosine (Pijls et al. 1996). Substituting into equation (1.1) gives:

$$FFR = \frac{P_d - P_v}{P_a - P_v}$$

(1.3)

Since the central venous pressure is generally close to zero this is negligible (Iwasaki and Kusachi 2010). Therefore, FFR can be given as:

$$FFR \approx \frac{P_d}{P_a}$$

(1.4)

After measuring the pressure at the distal and proximal ends of a stenosis and determining the FFR, values below 0.8 (i.e. where the narrowing results in a flow that is 80% or less of the normal flow) indicate that the stenosis should be treated with PCI along with medicated treatment (De Bruyne et al. 2014; Van De Hoef et al. 2013). Current pressure wire options for measuring the pressure clinically are expensive, can suffer from signal drift and are prone to electromagnetic interference from other equipment in the operating theatre (Achenbach et al. 2017; National Institute for Health and Care Excellence 2014).

The most popular pressure wires used in clinical practise are piezoelectric sensor based. Recent advances have seen fibre optic pressure sensors being developed to try and overcome the limitations of piezoelectric pressure sensors (see section 2.2). ACIST Medical have developed a microcatheter integrated with a fibre optic sensor that has a single monorail design and can be slid over any guidewire for use during FFR measurements (ACIST Medical 2017). The fibre optic pressure sensor used is based on a Fabry-Pérot design, making use of a silicon diaphragm (Diletti et al. 2015)

Work in this thesis focusses on polymer-based fibre optic pressure sensors. With fibre optic pressure sensors, the operating principle is based on optics instead of electronics. This optical solution removes the issue of electrical noise usually associated with electronic based sensors and also helps overcome limitations in miniaturisation, such as having pads to connect wires to. Fibre optic-based pressure sensors are also inherently compatible with MRI machines due to their lack of electromagnetic interference (EMI) (Roriz et al. 2013).

Through fibre optic sensing probes, physiological pressure measurements could be made in situ during minimally invasive procedures. The feedback from these sensors could be used to help evaluate the progression of procedures or help to identify issues that may arise.

1.1.6 Hydrophones

As well as being used to measure physiological pressure, optical fibre pressure sensors can also be used to detect acoustic pressure waves and build up ultrasound images. Coupling such detectors (hydrophones) with laser generated ultrasound transducers has led to all optical ultrasound imaging (Colchester et al. 2015).

Fibre optic hydrophones can overcome many of the shortcomings of piezoelectric polyvinylidene (PVDF) needle and membrane hydrophones. One such limitation for PVDF based hydrophones is creating element sizes smaller than the acoustic wavelength (in order to reduce spatial averaging errors) while still maintaining sensitivity, due to the fact that sensitivity decreases as element size decreases (Morris et al. 2009). Another limitation of PVDF hydrophones are that they are prone to damage when used in harsh environments such as the ultrasound field induced during high intensity focused ultrasound (HIFU) treatments. The damage is mainly due to cavitation and sharp temperature rises that are created during clinical HIFU (Morris et al. 2009). Compared to PVDF based hydrophones, fibre optic hydrophones can easily be manufactured with acoustically small element sizes due to the fibres

having small diameters. They are also flexible, robust, low cost and have immunity to EMI (Morris et al. 2009).

Increasing the sensitivity of fibre optic hydrophones would enable the detection of weaker ultrasound waves that may have reflected from a deeper location of the sample being imaged and allow for greater imaging depth.

1.2 Aims and Objectives

The overarching aim of this project is to create miniaturised imaging and sensing devices to aid with minimally invasive surgeries.

Currently there is a need in the medical field for reliable physiological pressure sensors. There is also a need for simpler fabrication of fibre optic hydrophones to aid with the uptake and expansion of optical ultrasound as an imaging modality. By utilising additive manufacturing techniques, such as high-resolution 3D printing, methods of fabricating these desired devices can be achieved. The development and exploitation of such manufacturing processes could also be applied to other applications both within and outside the medical field.

The following objectives were set up to achieve this aim:

- Develop techniques for printing high-resolution microstructures and precise material deposition
- Utilise high-resolution 3D printing to create polymer-based fibre optic pressure sensors
- Explore methods of adapting the fibre optic pressure sensors to enable the detection of ultrasound waves in all optical ultrasound imaging
- Investigate the feasibility of printing high-resolution microstructures directly onto the tips of optical fibres
- Examine other applications for such precision manufacturing techniques

1.2.1 Problem tackled

A key issue with the development of physiological pressure sensors and fibre optic hydrophones is centred around the convoluted manufacturing processes involved with fabricating them. To tackle this issue high-resolution 3D printing techniques were utilised as a method to easily and repeatably produce polymer-based membranes for fibre optic pressure sensors and fibre optic hydrophones.

By undertaking this work, further applications for the resultant manufacturing techniques were identified. The problem of manipulating laser generated ultrasound

beams at the tip of optical fibres was also investigated. A potential solution of using photoacoustic microscale structures was explored. High-resolution 3D printing was used to create acoustic holograms on the microscale scale for the first time and showed potential for reducing ultrasound beam divergence.

1.3 Thesis Outline

The work reported in this thesis is structured as follows. Firstly, a literature review of relevant subjects related to the work in this thesis is given in Chapter 2. This is followed by details of the fabrication and characterisation of novel parylene-C based fibre optic pressure sensors in Chapter 3. Chapter 4 investigates parylene-C based fibre optic hydrophones for optical ultrasound sensing. The work presented in Chapter 5 outlines the high-resolution 3D printing techniques developed and utilised throughout the project along with exemplar applications. Finally, Chapter 6 contains conclusions and discussions of the work presented and highlights the outlook for future work.

Chapter 2 – Literature Review

2.1 Introduction

A literature review relevant to the work undertaken in this thesis is contained in this chapter. The review covers a variety of topics necessary to fully explore the themes of this work.

It begins with an overview of minimally invasive surgery along with the tools and probes currently used in procedures. This gives an insight into the clinical environment where the resultant fibre optic sensors will be deployed.

The fundamentals of ultrasound imaging are then discussed along with the challenges associated with miniaturisation. These challenges highlight the advantages of using all optical ultrasound to aid with miniaturisation. The principles of all optical ultrasound are then outlined along with its use as an imaging modality.

This is followed by a review of fibre optic interferometric sensors. Interferometric sensors are typically used to optically detect ultrasound and other parameters. The manufacturing of the interferometric sensors is often complex and cumbersome, involving many multistep fabrication processes. Hence, in this work we aim to use high-resolution 3D printing as a convenient tool to manufacture and prototype miniature fibre optic imaging and sensing probes, while avoiding the limitations of previous procedures.

Following this, an outline of fluidic assisted additive manufacturing techniques and high-resolution 3D printing technologies are included, as these are the fabrication techniques that will be deployed throughout this work. Some of the key fluid mechanic features that influence fluidic assisted high-resolution 3D printing will then be explored to give a greater insight into how these technologies can be utilised to create highly miniaturised fibre optic imaging and sensing devices

2.2 Minimally invasive surgery

Minimally invasive surgery is now discussed. As the research in this thesis seeks to create imaging and sensing probes to enhance these types of clinical procedures a good understanding of the clinical environment is required. An appreciation of the

clinical environment was heightened by observing some of these clinical procedures being performed first-hand.

As described in section 1.1 minimally invasive surgical procedures have become more favourable to their traditional surgical counterparts due to their reduced risks, faster recovery times and decreased trauma. Despite this, there are still some limitations to performing procedures minimally invasively, owing in part to the spatial confinements of such operating environments. Minimally invasive procedures require specialised tools and imaging equipment to enable the procedure to be carried out through small incisions. There is an intrinsic lack of visual and tactile feedback compared to traditional 'open' surgeries. Providing better feedback to surgeons is a key area to improve on while working towards better and safer minimally invasive surgeries. Highly miniaturised imaging and sensing devices are one way to address this issue. Some of the options currently available to surgeons will now be discussed.

2.2.1 Miniaturised imaging tools

The success of many minimally invasive surgeries relies greatly on imaging, as direct open visualisation of the procedure is not possible (Skogås, J. , Myhre, H. , Ødegård, A. and Kiss 2016). The advances of minimally invasive surgeries have come hand in hand with advances in medical imaging. Pre-operative images have aided in the planning of minimally invasive procedures and post-operative images can be used to assess the success of procedures. Despite these, it is arguably the intra-operative imaging that proves to be most vital to minimally invasive procedures as surgeons require the indirect visualisation provided to safely carry out the procedures.

Several modalities have proven useful for intra-operative surgeries, with the most widely used being optical imaging. The miniature cameras used for optical imaging are called endoscopes. These tools are inserted into body cavities and illuminate the area. The light is then passed down optical fibres back out of the body where they can be viewed on a screen. Additional optical imaging techniques can also be employed alongside traditional optical imaging to give an insight beyond the surface of the tissue being imaged. Near-infrared fluorescence (NIRF) is one such technique. This method requires the use of a near-infrared fluorophore as a contrast agent. The fluorophore is injected and illuminated with near-infrared (NIR) light (700 – 900 nm). The illumination light is usually in the lower part of the NIR region. The fluorophore then fluoresces at a longer wavelength in the NIR region of the spectrum which can be captured by a NIR camera system to reveal additional anatomical information to a maximum depth of about 1 cm in real time (Schols, Connell, and Stassen 2015). This

technique has also shown potential for some minimally invasive procedures (Ashitate et al. 2011; Schols et al. 2013). It is limited by the need for a fluorophore to be injected and the reduced penetration depth available.

Another optical addition is optical coherence tomography (OCT). There are several different variations of OCT, but it is mainly based on the interference between two light signals. The initial light source is split to give two light paths, a reference and an object/imaging path. Each path has an associated path length. The difference between the two is called the optical path difference. Variations in the resulting interference between the two beams are then detected as long as the optical path length is less than the coherence length of the light source (Podoleanu 2012). By altering the reference path length, different depths of the object can be interrogated to build up a reflectivity profile. By collecting these profiles at adjacent points, images can be generated in a similar manner to ultrasound images (Podoleanu 2012). OCT systems have been used for some minimally invasive surgeries by miniaturising the systems and providing real time feedback for ophthalmic procedures (Li et al. 2014). Unlike NIRF a contrast agent is not required but OCT is limited by a shallow penetration depth of about 2 mm which prevents its use with deeper tissues (Schols et al. 2013).

Apart from the optical modality for intra-operative imaging, ultrasound can also be used. Despite the many uses of ultrasound transducers outside the body to view inside the body intra-operatively, it is currently not fully utilised for *in situ* imaging. However, endoscopic ultrasound (EUS) does make use of miniaturised ultrasound imaging tools to guide minimally invasive procedures. Initially a small ultrasound transducer was incorporated onto the tip of an endoscope. This design was then modified to create a catheter-based ultrasound probe with a mechanical, rotatable transducer that could be inserted through the inner channel of endoscopes. The catheter probes are 1-3 mm in diameter and can achieve penetration depths of about 20 mm (Santander et al. 2017). EUS has been used to diagnose esophageal disorders and to guide minimally invasive surgeries (Das et al. 2001; Pai et al. 2015; Yoshinaga et al. 2012). Compared to NIRF and OCT the penetration depth of EUS is much greater. However, a limitation of EUS is coupling the ultrasound waves to the tissue in air filled cavities. Novel solutions have been developed to overcome this issue, including instilling liquid into the oesophageal cavity or filling a balloon sheath over the end of the probe (Santander et al. 2017). As blood vessels and the intrauterine environment are fluid filled regions this coupling problem is intrinsically resolved and shows how well suited a miniature ultrasound imaging probe would be

for cardiovascular and fetal surgery applications. Dausch *et al.* have demonstrated *in vivo* intravascular ultrasound imaging experiments on animal models using miniature piezoelectric ultrasound arrays. The wired arrays were integrated into a 14 Fr (4.5 mm outer diameter) catheter. The catheter was filled with water to enable acoustic transmission from the elements to the blood. Details of the complex fabrication, cabling procedures and resultant images can be found in the reference (Dausch et al. 2014).

2.2.2 Miniaturised fibre optic sensing probes

There are many different types of sensors used during medical procedures. With such an array of sensors there is also a variety of sensing mechanisms. This section will focus on fibre optic based medical sensors. However there is promising work on microelectromechanical system (MEMS) based sensors in medicine also (Citerio et al. 2008; Mansouri and Shaarawy 2011; Polla et al. 2000; Roriz et al. 2013; Voldman, Gray, and Schmidt 1999).

A recent report has estimated that the total optical sensing market will grow to reach USD 3.47 billion by 2023 with the medical sector predicted to show some of the fastest compound annual growth rates (CAGR) (Markets and Markets 2017). With this in mind, many companies have been researching and releasing fibre optic sensing products specifically targeting medical applications.

One of the largest commercial companies providing fibre optic sensors are FISO Technologies (FISO Technologies 2019a; Poeggel, Tosi, et al. 2015; Roriz et al. 2013). They provide a range of pressure and temperature sensors of varying dimensions down to 200 µm. Their pressure sensors are based on Fabry-Pérot cavities and have a range of ±300 mmHg relative to atmospheric pressure with system accuracies of ±3 mmHg (FISO Technologies 2019a; Korolev and Potapov 2012). The temperature probes offered have a working range of 10 – 90 °C with system accuracies of ±0.5 °C (FISO Technologies 2019b; Korolev and Potapov 2012). FISO sensors are manufactured in accordance with ISO 13485:2016 (Quality management systems for medical devices) and have been successfully integrated into FDA and CE approved devices (FISO Medical 2020).

Another company offering fibre optic sensors for the medical market is Opsens Medical. Their main commercial product is the OptoWire 2nd Generation Fiber Optic Pressure Guidewire. This guidewire is designed for use in cardiovascular applications to perform Fractional Flow Reserve (FFR) (Opsens 2019). FFR is used to identify lesions responsible for ischemia. The nitinol guidewire has a fibre optic pressure

sensor embedded in the tip. It has been shown that this fibre optic pressure guidewire can reduce the frequency of severe pressure drift while making FFR measurements during cardiovascular procedures compared to conventional piezoelectric pressure guidewires (Tateishi et al. 2018).

Other companies, such as Maquet Getinge Group, RJC Enterprises and Arrow/Teleflex, have developed intra-aortic balloon catheters with integrated fibre optic pressure sensors (Korolev and Potapov 2012; Maquet Getinge Group 2019; RJC Enterprises 2020; Schreuder et al. 2005). The catheters are used with intra-aortic balloon pumps (IABP) to inflate and deflate the balloon at the correct part of the cardiac cycle in order to assist the heart during unstable angina or after a heart attack (Limbert and Amiri 2019). The Fabry-Perot based fibre optic pressure sensor in the catheter is used to record the aortic pressure waveforms so that the inflation and deflation of the balloon can occur at the correct time in the cardiac cycle. The use of fibre optic sensors in this application enables faster transmission of the measured pressure wave to the IABP and allows for smaller catheter design.

Neoptix is also a company with commercially available fibre optic sensors. They focus on temperature measuring fibre optic sensors for medical applications. The sensors are based on gallium arsenide (GaAs) crystals. As the temperature increases the crystals transmission spectrum shifts to higher wavelengths. By measuring the position of the shift, the temperature can be determined. Their sensor probes have a working range of -270 to +250 °C and an accuracy of ±0.2 °C (Korolev and Potapov 2012; Neoptix 2017). The Neoptix T1 probe has a sensing diameter of 400 µm. As fibre optic sensors are immune to electromagnetic interference these temperature probes have found use in temperature monitoring during MRI procedures and radiofrequency hyperthermia treatments (Schena et al. 2016).

2.3 Ultrasound imaging

Traditional ultrasound imaging will now be examined in more detail as it is an imaging modality of particular interest to this work. Many of the traditional ultrasound imaging principles and techniques are continued through to optical ultrasound. Much work has gone into replicating the capabilities of traditional ultrasound probes with miniature optical ultrasound probes instead. The end of this section describes some of the challenges of miniaturising traditional ultrasound transducers and how optical ultrasound can easily be adapted to overcome these. This section relates to the work in Chapter 5 to manipulate optical ultrasound fields.

Ultrasound has proven to be extremely useful in modern medicine. Since its introduction to the medical field in the latter half of the 20th century by H. Gohr and T. Wedekind it has found widespread use in clinics as an imaging modality due to its relatively cheap cost, ease of use and good safety profile. Ultrasound is non-ionising and thus does not have the potential to ionise atoms and cause damage to cells. The non-ionising property has led to the use of ultrasound in areas such as fetal medicine, where cell damage can have far greater implications on developing fetuses. Magnetic resonance imaging (MRI) is another non-ionising imaging modality that can be safely used on a fetus, but the associated financial costs of MRI are much greater. Outside fetal medicine ultrasound is used in many other areas of the body to image structures such as the heart and blood vessels. Focused ultrasound can also be used as technique to treat tumours, but the focus of this work is on generating and sensing ultrasound for applications such as imaging.

2.3.1 Principles of ultrasound imaging

Ultrasound waves are longitudinal/compressional waves with frequencies higher than 20,000 Hz, making them inaudible to humans. The idea behind ultrasound imaging is similar to that of ultrasonic detection systems such as SONAR (sound navigation and ranging) which can be used to detect submarines. Similar methods are also seen in nature such as bats using sound waves (echolocation) to navigate in the dark. In essence, sound waves are emitted from a source and as they travel away from the source they interact with objects. During the interactions at the interface of these objects, a portion of the wave is reflected back towards the source where a detector is used to detect them. By measuring the time between wave emission and detection (and knowing the speed of the wave) then the distance to the object can be calculated and this information can be used to determine where the objects are, or plot images. This is known as pulse-echo. Along with this basic principle, the strength of the reflected waves can also be measured and used to add further detail to the generated ultrasound images. The strengths of the reflected waves are converted to a brightness scale and can provide information to allow for differentiation between anatomical structures.

Traditional ultrasound transducers generate ultrasonic waves by utilising the piezoelectric effect (the conversion of electrical energy to mechanical energy and vice versa). When a piezoelectric material is stretched or compressed, an induced voltage can be measured across it. Conversely, when a voltage is applied to the material it will undergo an induced compression or extension. The duality of this effect has led to its use in ultrasound transducers. By applying voltages, mechanical movement can

be induced and cause ultrasound waves to be generated. As well as this, when the reflected waves reach the transducers their pressure compresses the same material and induces a voltage which is used to detect the reflected waves and determine their strengths. Thus, easily enabling both generation and detection in a single transducer.

The distance calculations in ultrasound imaging assume a constant velocity for the sound waves. In medical applications the speed of sound in tissue is often taken to be 1540m/s but this depends on the tissue. Some other assumptions are also used to simplify these calculations. Firstly, the biological tissue is assumed to be a liquid. This may appear abstract but the defining difference for waves in a solid or a liquid is that solids can support shear waves and liquids cannot. Shear waves are those where the oscillations are perpendicular to the direction of travel and the forces act across the surface. Therefore, assuming that the tissue behaves as a fluid is the same as neglecting shear waves. This assumption holds well for ultrasound imaging as the transducers do not efficiently produce shear waves. Any shear waves that are produced are also attenuated rapidly as they propagate through the tissue. On top of this, the propagation speed of shear waves is much slower than the compressional ultrasound waves, so they do not interfere with detected wave measurements. Another assumption that is made is called the continuum hypothesis. This hypothesis states that the tissue which the ultrasound is travelling is a continuous continuum, so it cannot be broken down into smaller constituents. The continuum hypothesis is a standard approximation in fluid dynamics and means that any spacing/gaps between the molecules in the tissue is small enough to be negligible. These assumptions all aid in the rapid calculations required to generate real-time ultrasound images.

The reflected ultrasound waves are caused by acoustic impedance mismatches at boundaries (note: the waves are usually only partially reflected, and the transmitted part continues to propagate and generate the rest of the image behind the object). Acoustic impedance is a measure of the resistance to travel imparted on the wave by the propagating medium. The acoustic impedance of a medium can be calculated by multiplying the density of the medium by the speed of sound in the medium.

$$Z = \rho c \tag{2.1}$$

Where Z is the characteristic acoustic impedance of the material, ρ is the density of the material and c is the speed of sound in the material.

At acoustic impedance boundaries two conditions must hold:

- Continuity of pressure – therefore no net force
- Continuity of normal particle velocity – therefore fluid must stay in contact

At the boundaries, the waves partially reflect. Following these boundary conditions, the amplitudes of the reflected and transmitted waves can be deduced. The pressure reflection coefficient (R) is the ratio of the reflected pressure (p_r) over the initial pressure (p_i) and is given by the equation below, where the indices 1 and 2 represent materials 1 and 2, respectively.

$$R \equiv \frac{p_r}{p_i}, \quad R = \frac{\rho_2 c_2 - \rho_1 c_1}{\rho_2 c_2 + \rho_1 c_1} = \frac{z_2 - z_1}{z_2 + z_1}$$

(2.2)

The pressure transmission coefficient (T) is given by the ratio of the transmitted pressure (p_t) over the initial pressure (p_i):

$$T \equiv \frac{p_t}{p_i}, \quad T = \frac{2\rho_2 c_2}{\rho_2 c_2 + \rho_1 c_1} = \frac{2z_2}{z_2 + z_1}$$

(2.3)

When the pressure coefficients are incident normal to the boundary, they can be related as $T = 1 + R$. As well as pressure coefficients, the boundary interactions can also be analysed using the energy coefficients R_e and T_e. R_e is the energy reflection coefficient and T_e is the energy transmission coefficient. These coefficients give the fraction of energy that is either reflected or transmitted. When using energy coefficients to analyse the interactions the relation between the coefficient's changes, compared to the pressure coefficients relation, to become $R_e + T_e = 1$, since the conservation of energy must now be observed. The two different coefficients can also be related, since intensity is proportional to pressure squared. This relation gives $R_e = R^2$ and $T_e = 1 - R^2$.

Ultrasound imaging can be performed in several ways. The simplest is using a single stationary ultrasound beam to determine the distance to a boundary. The amplitude of the reflected wave will also give information about the type of boundary it is since the amplitude is related to the reflection coefficient and in turn related to the acoustic properties of the material either side of the boundary. This single beam scan is called A-mode imaging.

A collection of A-mode scans from the same location can be used to generate an M-mode scan. M-mode scans are brightness modulated and show how the positions of

boundaries are moving in time. This type of scan is useful when analysing structures in the heart such as valves and chamber walls.

By spatially moving the ultrasound beam, a collection of A-mode scan lines can be gathered. These individual scan lines can be stitched together to generate a brightness modulated image showing depth and horizontal displacement, this is called a B-mode scan. In practise multiple elements in a transducer head can be used to generate the spatial changes without having to actually move the transducer.

Finally, 3D ultrasound scans can be generated by combining B-mode scans from two different orientations. It is difficult to align multiple one-dimensional scans so usually a two-dimensional array transducer is used. A converter is generally required to correctly combine the scans to generate the 3D images.

2.3.2 Challenges for miniaturisation

Traditional ultrasound transducers are made from piezoelectric materials, one of the most commonly used is lead zirconate titanate (PZT). PZT is a piezoelectric ceramic material and on the macroscale can easily be machined to create ultrasound transducers. Bulk piezoelectric ceramics, such as PZT, are preferred for fabrication as they have high piezoelectric constants (Wang et al. 2018). Actuators that are larger than ~2 mm in size can be processed using traditional grinding techniques (Morita 2003). Other machining techniques such as laser cutting have also been investigated (Li et al. 2002; Ohara et al. 1994).

When moving to miniaturised transducers some fabrication issues begin to emerge. The machining, polishing and dicing of piezoelectric ceramics becomes difficult on the microscale largely due to the small size and thickness of the material. Standard micromachining technologies have been found to struggle with this processing (Jung et al. 2017). Defects such as fractural damage, porosity and unlevel surface uniformity have been reported (Wang et al. 2018). Alternatives such as laser cutting and wafer sawing have proven to be more successful (Jung et al. 2017). Even after the piezoelectric ceramic is processed Brown *et al.* report difficulties in making electrical connections to the electrodes for a 2 mm diameter annular array (Brown, Démoré, and Lockwood 2004). To try and overcome these issues the industry has adopted microelectromechanical system (MEMS) technology.

Using MEMS technology, micromachined ultrasonic transducers (MUTs) have been developed. These can be categorised as capacitive MUTs (cMUTs) or piezoelectric MUTs (pMUTS). pMUTs are generally preferred as cMUTs have low ultrasonic

intensity and require a high bias voltage (Jung et al. 2017; Wang et al. 2018). Alternative piezoelectric materials have been investigated for use in pMUTs. These include piezoelectric polymers and piezoelectric ceramic/polymer composites (Wang et al. 2018). Unfortunately, the manufacturing processes for creating pMUT devices are complex and consist of many multi-step procedures. Some of the processes utilised during these procedures are spin coating, grinding, mechanical polishing, chemical polishing, sputtering, electron-beam deposition, chemical etching, photolithography, oxide etching, deep reactive ion etching (DRIE), physical vapour deposition, chemical vapour deposition (CVD) and plasma-enhanced chemical vapor deposition (PECVD) (Jung et al. 2017; Wang et al. 2018).

Due to these highlighted limitations, optical ultrasound has emerged as a convenient alternative for easily creating miniaturised ultrasound transducers. Optically generated ultrasound enables some of the complex fabrication procedures associated with miniature piezoelectric transducers to be avoided as well as removing issues surrounding electrical connections and cross talk. Optical ultrasound is the modality of choice for this work and will be of particular interest in Chapter 5. It is examined in more detail below.

2.4 Optical ultrasound generation

The photoacoustic effect is the conversion of light energy to sound energy. It was first discovered by Alexander Graham Bell in 1880 (Beard 2011). He observed that acoustic waves could be created when pulses of light were absorbed by certain materials (Beard 2011). This effect can be adapted and used as an imaging modality, photoacoustic tomography (PAT). PAT relies on the chromophores in tissues to act as the absorbing medium. Ultrasound is generated via the thermal expansion/thermoelastic mechanism (Tam 1986). Nanosecond laser pulses in the NIR spectral region (~750 → 1800 nm) are shone onto the surface of the tissue. The light penetrates the tissue to a depth of a few centimetres and as the photons propagate, they are scattered by the tissue which causes them to spread out and illuminate the area of interest. Chromophores in the tissue, such as haemoglobin, absorb the scattered laser light. The absorbed energy causes a slight temperature increase in the tissue (less than 0.1 K) (Beard 2011). Though the increase in temperature is small, due to the short duration of the pulse there is an associated pressure increase. The elastic property of the tissue then pulls it back to its original equilibrium position as it cools. The action of this expansion and contraction releases an acoustic wave from the chromophores with an amplitude less than 10 kPa (Beard

2011). This wave can then propagate back to the surface of the tissue where it can be detected using traditional piezoelectric based ultrasound detection techniques and used to form an image. The resulting image will show regions of absorption depending on the wavelength of laser/absorbing chromophore. For example, in the case where haemoglobin absorbs the light, blood vessels will be highlighted since haemoglobin is present in red blood cells and red blood cells are confined to blood vessels. PAT is limited by the short penetration depth achievable by the NIR laser pulses in tissue. This confines its obvious applications to shallow imaging depths or areas of the body that are easily illuminated e.g. the throat.

The photoacoustic principles of PAT can be modified to create alternative imaging techniques. For example, laser generated ultrasound can be created by changing the position of the absorbing medium. In PAT the absorbing medium is located within the tissue/imaging sample but by moving this to an external location an optical ultrasound transducer can be produced. The transducer can then be coupled to the sample and used in the same way as traditional piezoelectric ultrasound for imaging. Initially there was great interest in using laser generated ultrasound transducers for non-destructive testing (NDT). Some advantages of laser generated ultrasound are that it has non-contact excitation, high bandwidth and can be used in hostile environments where piezoelectric solutions struggle (Scruby 1989). These advantages also make it a good technique for medical applications. By depositing the absorbing material at the tip of an optical fibre, the optical ultrasound transducers can also be made to be highly miniaturised for use in minimally invasive interventions. A schematic diagram of how fibre optic ultrasound probes work is shown in Figure 2.1.

There are several different models in literature for describing the process of generating ultrasound waves in the thermal expansion/thermoelastic regime (Truong et al. 2018). Initial models developed analytical solutions, but these were simplified so that solutions could be reached. Several different models have been proposed to try and predict the features and enable optimization of laser generated ultrasound systems (Arias and Achenbach 2003; Rose 1984; Scruby et al. 1980; Spicer and Hurley 1996). When the models become too complicated, due to complex geometries or temperature dependant variables, finite element methods (FEM) can be used (Truong et al. 2018; Wang et al. 2007).

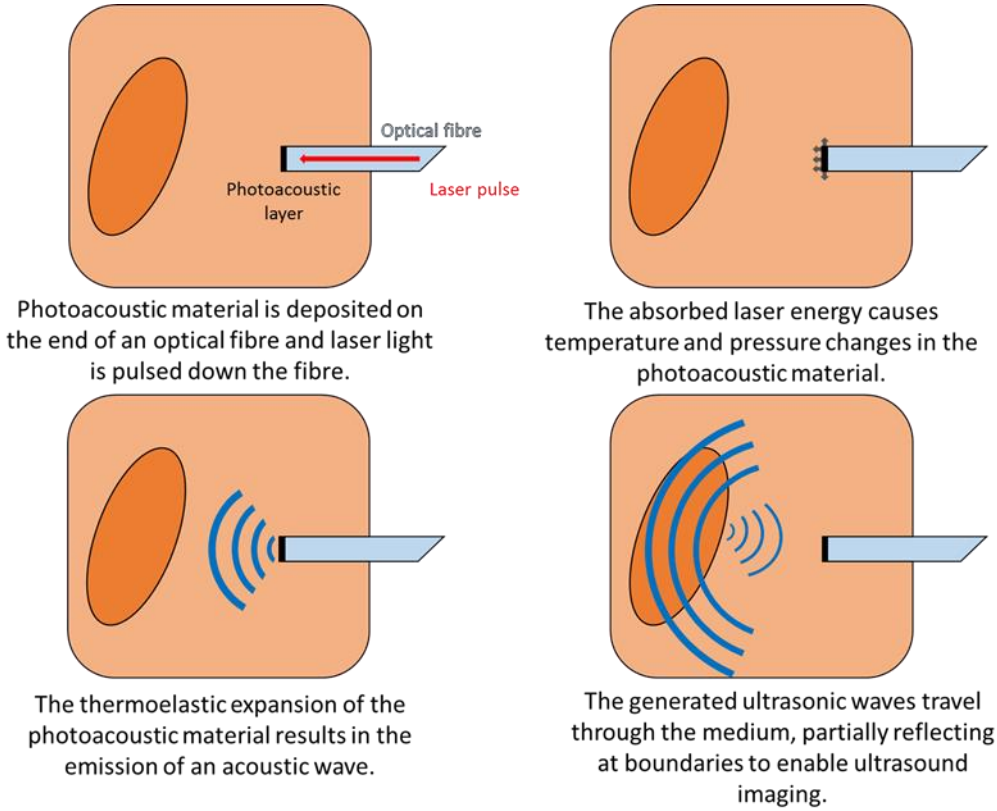

Figure 2.1 – Schematic diagram highlighting the key stages for miniaturised laser generated ultrasound probes.

A simplified thermodynamic approach was described by Wang *et al.* (Wang and Wu 2007) to explain the initial pressure generated. This approach makes two assumptions that must be held: stress confinement and thermal confinement. These assumptions enable stress propagation and thermal propagation to be assumed as negligible during heating. The conditions for these assumptions to be upheld are that the stress relaxation time and the thermal relaxation time must be greater than the pulse width of the excitation laser pulse.

$$\tau_s = \frac{d_c}{v_s} \gg \tau_l \tag{2.4}$$

where τ_s is the stress relaxation time, d_c is the characteristic dimension, v_s is the speed of sound and τ_l is the laser pulse width.

$$\tau_{th} = \frac{{d_c}^2}{\alpha_{th}} \gg \tau_l \tag{2.5}$$

where τ_{th} is the thermal relaxation time and α_{th} is the thermal diffusivity.

The fractional change in volume V can be expressed as:

$$\frac{dV}{V} = -\kappa\, dp + \beta\, dT \tag{2.6}$$

where κ is the isothermal compressibility, β is the thermal coefficient of volume expansion, dp is a change in pressure (in Pa) and dT is a change in temperature (in K).

Applying the conditions of stress and thermal confinement to equation (2.6) results in negligible volume change and it can be rewritten as:

$$dp = \frac{\beta\, dT}{\kappa} \tag{2.7}$$

Hence, the change in pressure is directly proportional to the change in temperature. The instantaneous change in temperature is defined in terms of optical energy as:

$$dT = \frac{\eta_{th}\, \mu_a\, F}{\rho\, C_v} \tag{2.8}$$

where η_{th} is the thermalisation efficiency (a measure of how much absorbed energy is converted into heat), μ_a is the optical absorption coefficient, F is the incident optical fluence (J/cm^2), ρ is the mass density and C_v is the specific heat capacity at constant volume. Combining equation (2.7) and equation (2.8) results in:

$$dp = \frac{\beta}{\kappa\, \rho\, C_v}\, \eta_{th}\, \mu_a\, F = \Gamma\, \eta_{th}\, \mu_a\, F \tag{2.9}$$

where $\Gamma = \frac{\beta}{\kappa\, \rho\, C_v} = \frac{\beta\, {v_s}^2}{C_p}$ is the Gruneisen parameter, a dimensionless parameter which describes the efficiency with which incident optical energy is converted into pressure (Wang and Wu 2007) and where C_p is the specific heat capacity at constant pressure and v_s is the speed of sound in the medium. This expression for the initial pressure shows what parameters need to be optimised in order to increase the efficiency of ultrasound generation and maximise the generated pressure. To do this, the Gruneisen parameter (and hence the thermal coefficient of volume expansion) should be maximised, along with the thermalisation efficiency and the optical

absorption coefficient for a given incident optical fluence. To create optical ultrasound transmitters with good efficiency and pressure generation composite materials are usually used to combine polymers possessing a high thermal coefficient of volume expansion with optical absorbers that have a high optical absorption coefficient. It should be noted that when increasing the optical absorption there will also be an increase in the induced heating in the material. It should also be mentioned that any fluorescence of the absorber will detract from the thermalisation efficiency (Stahl, Allen, and Beard 2014). Thus, to maximise optical absorption coefficient and the thermalisation efficiency, absorbers with little or no fluorescence should be used.

Using the photoacoustic effect, optical ultrasound transmitters can then be designed to efficiently transmit ultrasound.

2.5 Optical ultrasound transmitters

In traditional ultrasound transducers, piezoelectric elements are used to generate ultrasound waves. As discussed in the previous section, for optical ultrasound generation the choice of material is critically important for optimising the relevant parameters for efficient pressure generation. The chosen material should have high optical absorption, low heat capacity and a large thermoelastic expansion coefficient (Chen and Sung-Liang 2016).

Different absorber materials will be explored in this section in order to choose appropriate materials when designing photoacoustic inks and creating photoacoustic structures, underpinning work in Chapter 5.

Early investigations into optically generated ultrasound used thin films of metals as they have good optical absorption. Despite this metal films have low thermal expansion coefficients, in the region of approximately $0.1\text{-}0.2\text{x}10^{-4}$/K so the overall efficiency was poor (Buma, Spisar, and O'Donnell 2001; Guo et al. 2011). Polydimethylsiloxane (PDMS) has become a popular choice of material to improve the efficiency of generating ultrasound via the thermo elastic mechanism due to its large value of thermal expansion coefficient, $3.1\text{x}10^{-4}$/K (Buma et al. 2001; Guo et al. 2011). This thermal expansion is an order of magnitude larger than that of metal films but PDMS is a transparent polymer and has very poor optical absorption. Composite materials are generally made by combing PDMS with optical absorbers to create materials that have high thermal expansion coefficients as well as good optical absorption. With regards to the absorbing material, these can be categorised as metal

absorbers and carbon-based absorbers. Each of these types of absorbers will now be explored.

2.5.1 Metal absorbers

Creating laser generated ultrasound by irradiating metals was first proposed by White (White 1963). Metal films can create ultrasound by different mechanisms such as ablation and thermoelastic. The focus here will be thermoelastic as it is a non-destructive mechanism.

Gold (Au) nanoparticles (NP) (AuNP) have been used in several studies for optically generating ultrasound. One study created a 2D gold nanostructure of Au nanoparticles (Hou et al. 2006). The gold nanostructure was sandwiched between a transparent substrate and a 4.5 µm layer of PDMS. This technique was reported to produce ultrasound in the 100 MHz frequency range. Another study by Wu *et al.* used gold nanoparticles in a one pot synthesis method to create AuNP/PDMS composite films (Wu et al. 2012). Different thicknesses and concentrations of AuNP were used to optimise the ultrasound generation. The films were reported to give increased efficiency of 3 orders of magnitude when compared to a thin aluminium film generation method.

Apart from AuNPs other metallic absorbers have been investigated. Hwan Lee *et al.* describe how their work with a thin film of aluminium (Al) coated in reduced graphene oxide (RGO) led to an enhanced optoacoustic pressure 64 times that of an uncoated film (Hwan Lee et al. 2012). The improvement is thought to be due to the high thermal conductivity of the RGO. RGO is also combined with PDMS in a separate study that will be discussed in more detail in the following section (R. J. Colchester, Alles, and Desjardins 2019). Other metals that have been used to optically generate ultrasound are molybdenum, chromium and germanium (Von Gutfeld and Budd 1979; Yoo et al. 2016). Yoo *et al.* showed that by nanostructuring germanium it created pressure waves with an amplitude 7.5 times greater than a reference thin film chromium transmitter. Work has also been undertaken to explore one dimensional photonic crystal-metallic structures capable of high efficiency, wavelength selective, optical absorption (Guo et al. 2011).

2.5.2 Carbon-based absorbers

Carbon-based absorbers can be used as alternatives to metallic absorbers. Biagi *et al.* showed that by mixing graphite powder with epoxy, broadband ultrasound could be generated using a pulsed laser (Biagi, Margheri, and Menichelli 2001). They found

that the efficiency was two orders of magnitude larger than that of a reference thin film chromium transducer. Buma *et al.* used a slightly different technique and combined carbon black (CB) with PDMS to create a composite they term “black PDMS” (Buma et al. 2001). The black PDMS showed an efficiency increase of 24 dB compared to a reference chromium film. CB/PDMS was also used to generate ultrasound in (Hou et al. 2007). In this work they optimised the manufacturing of the black PDMS films so that they could create thinner films. Buma *et al.* had films which were 25 µm thick but the optical absorption was estimated to occur over only ~1 µm. By creating thinner films about 11 µm thick, excess CB/PDMS which was attenuating the generated ultrasound as it propagated through the film was removed. The thinner films enabled a further increase in efficiency of 11 dB compared to the initial black PDMS films. Further work has been done to investigate the use of candle soot nanoparticles (Chang et al. 2015) and carbon nanofibers (Hsieh et al. 2015) with PDMS and has shown that increased peak pressures can be generated compared to CB/PDMS.

Carbon nanotubes (CNT) composites have also been shown to generate high-frequency ultrasound with high efficiency (Baac et al. 2012, 2015; Colchester et al. 2014; Won Baac et al. 2010). CNT composites have demonstrated impressive efficiency 5 times greater than that reported for the AuNP/PDMS films (Hou et al. 2006). Some benefits of using CNTs is that nanoscale dimensions allow for fast heat transition and enables high-frequency ultrasound generation. They also have excellent thermal conductivity which allows for greater efficiency compared to AuNPs. The high damage threshold of CNTs also permits higher pressure waves to be created.

2.5.3 Transmitter design

Apart from the materials used, the design of the optical ultrasound transmitter and its geometry is also important in determining the overall performance. In its simplest form the transmitter is a planar film irradiated with laser pulses. The geometry can be extended to produce focused ultrasound by forming the film in a concave shape to create an optoacoustic lens. Arrays of transmitters can also be made to enable beam steering and high-resolution imaging. A selection of these designs are illustrated in Figure 2.2. The main transmitter design of interest for this work is fibre optic transmitters. This design is favourable as it allows for highly miniaturised, flexible transmitters which are well suited for the minimally invasive surgery applications of this work.

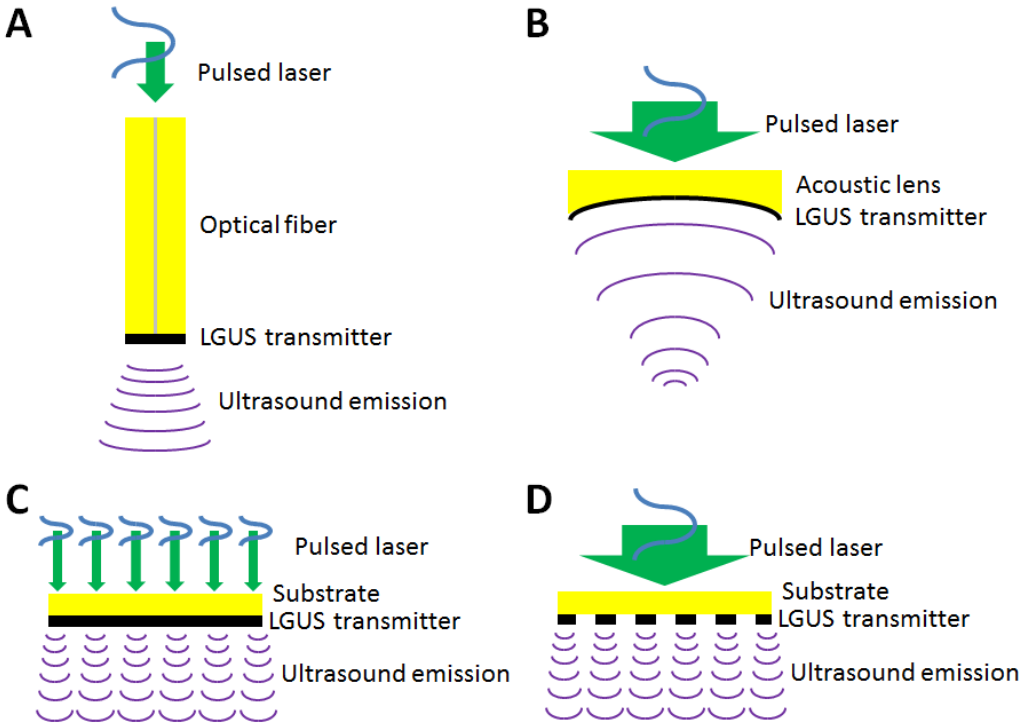

Figure 2.2 – Schematics of optical ultrasound transmitters: a) fibre optic transmitter, b) focussed optoacoustic lens transmitter, c) array transmitter where the pitch is defined by the spatially selective laser pulses, d) array transmitter where the pitch is defined by spatially variable absorber regions. The blue lines represent short laser pulses. Reproduced from (Chen and Sung-Liang 2016).

2.5.4 Fibre optic ultrasound transmitters

Designing laser generated ultrasound transmitters at the tip of optical fibres offers a unique way for highly miniaturised devices to be created. Such ultrasound probes could be used for *in vivo* imaging during many minimally invasive surgical procedures, including intravascular ultrasound (IVUS) and fetoscopic procedures. So far, most of the optical ultrasound transmitters discussed in this thesis have been created on the centimetre scale using manufacturing techniques such as spin coating to achieve thin film formations. Due to the dimensional restrictions of optical fibres, manufacturing techniques such as spin coating are not appropriate and have many challenges when applying to optical fibres.

One technique used by Tian *et al.* was to deposit a layer of gold onto an optical fibre with sputter coating. Additional focused ion beam (FIB) treatment was then applied to create highly absorptive gold nanopores in the gold layer on the fibre surface (Tian et al. 2013). The resulting transmitter produced ultrasound with an amplitude of 2.73 kPa and a 3-dB bandwidth of 7 MHz. Wu *et al.* deposited gold onto fibres in a different way. The fibre was initially submerged in a solution of polyethylenimine (PEI) polymer

and then dipped into a suspension of AuNPs to deposit the AuNPs onto the PEI layer. This process created a bilayer of AuNP/PEI at the fibre tip. The process was repeated to build up multiple bilayers on the fibre. Wu *et al.* reported ultrasound peak to peak pressures of 2.44 kPa and increasing the number of bilayers increased the generated pressure (Wu, Sun, and Wang 2011). The optical fibre transmitters reported by Tian *et al.* and Wu *et al.* were highly miniaturised, but the resultant pressures were not large enough for effective ultrasound imaging (~MPa). Zou *et al.* developed a composite of AuNP/PDMS using a one pot protocol and were able to dip coat it onto the end of optical fibres due to the high viscosity of the composite (Zou et al. 2014). This method produced ultrasound with larger amplitudes of 0.64 MPa and a bandwidth of 20 MHz. The resulting probe was then used to image a tissue sample with a resolution of 200 µm. Noimark *et al.* have demonstrated further ways of creating AuNP/PDMS composites on optical fibres by using 'top-down' manufacturing techniques (Noimark et al. 2018). The PDMS is initially dip coated onto the tip of the optical fibre and cured. The cured PDMS is then submerged in gold salt solution and the gold salt is reduced to gold nanoparticles in-situ, which embed themselves top-down into the layer of PDMS. This method of embedding AuNP into PDMS has proven to be effective (Dunklin et al. 2013; Goyal et al. 2009; Noimark et al. 2018; SadAbadi et al. 2012; Zhang et al. 2008). Noimark *et al.* achieved peak to peak pressures of 0.41 MPa with the AuNP/PDMS fibre optic transmitters and imaged swine abdominal tissue ex vivo.

Carbon-based fibre optic ultrasound transmitters have also been developed. Colchester *et al.* and Noimark *et al.* both used functionalised multiwalled carbon nanotubes (MWCNT) dispersed in PDMS to create a composite that could be applied to optical fibres by dip coating (Colchester et al. 2014; Noimark et al. 2016). A peak ultrasound pressure of 0.89 MPa at a distance of 2 mm and a corresponding bandwidth of 15 MHz was reported by Colchester *et al.* (Colchester et al. 2014). Pressures in excess of 3 MPa at 3 mm and corresponding bandwidths of 30 MHz were seen by Noimark *et al.* (Noimark et al. 2016). The higher pressures reported by Noimark *et al.* were due to optimisation of the coating technique, enabling thinner coatings to be achieved. Noimark *et al.* also demonstrated that bilayer coatings could be created by dip coating the MWCNTs dispersed in solvent onto optical fibres and then applying a PDMS layer on top (Noimark et al. 2016). The bilayer technique enabled thin submicron thick layers of dense MWCNT to be deposited and the over coating PDMS which infiltrated through this. The resultant ultrasound pressure from the bilayer technique was up to 4.5 MPa at a distance of 3 mm from the coating, with

a corresponding bandwidth of around 30 MHz (Noimark et al. 2018). Colchester *et al.* also created a bilayer design fibre optic transmitter. For this they first dipped 600 µm fibres into a functionalised RGO solution. Once dried, the fibres were then dipped into a PDMS solution to create an over coat. They reported pressures in excess of 0.4 MPa at a distance of 16 mm and a bandwidth of 24.3 MHz (R. J. Colchester et al. 2019).

Another coating mechanism investigated by Poduval *et al.* is electrospinning. Electrospinning was utilised to deposit MWCNT mixed with polyvinyl alcohol (PVA) directly onto the end of optical fibres. The electro spun fibres were then over coated with PDMS. The electrospinning of MWCNT/PVA allowed precise control over the coating thickness and also aligned the MWCNTs as they were deposited, enhancing their optical absorption (Poduval et al. 2017). Biagi *et al.* employed a different manufacturing method to create fibre optic ultrasound transmitters. In their design the absorbing material is carbonised photoresist. It is carbonised onto a micromachined silicon Micro Opto Mechanical System (MOMS) substrate that fits over the end of an optical fibre where it can then be secured in place (Biagi et al. 2009). The device was used to perform imaging of a 50 eurocents coin. The additional silicon MOMS support does increase the overall size of the device, but the dimensions still remain small enough for use in in-situ medical applications.

Fibre optic ultrasound transmitters have also been designed to emit ultrasound from the side wall of a fibre instead of the front face. Kochergin *et al.* reported how they removed the cladding from an optical fibre and replaced it with a graphite/epoxy composite to generate ultrasound (Kochergin et al. 2009). More recently Colchester *et al.* have reported how they are able to generate ultrasound from the side wall using their MWCNT/PDMS coating (Richard J. Colchester et al. 2019). Their technique involves polishing the fibre tip to create a 45° angled mirror to reflect the light outwards. The polished fibre is positioned in a housing which aligns the MWCNT/PDMS layer in the path of the light and generates ultrasound. They have shown how the probe can be used for rotational ultrasound intraluminal imaging.

Arrays of fibre optic ultrasound transmitters have recently been reported. These consist of several optical fibres of varying length arranged in parallel to each other to create a phased array (Zhou, Du, and Wang 2019; Zhou, Wu, and Wang 2019). The photoacoustic material used to create the transmitters is the same as that described by Zou *et al.* (Zou et al. 2014). The principles of the ultrasound beam manipulation are similar to the way traditional piezoelectric ultrasound transducers steer and focus

the beam. In this case, the time delay between each element is induced by the varying fibre lengths. The phased array was varied to steer the generated ultrasound beam and also to focus the generated ultrasound. For the beam steering arrangement, fibre lengths of 1, 5, 9 and 13 m were used to create a time delay of 0.02 µs between each transmitter. The interfering waves created a steering angle of 9.5°. For the focusing arrangement fibre lengths of 1, 5, 5 and 1 m were used. This created a focus with a focal length of 1.2 mm. The disadvantage of this method is that to add more elements the total size will rapidly increase. The fibres themselves have a diameter of 125 µm and they are spaced out so that their centre to centre measures 200 µm.

2.5.5 Ultrasonic lenses

In traditional ultrasound transducers there is an array of piezoelectric elements, each of which independently capable of generating ultrasound. By delaying the excitation pulses that determine the timing sequence which controls the activation of these elements, focussed or steered ultrasound beams can be created due to the interactions between the multiple waves (Shung, Smith, and Tsui 1992). Traditional piezoelectric arrays struggle to be miniaturised to the micro-scale (which is discussed in more detail later in this chapter). The piezoceramics are difficult to cut into micron sized elements, the electrical connections make assembly difficult and the cross talk between elements would also prove difficult to overcome (Hou et al. 2006). For optical ultrasound, a similar timed activation method of focussing would require an array of optical fibres to imitate an array of elements and generate a similar effect (Zhou, Du, et al. 2019). A more elegant solution, which would enable highly miniaturised dimensions to remain, is to deposit structured photoacoustic material appropriately on a fibre tip to create lens like micro-structures.

In optical applications a convex lens is usually used to focus light. In ultrasonics, lenses can also be used to focus ultrasound. Unlike in optics, a concave lens is usually used as the lens is made of a solid material so usually has a greater velocity of sound that the surrounding medium (water/tissue) as shown in Figure 2.3 (Shutilov 1988). Using standard approximations used in optics, for paraxial rays, a relationship between the focal length and the radius of curvature of the lens can be determined, provided that the velocity of sound is known in both materials.

As well as using lenses to focus ultrasound beams, focussed laser-generated ultrasound can be created by depositing thin films of photoacoustic material onto a pre-existing lens. The coating of a photoacoustic material onto a lens and using laser pulses to generate a focussed ultrasound beam is termed an optoacoustic lens (Baac

et al. 2012). A common photoacoustic coating used in optoacoustic lenses is a nanocomposite of carbon nanotubes (CNTs) and PDMS. Optoacoustic lenses are typically used on the millimetre and centimetre scale as below this fabricating the required smooth surfaces becomes difficult.

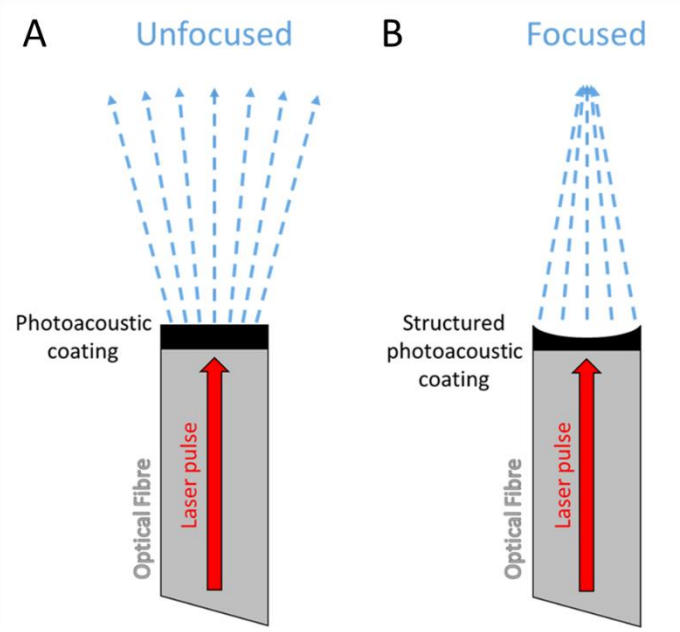

Figure 2.3 - Schematic diagram illustrating how structured photoacoustic material could be used to focus ultrasound beams. Typical fibre diameter: 100 to 800 µm.

2.5.6 Holographic lens structures

Apart from lenses, other devices can focus and manipulate ultrasound beams. Focussing the discussion on optically generated ultrasound, optoacoustic lenses can manipulate the generated ultrasound field. Another such technique involves the use of holograms. Acoustic holograms enable spatial steering and focusing of high frequency acoustic beams which is desirable for high resolution ultrasound imaging. Hologram designs are cheap to manufacture and can create complex acoustic field patterns. Brown *et al.* demonstrated how binary amplitude holograms could be used to focus optically generated ultrasound fields on the centimetre scale (Brown et al. 2014). This technique involves the use of concentric rings as optical absorbers. By patterning the absorbing material, the initial pressure distribution when a laser pulse is absorbed is then the same shape as the chosen 2D design. The generated ultrasound/pressure wave distributions then propagate outwards, constructively and destructively interfering with each other. By carefully designing the pattern of the photoacoustic material (and hence the initial pressure distribution) a focused acoustic field can be created in the chosen imaging plane (Brown et al. 2014). For focusing,

the required design is a pattern of alternating absorbing and non-absorbing concentric rings. The required radii of the concentric rings are given by:

$$r = \sqrt{nf\lambda + \frac{n^2\lambda^2}{4}} \tag{2.10}$$

where n is an integer number indicating the radius number, f is the focal depth and λ is the wavelength of the design frequency. By using a train of laser pulses multiple foci can also be created due to the interference of different harmonics in the ultrasound waves. This is illustrated in Figure 2.6.

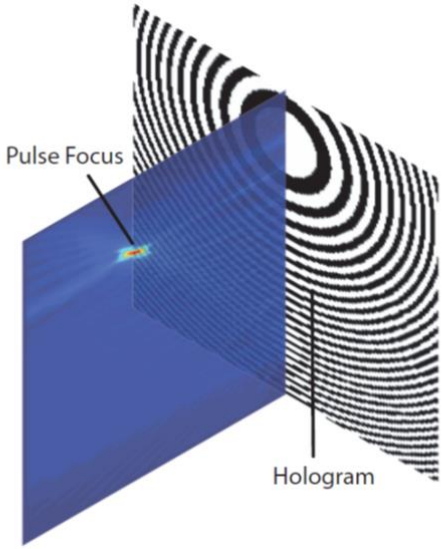

Figure 2.4 - Simulation of how acoustic holograms can be used to focus a laser generated ultrasound beam (Brown et al. 2014).

Acoustic holograms to focus ultrasound beams have been experimented with on the centimetre scale but they have not been investigated in the microscale before. The printing capabilities offered by high-resolution 3D printing and the developed printing techniques outlined in this thesis, such as micro-moulding, will enable this to be tested.

Another method of using holograms to manipulate acoustic fields is to introduce phase changes. By creating holograms with material patterns of varying thicknesses, phase changes can be introduced as the speed of sound in the hologram material and the surrounding material differs (M. D. Brown et al. 2017; Melde et al. 2016). These holograms create complex acoustic field patterns by coding phase profiles into their structure. They essentially create an array of pixels with independently

controllable phase (based on the pixel thickness). By controlling the phase, a planar waveform can be manipulated to give a desired phase distribution. Further complexities can be added by creating holograms that produce one pattern when the initial plane wave is at a specific ultrasound frequency and other patterns at different ultrasound frequencies (Michael D Brown, Cox, and Treeby 2017).

2.6 Optical ultrasound receivers

Moving on from ultrasound generation, ultrasound detection will now be explored. Ultrasound reception is a key topic of this work and is extremely relevant to the work undertaken in Chapter 4.

Most of the optical ultrasound transmitters mentioned so far were tested with piezoelectric hydrophones to measure the ultrasound field. These piezoelectric hydrophones have been shown to be capable of miniaturisation and have good measurement performance (Hurrell and Beard 2012). Despite this, to move towards truly all optical ultrasound imaging, the optical ultrasound transmitters need to be coupled with optical ultrasound receivers to detect the reflected ultrasound waves. All optical ultrasound imaging would remove the need for long wires attached to piezoelectric elements. This lack of wiring would in turn make it more suitable for minimally invasive surgery, ensure MRI compatibility and hopefully enable easier/cheaper manufacturing of such devices.

Hurrell and Beard go into detail on the properties of hydrophones in (Hurrell and Beard 2012). One important parameter that will be referred to in order to enable comparison between hydrophones is the noise equivalent pressure (NEP). This is the minimum measurable pressure above the noise level of the system and corresponds to a signal to noise ratio (SNR) equal to one. While this parameter is dependent on the noise level of the system, it is strongly dependent on the hydrophone. To detect weaker signals a low NEP value is required.

Here the focus is on fibre optic hydrophones (FOH). FOH can be divided into two different types: intrinsic and extrinsic. Intrinsic FOH sense a change in intensity, phase or polarisation of light within the optical fibre, so that the fibre itself is acoustically sensitive. Extrinsic FOH detect the intensity, phase or polarisation change as the light interacts with a sensor located at the distal end of the fibre and the fibre merely guides the light.

One of the first fibre optic acoustic sensing devices was the Eisenmenger fibre-optic hydrophone (Staudenraus and Eisenmenger 1993). This consisted of a cleaved

optical fibre coupled to a laser and two photodiodes using a 2x2 fibre coupler. Light from the laser travels down the optical fibre until it reaches the cleaved end. At this point a fraction of the light is reflected due to the refractive index mismatch between the silica of the fibre and the surrounding medium (water). The reflected light then travels back down the fibre and is detected by a photodiode. The second photodiode is used to monitor the output power of the laser in order to account for variations and improve the signal to noise ratio. As ultrasound waves hit the distal end of the fibre, they change the density of water and the density of the silica. This density change in turn causes a change in the refractive indices, which alters the refractive index mismatch at the fibre-water boundary. As the incident ultrasound waves modulate this change in refractive index mismatch, the reflected light is also modulated correspondingly. Thus, relating the reflected optical power to the pressure of the incident ultrasound waves.

The Eisenmenger fibre-optic hydrophone has advantages in its simple implementation combined with its good robustness. The hydrophone shows wide bandwidth response but the main limiting factor is its high value of NEP in the range of 0.5 – 1.0 MPa (Staudenraus and Eisenmenger 1993). These properties mean that this hydrophone has mainly been used to detect high amplitude ultrasound fields in relatively harsh environments.

The sensitivity of FOH can be improved by moving towards interferometry-based designs, as discussed below.

2.7 Fibre-optic interferometric sensors

For highly sensitive fibre optic hydrophones, interferometric sensors are utilised to detect ultrasound waves. The principles of interferometric sensors are outlined in this section before moving on to the discuss the Fabry-Pérot etalon. These sensing techniques will be utilised in Chapter 4 for ultrasound reception using fibre optic hydrophones. Low coherence interferometry is also utilised in Chapter 3 and is discussed further in the following section.

Interferometry is a method of extracting information from waves by examining their interference patterns. A classical Michelson interferometer works by splitting a beam of light into two and sending them down different paths. One path called the reference path directs the beam towards a reference mirror. The path length for this beam is defined as the distance from the splitter to the reference mirror and back. The other beam travels along a different path towards an object surface where it is reflected.

The path length for this beam is defined as the distance from the splitter to the object and back. When both beams return to the splitter they recombine and are directed towards a detector. If the beams travel different path lengths, then this difference will cause an interference pattern at the detector (constructive or destructive). By analysing the interference of the beams, the phase difference between the two beams can be determined and thus information can be extracted. A schematic diagram of these different light paths is shown in Figure 2.5.

Many fibre optic sensors employ interferometric techniques to measure parameters such as temperature, strain, pressure, refractive index and magnetic field (Coote et al. 2019; Dominguez-Flores et al. 2019; Fu et al. 2017; Islam et al. 2014; Pevec and Donlagić 2019; Wang et al. 2010). As well as being able to measure a wide range of parameters, interferometric fibre optic sensors are advantageous thanks to their small dimensions, durability in harsh environments, low cost, immunity to EMI and multiplexing capability.

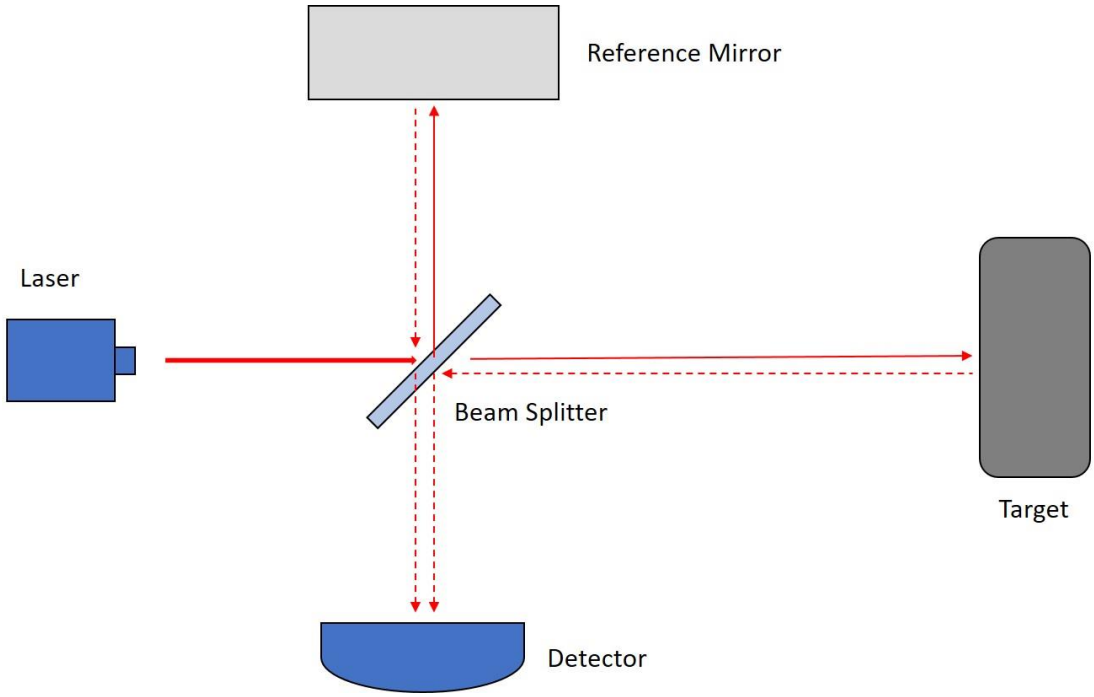

Figure 2.5 - Schematic diagram of Michelson interferometer.

2.7.1 Fabry-Pérot interferometer

One type of interferometric sensor design is the Fabry-Pérot (F-P) design. A F-P interferometer or etalon is an optical cavity formed of two parallel reflecting surfaces. Incident light undergoes multiple reflections within the cavity before escaping if the reflectivity values are less than 100%. A schematic of a F-P cavity is shown in Figure 2.6. Comparing the reflected light to a reference beam causes interference that can

be used to determine measurable parameters detected by sensors. F-P interferometer sensors have found many uses since their inception due to their simplicity, versatility, precision, responsiveness and immunity to environmental noise (Islam et al. 2014).

Hill *et al.* (Hill et al. 2007) studied the expected intensity of the reflected light with respect to the incident light and showed that it can be given as:

$$\frac{I_r}{I_i} = \frac{M + F\sin^2\left(\Phi/2\right)}{1 + F\sin^2\left(\Phi/2\right)}$$

(2.11)

where,

$$M = \left[\frac{\sqrt{R_1} - \sqrt{R_2}}{1 - R}\right]^2, \qquad F = \frac{4R}{(1-R)^2}, \qquad \Phi = -\frac{4\pi}{\lambda}L + \phi_1 + \phi_2, \qquad R = \sqrt{R_1 R_2}$$

(2.12)

Here, I_i is the intensity of incident light, I_r is the intensity of reflected light, Φ is phase shift acquired from one round trip in the cavity, M indicates the reflectance mismatch at the end of the interferometer, L is the cavity length, λ is the wavelength of the light and ϕ_1 and ϕ_2 are the phase shifts of the reflected light from the proximal and distal end faces of a single cavity F-P interferometer. R_1 and R_2 are the respective reflection coefficients for these interfaces. For an ideal F-P interferometer, the cavity would be lossless, so that $R_1 = R_2$ resulting in $M = 0$ and maximising the signal contrast in the reflectance spectrum.

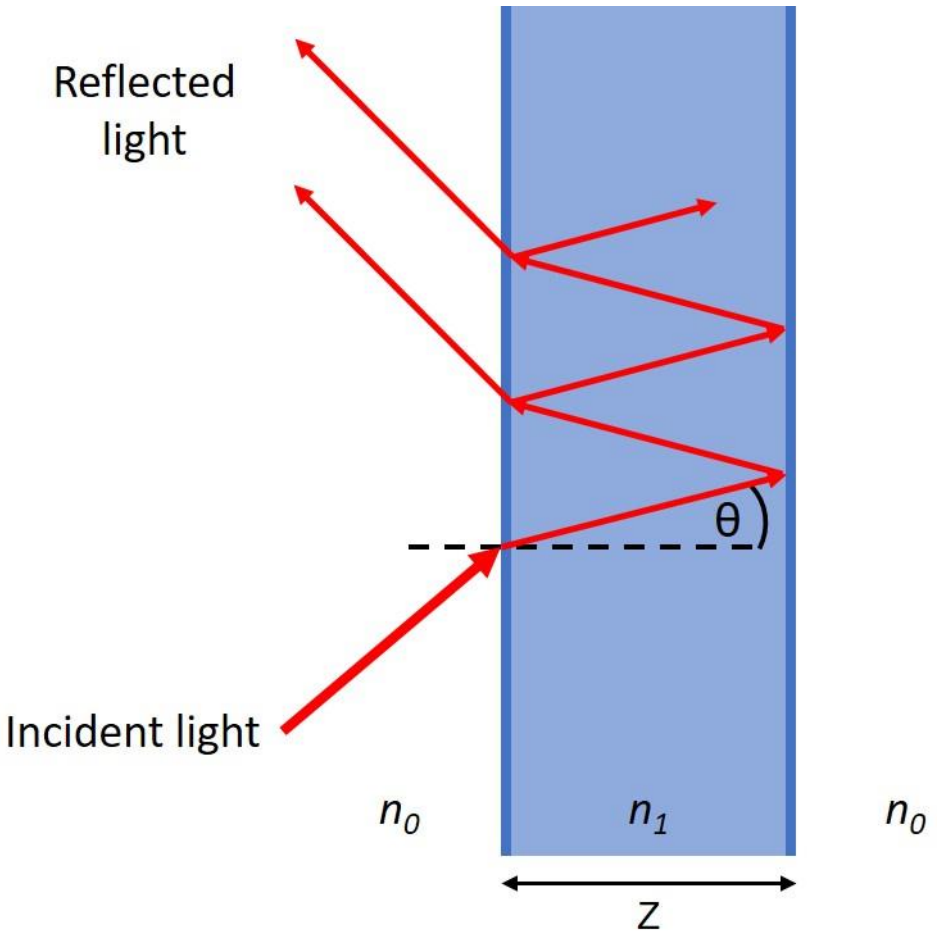

Figure 2.6 - Schematic diagram of a Fabry Perot cavity with refractive index n1.

The working principle of a F-P interferometric sensor is that one of the reflecting surfaces is displaced or the refractive index of the cavity changes, resulting in a change in the optical path length. These changes can be detected through optical interrogation of the cavity. The specific interrogation technique will depend on the light source used and the finesse of the cavity. Using a high coherent light source and a high finesse cavity, changes in the optical path length due to acoustic/pressure waves impacting on one of the reflective surfaces can be detected as modulations in the power of the reflected beam (Beard 2011). Examples of these sensors and interrogation techniques can be found in (Beard 1998; Guggenheim et al. 2017). Further details on interrogation techniques and multiparameter F-P sensing, as well as alternative interferometric sensing techniques can be found in (Pevec and Donlagić 2019).

2.8 Fabry-Pérot laser interferometry

The interferometry technique utilised to interrogate the F-P cavities in this work is now discussed. After light undergoes multiple reflections in a F-P cavity it re-enters the

optical fibre. The total optical power reflected back (P_r) is the superposition of all of the reflected beams. Each beam can have made an integer number of round trips in the cavity so there will be a relative phase difference between them. The phase shift induced by one round trip through the cavity is given by:

$$\phi = \frac{4\pi n l}{\lambda}$$

(2.13)

where n is the refractive index of the cavity (for air filled cavity n~1), l is the length of the cavity and λ is the wavelength of the interrogating light used (Morris et al. 2009).

When an acoustic wave hits the deformable surface of the cavity the change in length causes a change in phase and therefore modulates the total reflected optical power.

The acoustic response of a hydrophone is defined as the change in reflected optical power resulting from a given change in acoustic pressure.

$$R_A = \frac{\partial P_r}{\partial p}$$

(2.14)

where R_A is the acoustic response, P_r is the reflected optical power and p is the acoustic pressure.

The acoustic response can be separated into 2 parts: the optical phase sensitivity (I) and the acoustic phase sensitivity (A_s). The optical phase sensitivity is the change in reflected power for a given phase change. The acoustic sensitivity relates the change in acoustic pressure to the change in phase.

$$R_A = IA_s\,, \quad I = \frac{\partial P_r}{\partial \phi}\,, \quad A_s = \frac{\partial \phi}{\partial p}$$

(2.15)

To determine the optical phase sensitivity the relationship between the reflected optical power and the phase needs to be investigated. This relationship is called the phase interferometer transfer function (ITF). For a F-P cavity with non-absorbing surfaces and interrogated by a collimated beam, the ITF takes the form of an Airy function as shown in Figure 2.7.

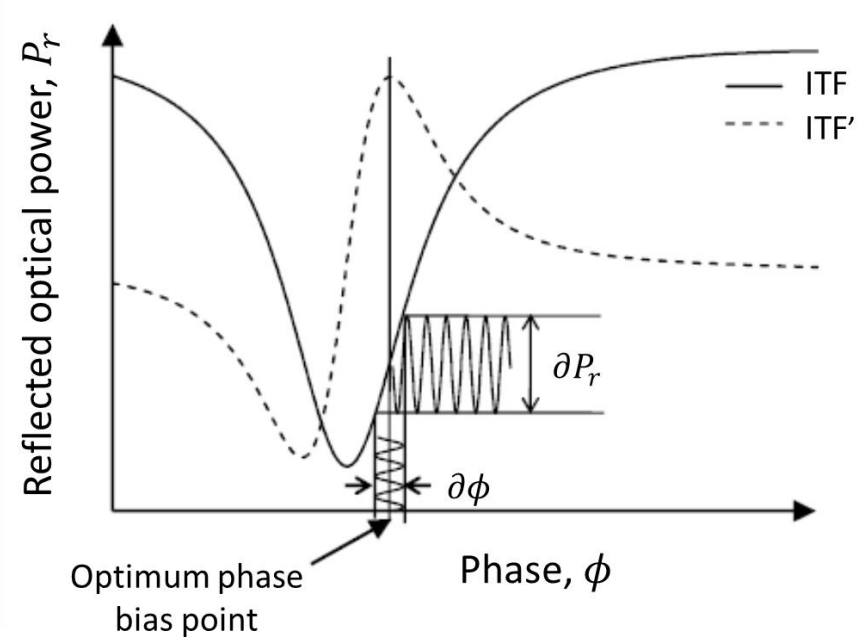

Figure 2.7 – Graph showing the IFT and its first derivative for a F-P cavity. Adapted from (Morris et al. 2009).

The first derivative of the interferometer transfer function (ITF) with respect to phase is the optical phase sensitivity ($\partial P_r/\partial\phi$). In Figure 2.7 it can be seen that there is a certain phase value where the derivative of the IFT is maximum. The maximum point on the derivative of the ITF is noted as the optimum phase bias point where the optical phase sensitivity is greatest, and the optical component is most sensitive. As the phase is related to the wavelength of the interrogating light beam (equation (2.13)) then a wavelength tuneable laser can be used to bias the sensor at this point to maximise the sensitivity of the optical phase component.

The acoustic phase sensitivity (A_s) is the change in phase for a given pressure. The pressure causes a change in phase by changing the optical path length of the cavity. The optical path length is a product of the refractive index (n) of the cavity material and the length of the cavity (l). The change in phase when acoustic pressure is applied (assuming that the acoustic wavelength is much greater than the cavity length) can be written as:

$$A_s = \frac{\partial\phi}{\partial p} = \frac{\partial\phi}{\partial l}\frac{\partial l}{\partial p} + \frac{\partial\phi}{\partial n}\frac{\partial n}{\partial p} = \frac{4\pi}{\lambda}\left(n_0\frac{\partial l}{\partial p} + l\frac{\partial n}{\partial p}\right) \tag{2.16}$$

where n_0 is the equilibrium refractive index and λ is the wavelength of the interrogating light. Since ultrasound has a wavelength on the order of centimetres and the cavity length is of the order of micrometres this expression holds.

In order to maximise the total acoustic response both the optical phase sensitivity and the acoustic phase sensitivity must be addressed. The acoustic phase sensitivity is mainly dealt with in the hydrophone design. The optical phase sensitivity can be addressed in the interrogation system used. The main component of the interrogation system used is a wavelength-tuneable CW laser. Reflected light from the FOH is detected by a photo-receiver system. The photo-receiver system tends to have 2 outputs, a low frequency and a high frequency output. The low frequency output can be used to measure the ITF of the F-P cavity. Knowing the ITF, the interrogating wavelength can be adjusted to reach the optimum bias point and maximise the optical phase sensitivity. The high frequency output is used to measure the response of the F-P sensor.

2.9 Biomedical pressure sensors

Biomedical pressure sensors will now be discussed as the work in Chapter 3 of this thesis has a strong focus on physiological pressure sensing. Chapter 3 details research into fibre optic pressure sensors. A broader view of biomedical pressure sensors is initially provided here before focussing on fibre optic based sensors.

Biomedical pressure sensors can usually be classified as one of three main types based on their principle of measurement, these are: *capacitive*, *piezoresistive* and *fibre optic* (Clausen and Glott 2014; Roriz et al. 2013). Capacitive sensors are based on a capacitive structure where a layer of dielectric material has an electrode attached on top and on bottom, creating a sandwich like structure. Any pressure applied to this structure will cause a displacement which alters the distance between the two electrodes. Such a change will result in a change in the measured capacitance across the electrodes and thus the pressure applied can be determined. Capacitive sensors are preferred for environments where low pressures are experienced due to the fact that their operating principle is highly efficient for this application (Fraden 2004). Despite this, a main drawback of capacitive sensors is due to the associated electronics. Even though the sensors can be highly miniaturised, bulky electronic chips are usually necessary. The associated electronic components must also be located close to the sensing element in order to reduce stray/unwanted capacitance in the wires. Recent work has shown that parts of the electronic circuitry can be separated from the sensing components and housed elsewhere, enabling a reduction in total sensor size (Melki, Todani, and Cherfan 2014). The detached electronics are usually responsible for powering the sensor and extracting the data. The elements

can communicate with each other by inducive coupling, allowing wireless energy and data transfer.

For piezoresistive pressure sensors the operating principle is based on the piezoresistive effect, which manifests as a change in resistance when an external pressure is applied. The applied pressure causes a geometrical change in the sensor which undergoes elastic deformation and changes the resulting resistance (Fiorillo, Critello, and Pullano 2018). Compared to capacitive sensors, piezoresistive sensors are more prone to electrical noise (Clausen and Glott 2014). Despite this shortcoming, they have an advantage over capacitive sensors in that they do not suffer from stray/unwanted capacitance in the wires. The removal of unwanted capacitance in the wires enables the electronic circuitry of the sensor to be located far away from the sensing element and they can be connected via long thin wires. If the sensing element is highly miniaturised, then it can be inserted into a highly confined space while the bulky electronic components remain outside of the confined space and the two components are connected through long thin wires or alternatively they can be wirelessly connected (Agarwal et al. 2018).

With fibre optic pressure sensors, their operating principle is not based on electronics. Their optical nature eliminates the issue of electrical noise usually associated with electronic based sensors and also helps overcome limitations in miniaturisation, such as removing the need to have pads to connect wires to. Another main advantage of fibre optic based sensors is that they are compatible with MRI machines due to their lack of electromagnetic interference. Fibre optic pressure sensors are also well suited for biomedical applications due to their inertness, biocompatibility and small dimensions (Roriz et al. 2013).

As the research in this thesis is based on utilising optical imaging and sensing techniques to ease miniaturisation, fibre optic pressure sensors are examined in more detail below.

2.9.1 Fibre optic pressure sensors

There are three main methods of using optical fibres to sense pressure: *intensity modulated*, *wavelength modulated* and *phase modulated*. Intensity modulated techniques are based on variations in intensity or amplitude of input light that is coupled to as secondary fibre (or back to the original fibre). The intensity/amplitude of the coupled light varies as the distance between the input and output fibres changes (Roriz et al. 2013). External pressure that alters this coupling distance can therefore be determined through the intensity changes. Several different

configurations (some with multiple coupled fibres) can be used with intensity modulated techniques as well as micro and macro bending of a single fibre, which can also reduce the intensity of output light (Roriz et al. 2013). Wavelength modulated and phase modulated methods rely on interferometric based techniques. They were developed after intensity modulated techniques and are more sensitive, although require more complex setups.

The most common form of wavelength modulated sensing is the fibre Bragg grating (FBG). For this the refractive index of the core of an optical fibre is altered to give a periodic variation (grating). These refractive index variations are selected so that only certain wavelengths of light are reflected (Bragg wavelength) (Rao 1997). When strain is applied to these sections of fibre the Bragg wavelength shifts, causing a shift in the wavelength of light to be reflected. By monitoring these shifts the amount of strain applied can be calculated. For certain applications this can be calibrated to give pressure measurements (Urban et al. 2010).

In this project the phase modulated technique of interest is the Fabry-Pérot (F-P) interferometer-based technique which is capable of optically detecting ultrasound. In order to detect the high frequency ultrasound waves, high finesse F-P cavities are required. To sense more modest low frequency physiological pressure changes low finesse cavities can be used and interrogated with low coherence interferometry setups.

2.9.2 Low coherence interferometry for fibre-optic sensors

Low coherence interferometry (LCI) is a method of interrogating F-P cavities which have a low finesse and partially reflecting surfaces (reflectance mismatch, $M > 0$). This interrogation technique is of particular importance to fibre optic pressure sensors and the work outlined in Chapter 3.

LCI fibre-optic systems are generally based on classical Michelson interferometers. Typically, a broadband near infra-red (NIR) light source is used. The incident light beam is split into a measurement beam and a reference beam. The measurement beam is passed down an optical fibre to illuminate the interferometric sensing cavity. The higher value of M reduces the signal contrast in the reflectance spectrum and can be due to different materials being used for the 2 reflecting surfaces or significantly different surface features causing optical modulation. Additionally, the alignment of the two reflecting surfaces will affect the coupling of the reflected light back into the optical fibre and to the photodetector. Therefore, the precise alignment of the sensor surfaces is essential to create efficient sensing with a high signal to

noise ratio (SNR). LCI fibre-optic sensors have been used to detect different physical parameters such as pressure, temperature, refractive index and humidity (Coote et al. 2019; Hirsch et al. 2017; Maciak 2019; Poeggel, Tosi, et al. 2015).

LCI is the same technology utilised in optical coherence tomography (OCT) where biological tissue is used in place of a partially reflective surface (Drexler and Fujimoto 2008). OCT can be used to characterise and diagnose biological tissue in areas such as ophthalmology, dermatology and cardiology. In OCT the interrogation technique can be used to interrogate multiple layers of the tissue to build up axial images, up to a depth of a couple of millimetres. By transversely scanning the beam in *x* and *y* as well, 3D volumetric images can be achieved (Drexler and Fujimoto 2008). There are two main methods of OCT, time domain (TD)-OCT and spectral domain (SD)-OCT. In TD-OCT the length of the reference optical path is mechanically altered in order to interrogate different axial depths. In SD-OCT this mechanical movement is not needed as a spectrometer can be used instead of a photodetector to process all of the light from the broadband light source. Using Fourier transforms the modulations in the detected spectrum can be differentiated into the sample depths which they came from (Podoleanu 2012). Alternatively, a tuneable laser (sweep source) can be used along with a standard photodetector.

2.9.3 Development of fibre optic pressure sensors

Some of the current commercially available fibre optic pressure sensors which have been used in medical applications have been summarised in section 2.2. At this point more recent research developments will be discussed.

Islam *et al.* summarise the development of F-P pressure sensors well up to 2014 (Islam et al. 2014). At this point fibre optic pressure sensors with sensitivities of around 0.11 radian/kPa or >1000 nm/kPa were reported. Eom *et al.* also reported a pressure sensitivity of 1410 nm/kPa and a minimum detectable pressure of 0.03 kPa using a lensed fibre and polymer diaphragm (Eom et al. 2015). Li *et al.* investigated using thin graphene sheets as the deformable diaphragm and report pressure sensitivity values of 2380 nm/kPa (Li, Gao, et al. 2015). Yu *et al.* have used layers of molybdenum disulphide to create ultra-thin diaphragms and report sensitivity values of 89300 nm/kPa (Yu et al. 2017).

Fabricating the nanometre thick diaphragms required to achieve these high sensitivities and assembling them into sensors is a complex and highly expensive process. Recently research has turned towards more cost effect methods of creating sensors with high sensitivities for a reduced cost, suitable for use in the medical field.

Polymers have proved to be the material of choice for creating these low-cost fibre optic pressure sensors. Zhao *et al.* have shown how polydimethylsiloxane (PDMS) can be used to create sensors with a low frequency response and sensitivity of 0.427 mV/mPa (Zhao et al. 2018). Wang *et al.* have demonstrated how polyethylene terephthalate (PET) can be utilised (Wang et al. 2016). Coote *et al.* and Fu *et al.* have carried out further work with PDMS and shown how fibre optic sensors capable of measuring temperature and pressure can be created (Coote et al. 2019; Fu et al. 2020).

2.10 Fabrication techniques for miniature ultrasound probes and fibre optic sensors

This section highlights some of the current manufacturing processes utilised to create miniature ultrasound probes and fibre optic sensors. Some of the challenges and limitations of current fabrication techniques for miniature ultrasound probes are highlighted and point to the use of optical ultrasound probes, which have comparatively simple fabrication techniques. This motivates the work on optical ultrasound probes documented in Chapter 5.

The current fabrication processes for producing fibre optic sensors are also examined. Difficulties are identified and previous work to utilise polymer materials to heighten sensitivity and reduce costs are discussed. This prefaces the work in Chapters 3 and 4, which aim to create a simplified microfabrication technique for polymer-based fibre optic pressure sensors and FOH.

2.10.1 Miniature ultrasound probes

As discussed previously, some of the main challenges of miniaturising traditional ultrasound probes are due to the complex fabrication processes. These processes are based on microelectromechanical system (MEMS) technology. MEMS technology can be used to fabricate devices from a variety of materials; including silicon (and its oxide, nitride, and carbide derivatives), silicon–germanium, diamond, III-V semiconductors, aluminium oxide, and other semiconductor/dielectric materials used as structural, sacrificial, and passivation layers (Mishra et al. 2019). Some common MEMS fabrication techniques are chemical vapour deposition (CVD), physical vapour deposition (PVD), atomic layer deposition (ALD), spin coating, bulk micromachining, surface micromachining, lithography/photolithography, wet etching, dry etching and deep reactive ion etching (DRIE). Details on these techniques and others can be

found in the following references (Eaton and Smith 1997; Huff 2002; Judy 2001; Mishra et al. 2019).

Some examples of the fabrication processes involved in creating piezoelectric micromachined ultrasonic transducers (pMUTs) are explored. pMUTs are designed with flexible membranes of piezoelectric materials. The membranes must possess both piezoelectric and elastic properties as well as having electrodes across the piezoelectric component. There are several methods for producing the membranes for pMUTs; diaphragm defined with sacrificial layer releasing, diaphragm defined with back-side etching, diaphragm defined with front-side etching and wafer transfer diaphragm formation (Qiu et al. 2015).

Diaphragm defined with sacrificial layer releasing is usually achieved by initially depositing a sacrificial layer on the substrate. Once all of the layers of the diaphragm are patterned and complete, the sacrificial layer is etched away through a small hole to form a cavity beneath the diaphragm (Qiu et al. 2015). An example fabrication process using this technique is described by Percin *et al.* (Perçin et al. 1998). A sacrificial layer of silicon oxide is initially grown on a silicon substrate. Low pressure CVD is used to deposit silicon nitride. E-beam evaporation is then used to deposit a layer of Ti/Au electrode. The metal layer is patterned by wet etching and access holes for sacrificial layer etching are created by plasma etching. The piezoelectric ZnO layer is then deposited on top of the bottom electrode by DC planar magnetron reactive sputtering (20%–80% argon-oxygen, flow rate of 26.6 sccm, pressure of 7 mTorr and substrate temperature 145 °C). The top Cr/Au electrode layer is formed by e-beam evaporation at room temperature and patterned by lift-off. The sacrificial layer is then removed by wet etching to create the cavity under the diaphragm (Perçin et al. 1998).

For diaphragm defined with back-side etching, this etching can take place before or after the other fabrication steps. Essentially the diaphragm material and electrodes are created on one side of a wafer and then material is removed from the opposite side until a thin diaphragm is created underneath (Qiu et al. 2015). A process utilising this method was used by Dausch *et al.* (Dausch et al. 2014). Holes were etched in a silicon wafer. Silicon dioxide was then grown all over it. After this the holes were filled by plating platinum which also created the bottom electrode. Chemo-mechanical polishing was performed to remove the plating overburden. Spin coating was used to deposit the piezoelectric layer which was crystalized at 700°C. The piezoelectric layer was patterned using wet chemical etching. The bottom electrode was patterned using ion milling for electrical isolation of each element. Further etching of the silicon

substrate was performed to ensure electric isolation. A dielectric film was then deposited followed by the top electrode. DRIE was then performed from the back-side under each element to create diaphragms. A conformal parylene layer was deposited in these channels to cover the side walls. A conformal copper layer was the deposited into the DRIE channels by metalorganic chemical vapor deposition (MOCVD) to enable further cable connections. The copper layer was then patterned and etched on the back side of the silicon substrate to form individual electrical contacts. Separate ground contacts were formed by etching away the piezoelectric layer so that the top electrode had an electrical path through to the back-side (Dausch et al. 2014).

The advantage of diaphragm defined with front-side etching is that cavities of relatively small diameters can be achieved more easily. Etching is performed through small channels (vias) in the diaphragm structure to etch cavities beneath and then the vias are closed with additional material. The need to fill the access channels with additional material generally increases the effective stiffness of the membrane (Qiu et al. 2015). Griggio *et al.* used this technique to create pMUTs (Griggio et al. 2012). On a platinised silicon wafer, piezoelectric material was grown using RF sputter deposition. A top electrode was then sputtered onto the piezoelectric layer and patterned using contact lithography and reactive ion etching (RIE). Using a thick photoresist mask, RIE was also performed on parts of the piezoelectric layer to create access to the bottom electrode. Silicon dioxide was then deposited onto certain areas of the piezoelectric layer using sputter deposition and lift-off. The top electrode was then sputtered on top and patterned using lift-off. Etch vias were then created through the structure using RIE to access the silicon beneath. Further etching was performed to remove any native oxide present and then RIE was performed again to create the cavities beneath the piezoelectric layer. The diaphragms were then laminated with a thick negative photoresist film to seal the access channels in the structure. The laminate was then patterned to expose the bond pads for wire bonding (Griggio et al. 2012).

In wafer transfer diaphragm formation, the cavities and the pMUT membrane are fabricated separately and then bonded together. The alignment of the two components is important in this technique (Qiu et al. 2015). Yang *et al.* detailed how they used this technique to create a pMUT array (Yang et al. 2013). Initially silicon dioxide and silicon nitride are grown on a silicon wafer. These are then patterned, and wet etching is performed with potassium hydroxide to create cavities in the silicon substrate. A silicon on insulator (SOI) wafer, attached to a larger handling wafer, is

then bonded over these to create sealed cavities. The handling layer is then mechanically attenuated to remove large parts of it. The SOI is then wet etched to create a thin membrane above the cavities. The process then continues, similar to those mentioned previously, with cycles of deposition, patterning and etching to create the desired stack structure of electrode/piezoelectric material/electrode above the cavities with the appropriate connection pads for further wiring of the elements.

Though these MEMS based fabrication processes have been successful in creating pMUT elements and arrays for miniaturised ultrasound transducers, the fabrication processes are undeniably complex. The specialised equipment and environments used throughout add great costs to these processes.

As highlighted previously, optical ultrasound has emerged as a convenient alternative for easily creating miniaturised ultrasound transducers. Optically generated ultrasound enables some of the complex MEMS fabrication procedures associated with miniature piezoelectric transducers to be avoided.

As discussed in section 2.5 there are many different materials that can be deposited on the tip of optical fibres in order to create photoacoustically generated ultrasound transmitters. Many of these fabrication techniques simply involve dipping the tips of the optical fibres into the appropriate solutions and allowing to dry, creating a much simpler fabrication process (Colchester et al. 2014; Noimark et al. 2016, 2018; Wu et al. 2011; Zou et al. 2014).

2.10.2 Fibre optic sensors

The fabrication of fibre optic F-P cavities can generally be split into methods, those which require splicing and those which do not. Splicing is when two optical fibres are fused together, usually by an electrical arc.

2.10.2.1 With splicing

Splicing can be used to attach dielectric mirrors to fibres to create a reflective cavity for F-P measurements (Lee et al. 1989). Splicing can also be used to create all glass F-P sensors. Pinet *et al.* describe how they used splicing to create an all-glass F-P sensor. They spliced hollow core fibre to a coreless fibre, the hollow core fibre was then cleaved and polished to achieve a specific size/length from the splice joint. This fibre joint then needed to be carefully cleaned in an ultrasonic bath to remove polishing debris. After this a multimode fibre was spliced to the hollow core fibre segment to create an air cavity. The coreless silica fibre is then cleaved close to the hollow core fibre and polished to create a thick membrane. The silica membrane fibre

can be mechanically polished to make it thinner and more pressure sensitive (Pinet, Cibula, and Đonlagić 2007; Poeggel, Duraibabu, et al. 2015). A similar technique can be used to splice a glass capillary tube onto a single mode fibre and by heating and melting the capillary, a micro bubble shaped reflective cavity is formed (Yan et al. 2017).

There are many different variations on this process where segments of fibre or hollow fibre/capillaries are spliced together to create F-P cavities at the tips of fibres. Splicing is usually used to create all glass sensors and avoid the use of polymer adhesives. The main drawback is that splicing relies on thermal effects to bond the materials which can be detrimental/damage certain materials used for pressure sensitive membranes, so the choice of material is limited.

2.10.2.2 Without splicing

Fabrication techniques which avoid splicing are mainly used to avoid potentially damaging thermal effects during manufacture. Avoiding thermal effects allows for different membrane materials to be used. Li *et al.* used Van der Walls forces to attach a graphene membrane to a ferrule and by inserting a fibre created a F-P cavity (Hernaez et al. 2017; Li, Liu, et al. 2015). The downside of using Van der Walls forces is that the bonding strength is low compared to other methods. Other bonding techniques such as hydroxide catalysis bonding (HCB)/silicate bonding can also be used to attach extrinsic F-P cavities while avoiding thermal effects but cannot be used with all materials (Liu et al. 2020). However, most techniques use adhesives to attach extrinsic F-P cavities over single mode fibres.

The extrinsic F-P cavities can be made in multiple ways including micromachining techniques, 3D printing, photolithography/etching and moulding (Bae and Yu 2012; Hill et al. 2007; Pevec and Donlagić 2019; Rajibul Islam et al. 2014; Shen et al. 2019; Zhang et al. 2019). The current 3D printed structures are relatively large, on the order of millimetres to centimetres. Micromachining techniques usually result in silicon diaphragms, though silicon derivatives, metals and ceramics are noted in Song *et al.* (Hill et al. 2007; Islam et al. 2014; Pevec and Donlagić 2019; Song et al. 2020; Wang et al. 2014). Laser micromachining can also be used to create F-P cavities within the fibre, near the tip, by creating small air gaps (Ran et al. 2008). Photolithography/etching techniques are mainly used to produce silicon diaphragms but other materials have been reported (Hill et al. 2007). After processing, these diaphragms can be attached to ferrules or tubes for easier fibre integration (Ge et al. 2018; Ma et al. 2019; Pevec and Donlagić 2019). Bae and Yu presented a method of

moulding UV curable polymer to create an extrinsic cavity on the tip of a optical fibre and then added a polymer diaphragm via additional steps (Bae and Yu 2012; Nesson et al. 2008).

Using various techniques membranes can be created from many different materials and composites. Polymers are a popular choice due to their favourable material properties and relatively low cost. Wang *et al.* investigated the response of polyethylene terephthalate (PET) membranes (with additional aluminium foil attached to increase its reflectivity) by using a large external housing to position it (Wang et al. 2016). Coote *et al.* have used polydimethylsiloxane (PDMS) to form membranes by wicking small amounts into microcapillaries and integrating with optical fibres (Coote et al. 2019). Nesson *et al.* developed a way of creating polyimide membranes and transferring them onto glass capillaries. The polyimide was initially poured on water to create a thin film which was partially cured. The fragile films were then lifted from the water and placed over the tops of the capillaries before being fully cured to adhere in place (Nesson et al. 2008). Chen *et al.* have also explored using chitosan as a membrane material. Chitosan is a polysaccharide with good diaphragm forming abilities, good adhesion and elastic properties. By dipping capillaries in solution and allowing them to dry in specially designed drying chambers, chitosan membranes were formed (Chen et al. 2010).

Further fibre optic F-P fabrication details are summarised well by Islam *et al.* (Islam et al. 2014).

In this work one of the aims is to utilise high-resolution 3D printing, to simplify the fabrication and enable rapid prototyping of such imaging and sensing devices. The following sections explore 3D printing in greater detail and highlight some of the fluid mechanic features that will be encountered when using high-resolution (<10 µm) 3D printing techniques throughout this work.

2.11 3D printing

To fully understand 3D printing, its benefits, and its potential for simplifying the fabrication of fibre optic sensors, the following review was conducted. High-resolution 3D printing techniques are utilised throughout this thesis.

3D printing is an additive manufacturing technique. This means that instead of removing material to create the shape of a structure it is added, usually layer by layer, to create the final shape (Schubert, van Langeveld, and Donoso 2014). This method of manufacturing is advantageous as it creates less wastage and is thus more

economical. It also enables rapid manufacturing processes, making it more time efficient compared to traditional manufacturing techniques (Wong and Hernandez 2012).

There are different methods of achieving 3D printing additive manufacturing, the most common are; stereolithography (SL), selective laser sintering (SLS), fused deposition modelling (FDM) and 3D direct-write (DW) (Vaezi, Seitz, and Yang 2013).

Stereolithography (SL) was the first additive manufacturing technique to be developed (Vaezi et al. 2013). It works by using a photopolymer in a liquid form that can be hardened to a solid by curing with an ultraviolet (UV) laser. The photopolymer is held in a vat and the UV laser passes over the surface to create the pattern of each layer. The structures are adhered to a movable platform that adjusts after each layer to allow fresh photopolymer to flood the area where the next layer will be created (Vaezi et al. 2013). Once the design is complete it usually needs to be rinsed with a solvent. The resolution of these prints are determined by the focal spot size of the laser and the amount of heat transfer that occurs in the photopolymer (Vaezi et al. 2013).

Selective laser sintering (SLS) is very similar to stereolithography except powders are used instead of liquids. Lasers are again used to create the desired pattern. They do this by heating a thin layer of powder causing it to sinter (coalesce into a solid) (Vaezi et al. 2013). The stage that the structure is being constructed on then lowers and a fresh layer of powder is deposited by a roller and the process then repeats, building the object layer by layer. SLS is usually carried out under vacuum to prevent humidity and oxidation problems (Vaezi et al. 2013). The resolution of this method is determined by the focal spot size of the laser and the size of the powder particles. Excess powder can be removed from the final structure and reused for future prints (Vaezi et al. 2013).

Fused deposition modelling (FDM) differs from the previous methods as excess/surrounding materials, like powder or photopolymer, are not required (Vaezi et al. 2013). The solid printing material is melted in the printer head and deposited layer by layer to create the desired structure. The temperature applied needs to be sufficient enough to melt the material and create a filament between the nozzle and the substrate while maintaining a constant flow (Vaezi et al. 2013). Also, the material needs to solidify quickly once extruded to prevent it from spreading over the surface. By careful control of the material and the temperature, the layers can solidify rapidly enough to enable the printing of multiple layers on top of each other to give 3D

structures. The printers can be designed so that either the nozzle is stationary and the stages beneath move, or the stage is stationary and the nozzle above moves or some combination of both to enable motion in the x, y and z directions. Thermoplastics are the most commonly used materials in FDM printers and the resulting objects are of good mechanical quality, leading to their use to manufacture mechanical parts (Vaezi et al. 2013). Should certain designs require it, additional support material can be deployed. This support material can be of the same material as the main object or a different material to aid its removal. The resolution of FDM is determined by the size of the printing nozzle and the material used.

3D direct-write (DW) is similar to FDM but does not require a heating element. The printing material is an ink which must be fluid enough to be extruded through a nozzle (Vaezi et al. 2013). Some common examples of inks are colloidal suspensions, colloidal gels, colloidal fluids, waxes and polymer melts (Lewis 2006). Pressure is usually applied to the ink by a pneumatic control system, which forces the ink through the nozzle continuously so that a filament is created between the nozzle and the substrate. By carefully controlling the surface and ink properties, the ink will adhere to the surface once extruded and then a combination of capillary and pressure forces will act to replace the material in the filament and enable continuous printing onto the surface (Lewis 2006). Once deposited the ink then needs to solidify to stop it spreading across the surface and to enable additional layers to be built on top. Depending on the design of the ink this hardening process can be due to evaporation, temperature change or solvent induced (Lewis 2006). Positioning stages can be used to move either the substrate or the nozzle to create relative motion for 3D patterning. Print resolution in this case depends on nozzle size, nozzle and substrate wettability, the stability of the filament, ink rheology and evaporation characteristics (Caulfield, Fang, and Tiwari 2018).

2.12 High-resolution 3D printing[1]

In order to utilise 3D printing to aid with the production of fibre optic imaging and sensing probes, the ability to create microscale structures and patterns is necessary.

High resolution 3D printing is usually defined as that with a resolution of 10 µm or less. Printers capable of achieving these sorts of resolutions are not widely available,

[1] Sections 2.12 - 2.13 were published as a book chapter, Caulfield R., Fang F., Tiwari M.K. (2018) Drops, Jets and High-Resolution 3D Printing: Fundamentals and Applications. In: Basu S., Agarwal A., Mukhopadhyay A., Patel C. (eds) Droplet and Spray Transport: Paradigms and Applications. Energy, Environment, and Sustainability. Springer, Singapore.

for example the popular Formlabs Form2 commercial printer has a laser spot size of 140 µm. With this in mind, we limit our discussion to printing techniques that are fluidic assisted. Fluidic assisted high-resolution printing techniques exploit micro- and nano-fluidic features to achieve high resolution, though they also have some challenges that must be overcome.

There are several challenges related to fluidic assisted high-resolution 3D printing. Firstly, printing on this scale usually requires flow through small capillaries and channels. Since pressure drop scales as $\sim D^4$ (Poiseuille relationship, where D is the diameter of the capillary/channel) this indicates a pressure drop increase of 16-fold when the printing nozzle diameter is halved. Therefore, going from a 100 µm nozzle to a 10 µm nozzle has an associated pressure drop increase of 4 orders of magnitude.

Secondly, at this scale capillary and wettability effects become highly dominant (de Gennes, Brochard-Wyart, and Quéré 2004). Thus, a high level of control over the wettability of the nozzle and substrate are required but this is not straight forward and can be problematic.

Thirdly, evaporation of a liquid scales with surface area. For a sessile droplet the evaporation scales as $\sim d_c^2$ (where d_c is the contact diameter of the droplet) (Popov 2005). Therefore, inks designed for standard printing will evaporate at an accelerated rate when used in high-resolution setups and can lead to clogging problems.

Finally, the successful utilisation of high-resolution printing partially relies on its ability to be integrated with existing devices. This integration can lead to printing on application specific substrates, which poses a materials challenge and packaging issues but similar to other technological industries this is resolvable.

2.12.1 Types of fluidic assisted high-resolution printing

In this project we focus on a subset of high-resolution printing techniques which are fluidic assisted. There are several different high-resolution printing techniques which fall under this category. Examples are, electrohydrodynamic printing (EHD), dip-pen nano-lithography, direct-write printing (DW), transfer printing, pyroelectrohydrodynamic printing and laser-induced forward transfer printing (LIFT). A brief description of each follows and further details can be found in the included references (Caulfield et al. 2018).

Electrohydrodynamic printing (EHD) takes advantage of electric fields to eject material through nozzles (Onses et al. 2015). The nozzles are either coated with a layer of metal (usually gold) or have a metallic filament in their centre, to enable the

formation of the electric field between the nozzle and the substrate. Pneumatic backpressure can be applied to force the ink to the tip of the nozzle where the electric field mechanism takes over and causes ejection of the ink. The liquid ink forms a meniscus at the tip of the nozzle and maintains its shape thanks to surface tension. When the electric field is applied it causes a movement of ions in the ink and leads to an accumulation of mobile-ions at the surface of the meniscus (Ru et al. 2014). This increased number of ions causes an elevated concentration of Maxwell stresses in the meniscus. The Maxwell stresses act against the surface tension of the ink, and beyond a threshold they cause the meniscus to deform into a cone shape (Park et al. 2007). Material can then be ejected from this cone and deposited onto the surface beneath. By careful control of the ink properties and field strength, several different material ejection modes can be achieved (Basaran 2002; Collins et al. 2008; Jaworek and Krupa 1999). The ejection modes give drop-by-drop printing or jetted material printing, both capable of high-resolution printing. Examples of these ejection modes are illustrated in Figure 2.8b where the dashed box indicated the modes capable of high-resolution 3D printing.

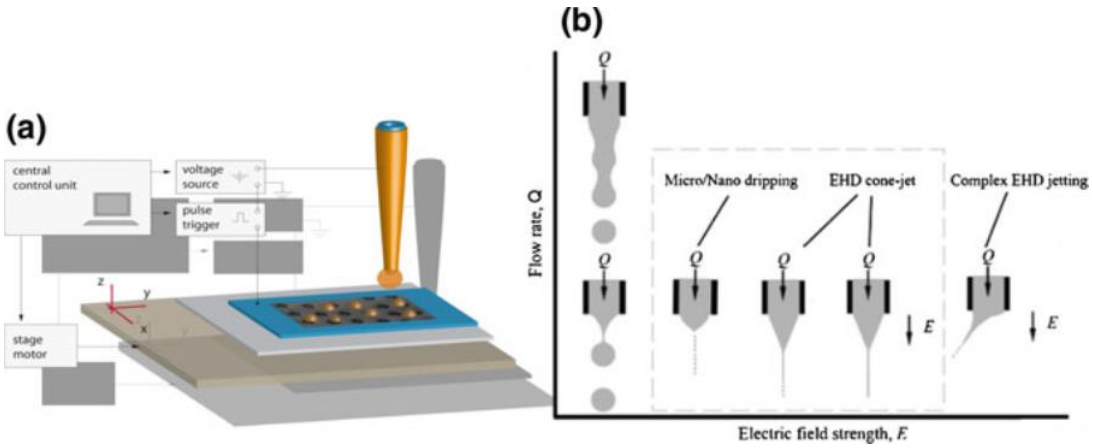

Figure 2.8 - a) Schematic diagram of EHD printing, reproduced from (Schirmer et al. 2010), b) Different ejection modes of EHD under different conditions with the high-resolution printing modes highlighted by the dashed box, reproduced from (Caulfield et al. 2018).

Dip-pen nano-lithography is similar, in principle, to using pens to write on paper. The basic concept is that ink is transferred from the "pen" tip to the surface by a liquid bridge (capillary bridge) (Bostwick and Steen 2015; Kumar 2015). In dip-pen nano-lithography the "pen" is an atomic force microscopy (AFM) tip. The technique was pioneered by Mirkin's group (Piner et al. 1999). The tip is coated with ink in a similar manner to how quill pens are coated with ink. When the tip is brought close to the substrate surface, under ambient conditions, residual water condensates between the tip and the surface to form a liquid bridge (Weeks et al. 2002). The ink molecules can then diffuse across this bridge, from the tip to the substrate below where they are

deposited in the wake of the tip as it moves across the substrate surface as shown in Figure 2.9. By controlling variables such as humidity, temperature and tip speed the printing resolution can be adjusted to ~10 μm (Hong et al. 2006). The technique is also useful for biological applications as it allows printing of soft materials onto a multitude of substrate surfaces (Salaita, Wang, and Mirkin 2007).

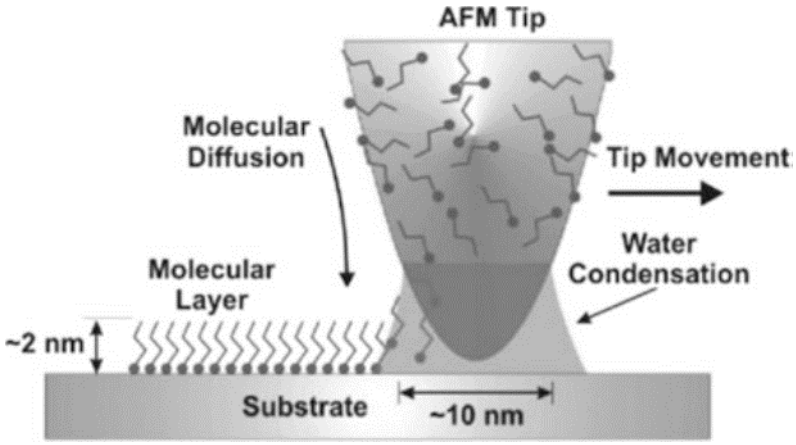

Figure 2.9 - Schematic diagram of dip-pen nano-lithography, reproduced from (Hong et al. 2006; Piner et al. 1999).

Direct write printing (DW) is a filament-based printing technique. In this technique inks are extruded through microscale nozzles and a filament forms between the nozzle and the substrate (Lewis 2006). Pneumatic backpressure and capillary action (between the ink and substrate) forces the ink to be extruded. The relative motion between the nozzle and the substrate creates deposition patterns. By using microscale nozzles and positioning stages with micrometre or nanometre repeatability, these patterns will have high-resolution features. An exemplar setup is shown in Figure 2.10. One of the main advantages of DW printing is that the printing can be carried out without the need for a temperature control system, provided the inks are suitably formulated. Many different types of inks have proven to be printable with DW setups such as colloidal suspensions, fugitive organic inks, hydrogels, sol-gels, polymers and nanoparticle filled inks (Ahn et al. 2009). Additional stability can be provided to the printed structures by applying post-printing treatments such as thermal annealing or UV curing. The factors that determine if high-resolution is possible are nozzle size, nozzle and substrate wettability, the stability of the filament, ink rheology and evaporation characteristics (Caulfield et al. 2018).

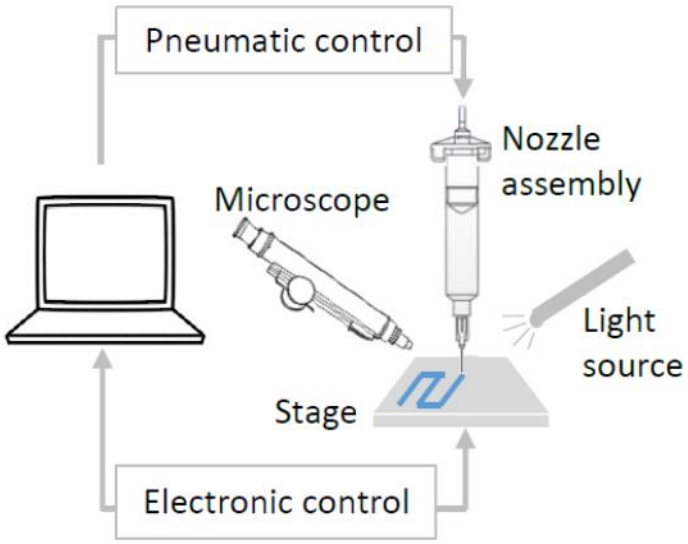

Figure 2.10 - Schematic diagram of DW printing, reproduced from (Fang et al. 2017).

Transfer printing shares the same basic principle as traditional stamping. That is, a patterned stamp is coated with a suitably formulated ink and then the stamp is pressed into contact with the printing surface where capillary transfer allows the pattern of the stamp to be copied onto the intended substrate. This might not immediately appear to be a high-resolution technique but by using methods such as photolithography, stamps with micrometre and nanometre features can be created. The successful transfer of these high-resolution features from the stamp to the substrate surface relies on careful control of the ink rheology, wettability and elastic properties of the stamp/substrate (Carlson et al. 2012). There are several possible types of transfer printing, which depend on the precise design of the ink and stamp: relief, intaglio, lithography and screen (Kumar 2015; Michel et al. 2002). These different types of transfer printing are summarised in Figure 2.11. Relief is the classical stamp design with raised areas that get coated with ink and transfer the pattern when they make contact with the substrate. Intaglio is the inverse of relief transfer printing, instead of raised areas the stamp is composed of sunken wells. The wells are filled with ink and the substrate is placed on top where the transfer occurs. Lithographic transfer printing is similar to relief but instead of raised areas collecting and transferring the ink, the wettability of a planar stamp is altered so that in certain areas the ink sticks and in other areas the surface is phobic to the ink, thus creating the desired pattern. Screen transfer printing differs as it uses a stencil instead of a stamp. The stencil is placed onto the substrate and ink is applied. The ink only transfers to the substrate in the chosen areas. The stencil and excess ink are then removed leaving the patterned substrate. Transfer printing has been used to create

multi-layer and 3D structures (Zaumseil et al. 2003). It has also been used in conjunction with self-assembly block copolymers to achieve sub-10 nm resolutions (Jeong et al. 2012). Despite this impressive resolution the durability of stamps with these features sizes is very poor. One solution has been to use elastomeric, conformal, stamps (Meitl et al. 2006).

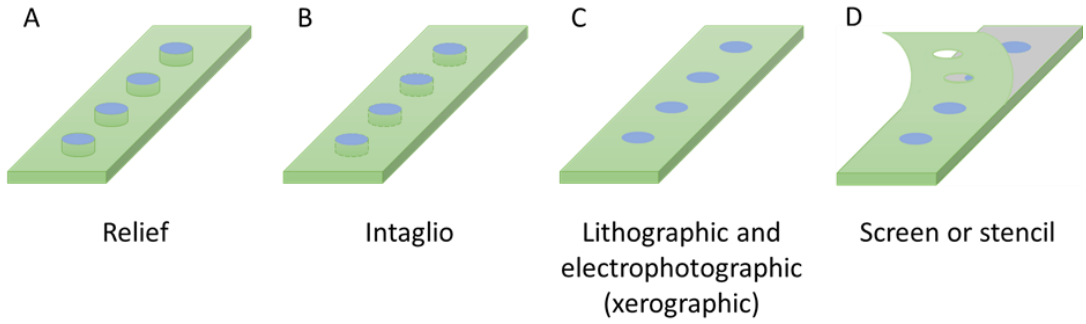

Figure 2.11 – Schematic diagram showing different types of transfer printing, reproduced from (Caulfield et al. 2018).

Pyroelectrohydrodynamic printing is a nozzle-less technique. Pyroelectrohydrodynamic printing setups are composed of a drop reservoir, a slab of pyroelectric material (such as lithium niobate) and a heat source (infrared laser or soldering tip) (Ferraro et al. 2010) as depicted in Figure 2.12. The substrate to print on is placed between the drop reservoir and the pyroelectric material. The printing method shares similarities with EHD. When the heat source is turned on it creates local electric potentials in the pyroelectric material, these then act to distort the shape of the drop reservoir meniscus and causes droplet or jetting ejection towards the substrate. Patterns can be created by scanning the heat source or substrate to generate relative motion and by altering the angle of the heat source (Ferraro et al. 2010; Rogers and Paik 2010). The resolution is similar to EHD and limited by the

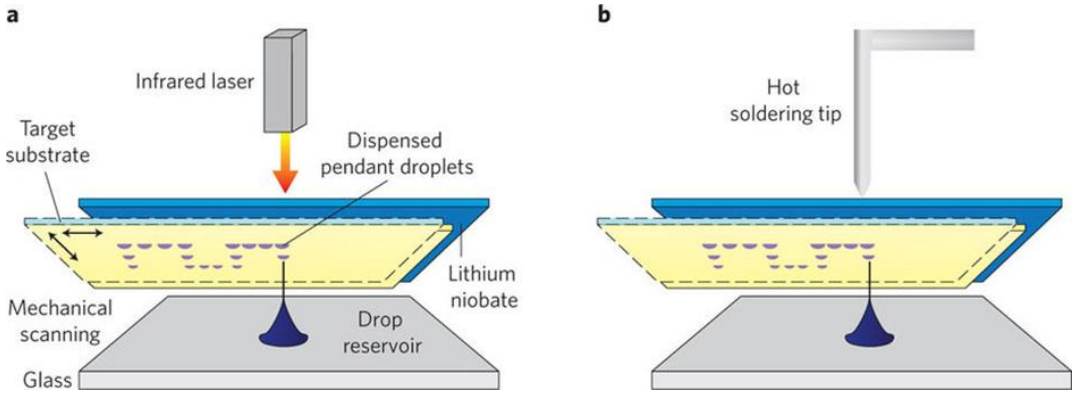

Figure 2.12 - Schematic diagrams of pyroelectrohydrodynamic printing setups, reproduced from (Rogers and Paik 2010).

same variables except for nozzle size. By removing the nozzle any clogging issues are also removed and removes some of the limitations on the ink design.

Laser-induced forward transfer printing (LIFT) is also a nozzle-less printing technique. Focused laser pulses are shone at a surface where they are absorbed and cause the ejection of material onto the substrate beneath. A scematic LIFT setup is shown in Figure 2.13. The simplest design has a two-layer absorbing plate positioned above the substrate. The first layer is a transparent glass layer called the carrier/support layer. Below this is a thin film of the material to be printed called the donor layer (Hirt et al. 2017). The laser pulse travels through the glass carrier layer and is absorbed by the donor layer. If the fluence of the laser is great enough this will cause the donor layer to melt or vaporise. This melting/vaporisation causes a pressure change at the carrier/donor interface which forces the ejection of donor material from the surface. By moving the donor layer to a fresh position and moving the substrate beneath printing patterns can be created. After ejection the donor material to be printed cools on the substrate surface and solidifies (Hirt et al. 2017). The induced phase change associated with the melting/vaporisation and re-solidifying can alter the properties of the donor material. To overcome this, an additional layer is sandwiched between the carrier and donor layers. This additional layer is called the dynamic release layer (DRL) (Piqué et al. 2016). The role of the DRL is to absorb the incident laser energy and to melt/vaporise/deform accordingly, dependant on the laser fluence. A pressure change now occurs at the carrier/DRL layer interface. By tuning the laser and DRL properties the generated pressure can eject the donor material without the need for it to undergo a phase change. This printing technique has been shown to be capable of sub-micrometre printing resolution (Zywietz et al. 2014).

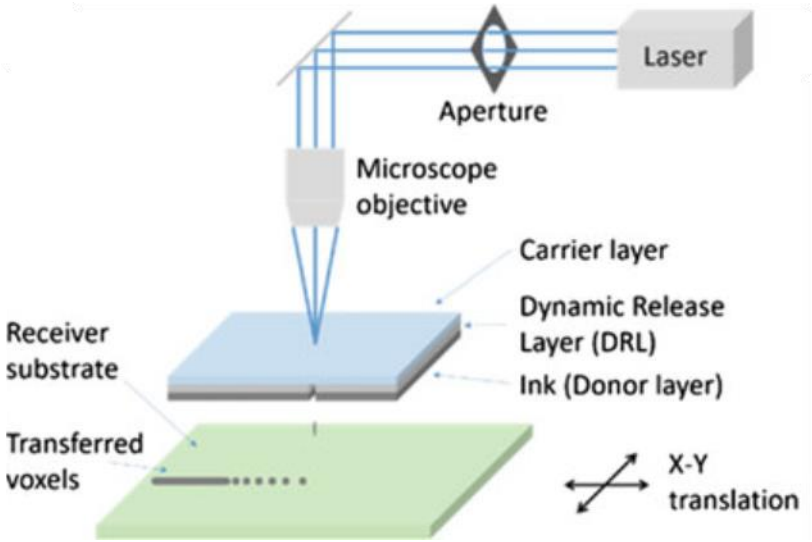

Figure 2.13 - Schematic diagram of LIFT, reproduced from (Caulfield et al. 2018).

2.13 Fluid mechanics features

In this section some of the key fluid mechanics features that influence fluidic assisted high-resolution 3D printing will be explored. The section begins by defining key rheological parameters. It then moves on to substrate wetting followed by nozzle properties, such as nozzle size and wettability and their influence on printing. Finally, the section looks at dynamic effects. For each feature, techniques used to tune the print resolution/quality will be examined, methods to overcome potential limitations will also be discussed. This information is extremely important for the development of the microfabrication processes discussed in Chapters 3 and 4, as well as the precise material deposition outlined in Chapter 5.

2.13.1 Ink rheology and pressure drop

Ink properties have a huge influence over print resolution and the stability of printed structures. Properties such as viscosity and viscoelasticity will be explored and placed in the context of their influence on nozzle pressure drop and structural stability. The viscosity of an ink is a measure of the ink's resistance to deformation from an applied stress (Caulfield et al. 2018). Fluids are defined as either Newtonian or Non-Newtonian depending on the relationship between their viscosity and strain rate. Newtonian fluids have a viscosity that is independent of strain rate and Non-Newtonian fluids have a viscosity that is dependent on strain rate. Non-Newtonian fluids can be sub-divided into more specific categories. Shear thickening liquids have a viscosity that increases with increasing shear rate and shear thinning liquids have a viscosity that decreases with increasing shear rate (Caulfield et al. 2018).

Thixotropic liquids have a time-dependent viscosity which decreases at a constant shear rate and rheopectic liquids have a time-dependent viscosity which increases at a constant shear rate. Bingham plastics are fluids that display solid-like properties at low stress and viscous characteristics at high stress. Herschel–Bulkley fluids have solid-like behaviour at low shear rates and a shear-dependent behaviour at higher shear rates (Batchelor 2000; Kirby 2010). Non-Newtonian fluids are common materials in high-resolution 3D printing. Recently, there has been an increased interest in printing softer materials for applications such as tissue engineering, bio-scaffolds and flexible electronics. These materials do not show the properties of pure liquids with viscous dissipation and they also do not show the properties of pure solids with elastic behaviour. In fact, they show varying degrees of elastic (solid-like) and viscous (liquid-like) properties and thus are termed viscoelastic materials. The behaviour of these materials is best described by using the dynamic modulus (G). The dynamic modulus relates the materials dynamic stress and strain. It can be expressed as:

$$G = G' + iG''$$

(2.17)

Where i is the square root of -1. The equation essentially states that the dynamic modulus can be separated into two components, the storage modulus (G') and the loss modulus (G''). The storage modulus captures the elastic properties of the material and the loss modulus captures the viscous properties. Each of these moduli can be measured by subjecting the material to an oscillatory shear deformation (Meyers, Chawla, and Meyers 2009) and measuring the resulting dynamic stress and strain parameters using a rheometer as:

$$G' = \frac{\sigma_0}{\varepsilon_0}\cos\delta\,; \quad G'' = \frac{\sigma_0}{\varepsilon_0}\sin\delta$$

(2.18)

where σ_0 and ε_0 are, respectively, the stress and strain amplitudes recorded by the rheometer, and δ is phase difference between these two moduli.

A high value of G' indicates mechanical stiffness and thus enables stability of printed structures (Zhu and Smay 2012). A study by Duoss *et al.* examined a silica-filled polydimethylsiloxane (PDMS) ink and the behaviour when different silica concentrations were exposed to oscillatory stresses. The most dilute inks had lower G' values and small amounts of oscillatory stress caused this value to sharply drop to

zero. Inks with more silica had higher values of G' and required much more oscillatory force to cause it to decrease (Duoss et al. 2014). This result indicates that dilute inks are more liquid-like and are therefore not suitable for stable 3D printing and this property can be monitored by observing the storage modulus (G'). The minimum temperature for thermal annealing of an appropriate ink can also be determined by monitoring the storage and loss moduli with increasing temperature. Once the minimum cure temperature is reached G' will increase as the ink solidifies and there will be an associated drop in G''.

As printing materials with a low value of G' is desirable for many applications, ways to overcome this lack of stability have been developed. One solution is to print the material within a supportive gel-like medium (Bhattacharjee, Steven M. Zehnder, et al. 2015; Hinton et al. 2015). The gel-like medium has yield shear thinning properties to allow the printing nozzle to move within it but after printing the yield stress helps to support the printed soft material. Another method to structure materials with low G' values is to use sacrificial materials. One example involves creating a vasculature network (Miller et al. 2012). Sugar structures were printed to create a vasculature network, but the goal was to create the network out of soft material, so the sugar structure then had cells grown around it. Once the cells had encapsulated the whole sugar structure the sugar was dissolved away, leaving behind a low G' vasculature network structure.

Another important parameter for high-resolution 3D printing is pressure drop in the printing nozzle. To estimate this parameter the printing nozzle can be approximated as a capillary of uniform diameter. Using this approximation, the flow rate and pressure drop relationship for a power law fluid (common type of printing ink) can be given as (Fang et al. 2017):

$$Q = \frac{n\pi}{3n+1}\left(\frac{1}{2\mu}\frac{\Delta p}{l}\right)^{1/n} R^{3+1/n} \qquad (2.19)$$

Where Q is the flow rate, μ is the dynamic viscosity, R is the inner radius of the capillary and Δp is the pressure drop over a length l. By substituting in $n=1$ the relationship for a Newtonian fluid is obtained (Poiseuille relationship). Analysing the relationship allows conclusions to be drawn; for a fixed flow rate, the reduction of radius diameter results in a very high increase in pressure drop. If the radius is reduced by a factor of

2 then the resulting pressure drop increases by a factor of 16. The increased pressure drop highlights one of the challenges of high-resolution 3D printing.

2.13.2 Substrate wetting

Every surface has an associated surface energy related to surface forces. Consider two bodies in contact, to separate them (and hence create a new surface) energy needs to be input into the system to overcome the attractive surface forces between them. Therefore every surface has an associated energy that was required to create it, termed surface energy (Johnson, Kendall, and Roberts 1971).

Wettability is used to describe the ability of a liquid to 'stick' to a surface. If the liquid spreads across the surface it presents a larger surface area for attractive forces between the liquid and the surface to keep the liquid and surface in contact. This spreading of the liquid over the surface also makes the surface 'wet', hence the terminology, wettability.

The substrate wetting of an ink directly affects the resolution and the adhesion of the printed structure. When printing, a certain level of wettability is required so that the ink filament can adhere to the substrate to lay down the desired pattern. However, too much wetting will result in the ink spreading all over the surface, reducing the level of resolution and distorting the print pattern as lines begin to merge. The wettability of a substrate can be interrogated by placing a droplet on the surface. When a droplet is placed on a surface three interfaces are formed solid-liquid, liquid-gas and solid-gas. Each interface has an associated surface energy (γ_{SL}, γ_{LG}, γ_{SG}) and these will determine the shape of the droplet as it tries to minimise its surface energy. If the substrate is partially wetting the droplet will take the form of a spherical cap (see Figure 2.14a). The contact line runs circularly around the edge of the cap and at this point all 3 interfaces meet and their interfacial tensions are balanced. The contact angle is used to quantify the wettability of a surface. It is taken from the contact line along the liquid-gas boundary and is the angle this line makes with the solid-liquid interface (see Figure 2.14a). It is more precisely called the Young's contact angle, θ. If $\theta = 0°$, the substrate is referred to as perfectly wetting, for angles between 0° and 90° it is called wetting (or hydrophilic if the liquid is water). In the range of 90° up to 180° it is termed non-wetting (or hydrophobic if the liquid is water). If $\theta = 180°$ then the substrate is completely non-wetting.

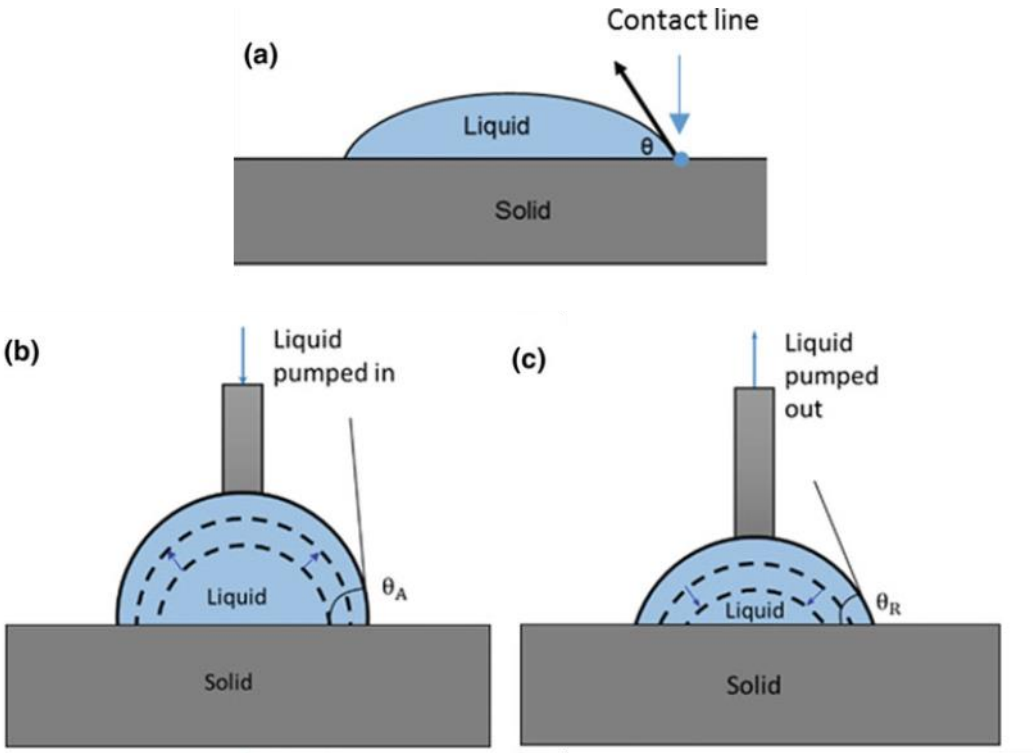

Figure 2.14 – Schematic diagrams of a) Contact line of a droplet on a partially-wetting surface, b) Advancing contact angle, c) Receding contact angle. Reproduced from (Caulfield et al. 2018).

All 'real' substrates have a minimal surface roughness so are not truly homogeneous. These heterogeneities manifest themselves as differences in surface wettability, resulting in different angles for advancing and receding liquid interfaces. The advancing (θ_A) and receding (θ_R) contact angles can be measured by slowly increasing or decreasing the volume of the droplet as illustrated in Figure 2.14 b and c.

The difference between the advancing and receding contact angles is called hysteresis. Hysteresis also affects high-resolution printing. For a substrate with a large hysteresis a printed droplet can become 'pinned' to the surface and as the solvent evaporates out, the ink particles are deposited in a non-uniform manner, known as the "coffee ring" effect (de Gennes et al. 2004). There are several techniques that can be used to modify the substrate wettability and tune it for specific printing applications. Some common surface modification techniques are plasma treatment and surface functionalisation (Tiwari et al. 2010).

The surface energies at each interface (γ_{SL}, γ_{LG}, γ_{SG}) are directly related to the work of adhesion (W_{ad}), which is a measure of the liquid adhesion with the substrate. The work of adhesion is essentially the energy (per unit area) required to separate a liquid from the solid it is lying on and can be shown to be (Israelachvili 2011):

$$W_{ad} = \gamma_{LG}(1 + \cos\theta)$$

(2.20)

Equation (2.20 highlights that the hysteresis between advancing and receding angles also indicates a hysteresis in energy. There is a difference between the energy 'spent' to destroy the liquid-solid interface (separating them) and the energy 'gained' by creating it. For 'real' substrates θ_R is smaller than θ_A, this means that there is a positive energy penalty associated with the removal of liquid from a surface. Though substrates with high hysteresis can 'pin' droplets and cause non-uniform "coffee-ring" deposition, the large hysteresis can also enhance adhesion and the stability of filaments or liquid bridges.

2.13.3 Nozzle properties

For printing techniques that use nozzles the nozzle properties clearly have a large impact on printing. In this project fine nozzles on the order of micrometres were prepared in the lab using a Sutter micropipette puller that heats and stretches glass capillaries. Nozzle size and wettability are discussed below.

2.13.3.1 Nozzle size

The diameter of the nozzle directly affects the achievable resolution of printing. In DW and other extrusion-based techniques, the nozzle diameter is a key contributing factor in determining the size of the printing filament. Wettability and evaporation also play important roles in determining the filament size and hence resolution.

In EHD printing the size of the droplets and jets produced are generally an order of magnitude less than the size of the nozzle due to the applied electric fields. This reduced size is advantageous as high-resolution structures can be printed with relatively large nozzle diameters and thus avoiding many problems with ink clogging in the nozzle (smaller nozzles are more prone to clogging issues). Though this loosens the restrictions on nozzle size and clogging issues it also increases the dependence on the applied voltage and the nozzles must be metal coated or have a metallic filament to comply with these printing regimes.

2.13.3.2 Nozzle wetting

Nozzle wettability also has a role in determining the size of droplets/filaments and hence print resolution. By tuning this parameter, the stability of printing filaments can also be improved. Dong *et al.* examined nozzles of differing wettability, ranging from hydrophilic to super-hydrophobic (Dong, Ma, and Jiang 2013). For hydrophilic nozzles they reported that the water spreads from the inner diameter across to the outer

diameter and up the outer wall of the nozzle, so the contact line has moved away from the tip and is around the outer diameter. For hydrophobic nozzles it was observed that the droplet was pinned and had a contact line at the outer diameter of the nozzle and for super-hydrophobic it was pinned with a contact line at the inner diameter. By balancing the capillary and gravity forces the maximum volume of a droplet can be extracted.

$$V = \frac{\pi \gamma D \sin\theta}{\rho g} \tag{2.21}$$

Where V is the volume of a droplet, γ is the surface tension, D is the diameter of the droplet contact line, θ is the liquid contact angle, ρ is the density of the ink and g is gravitational acceleration.

The contact angle is measured as previously described, from the point where the solid, liquid and gas phases meet and along the liquid-gas boundary. In Figure 2.15, progressing from hydrophilic to super-hydrophobic the contact angle increases and the surface area of attachment decreases. As the attachment area shrinks, less mass can be supported by the capillary forces and thus smaller droplets can be created which in turn improves the print resolution.

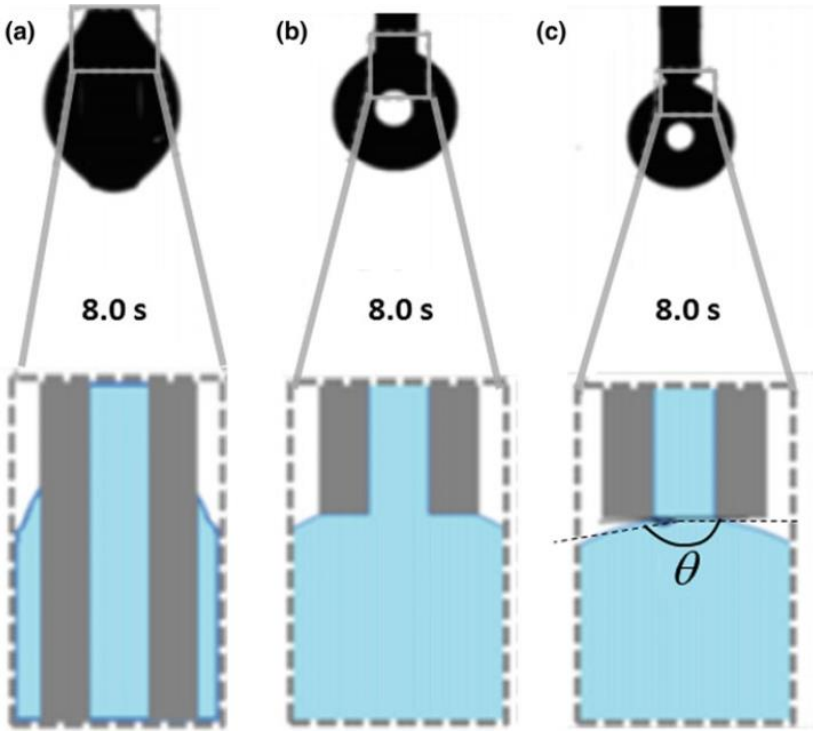

Figure 2.15 – Images and schematics of nozzles with different wettabilities, a) Hydrophilic nozzle where contact line has moved up the outer diameter, b) Hydrophobic nozzle where contact line is pinned at the outer diameter, c) Super-hydrophobic nozzle where contact line is pinned at the inner diameter. Reproduced from (Dong et al. 2013).

2.13.4 Dynamic effects

Printing is a dynamic process and therefore is influenced by dynamic effects such as evaporation. Controlling evaporation is crucial for many aspects of high-resolution 3D printing. Starting in the nozzle, if the evaporation rate is too high then the solvent will evaporate out and the ink will solidify in the nozzle before it is extruded and deposited onto the substrate. Assuming that the evaporation rate is not too high, and the ink can be successfully extruded and deposited onto the substrate, the evaporation still has an important role. After deposition the evaporation will influence the extent of spreading of the ink, the ability to produce 3D structures and the homogeneity of the cured ink. These evaporation features and resulting influences can be investigated further by considering the relevant timescales.

As previously stated, most real surfaces have a contact angle hysteresis which causes droplets to become pinned to the surface along their contact line. The timescale of evaporation (τ_{evap}) for a droplet with pinned contact line, in a regime of low contact angle, can be given as (Popov 2005):

$$\tau_{evap} = \pi \, {d_c}^2 \, \frac{\theta_0 \, \rho_l \, RT}{64 \, D_l \, M_l \, \Delta p}$$

(2.22)

Where d_c is the pinned contact diameter, θ_0 is the low contact angle, ρ_l is liquid density, R is the gas constant, T is the temperature, D_l is the diffusion coefficient of the liquid vapour, M_l is the molecular weight and Δp is the partial pressure difference. The partial pressure difference is calculated between the pressure at the liquid gas interface and the pressure at infinity (very far from the interface). This difference is the driving potential for evaporation.

For 3D printing, consecutive layers need to be printed on top of each other. This construction technique means that the previous layer should solidify before the next one can be printed. Therefore, the evaporation time must be less than the time between layers, for an ink that cures via solvent evaporation. This dependence on evaporation is avoided in some printing setups by using inks that solidify due to chemical reactions or by cooling through a transition temperature.

As the regime being investigated is that where the contact line is pinned, it is also true that the evaporation is greater at the contact line than in the centre of the droplet. This difference leads to non-uniform vapour flux which in turn causes a flow of ink from the centre of the droplet to the contact line (the edge). Since the evaporation is greater at the edge to begin with, the solvent is rapidly removed, and the ink particles are deposited at this location. The resulting non-uniform deposition appears as a darker ring around the edge of the droplet when all of the solvent has evaporated. Due to the resemblance between the deposition pattern and that observed when coffee drops evaporate, the pattern is called the “coffee-ring” effect (Deegan et al. 1997). When 3D printing, a uniform distribution is desirable for resolution and stability therefore efforts have been made to overcome the coffee-ring effect.

To fully explore the coffee-ring mechanism another timescale is introduced, the timescale of particle diffusion (τ_{part}). The timescale of particle diffusion gives a measure of the time it takes for the particles in the ink to diffuse through the droplet. To overcome the coffee-ring effect, one idea is to create an ink where $\tau_{evap} < \tau_{part}$. By imparting this restriction, the timescale for evaporation is so short that the solvent completely evaporates before the particles have time to diffuse away from their original homogeneous dispersion. Rapid evaporation has the added benefit that if it is continuous then it can alter the contact angle of the droplet. If the contact angle can be altered so that it is below the critical receding angle limit (θ_{rec}) then the contact line

becomes un-pinned from the substrate and the coffee-ring effect no longer occurs. Considering this, an updated equation for the timescale of evaporation is:

$$\tau_{evap} = \pi \, {d_c}^2 \, \frac{(\theta - \theta_{rec}) \, \rho_l \, RT}{64 \, D_l \, M_l \, \Delta p}$$

(2.23)

The timescale of particle diffusion can also be calculated following the Einstein–Smoluchowski analysis of Brownian motion (Einstein 1926).

$$\tau_{part} = \frac{\bar{L}^2}{2D_p}$$

(2.24)

Where L is the average separation between particles and D_p is the diffusion coefficient. The diffusion coefficient is given by the Stokes-Einstein relation (Shen, Ho, and Wong 2010).

$$D_p = \frac{k_B T}{3\pi\mu d_p}$$

(2.25)

Where k_B is the Boltzmann constant, T is the temperature, μ is the dynamic viscosity and d_p is the particle diameter.

The average particle separation can be calculated as (Schirmer et al. 2011):

$$\bar{L} = \left(\sqrt[3]{\frac{\pi}{6\Phi}} - 1 \right) d_p$$

(2.26)

Where Φ is the particle volume fraction and d_p is the particle diameter.

McHale *et al.* (McHale et al. 1998) carried out further investigations on evaporation time, including hydrophobic surfaces. Hydrophobic surfaces have a low contact angle hysteresis and droplets therefore find it difficult to adhere. As the droplets are not pinned their contact line can move, which makes it difficult to maintain a constant contact angle to enable evaporation. By including this result the equation for the timescale of evaporation is altered again to give:

$$\tau_{evap} = {d_c}^2 \frac{\rho_l RT}{16\, D_l\, M_l\, \Delta p} \frac{(1 - \cos\theta)(2 + \cos\theta)}{sin^2\theta}$$

(2.27)

Where all variables mean the same as previously defined.

For all three discussed equations for the timescale of evaporation, the timescale is related to the square of the contact diameter (d_c). This relation highlights one of the challenges of high-resolution 3D printing, as the resolution is increased (the contact diameter is reduced), the evaporation time also decreases. For example, if the resolution/contact diameter is reduced by a factor of 10 then the evaporation time is sped up by two orders of magnitude. This increased evaporation must be considered when designing inks for use in high-resolution fluidic assisted 3D printing.

As previously stated, the coffee-ring effect is undesirable in 3D printing and a few methods of overcoming it have been developed. The simplest solution was devised by Shen *et al.* (Shen et al. 2010) who showed that coffee-rings could be avoided by using smaller droplets. By equating the equations for the timescale of evaporation and the timescale of particle diffusion, a critical droplet size can be determined where the timescale for evaporation is less than the timescale of particle diffusion and hence the original homogeneous particle dispersion is maintained after solvent evaporation. In this regard moving to high-resolution, and hence smaller droplet sizes, is an advantage to overcoming the coffee-ring effect. Another method to overcome the coffee-ring effect is to make use of Marangoni flow (Hu and Larson 2006). This method was proposed by Hu and Larson and uses the non-uniform evaporation responsible for the coffee-ring effect to act against itself. The non-uniform evaporation of a pinned droplet can lead to a temperature gradient at the liquid-air boundary which in turn can lead to Marangoni flow. Marangoni flow circulates the liquid along the liquid-air boundary to the centre of the droplet where it then forces it downwards to the bottom, then back out towards the contact line and returning along the liquid-air boundary (see Figure 2.16b). The Marangoni flow can be strong enough to overcome the capillary flow of the ink which leads to coffee-ring deposition. By maintaining particle movement, the homogeneous dispersion remains. A third strategy was devised by Yunker *et al.* This method uses the shape of the ink particles to evade the coffee-ring effect (Yunker et al. 2011). They showed that by using high aspect ratio particles (such as ellipsoids) uniform deposition could be obtained. When these particles reach the droplet-air interface there is a strong interparticle attraction between the ellipsoids. This interparticle attraction is two orders of magnitude greater

than that for spherical particles. The attraction strongly binds the ellipsoids to each other and to the interface. The energy required to disrupt these bonds is quite large, so the particles undergo minimal movement and therefore give a uniform deposition after solvent evaporation. It was also shown that by adding a small proportion of ellipsoidal particles to spherical particles a near uniform particle deposition could also be achieved. These methods of preventing coffee-ring formation are of great practical importance to high-resolution 3D printing.

Further dynamic effects can be studied for a greater understanding of their role in high-resolution 3D printing, but they are more specific to drop by drop printing setups which are not the primary focus of the DW based high-resolution printing in this project.

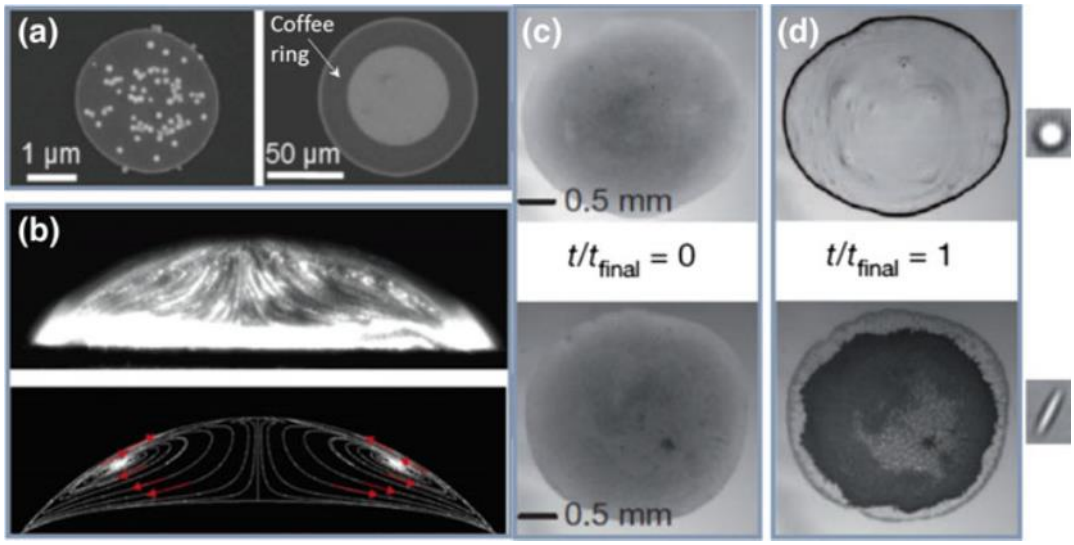

Figure 2.16 – The coffee-ring effect and its ameliorations a) Coffee-ring on the right can be minimised by decreasing the droplet size as on the left (Shen et al. 2010), b) Marangoni vortices in an octane droplet (Hu and Larson 2006), c) The initial homogeneous dispersion of both spherical (top) and elliptical (bottom) particles, d) The same droplets from c) after drying, visible coffee-ring in top image (spherical particles) and prevented coffee-ring in bottom (elliptical particles) (Yunker et al. 2011).

2.14 Additive manufacturing in optics

Much of the development of additive manufacturing is traditionally focussed on creating mechanical components. Utilising these techniques to create devices suitable for optical applications also has a lot of potential.

Additive manufacturing enables increased flexibility to the design and manufacturing of optical components (Zolfaghari, Chen, and Yi 2019). This flexibility makes it a good choice when creating customized components. Traditionally glass has been used to create lenses for the visible range of the optical spectrum. More recently polymers

have been used to produce optical components for these applications and have been found to be comparable to glass lenses (Gawedzinski, Pawlowski, and Tkaczyk 2017).

Selective laser sintering (SLS) has been used to create optical components. The most common use for this technique is to create reflective optical components, such as metallic mirrors. Metallic powders are used to deposit the reflective material onto a substrate but the surface roughness of this technique means that post-processing, such as grinding and polishing, is required to create reflective surfaces suitable for optical applications (Sigel, Merkel, and Heinrich 2017).

Stereolithography (SL) has also been used to create optical components. Instead of creating reflective optical components, such as mirrors, SL has been used to create lenses. Kukkonen *et al.* showed how nonlinear polymer based optical lenses could be produced using SL 3D printing. The photopolymerizable resin had microcrystals dispersed throughout it prior to printing (Kukkonen et al. 2018). Using a similar technique of two-photon polymerisation, Guo *et al.* were able to create micro lens arrays and Fresnel lenses with diameters of 15 µm and 17 µm respectively (Guo et al. 2006). Recently femtosecond lasers have been used to create optical components with sub-diffraction-limited feature sizes as small as 100 nm (Chen et al. 2018). The drawback of this technique is the large amount of time required for fabrication due to the small voxel size and point-by-point scanning mechanism (on the order of weeks to fabricate millimetre sized optical components). Chen *et al.* have reported a method of reducing the fabrication time for printing such optical components. They have developed a projection micro-stereolithography process which combines both grayscale photopolymerization and post curing methods. Using their technique, the need for point-by-point scanning is removed as dynamic masks are used to expose and photopolymerize the material. The prints are then treated post cure to achieve the smoothness required for optical components. This has resulted in reduced fabrication times (on the order of hours vs. weeks) for millimetre scale aspheric lenses, while still maintaining surface roughness values of sub 7 nm (Chen et al. 2018). This technique has been improved further to reduce the fabrication time of optical components even more. This enhanced technique results in print times down to the order of minutes to create millimetres sized components (Shao, Hai, and Sun 2020). This further enhanced technique utilises a micro-continuous liquid interface production process which removes the need to stop between each printing layer, which enables the rapid fabrication.

Droplet based printing techniques, such as inkjet printing, have also been used to fabricate optical components. This method presents challenges such as maintaining smooth surfaces and combining droplets to create continuous structures. Despite this, droplet based printing has the ability to utilise a wide array of materials and solvents (Zolfaghari et al. 2019). Gawedzinski *et al.* compared polymer Luxexcel lenses fabricated with inkjet printing methods with standard glass lenses fabricated with traditional techniques. They showed that the surface roughness of printed lenses were comparable to that of injection moulded lenses and they possessed a root mean square wavefront error comparable to that of glass lenses (Gawedzinski et al. 2017).

High-resolution printing techniques such as dip-pen nano-lithography have also been used to successfully print optical components. Jang *et al.* have demonstrated how dip-pen nano-lithography can be used to create micro-lens arrays where the diameter of each individual lens is 900 nm (Jang et al. 2010). Other high-resolution printing techniques such as EHD have also been used to create optical components. EHD has successfully been used to create micro-lens arrays, optical waveguides and diffraction gratings (Sutanto et al. 2014). Zhou *et al.* have shown how EHD printing techniques can be used to create nano-lens arrays with minimum lens diameters of 120 nm (Zhou et al. 2020).

Alongside using polymer materials to print optical components, much work has been done in using glass as a printing material as well. 3d printed glass structures can be used to create optical components for diffraction, scattering and other functions (Zhang, Liu, and Qiu 2020). Printing techniques such as FDM, SL, SLS and DW have all been used to investigate 3D printing of glass. In FDM high temperatures are required to create molten glass which can then be extruded through nozzles for printing. The research group at the Ningbo Institute of Materials Technique and Engineering, Chinese Academy of Sciences have developed a FDM system which can print glass with a resolution of 50 µm (Zhang et al. 2020). Generally, the high operating temperatures required to print glass have a negative impact on the FDM printing process by making it difficult to accurately control the extrusion of material. This issue, along with the 'step effect' between layers, means there are still problems with using FDM to print large glass optical components (Zhang et al. 2020). Successful SL printing of glass centres around the design of the slurry/resin used. By combining silicon dioxide (SiO_2) nanoparticles with a UV curable monomer Kotz *et al.* were able to print glass components with a resolution of a few tens of micrometres (Kotz et al. 2017). The process used by Kotz *et al.* uses SL printing to create components out of the SiO_2 nanocomposite resin. The polymerized composite is then

heat treated to 1300 °C to achieve de-binding and sintering, resulting in transparent 3D printed glass components with the optical clarity of commercial fused silica glass (Kotz et al. 2017). C. Liu *et al.* have also shown that using a similar SL method, the 3D printed glass components can be doped with rare earth ions to created coloured glass components (C. Liu et al. 2018). SLS printing, by sintering glass powder, has also been investigated (Klocke, McClung, and Ader 2004; Luo et al. 2017). 3D printing glass optical components with a SLS technique is promising but requires further improvements in precision to produce precise optical components (Zhang et al. 2020). DW printing can also be used to create glass structures by using an ink containing glass powder. Unlike FDM high temperatures are not required to extrude the ink from the nozzle however the ink must have good rheological properties. Once printed, the structures need to be post processed in order to achieve characteristics equivalent to that of commercially available glass (Destino et al. 2018).

2.15 Summary of previous literature

The following conclusions can be drawn from the available research concerning ultrasound imaging in minimally invasive surgeries:

- There is a need to provide surgeons with better imaging and sensing equipment to aid with feedback and guidance during minimally invasive procedures. Cardiology and fetal medicine provide appropriate fluid filled environments to aid acoustic transmission, thus making them well suited for in vivo ultrasound imaging.
- Traditional piezoelectric ultrasound transducers can be used to create miniature imaging probes. Miniaturisation is difficult due to the need to have physical electrical connections and wiring. MEMS technology has assisted in the creation of miniaturised ultrasound transducers, but the manufacturing processes are complex. Fabrication requires multiple steps and access to many specialised pieces of equipment.
- Photoacoustically generated, all-optical ultrasound can be utilised to overcome some of the limitations of miniaturised piezoelectric ultrasound transducers. Using optical ultrasound, the manufacturing processes are drastically simplified. The simplest processes simply involve dipping a fibre into the appropriate solution.
- There are many different materials/combinations of materials which can be used to effectively generate ultrasound photoacoustically in the thermoelastic regime. The material must possess good optical absorption and a high

coefficient of thermoelastic expansion. Carbon and metallic based absorbers have shown great potential when combined with PDMS.

Regarding interferometric sensors, the following conclusions can be reached from the work reviewed:

- Interferometric sensors can be used to measure many different parameters. For axial pressure sensing, Fabry-Pérot cavities are the sensing technique of choice.
- Fibre optic biomedical pressure sensors have advantages over capacitive and piezoresistive, such as simplified miniaturisation, biocompatibility, and immunity to electromagnetic interference.
- For low frequency physiological pressure sensing, F-P cavities can be interrogated using a low coherence interferometry technique. The sensing element for fibre optic physiological pressure sensors can be created from many different materials. Polymers are a popular choice as they are low cost and possess many favourable material properties, such as low Young's modulus. For pressure sensitive polymer membranes, fabrication techniques without splicing are preferred as the potentially damaging excessive heating aspect is avoided.
- For fibre optic hydrophones high finesse F-P cavities are the preferred sensing technique. To maximise the optical sensitivity a tuneable wavelength laser is used to interrogate the cavities. By tuning the lasing wavelength, the optimum bias point in the interferometer transfer function can be maintained throughout, thus maximising optical sensitivity.

The following conclusions can be made from previous studies investigating high-resolution microfabrication techniques:

- MEMS technologies have enabled the fabrication of miniature piezoelectric ultrasound transducers. Despite this, the fabrication techniques are complex, requiring many different steps and specialised equipment making the process expensive. MEMS fabrication techniques have also been utilised to create membranes and diaphragms for fibreoptic pressure sensors, but again the fabrication processes are lengthy and complex.
- High-resolution, fluidic assisted, 3D printing technology has the potential to enable simplified fabrication processes for fabricating miniature fibre optic imaging and sensing probes. These microfabrication techniques offer the

ability to manufacture probes out of a wider range of materials/combinations of materials.

- Fluidic assisted 3D printing technologies require careful optimisation of the printing ink. Properties such as the rheology, wettability and dynamic effects need to be considered and tuned for successful high-resolution printing.

2.15.1 Literature analysis

The literature reviewed covered a broad range of research areas. Starting with minimally invasive surgeries, some of the difficulties faced by the surgeons were examined and current imaging and sensing tools were discussed. The use of ultrasound as an imaging modality was then explored along with the challenges that are encountered when trying to miniaturise the transducers to meet the requirements of minimally invasive surgeries. Photoacoustically generated ultrasound was then presented as a simplified solution to overcoming the limitations associated with miniaturising traditional piezoelectric transducers. The required material properties necessary to generate optical ultrasound in the thermoelastic regime were then reviewed and the development of these devices were investigated. From optically generating ultrasound the attention then turned to optically receiving ultrasound and other lower frequency sound waves. The principles of interferometric sensors were discussed, and other biomedical sensors were summarised. The fabrication of miniature imaging and sensing probes were then examined. As an alternative fabrication technique to MEMS technologies, fluidic assisted high-resolution 3D printing technologies were analysed in detail. Fluidic assisted printing techniques showed potential to aid in rapidly producing miniature fibre optic imaging and sensing probes. Despite this potential the techniques require careful ink synthesis and tuning with cycles of optimisation.

From this review of the literature, it can be seen that there are some outstanding areas for scientific research. Firstly, there is still a lack of feedback being provided to surgeons during minimally invasive procedures to help them guide and deliver treatments. Despite the many advances within optical imaging and sensing, the associated costs of devices fabricated with MEMS technology is too high for single use medical devices. Dip coating fibres has enabled simplified fabrication of optical ultrasound transmitters, but the design of optical ultrasound receivers is more complex. This is a gap which new microfabrication techniques could fill and enable simplified fabrication processes for fibre optic pressure sensors and ultrasound receivers. Novel fabrication techniques based on fluidic assisted high-resolution 3D

printing would also offer the ability to additively manufacture sensing elements directly onto the tips of optical fibres. Fluidic assisted high-resolution 3D printing enables microfabrication with a relatively large range of materials, but more can be done to increase this. Currently materials with a low storage modulus (soft materials such as silicones and PDMS) are unable to be rapidly prototyped or structured on the microscale due to their low storage modulus. Techniques have been developed on the millimetre to centimetre scale to deposit them within supportive gels or cure them over sacrificial layers, but these have not advanced to the microscale yet. The ability to create microstructures of these types of materials could have significant impacts in the fields of biomedical engineering, flexible electronics and microfluidics.

Chapter 3 - Free-standing parylene membranes for all-optical fluid pressure sensing

3.1 Introduction

As outlined in section 1.1, knowledge of the pressure in vivo is an important physiological parameter in the medical field due to its usefulness during diagnosis, as feedback during surgery and in monitoring chronic conditions. This variety of applications highlights the need for stable pressure sensors capable of providing accurate pressure measurements in healthcare. Again, as discussed previously, there is a large range of different pressures across the human body starting as low as 10 mmHg in areas such as capillaries, the brain and bladder up to maximum normal pressures of approximately 150 mmHg experienced in the hips and knees. (Clausen and Glott 2014; Correia et al. 2018; Poeggel, Tosi, et al. 2015). Due to this range, sensors are usually optimised to function in a particular pressure range. The use of medical pressure sensors, their applications and categorisation are all regulated by governing bodies and standardisation agencies such as the International Organization for Standards (ISO) and the Food and Drug Administration (FDA). The regulations surrounding different sensors will depend on a variety of factors such as the specific application of the sensor, the placement of the sensor, the length of deployment and the method of deployment.

The focus of this chapter is on the development of fibre optic pressure sensors. These use optical methods of interrogation and can be fabricated in a variety of ways. As discussed in Chapter 2, the current fabrication techniques can be complex and expensive. This chapter describes the development of a simpler manufacturing process which utilises high-resolution 3D printing technologies to create fibre optic pressure sensors with deformable parylene-C membranes.

3.1.1 Fabry-Pérot fibre optic pressure sensors

As this research is focussed on fibre optic pressure sensors, an optical interrogation method is required. This work takes advantage of phase modulated interferometric

techniques. More specifically, the Fabry-Pérot (F-P) interferometer-based technique and associated cavities are utilised.

For extrinsic F-P based techniques an optical cavity is positioned at the end of an optical fibre (typically single mode) to create two parallel reflective surfaces as shown in Figure 3.1. The first partially reflective surface is the boundary at the end of the fibre since there is a difference in refractive index between the glass and the cavity. This beam is used as the reference beam for interferometry techniques and removes the need for a second branch in the interferometer to generate a reference beam. The second reflective surface is a deformable diaphragm at the end of the cavity. Light is shone down the fibre and when it reaches the end is partially reflected by the first surface (beam *A*). The remaining light is transmitted through the cavity to the second reflective surface (beam *B*) where it is again reflected. This results in two reflected light beams travelling back down the fibre. Interferometry is used to analyse these light beams to calculate the phase difference between them. The first reflected beam is taken to be the reference (beam *A*). If external pressure is applied, the position of the deformable diaphragm at the end of the cavity changes. This change in position results in a change in the phase of the reflected beam (beam *B*) which can be measured interferometrically. By monitoring the change in phase, the external pressure can therefore be determined. High finesse and low finesse cavities can be created by tuning the reflectivity of the surfaces/mirrors used. In this chapter low finesse cavities are used to measure low frequency physiological pressure changes.

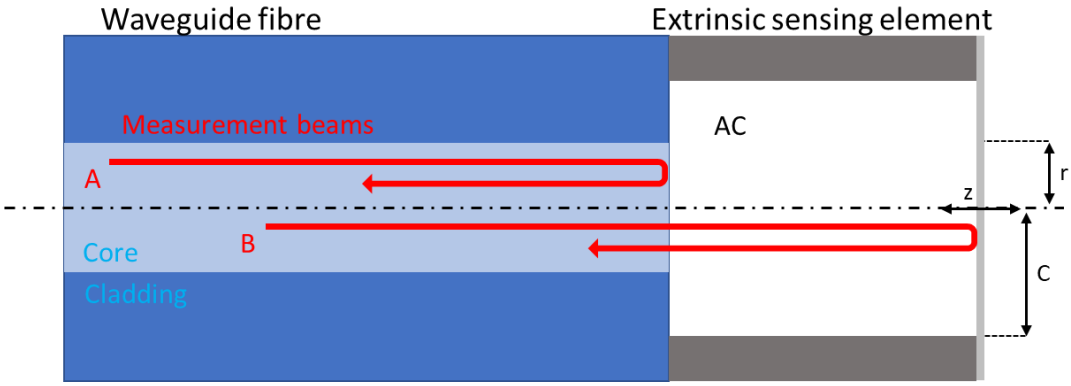

Figure 3.1 - Schematic diagram of an extrinsic F-P sensor. The extrinsic tip has a deformable diaphragm at the distal end. AC indicates an air cavity between the fibre and the diaphragm, C is the diameter of the diaphragm, z indicates the axial deflection direction, r is the radial distance from the centre point of the circular diaphragm.

As well as being used to detect pressure, single arm extrinsic F-P cavities can also be used to detect temperature. If the material used to create the deformable diaphragm is temperature sensitive, then it can undergo thermal expansion and

contraction. This expansion/contraction will cause the position of the diaphragm to change and hence induce a change in the phase of the reflected light beam. Another method to detect temperature is via changes in refractive index (Wolthuis et al. 1991). For this technique, the cavity is filled with a material such as silicon which undergoes changes in refractive index as the temperature changes. For silicon the relative refractive index change with temperature is larger than other material changes including its thermal expansion (Wolthuis et al. 1991). As the refractive index changes, the optical path length also changes relative to the reference beam and temperature changes can be extracted.

For F-P pressure sensors, if the deformable diaphragm is assumed to be a flat circular plate fixed around the circumference then it can be analytically investigated. For a thin circular diaphragm fixed around the circumference, the maximum deformation experienced under uniformly applied pressure occurs at the centre point and can be given by:

$$\omega_{max} = \frac{P\,R^4}{64\,D} \tag{3.1}$$

where P is the uniformly applied pressure, R is the radius of the diaphragm and D is the flexural rigidity (Zhang et al. 2015). The flexural rigidity is given by:

$$D = \frac{E\,z^3}{12\,(1-\nu^2)} \tag{3.2}$$

where E is the Young's modulus of the material, z is the thickness of the diaphragm and ν is the Poisson ratio of the material (L.D. Landau and E.M. Lifshitz 1986).

Equations 3.1 and 3.2 indicate that a thinner diaphragm will result in a larger maximum deflection and hence give greater sensitivity. If the diaphragm is positioned perpendicular to the direction of propagation if the interrogating light beam, then there is a linear relationship between the changes in pressure and the diaphragm deformation. As the maximum deformation occurs in the centre of the diaphragm, having the interrogating light well aligned with this position will also increase sensitivity.

3.1.2 Temperature measurements

Monitoring the temperature during minimally invasive procedures is also an important clinical parameter. During anaesthesia, the oesophageal temperature is monitored by inserting a probe through the nose/mouth and positioning it in the lower third of the oesophagus. The oesophageal temperature is in most cases considered to be an accurate and precise estimate for core temperature but misplacement of the probe can result in false measurements (Kyriacou 2010).

Pulmonary artery catheter (PAC) thermometry is considered to be the 'gold standard' in temperature monitoring and is used as a reference for other thermometry methods. The measurement is made by inserting a PAC (Swan-Ganz catheter) into the pulmonary artery. The catheter has a thermistor positioned near the tip in order to make temperature measurements. Due to the invasiveness of this it is not suitable for many patients and is only used in patients who are undergoing haemodynamic monitoring (Kyriacou 2010). Catheter based temperature measurements are also used to monitor temperature in the bladder. In this case the catheter used is a Foley catheter with a thermistor at the tip.

In the examples mentioned, thermocouples or thermistors are typically used. These electrical measuring methods have limitations such as electromagnetic interference and the high heat conductivity of the metallic wires causing over or under estimations (Schena et al. 2016). These limitations can be overcome by fibre optic sensors as they are immune to electromagnetic interference and are composed of silica which is a thermal insulator with low heat conductivity (Schena et al. 2016). Examples of commercially available fibre optic temperature sensors for medical use are described in section 2.2.

3.2 Sensor design considerations

When designing a fibre optic F-P pressure sensor there are several factors that need to be considered. Based on the literature and background information outlined, the following considerations were proposed.

1 The fibre optic sensor should be composed of a single mode fibre as the waveguide and an integrated extrinsic F-P sensing element.
2 The integrated fibre will be a single mode optical fibre, cleaved at normal incidence with a cladding diameter of 125 µm.

3 The interrogation system will be a phase resolved low coherence interferometry (LCI) system using a broadband super luminescent light emitting diode (LED) as a light source.

4 A deformable polymer membrane should be present at the distal end of the extrinsic F-P sensing element which can respond to environmental pressure changes.

5 The optical cavity between the polymer membrane and the cleaved single mode fibre should be air filled.

6 For LCI based interrogation the F-P sensing element can be low finesse using only moderately reflective surfaces.

7 For intravascular pressure sensing applications, the sensor will need to respond to pressures in the range of systolic/diastolic blood pressure (around 120 – 180 mmHg in normal adults).

8 The temperature response of the sensor should be well characterised around average human body temperature, 37 ± 3 °C.

9 The dimensions of the sensor should be small enough to enable integration into a cardiac catheter or guidewire and be deployable for PCI. The clinically preferred needle for PCI is an 18-gauge single wall puncture needle (Baim 2006), this correlates to an inner diameter of 0.8 mm. To enable integration into a device and the resulting device to be capable of insertion through an 18-gauge needle, the sensor dimensions should be limited to 300 µm or less.

10 The materials used in the sensor should be biocompatible.

11 The fabrication method should be able to facilitate the production of multiple sensing elements per batch.

12 The thickness of the deformable sensing membrane should be easily changed to allow investigations of how membrane thickness affects overall sensitivity.

3.3 Sensor design

Based on the design considerations outlined, the initial sensor design proposed was an extrinsic F-P fibre optic sensor where the extrinsic sensing element was a deformable free-standing polymer membrane supported on the distal end of a glass microcapillary. The microcapillary would then be integrated with a single mode optical fibre and secured in place with epoxy to create a low finesse fibre optic F-P pressure sensor, as illustrated in Figure 3.2.

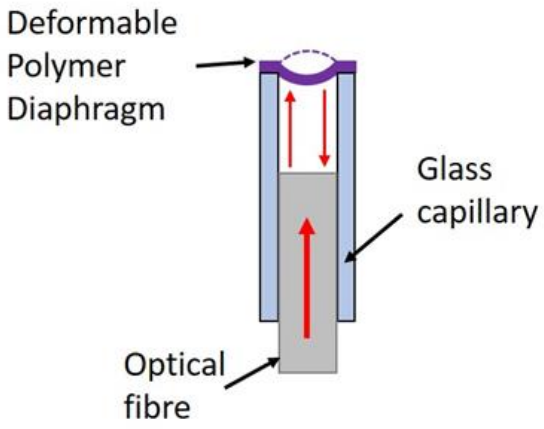

Figure 3.2 – Schematic of proposed sensor design.

As the proposed design is based on a free-standing polymer membrane, creating this was a critical component. Determining what polymer to use was also vitally important. To try and maximise the deformability of the membrane, and hence the sensitivity of the sensor, a thin and flexible polymer should be used. Previous work based on similar sensor designs have used a selection of polymers across a range of thicknesses and provided a variety of sensor sensitivities (Coote et al. 2019; Eom et al. 2015; X. Liu et al. 2018; Zhao et al. 2018). The polymer of choice for this work was parylene-C.

Parylene-C (polychloro-para-xylylene) is a crystalline material. It is deposited via vapour phase deposition which allows it to form highly conformal, structurally continuous, thin films. Parylene-C has many properties that make it well suited for this application. The mechanical properties of parylene-C are very favourable as it has a relatively low Young's Modulus (~ 2.8 GPa) indicating that it can easily deform when exposed to external forces, providing good sensitivity when assembled into a diaphragm-based pressure sensor. It also has high tensile strength (~ 69 MPa) and can be elongated up to 200% its original length before breaking, indicating that it should be able to withstand the environments that it will be exposed to. It provides excellent barrier properties, with low gas permeability and water vapor transmission rates compared to other similar polymers (SCS datasheet). For an air backed fluid pressure sensor low permeability is crucial. As well as this parylene-C has been shown to have good biocompatibility and biostability conforming to ISO requirements (SCS datasheet) which is very important for biomedical applications.

Equations (3.1 and (3.2 can be used to determine the maximum deformation of a flat membrane fixed around its circumference.

Following Equation (3.2 the flexural rigidity for parylene-C can be calculated by taking values of the Youngs modulus (E) and the Poisson ratio (v) from literature. E = 2.75 GPa and v = 0.4. The remaining variable for the flexural rigidity is the thickness of the membrane. Values for the flexural rigidity can then be inserted into equation (3.1), where the radius of the membrane in the sensor design is 75 µm, to determine the maximum deformation when a uniform load is applied. To replicate the physiological pressures applied in experiments a load of 140 mmHg was assumed (18.6 kPa).

Thickness (µm)	Flexural rigidity (Pa m^3)	Max. deformation (µm)
2.0	2.18×10^{-9}	4.2
1.0	2.73×10^{-10}	34
0.5	3.41×10^{-11}	270

Table 3.1 - Analytical solution for maximum deformation of a flat membrane.

The resultant deformation values for 1.0 and 0.5 µm seem excessively large based on the experimental results observed in this work, though the membrane geometry differs.

3.4 Interrogation system

A key component to extract pressure information form the fibre optic sensors is the optical interrogation system. The system used in this work was a phase resolved low coherence interferometry (LCI) setup. An introduction to LCI is provided in section 2.9. The system used comprised of a superluminescent light emitting diode (SLED) which had a central wavelength of 1550 nm, a spectral width of 100 nm and an output power of 10 mW (Exalos, EXS210048-02 with driver EBD5200). This was connected to a broadband spectrometer (Ibsen, IMON-512). The system design is very similar to that described by Coote *et al.* (Coote et al. 2019).

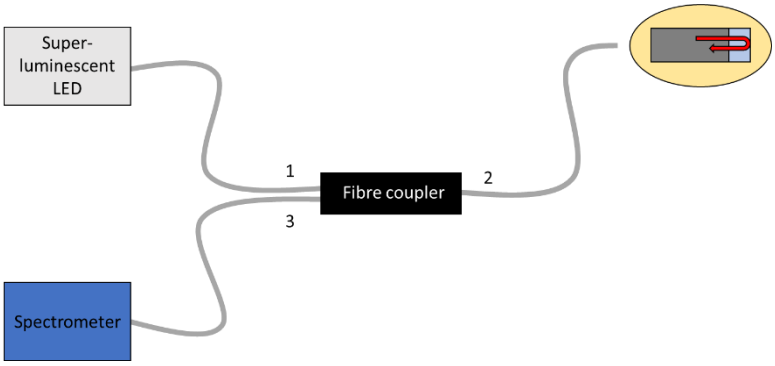

Figure 3.3 - Schematic diagram of LCI interrogation setup.

Light from the SLED travelled down the fibre labelled 1 (Figure 3.3), through the coupler, along fibre 2 (Figure 3.3) where it was partially reflected at the tip of the fibre (reference reflection) and from the diaphragm beyond this. The two reflected beams then travelled back down fibre 2 (Figure 3.3), through the coupler again and finally along fibre 3 (Figure 3.3) where they interfered with each other and were detected by the spectrometer. The reference beam was taken to be the first reflection from the fibre/air cavity boundary. The interference is visible as interference fringes in the detected spectrum. The inverse Fourier transform of the spectrum was then taken and the maxima in the spectrum corresponds to the reflection point of the diaphragm and its distance from the tip of the fibre (red arrow Figure 3.4). Further details on the underlying mathematics of these operations can be found in (Coote et al. 2019). By tracking the change in phase of the maxima peak of the inverse Fourier-transformed spectrum, the deformations of the diaphragm were monitored and hence the pressure was calculated.

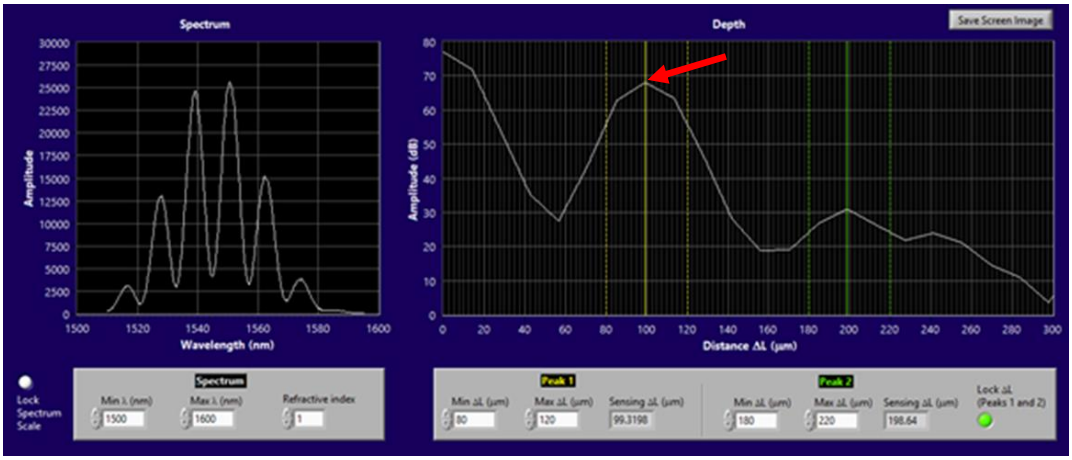

Figure 3.4 - Screenshot of the interrogation system software. (left) Raw intensity spectrum with interference fringes, (right) Inverse Fourier-transformed spectrum with maxima peak indicated by the red arrow at 99 μm.

3.5 Manufacturing with vacuum oil

Following the outlined sensor design, free standing parylene-C membranes need to be created at the distal end of glass microcapillaries. In order to fabricate these a bespoke DW high-resolution 3D printing setup was utilised. 3D printing techniques were used to deposit sacrificial layers which were then overcoated with parylene-C. Once the sacrificial layer was removed only the parylene-C remained.

The main components of the high-resolution 3D printing setup were a piezoelectric nano-positioning stage (PI P-615 NanoCube XYZ Piezo System), a pneumatic control system (Festo proportional pressure regulator VPPM) and an objective microscope lens (Mitutoyo M Plan Apo SL 50X) with a complementary camera (Thorlabs DCC1545M) as outlined in Figure 3.5.

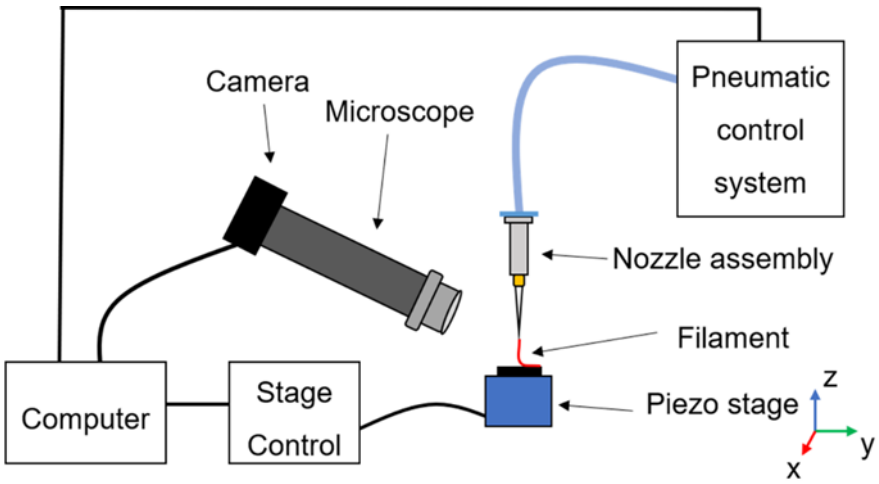

Figure 3.5 - Schematic diagram of the high-resolution 3D printing setup.

The piezoelectric stage had a resolution of 1 nm and a maximum range of 350 x 350 x 250 µm (*x,y,z* directions). The repeatability was 7.5 nm in the x and y directions, and 0.5 nm in the *z* direction. The stage position was controlled by applying voltages which are regulated by a piezo controller (PZT-Servo Controller, LVPZT-Amplifier). The voltages ranged from 0 V to 10 V, where 10 V was associated with the maximum displacement.

The pneumatic control system was connected to a nitrogen gas supply and was used to move a piston in the syringe to extrude material through the connected micro-nozzle assembly.

The 3D printing setup utilises glass micropipettes as the printing nozzles. These were manufactured in house using a Sutter Instrument P-1000 Micropipette puller. This device heats and stretches glass capillaries to form them into micro-nozzles. There are several adjustable parameters such as temperature, pull, velocity, time/delay and pressure. These parameters can be altered to create nozzles of different dimensions and taper, as shown in Figure 3.6. Additional information can be found in the accompanying manual (Oesterle 2018).

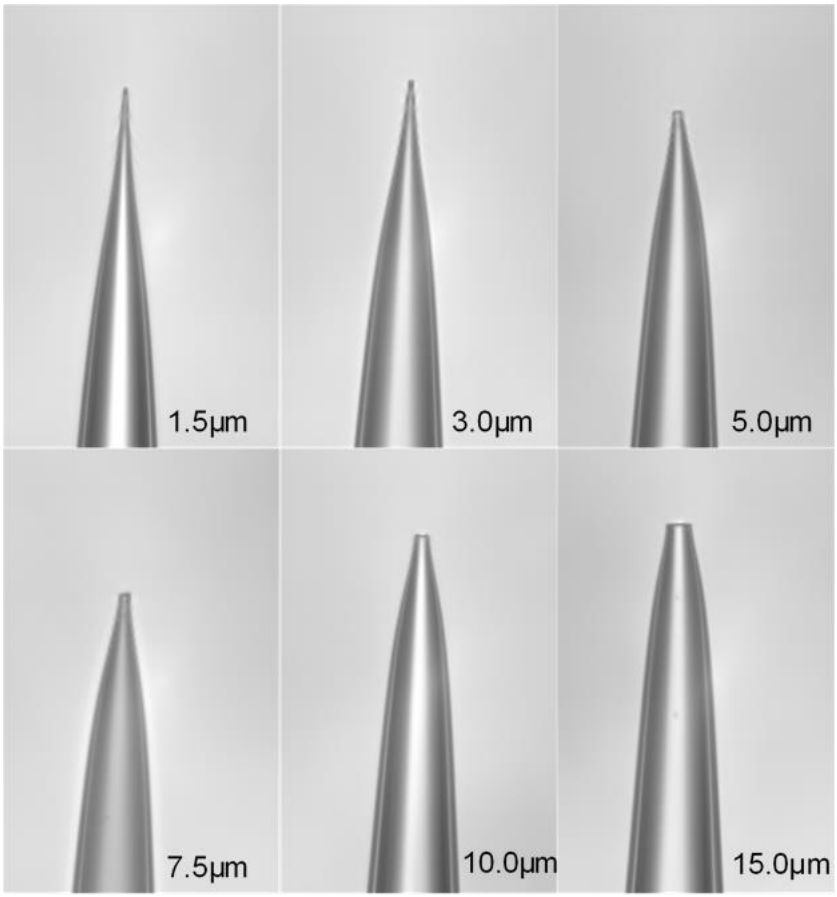

Figure 3.6 – Microscope images of glass micro-nozzles manufactured with different tip sizes.

The printing setup described was altered to enable easier manufacturing of parylene membranes. A larger translational stage was included to extend the range of motion of the setup. This translational stage was used to coarsely move and position the nozzle assembly above the piezoelectric stage while precise movements were performed using the piezoelectric stage.

From the design considerations, single mode fibre (Thorlabs, SMF-28) was chosen. This fibre has a diameter of 125 µm. In order for an extrinsic sensing element to fit over this it was decided that glass micro-capillaries with inner diameter of 150 µm should be used. Two types of micro-capillaries were purchased from CM Scientific, Borosilicate glass capillaries and Quartz glass capillaries (CV1525, CV1525Q). Both had an inner diameter of 150 µm and outer diameter of 250 µm, meeting the requirements outlined in the design considerations. Initially the capillaries were cleaved by hand using a tungsten blade to create segments which were between 2-3 mm in length. It was found that the quartz capillaries were much more brittle. Due to their enhanced robustness, the borosilicate glass capillaries were used hereafter.

To deposit material into these capillary segments, complimentary micro-nozzles with long tapers were manufactured with the micro-pipette puller. To fit inside the capillary segments, the nozzles tapered from 20 µm at the tip to an outer diameter of 150 µm over a length of ~4 mm. These were then integrated into Luer lock fittings (EFD 15-gauge tips, Nordson) to enable easy assembly with the syringe fittings. When adjusting the pipette puller parameters to create long tapered nozzles, the tips of the nozzles ended up being extremely small, < 0.5 µm, and polymer would not flow through them. It was found that by cleaving these very fine nozzles about 2 mm from the tip that a nozzle size of ~ 20 µm could repeatably be produced while still maintaining a taper long enough to still fit inside the 150 µm inner diameter of the capillaries for a length of ~4 mm. The cleaving of the nozzles was done by hand using another glass capillary to score the glass as described by Oesterle (Oesterle 2018).

The capillary segments were mounted vertically on a glass microscope slide using double sided Kapton tape, ready for deposition of the sacrificial layer.

3.5.1 Sacrificial layer material

The requirements of the sacrificial layer are:

- Can be deposited via 3D printing techniques.
- Can easily be removed when required.
- Will form a smooth surface for parylene to be deposited on to

Initially vacuum oil was investigated as an option for the sacrificial layer. The idea was that by filling the capillary segments to the brim with vacuum oil (without allowing air bubbles to form) then parylene could then be deposited over the top of this and the oil could be washed away after deposition. Agarwal *et al.* showed that parylene could be deposited on oil. They submerged a pressure sensor in silicone oil then deposited parylene on top to act as a barrier (Agarwal et al. 2018).

To minimise air bubble formation while filling the capillary segments the nozzle wettability was altered. The glass nozzles were functionalised using a mixture of hexane and perflurooctyl-trichlorosilane (PFOTS) to induce oleophobicity. Oleophobicity is when the surface energy is so low that oil will bead up and be repelled by the surface. The nozzles were submerged in a hexane and PFOTS mixture while nitrogen gas was bubbled through them to ensure only the outer surfaces were treated and the tip remained unclogged (Hsu et al. 2008; Psarski et al. 2012).

To fill the capillaries the functionalised nozzle was inserted all the way to the bottom of the capillary segment. Back pressure was then applied to the syringe until the oil

began to slowly flow. The addition of pressure is a critical point in the process as applying too much back pressure will cause the oil to spurt out of the nozzle uncontrollably. As the oil began to fill up the capillaries, the nozzle was raised in line with the meniscus which was visible through the capillary wall using the microscope system. The applied back pressure was increased during the process once the initial air bubbles were avoided. As the oil meniscus got close to the top of the capillary the applied pressure was decreased again to enhance control and prevent over filling. The filling process proved to be lengthy, due to the low flow rates used to ensure control and minimise air bubble formation. Once filled, the samples were overcoated with parylene-C using an in-house parylene coater.

As visible in Figure 3.7 the shape of the meniscus at the brim of the capillaries forms a concave shape and hence the parylene membrane follows the same shape. To remove the vacuum oil, the capillaries were sonicated in isopropyl alcohol (IPA) for 30 mins. This IPA sonication was required as milder washing techniques with soap did not fully remove the oil. Once washed the capillaries were then integrated with optical fibres and tested.

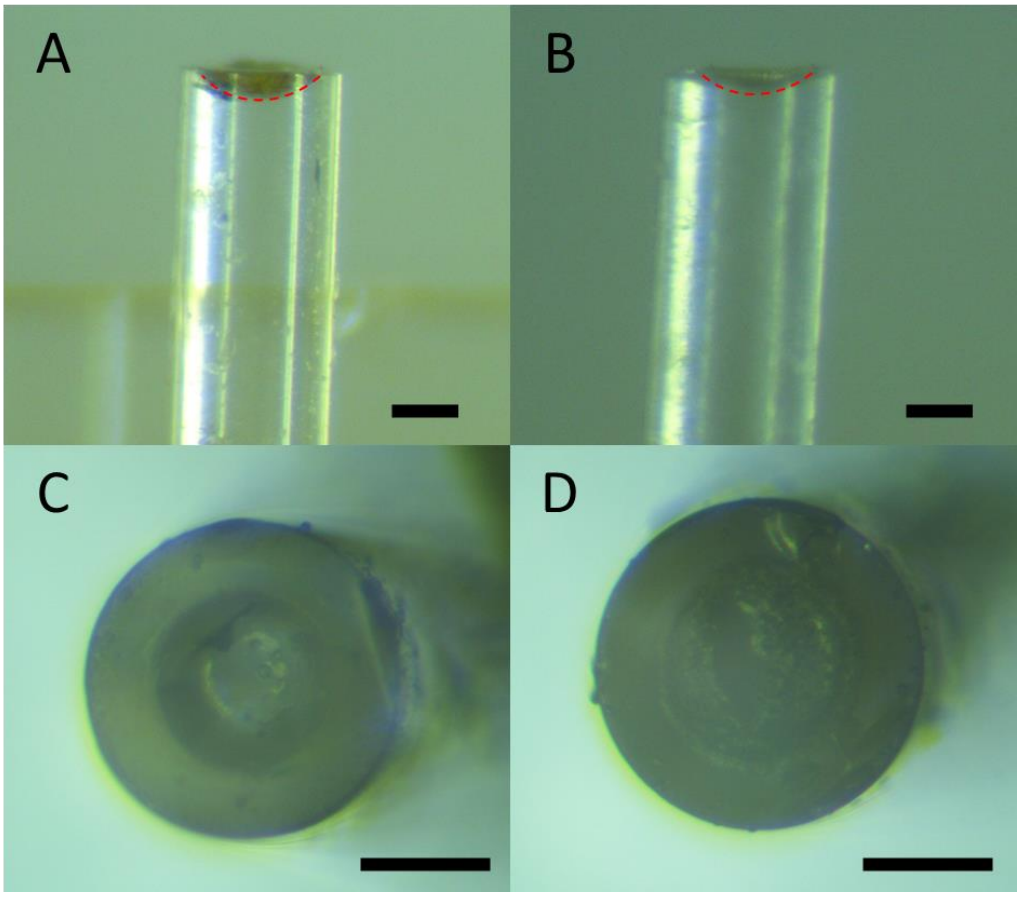

Figure 3.7 - A) and B) Side view microscope images of capillaries filled with vacuum oil and coated with parylene-C, red line indicates oil meniscus, C) and D) Top view microscope images of the same vacuum oil filled, parylene-C coated capillaries. All scalebars are 100 µm.

3.6 Manufacturing with polymers

After initial vacuum oil tests, different materials for the sacrificial layer were investigated. It was proposed that by using polymers which solidify, only the bottom portion of the capillaries need to be filled and then by flipping them when cured and coating with parylene-C, flat membranes could be achieved. This process is illustrated in Figure 3.8. Water soluble polymers such as polyvinyl acetate (PVA) and polyvinylpyrrolidone (PVP) were proposed as suitable polymers for this process.

Based on previous experience with 3D printing with polymers, a solution of 10% by weight of PVP (360K molecular weight) in deionised (DI) water was prepared. The solution was left on a hotplate to mix at room temperature for approximately 5 days to ensure the solution was homogeneous and was used as a starting point to determine the optimum polymer and concentration required.

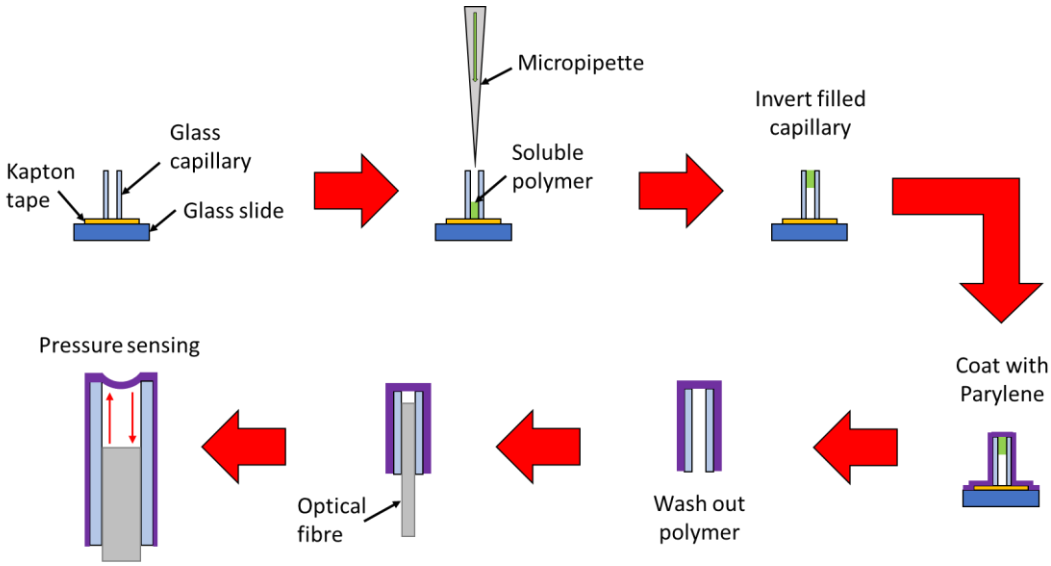

Figure 3.8 - Schematic diagram of the process for creating flat parylene membranes with water soluble polymers.

A solution of PVA was also prepared as PVA is another widely used water soluble polymer. To begin with a commercially available PVA adhesive (Pritt, craft glue) was purchased and diluted with DI water to create a solution suitable for depositing inside the capillaries (a ratio of 1-part glue to 3-parts DI water worked best). Solutions of DI water and PVA powder (Merck, partially hydrolysed, molecular weight approx. 30,000). were also mixed but required excessive heating to dissolve the PVA and did not perform as well.

Hand cleaved sections of capillaries were prepared and mounted vertically onto double-sided Kapton tape. Solutions of either 10% PVP or 1:3 PVA were then deposited. Due to the low polymer concentration of the solutions, the capillary segments were filled to about halfway up so that enough polymer would remain to form a solid plug after the solvent had evaporated out. Once the solvent had evaporated, the capillaries were removed from the Kapton tape using tweezers, flipped over, and mounted vertically again with the polymer plug facing upwards. Optical microscopy was used to visually inspect the polymer plugs at the capillary ends. As both PVP and PVA are transparent polymers it was difficult to determine the shape of the polymer plug and establish if flat surfaces were being formed. To improve visibility a water-soluble fluorescent dye was added during the polymer solution preparation, rhodamine 6G. Figure 3.9 illustrates how the visibility was increased for both PVP and PVA polymer plugs.

At this point other materials were also investigated as potential plugs in the capillaries, but the results did not lead to further use. The materials investigated included coconut

oil and carnauba wax. The coconut oil was initially warmed so that it would flow through the nozzle. Once deposited the capillaries were placed in the freezer where the coconut oil would solidify. The carnauba wax was dissolved in xylene and warmed to enable it to be deposited through the nozzles. Once deposited in the capillaries the wax cooled and the xylene evaporated out, leaving it solidified inside the capillaries. For both materials, the plug could be removed by washing with solvents and heating, though this was not a straight forward procedure.

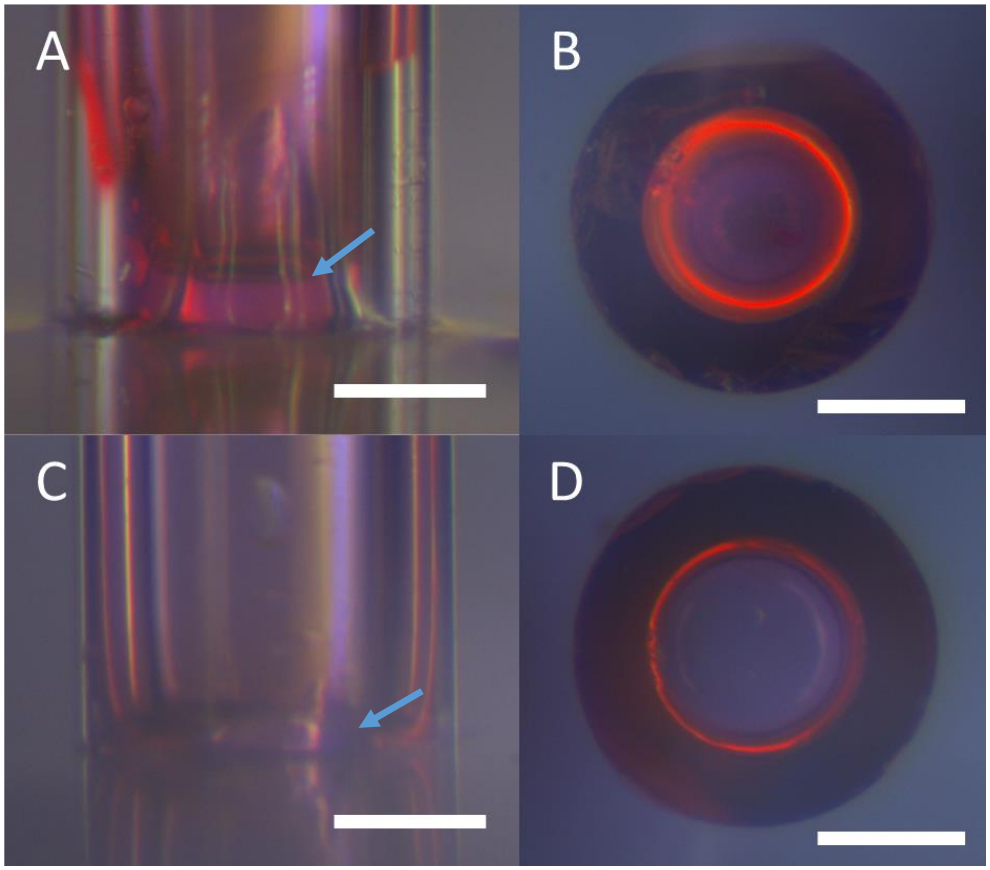

Figure 3.9 - A) and B) Side and top view microscope images of capillaries filled with PVP, C) and D) Side and top view microscope images of capillaries filled with PVA. Rhodamine dye was blended with polymers to aid visualisation. Blue arrows indicate polymer plugs. All scalebars are 100 µm.

3.6.1 Dissolving the sacrificial layer

Once solid polymer plugs were created at the tip of the capillaries parylene-C could be deposited over them. The next step in the manufacturing process was determining how best to remove the sacrificial polymer layers. PVP and PVA were chosen for their solubility properties. Instead of proceeding with parylene coating, at this stage the capillaries were dipped into epoxy to mimic a parylene membrane and test how best to wash out the sacrificial layer. The capillaries were placed in beakers of DI water to assess how readily the polymers could be dissolved. When left at room temperature

with no agitation the polymers were very slow to dissolve. To improve this, treatment in a sonication bath and stronger solvents were used.

The use of water bath sonication improved the rate at which the polymers were dissolved and brought the time for PVP to washout down to ~30 minutes and for PVA down to ~2 hours. The problem with this method was that the capillaries were becoming chipped and damaged during the sonication. Even with robust epoxy caps these were becoming detached. For thin flexible parylene membranes, sonication would not be a suitable method as the capillaries bumping into each other could cause significant damage to the membranes.

For PVP the solubility increases with more polar solvents. With this in mind, a washout procedure involving multiple solvents was devised. After an initial wash in DI water the solvent polarity was increased by washing in IPA, then increased again by a final wash in acetone. This washout procedure seemed to be successful but when inserting optical fibres transparent lumps of polymer were still present and blocking the capillaries. It was noticed that at each stage of the washout procedure the solvent trapped inside the capillary evaporated rapidly when in the air. The problem was that it was not just solvent trapped inside the capillaries, partially dissolved polymer was also present. With the rapid evaporation of the solvent the partially dissolved polymer re-solidified and lead to blockages. To overcome this a solution was to wick out the partially dissolved polymer/solvent mixture before it re-solidified inside the capillaries. To do this paper tissue fibres were inserted into the capillaries to wick it out. An example of this can be seen in Figure 3.10.

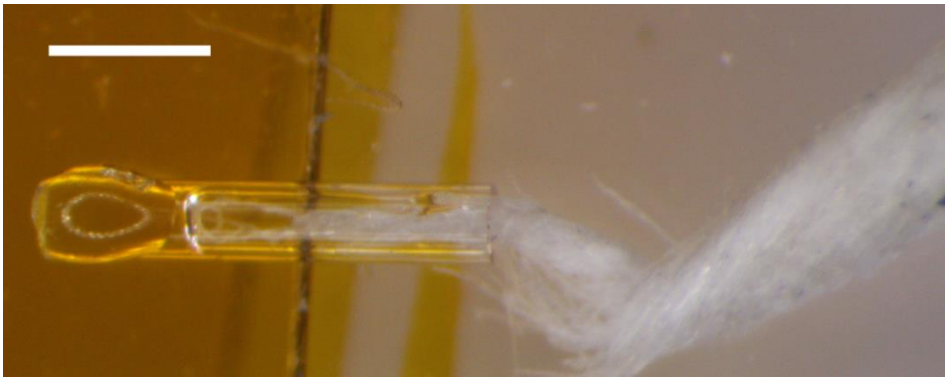

Figure 3.10 - Microscope image of an epoxy capped capillary and a tissue fibre being used to wick out the partially dissolved polymer and solvent. Scalebar is 500 µm.

For PVA increasing the polarity of the solvent would not increase its solubility, instead heating the DI water was tested. It was found that heating the water increased the solubility of the PVA and decreased the time required to wash out the capillaries, but it was still of the order of hours.

The addition of the rhodamine 6G dye not only made it easier to visually see the polymer but by utilising its fluorescent properties, fluorescence imaging could be performed to confirm that the polymer was completely washed out. Fluorescence imaging was used to validate the washout procedure for the PVP.

As shown in Figure 3.11, images A and B show microscope images of a capillary to be washed. Greyscale images of the capillary mounted in the fluorescence imaging system were then acquired (images C and D) and fluorescence imaging was performed (images E and F). The images highlight the rhodamine 6G in the polymer material. After performing the washout procedure, the capillary was re-imaged in the same set up and resulted in images G and H. These appear as entirely black due to the fact that no rhodamine 6G is present. The lack of fluorophore indicates that the polymer it was blended with was removed by the washout procedure.

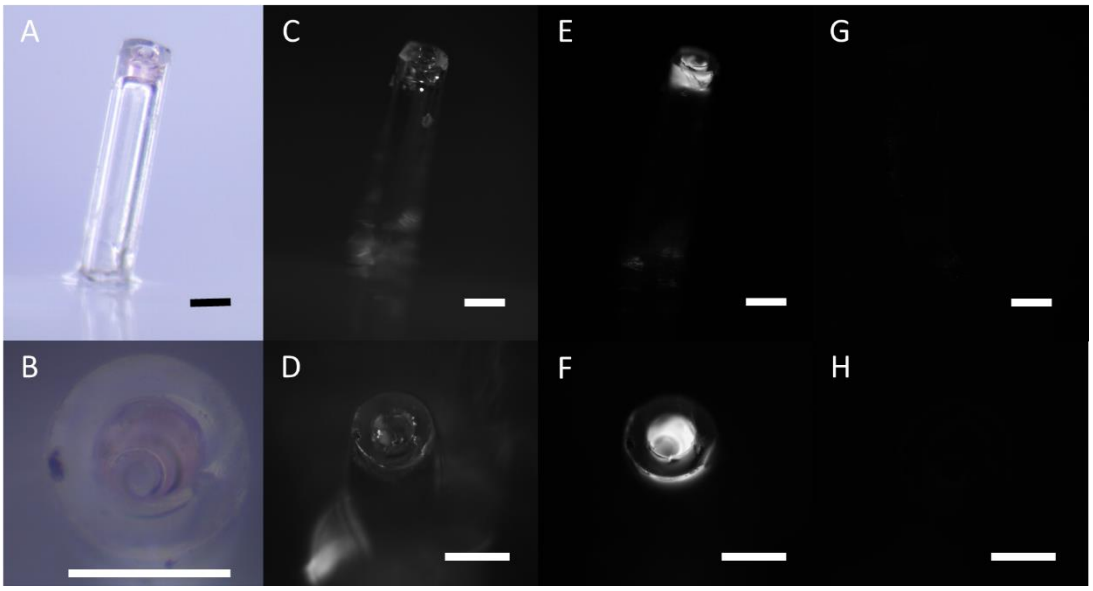

Figure 3.11 – A) and B) Microscope images of PVP filled capillary, C) and D) Greyscale images of the capillary, E) and F) Fluorescent images indicating regions of polymer inside the capillary, G) and H) follow up fluorescent images after washout process showing no fluorescent polymer is present. All scalebars are 200µm.

Despite the fluorescence imaging validation, the washout procedure was not well suited for producing large batches of capillaries due to the need to insert tissue fibres. To improve the washout lower molecular weight polymers were investigated. PVP with molecular weights of 10k and 55k were used. Both 10k and 55k molecular weights had improved solubility compared to the 360k molecular weight PVP initially used. The 10k molecular weight did not hold its shape well in the capillaries when inverted so the 55k molecular weight PVP was chosen as the best option to continue with.

3.6.2 Functionalisation

It was observed during the manufacturing process that once filled, some of the capillaries developed gaps between the bottom capillary edge and the polymer plug despite the material being deposited all the way at the bottom of the capillary initially. One thought was that capillary action was influencing the material as the solvent was evaporating causing it to be drawn up inside the capillary, away from the edge and cause a recession. To overcome this and ensure the polymer plug remained flush with the rim of the capillary, functionalising the capillaries was explored.

Similarly to how the nozzles were functionalised to alter their wettability and ensure material was only deposited from the nozzle tip, functionalising the inner capillary walls should overcome capillary action and help keep the polymer solution at the very bottom until the solvent has evaporated and it has solidified in place. A functionalisation procedure was developed based on PFOTS as the functionalising silane (Hsu et al. 2008; Psarski et al. 2012). The procedure began with submerging the borosilicate glass capillaries into IPA for 10 minutes and then washing them in DI water for a further 10 minutes. These steps produced OH groups on the surface which in turn helped the silane to adhere. The next step was to soak the capillary segments in a 0.1% solution of PFOTS/hexane for 30 minutes. They were then removed from the solution and air dried for a further 30 minutes before being rinsed in IPA for 5 minutes to remove any excess silane that was not adhered to the glass.

The functionalised capillaries were then vertically mounted on double sided Kapton tape as before and polymer was deposited inside them.

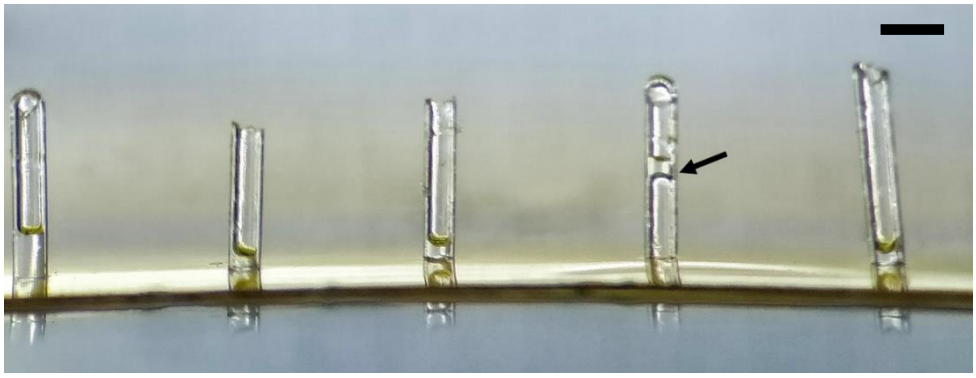

Figure 3.12 – Microscope image of PVP filled functionalised capillaries. The image illustrates how fewer (only 1 out of 5) have experienced strong capillary action causing the polymer to move up inside the capillary, indicated by black arrow. Scalebar is 500 µm.

Functionalising the capillaries resulted in far fewer capillaries having a shifted polymer plug, as shown in Figure 3.12. In order to proceed with this and to functionalise larger

numbers of capillaries at a time a capillary mount/jig was constructed. The jig held the capillaries in place and facilitated moving them between different functionalisation steps quickly and easily, as picking up and moving individual capillaries with tweezers was extremely time consuming. The jig needed to be resistant to the solvents used in the functionalisation process, this limited the choice of materials. It was decided to use polytetrafluoroethylene (PTFE) as the main body of the jig. A 3 mm thick sheet of PTFE was cut to size and had holes of 400 µm drilled in an array of 20 holes. 4 larger M3 holes were drilled in the corners as well. The smaller holes were to hold the capillaries in place and the larger holes were to secure a stainless-steel mesh on top and bottom to prevent the capillaries falling out of their positions. The stainless-steel wire mesh had a pore diameter of 35 µm to allow solvents and functionalisation agents to enter and interact with the glass capillaries while still keeping the capillaries in place. The resultant jig is shown in Figure 3.13. Despite the design of the jig allowing solvents to flow through to the capillaries, the functionalisation procedure had to be modified to maintain the same level of functionalisation that was achieved without the jig. Periods of sonication were added to agitate the solvents and help them penetrate fully into the jig and reach the entirety of the capillary walls. The updated functionalisation procedure was to sonicate the capillaries in IPA for 15 minutes then leave them submerged for a further 15 minutes. They were then transferred to a beaker of DI water and again sonicated for 15 minutes before being left in the DI water for a further 15 minutes. After this they were moved to the 0.1% PFOTS/hexane solution and sonicated for 15 minutes before being left to soak for a further 45 minutes. The jig containing the capillaries was then removed and allowed to air dry for 1 hour. Following this, 5 minutes of sonication in IPA was performed before leaving for a final 5 minutes in the IPA to remove any excess silane.

Figure 3.13 - Photograph of the capillary functionalisation jig being placed in a beaker of IPA with complimentary PTFE tweezers. Scalebar is 2 cm.

Microscope inspection of the polymer filled functionalised capillaries showed that the objective to prevent the polymer wicking up the inside of the capillaries had been achieved (Figure 3.14).

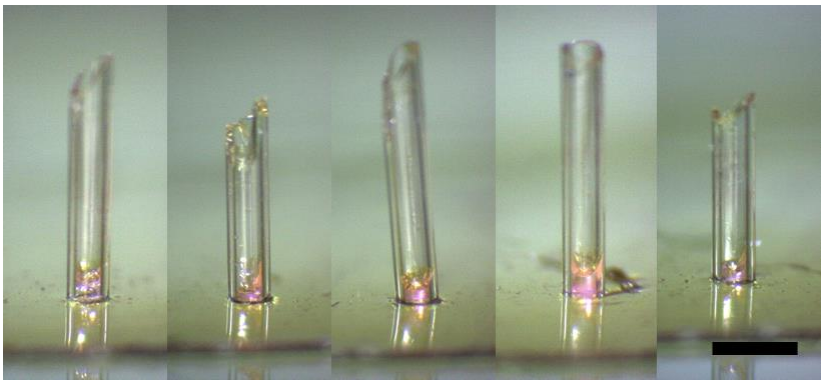

Figure 3.14 - Microscope images of functionalised capillaries filled with fluorescent PVP. Scalebar is 500 µm.

3.6.3 Capillary cleaving

As visible in Figure 3.12 and Figure 3.14, the hand cleaved capillaries were not very even in length and most cleaves were sharp with ragged edges. For hand cleaving, a tungsten carbide blade was used to score the cleave position on the capillary. Pressure was then applied to the scored region to induce the breakage. Placing the scored region at the edge of an overhanging surface was found to give more

repeatable results. For easier scalability and simpler sensor assembly, the cleaves needed to be improved.

No in-house solutions were viable so an external laser cutting company (Laser Micromachining Limited) was approached to laser cut the capillaries into 2 mm length sections.

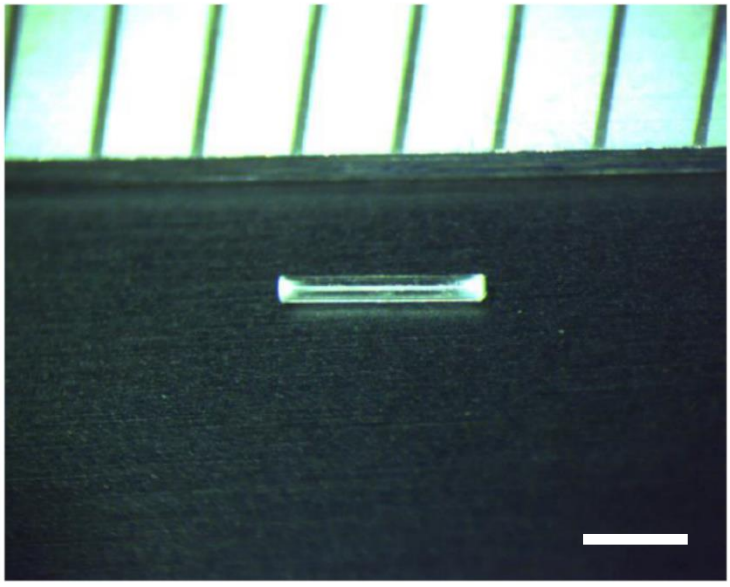

Figure 3.15 - Photograph of a laser cut 2 mm capillary section, the ticks in the image background represent millimetre marks. Scalebar is 1 mm.

The laser cut capillaries had opaque ends, visible in Figure 3.15, which made it difficult to accurately view the nozzle inside the capillaries while depositing the polymer. Further inspection suggested that the heating from the laser had caused the glass to melt and re-solidify, causing the transparent borosilicate glass to become opaque. There was also a discrepancy in the lengths of approximately ±5%. Scanning

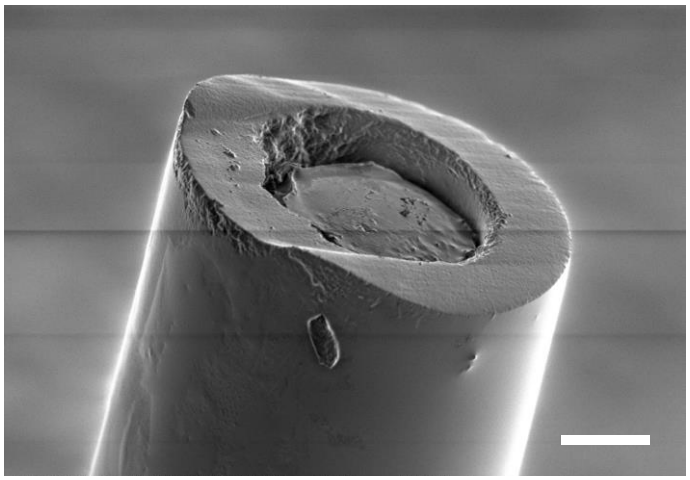

Figure 3.16 - SEM image of a laser cut capillary highlighting the unevenness of the laser cut capillary ends. Scalebar is 50 µm.

electron microscope (SEM) imaging was performed to better visualise the effect of laser cutting on the capillaries.

As visible from Figure 3.16 and Figure 3.17 the laser cut capillaries have a much rougher structure compared to the polished capillary ends directly from the manufacturer (however the opposite end of the polished capillary was very ragged due to hand cleaving). The extreme heating from the laser cutting process also seemed to have altered the shape of the inner lumen of the capillaries so that they were not as circular as they were originally. The uncertainty in the laser cutting also caused the capillary ends to be angled. The angled ends meant that they were not completely vertical when mounted for polymer filling and made it more likely that gaps between the capillary and the Kapton tape would form and enable polymer to leak out.

An alternative method of cutting the capillaries into 2 mm segments is saw cutting. A partner company (Vitrocom) of the supplier (CM Scientific) was able to offer this. They also quoted a ±5% uncertainty in capillary lengths but the saw cutting should not damage the capillaries as drastically and the cutting angle should be more controlled compared to the laser cutting technique.

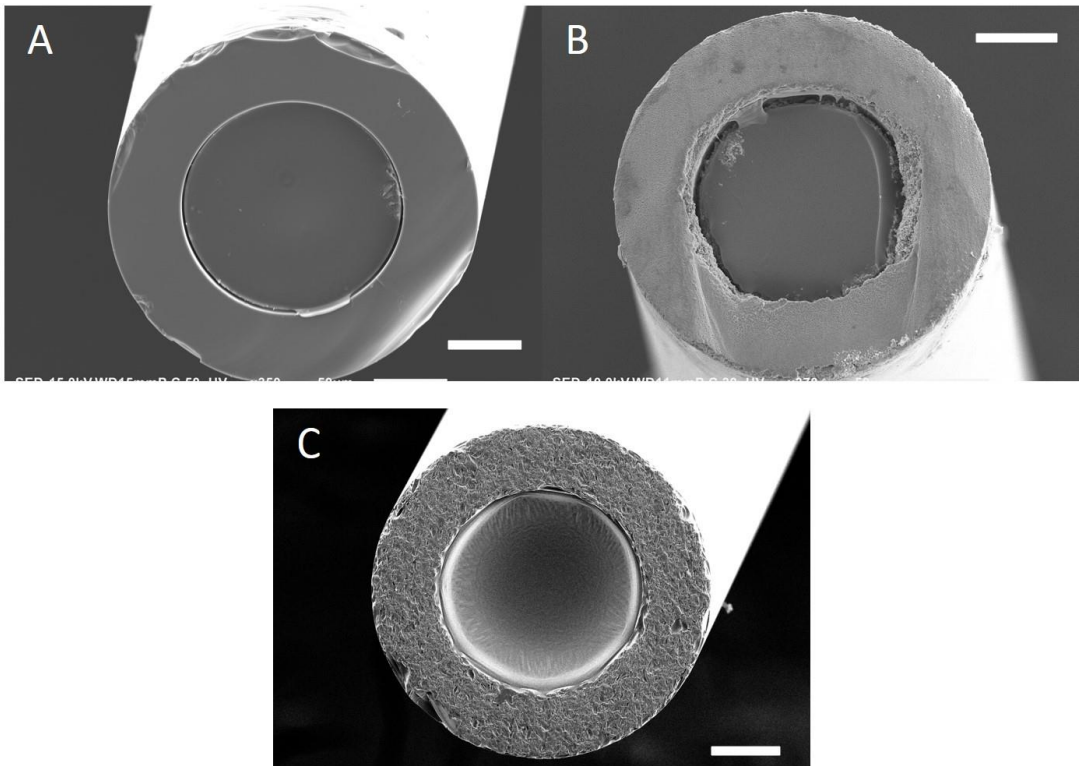

Figure 3.17 - Comparison of capillaries filled with polymer, SEM images, A) Polished capillary end direct from the manufacturer, B) Laser cut capillary end, C) Saw cut capillary end. All scalebars are 50 µm.

The saw cut capillaries remained transparent as opposed to the opaque laser cut capillaries. This transparency helped to view the nozzle inside the capillaries and to monitor the deposition of the polymer. From Figure 3.17 the inner lumen of the saw cut capillaries was still very circular and undamaged. There was still some microroughness visible on the brim of the capillary ends, but the cut angles seem to be much flatter and repeatable. The saw cut capillary segments looked the same at both ends compared to the hand cleaved polished capillary ends where one side was smooth and polished while the other had a large cleave angle and was usually sharp/ragged.

3.6.4 Vertical mounting of the capillaries

It was noticed during SEM imaging that the polymer plug was still recessed from the end of the capillary by 10 to 25 µm (Figure 3.16 and Figure 3.17 A and B). The source of this recession was unclear, and its magnitude varied up to a few 10's of micrometres. It was theorised that it could be due to the silicone adhesive from the Kapton tape being forced into the end of the capillary during mounting and displacing the polymer when filled. The total thickness of the polyimide tape used was 65 µm and the layer of silicone adhesive was about 40 µm. Another theory was that the recession was being caused by the polymer plug shrinking as it dried. Both theories had merit and were addressed individually.

To prevent any of the adhesive layer from penetrating the bottom of the capillary and causing recession an alternative method of mounting the capillaries was devised. Spin coating a thin layer of silicone onto a glass substrate and then positioning the capillaries vertically was tried. This method proved to be quite intricate to place the capillaries on the spin coated layer without them falling over. The spin coated layer also needed to be heat cured which added further steps to the process.

The use of an alternative tape was explored. Nitto ultra-thin PET-based 5µm double sided tape No.5600 was acquired and tested. The Nitto ultra-thin 5600 was a polyethylene terephthalate (PET) based tape with a layer of acrylic adhesive on either side, culminating in a total tape thickness of 5 µm. As the adhesive was on both sides, only a layer of approximately 2 µm thickness was exposed to the capillary. A drastic reduction compared to the 40 µm adhesive layer exposed in the case of polyimide tape.

After minimising the potential impact of the tape adhesive to cause recession during vertical mounting, the possibility of polymer shrinkage was investigated next.

3.6.5 Minimising polymer shrinkage

Under SEM imaging clear recession was seen between the surface of the polymer plug and the capillary end (Figure 3.16). Shrinkage was most likely to be occurring in all directions, causing the recession seen but also creating smaller gaps between the inner lumen wall and the polymer plug. Possible ways to overcome this issue was to change the polymer being deposited to one that does not undergo shrinkage or to modify the PVP to reduce the amount of shrinkage experienced.

Another water-soluble polymer called hydroxypropyl methylcellulose (Hypromellose) was investigated due to its good film forming properties. Concentrations of 1, 3 and 5% of Hypromellose in DI water were deposited into capillaries. Beyond 5% it because to viscous to deposit effectively through micro nozzles.

As seen in Figure 3.18, lower concentrations of Hypromellose did form relatively smooth films with little to no shrinkage or recession visible using the ultra-thin Nitto tape. At 5% concentration cracks began to form and the films were not as uniform. However, all of the concentrations showed leakage from the inner lumen of the capillary resulting in polymer on the brim of the capillary. The amount of leaked polymer means that they were not suitable for over coating with parylene. The excess polymer on the brim would reduce the surface area of the glass for the parylene to adhere to. After parylene coating when the sacrificial layer is washed away these overflow regions would dissolve as well and could lead to a saggy, slow response, parylene membrane instead of a tight, fast response, pressure sensitive one.

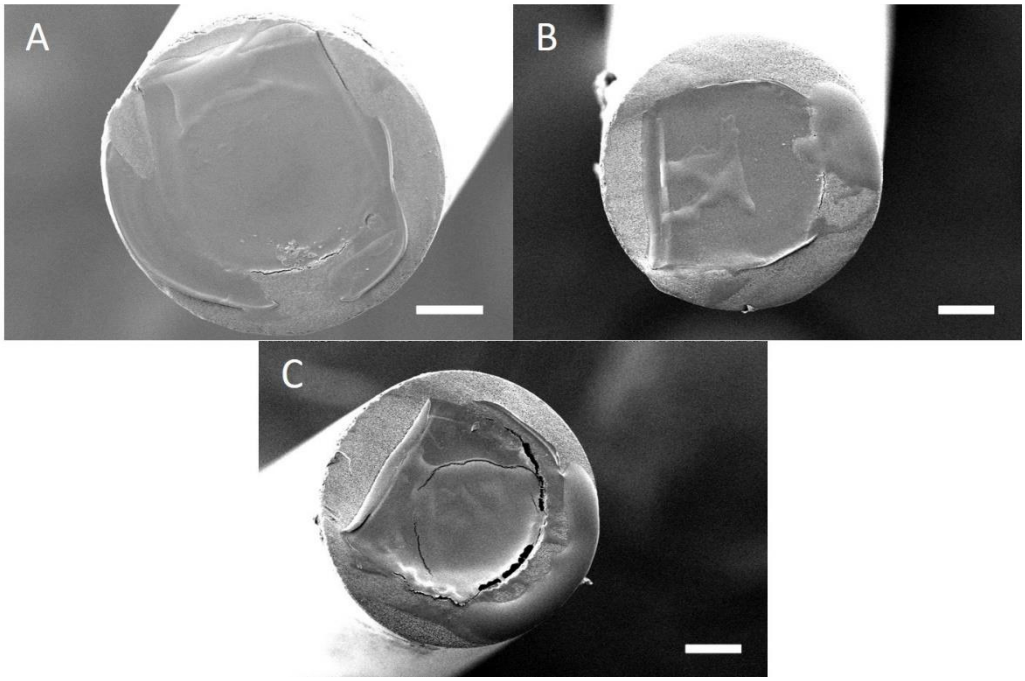

Figure 3.18 - SEM images of Hypromellose filled capillaries. A) 1% concentration, B) 3% concentration, C) 5 % concentration. All scalebars are 50 µm.

Sticking with PVP as the water-soluble polymer, its film shrinkage was reduced by adding a plasticizer. A plasticizer is defined by the International Union of Pure and Applied Chemistry (IUPAC) as “a substance or material incorporated in a material (usually a plastic or elastomer) to increase its flexibility, workability, or distensibility” (Vieira et al. 2011). Plasticizers influence the organisation of polymer chains and lower their glass transition temperature (Boonsuk et al. 2018). A suitable plasticizer for PVP is glycerol (GLY). Different amounts of GLY were investigated with different concentrations of PVP. The blended mixtures were drop cast onto glass slides where they were allowed to cure at room temperature before being visually assessed.

	GLY 1%	**GLY 3%**	**GLY 5%**	**GLY 7%**	**GLY 11%**
PVP 5% (55k)	Not viscous enough				
PVP 10% (55k)	Films still had cracks and shrinkage after drying	Films shrunk during drying	No cracks or shrinkage visible in films after drying	Films were tacky after drying	Films did not cure properly to form a solid
PVP 20% (55k)	Too viscous				

Table 3.2 – Summary of how the addition of glycerol affects the shrinkage of PVP films.

It was found that a blend of 10% 55k PVP with 5% GLY gave the best results. It was also noted that the addition of glycerol tended to slow the evaporation of the solvent once deposited inside the capillaries. Further investigations with functionalised and non-functionalized capillaries showed that there was no drastic difference between

the amount that were unusable due to the polymer wicking away from the capillary end. The fact that functionalisation was no longer a necessary step improved the speed at which batches of capillaries could be produced.

A final step in the manufacturing process was added to ensure all of the solvent had evaporated from the polymer blend. To ensure this, the filled capillaries were placed in a vacuum oven at 75 °C for 30 minutes after the polymer was deposited to ensure complete curing before the capillaries were flipped for parylene coating. 75 °C was chosen as the ultra-thin tape was heat resistant up to 80 °C. Also, the vacuum oven should also aid in removing any air pockets that might form during filling. This updated manufacturing process was used to fill several capillaries which were imaged to assess the effectiveness. The procedure followed was:

- Use saw cut capillaries
- Mount them vertically on ultra-thin Nitto tape
- Functionalise micronozzles with PFOTS
- Deposit a polymer blend into the capillaries (10% 55k PVP with 5% GLY)
- Cure at room temperature for 2 hours
- Final cure in a vacuum oven at 75 °C for 30 mins

The final vacuum oven treatment not only ensured complete solvent evaporation, but heating has been found to anneal PVP and make it more robust. Despite this, drop cast films that were prepared and treated in the same way dissolved within 5 minutes in DI water without agitation.

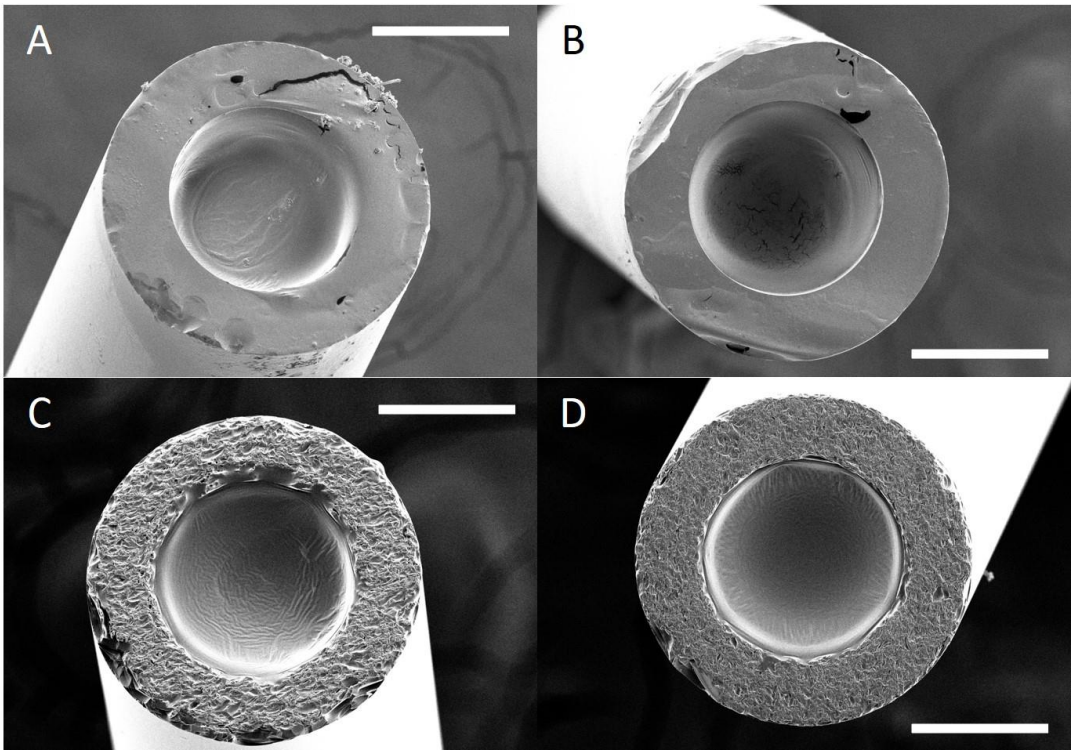

Figure 3.19 - SEM images of capillaries filled with a 10% PVP+5% GLY blend A)+B) Were prepared without the additional vacuum oven treatment, C)+D) Did have additional vacuum oven treatment. All scalebars are 100 µm.

As shown in Figure 3.19 the additional vacuum oven step helped to secure the polymer plug in place. In the images without vacuum oven treatment the polymer film was smooth, but leakages occurred onto the brim of the capillaries. In the images of capillaries that did undergo vacuum oven treatment, the polymer films were still smooth, though some slight ripples were visible. There was no visible leakage of the polymer onto the capillary brim. A slight recession of the polymer was visible in image D) but this is minimal.

3.6.6 Capillary action

Between capillary preparation and eventual parylene coating it was observed that the recession between the end of the capillaries and the polymer plug returned. After the capillaries were removed from the tape, inverted and re-mounted for parylene coating there was usually a waiting period on the order of days before the parylene coating was actually performed. It was proposed that the change in position of the polymer plug was due to capillary action moving it towards the centre of the capillary. It was also proposed that after inversion, gravity was helping to cause the change in position. To test this several capillaries were prepared following the vacuum oven procedure. They were then removed from the ultra-thin tape, inverted, re-mounted on

polyimide tape and prepared for parylene coating by sealing around the bottom with Ecoflex (this is included to prevent any parylene to be deposited inside the capillaries, only outside and over the polymer). The glass slide with the final mounted capillaries was then itself inverted so that the polymer filled capillary ends were facing downwards. Supports were used to hold the glass slide in place and a prism was used to obtain a side view of the capillaries. The capillaries were observed over a period of 26 hours. Over the observation time the movement of the polymer was visible. Not all of the capillaries experienced the drastic change in position of the polymer, there was a variety of polymer positional shifts observed (Figure 3.20).

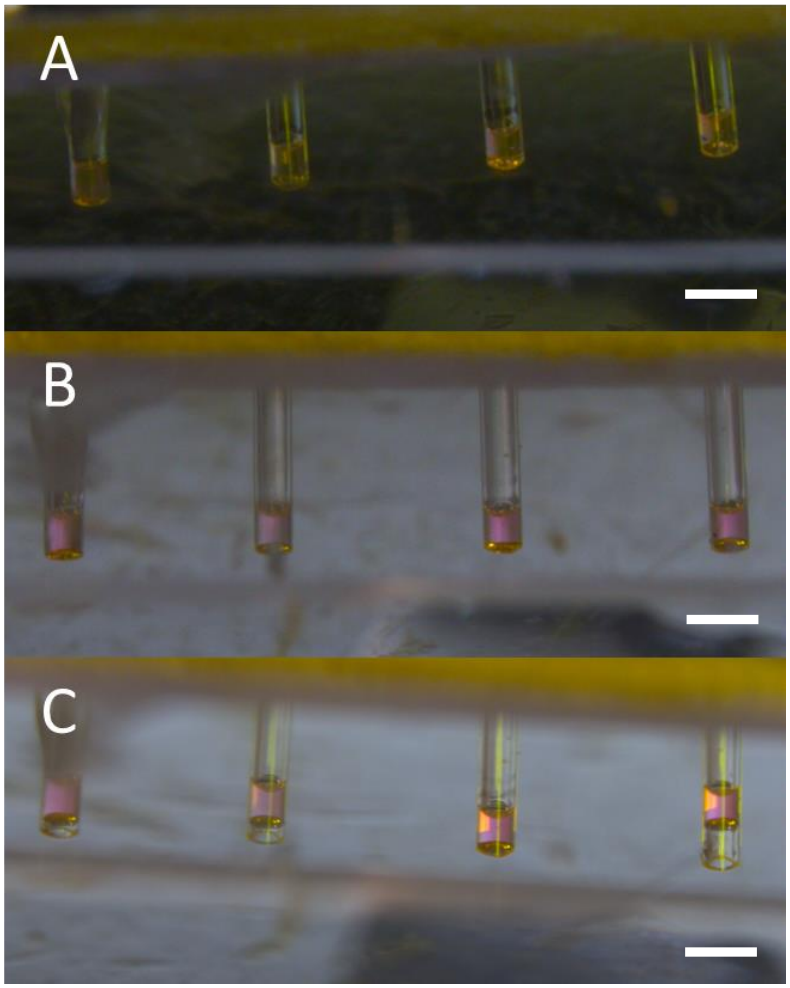

Figure 3.20 - Time interval microscope images of capillaries. A) Initial, B) After 1 hour, C) After 26 hours. All scalebars are 500 µm.

The polymer plug moving was a complex issue to overcome. Several attempts at filling the air gap behind the polymer plug with additional material were tried but had little effect. Additional layers of PVP of varying molecular weights were added but did not prevent the polymer from creeping inside the capillary. The creeping could be delayed for approximately 24 hours by adding 2 additional layers of 10% PVP 55k but not prevented (Figure 3.21). The addition of extra layers also made the washout

process more difficult. Vacuum oil was also tested as a filler material but did not affect the outcome as the polymer plug still became recessed.

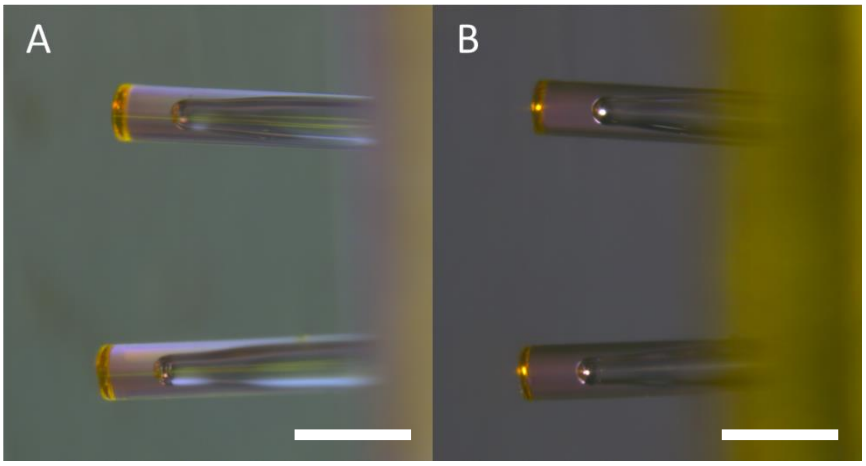

Figure 3.21 - Microscope images of capillaries with additional layers of 10% 55k PVP added A) initially and B) after 27 hours. Both scalebars are 500 µm.

3.6.7 Curved membranes

As there was usually a delay on the order of days between final capillary preparation for coating and the parylene coating taking place, recession of the polymer plug was inevitable. One way to overcome this would be to prepare the capillaries and then parylene coat them immediately but as the in-house parylene coater was a shared specialist piece of equipment with limited access and restricted users, this was not possible. Instead, what was proposed was to leave the capillaries on the tape with the polymer plugs facing downwards and coat down the inside of the capillaries, over the inside of the plug to create curved parylene membranes.

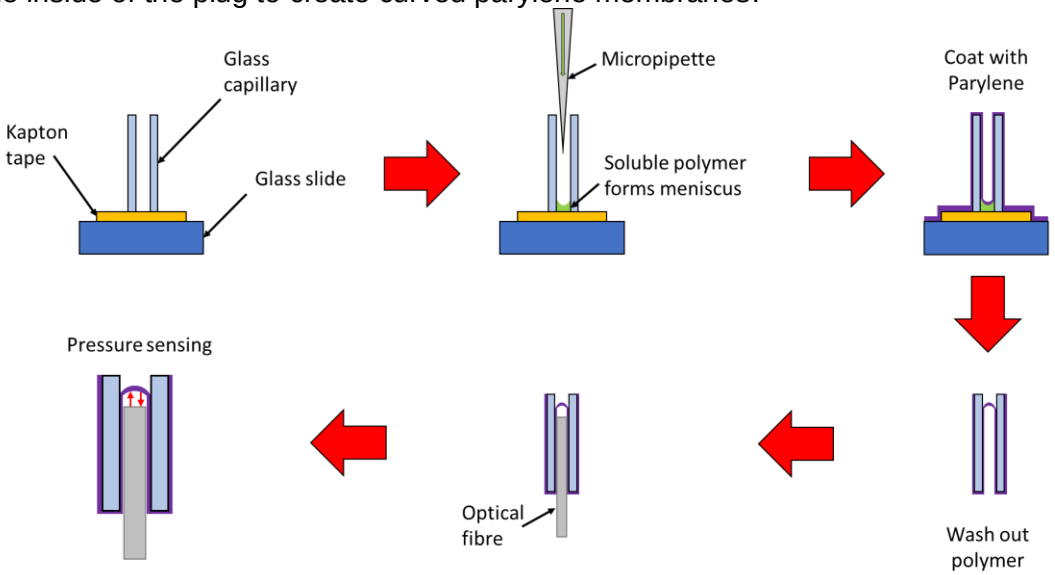

Figure 3.22 - Schematic diagram of the process for creating curved parylene membranes with water soluble polymers.

The process of filling of the capillaries with 10% PVP 55k + 5% GLY remained the same up until the vacuum oven treatment stage. After this they were no longer removed, inverted and re-mounted. They were simply left in their current position/orientation and sealed around the bottom edge with Ecoflex to prevent parylene from being deposited here, which would completely encapsulate the polymer plug with parylene. Once parylene coated the capillaries were removed from the substrate by using fine tweezers to break the parylene barrier around the edge and lift off. As the 10% PVP 55k + 5% GLY polymer blend was used this was simply dissolved away in DI water within a matter of minutes to leave just the parylene membranes. This process is summarised in Figure 3.22.

From Figure 3.23 the curvature of the membranes can be seen in the top row of images. The area where the Ecoflex was covering looks clear of parylene as expected. The parylene on the outer wall of the capillaries appears rougher than expected but this is likely due to the manipulation with tweezers causing damage to the smooth parylene layer during the detachment procedure.

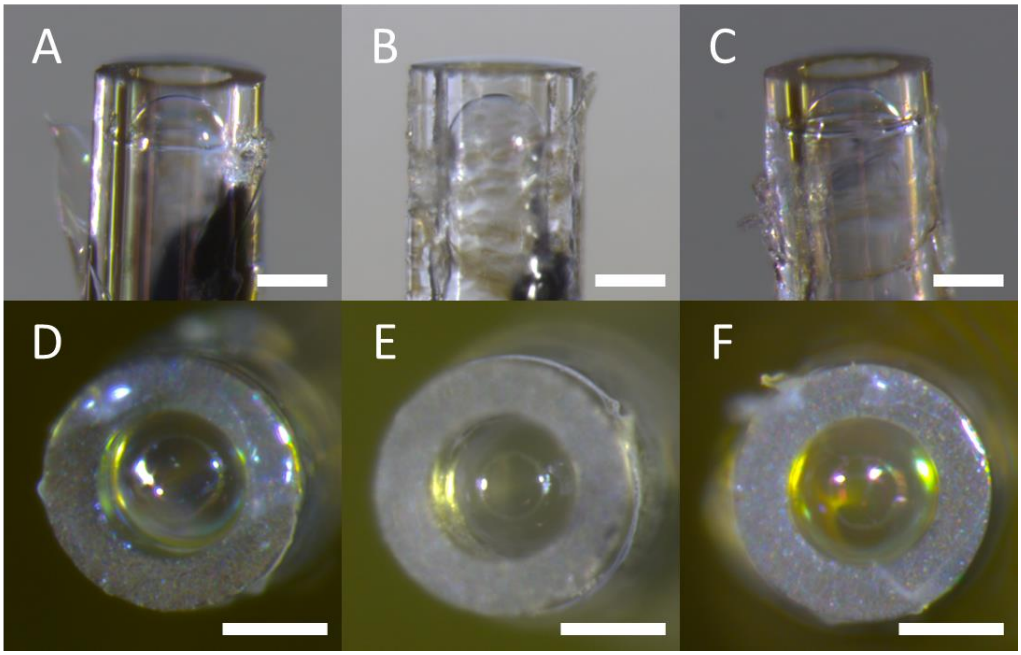

Figure 3.23 – Optical microscope images of the resultant curved parylene-C membranes at the tips of the capillaries. All scalebars are 100 µm.

The position of the membrane could be altered by changing the amount of polymer that was deposited to create thicker/thinner plugs. The thickness of the membrane could also be controlled by altering the thickness of the deposited parylene-C coating. After several test runs with large uncertainties in thickness it was decided to focus on thicknesses of 0.5, 1.0 and 2.0 µm.

3.6.8 Capillary detachment

Once parylene coated, the capillaries had to be removed from the coating substrate (double sided tape on a glass microscope slide). Initially, the silicone (Ecoflex, 00-50) used to seal the capillaries and prevent parylene deposition at the bottom was cut with a scalpel to remove it. Despite making incisions close to the capillaries there was still a large amount of silicone that remained around the edge of the capillaries. An alternative technique was to use fine tweezers to break the parylene barrier around the edge of the capillaries to expose the silicone underneath. Since the applied silicone adhered better to the substrate than to the capillaries, when the capillaries were pulled upwards the adhesion to them was overcome and they detached. Once detached they were washed out and assembled.

3.7 Sensor assembly

Once parylene-C membranes were created at the tips of the capillaries these extrinsic F-P sensing elements were integrated with single mode optical fibres to create optical pressure sensors. This process was performed under an optical microscope with a 3-axis translational stage. Initially 830 nm single mode optical fibre with a cladding diameter of 125 µm was used. The 125 µm fibre was easily be inserted into the 150 µm inner diameter of the capillaries. As the fibre was inserted and brought closer to the membrane, its position was monitored using the LCI setup. The position was optimised until maximum reflections were observed in the inverse Fourier-transformed spectrum, usually apparent at 40–50 µm from the membrane where its curvature seemed to cause a focusing of the reflected light. Once in position epoxy was applied to ensure the fibre stayed in position. Ultraviolet (UV) light curable epoxy was used (Norland Optical Adhesive 81). A small amount of epoxy was placed at the interconnect between the base of the capillary and the optical fibre using a second optical fibre to ‘paint’ it on. The epoxy was allowed to wick inside the capillary, in order to partially fill the gap between the 125 µm fibre and the 150 µm capillary diameter. The epoxy was then cured using a UV light source (Thorlabs). An example of an assembled sensor is shown in Figure 3.24.

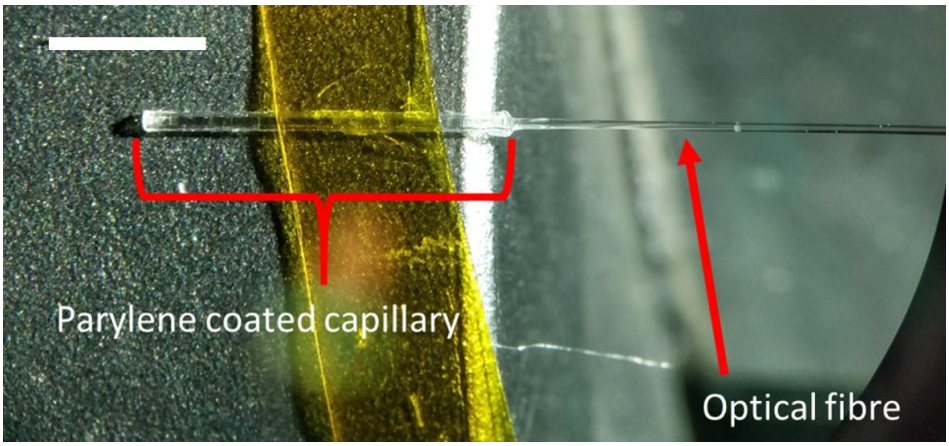

Figure 3.24 – Microscope image of assembled parylene-C membrane pressure sensor. Scalebar is 2 mm.

After initial preliminary results were obtained, the sensor assembly was changed. It was found that the Ocean Optics spectrometer in the initial 830 nm LCI system that was being used had a response rate that was too low to properly sample and capture the information from the sensors. The phase changes of the light were too large for the spectrometer and supporting software to accurately track, resulting in lost phase and large changes of 2 pi or more being misread as smaller phase shifts.

To overcome this a spectrometer with a faster response was used in an improved LCI setup. The workings of the updated LCI system were the same as the previous system but the wavelength range of the new, faster, spectrometer (Ibsen, IMON-512) was different. The altered wavelength range meant using a different, complementary light source and different, better suited optical fibres. The new wavelength range was 1500 – 1600 nm, therefore a 1550 nm light source was used, and 1550 nm optical fibre was used (SMF-28, Thorlabs). Apart from the fibre change, the assembly method remained the same.

3.8 Sensor characterisation

Once fully assembled the sensors were characterised *in vitro*. The characterisation consisted of several pressure and temperature response tests. To test the pressure response a testing rig was used (Figure 3.25). The rig consisted of a sealed fluid filled vessel where the sensor was positioned and pressurised using an electropneumatic regulator (SMC Pneumatics). A commercial pressure transducer (Omega Engineering) was used as a reference for the pressure levels inside the vessel. The whole setup was positioned in a water bath to maintain constant temperature at 37 °C and a thermocouple (RS Components) was used to monitor any fluctuations. Using the setup, sensors were characterised using several different pressure response

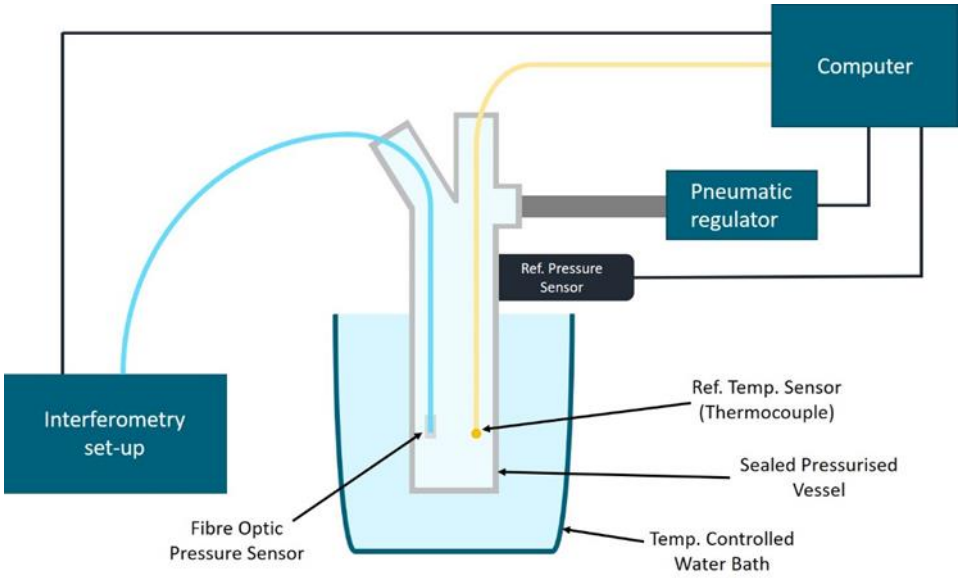

Figure 3.25 - Schematic diagram of sensor pressure characterisation setup.

tests. The first involved stepping the pressure up from atmospheric pressure (~760 mmHg) in fixed intervals to a maximum and then decreasing in steps back to atmospheric pressure. The next was to apply a fixed constant pressure and hold it for a set period of time to determine the sensor drift under pressure. Finally, the pneumatic regulator was programmed to replicate arterial waveforms to provide more physiologically relevant pressure responses to test the sensors against. An arterial waveform is illustrated in Figure 3.26. It is composed of a systolic phase and a diastolic phase. The systolic phase occurs when the heart muscles contract and pump blood through the arteries. The dicrotic notch represents the closing of the aortic valve. The diastolic phase corresponds to when the muscles relax and the chambers

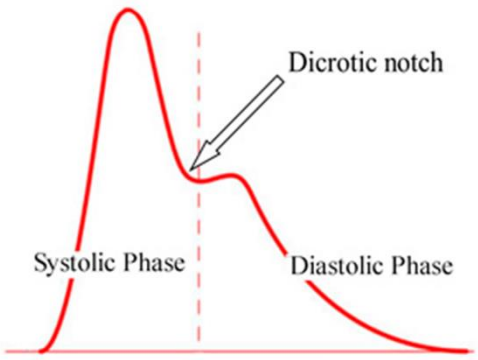

Figure 3.26 – Normal arterial pulsation waveform (Levine 2010).

of the heart refill with blood.

This setup could also be used to characterise the temperature response of the sensors by changing the temperature of the hotplate. However, for more detailed

temperature response tests an alternative setup was used which was similar in design but had a calorimeter (Omega Engineering, TCL-3M165E) incorporated to provide accurate temperature variations. The calorimeter allowed temperature variations and precise temperature holds to be performed. As the sensors are designed for biomedical applications a temperature range between 30 and 40 °C was focussed on. The calorimeter tests increased the temperature to 40 °C, down to 34 °C and then back up to 37 °C.

3.9 Results/discussion

The results of the development and testing of the parylene pressure sensors are presented in this section.

3.9.1 Manufacturing results

The results of the manufacturing process are shown in Figure 3.23. Free-standing, curved parylene-C membranes are visible, and they maintain their domed shape. These were then assembled with optical fibres to create pressure sensors.

Figure 3.27 shows how the assembled sensors adhered to the size constraints outlined in the design considerations as they had a maximum diameter of 250 µm and could easily fit within the inner lumen of surgical needles. A dashed line is included in the image to help identify the sensor as it is difficult to distinguish from the background due to the transparent nature of the materials used.

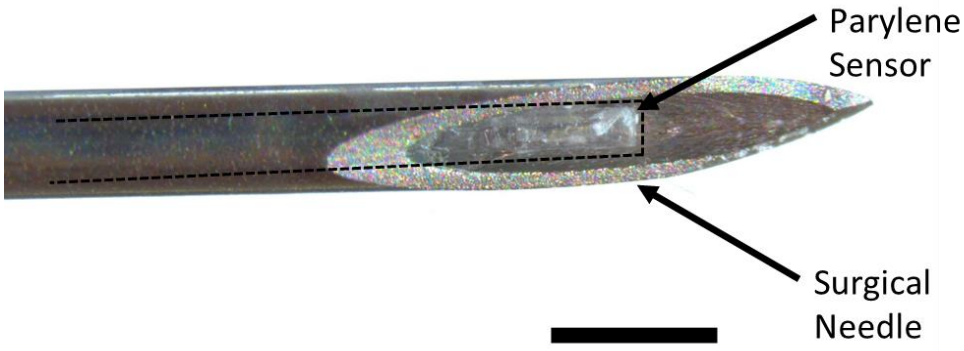

Figure 3.27 – Microscope image of an assembled parylene pressure sensor inserted through the inner lumen of a surgical needle. Dashed line indicates the position of the sensor. Scalebar is 1 mm.

With the small in-house setup hundreds have been produced at a time and parylene coated. Parylene coating is a highly scalable process mainly limited by the size of the coating chamber.

The main materials used in the sensor fabrication are parylene-C and glass. Both of these materials are biocompatible and safe for use in medical devices. PVP is also a biocompatible polymer so if any residue were to remain it should not pose any problems. The Norland epoxy used will need to be replaced with a medical device approved adhesive such as Dymax MD® Medical Device 250-CTH in future iterations.

The creation of the parylene-C membranes shows how high-resolution 3D printing techniques can be utilised to rapidly produce micro-structures outside of a cleanroom while maintaining high levels of control and repeatability in the process.

Many different variables had to be investigated and optimised to result in a process capable of batch producing curved pressure sensitive parylene-C membranes. These included surface functionalisation of the micro-nozzles and the capillary walls, optimising the choice of polymer to aid sacrificial layer removal, the addition of fluorescent dye to help visualise, investigating alternative techniques for wicking out the residue of the sacrificial polymer, using polymer blends to promote conformal film forming surfaces, experimenting with vacuum and heat treatment to cure the polymer for parylene coating, effectively sealing the capillaries to prevent total encapsulation during coating and the removal of the capillaries from the substrate.

The sensor assembly was successful as can be seen in Figure 3.24 and Figure 3.27. The fibre integration was a bottle neck in the procedure as it had to be performed for each capillary individually under a microscope. A more scalable solution could be to integrate the fibres before the capillaries are detached from the coating substrate. When the capillaries are still attached to the substrate they are still in well-known fixed positions and fibres could potentially be automatically inserted and moved to known positions. Manual adjustment would then be minimised and only necessary to fine tune the fibre positions using feedback from the LCI system.

The robustness of the assembled sensors was not explicitly tested but minimal damage was observed throughout all the experimental procedures. As the intended application is for single-use medical devices the sensors seem to be more than capable of meeting the durability standards required for this.

3.9.2 Pressure sensing results

The results from the pressure characterisation are highlighted below. The pressure sensitivities were calculated and varied for the sensors tested. Starting with the initial

vacuum oil filled capillaries, as seen in Figure 3.7 the oil meniscus is concave and thus the resulting parylene-C membranes were also concave.

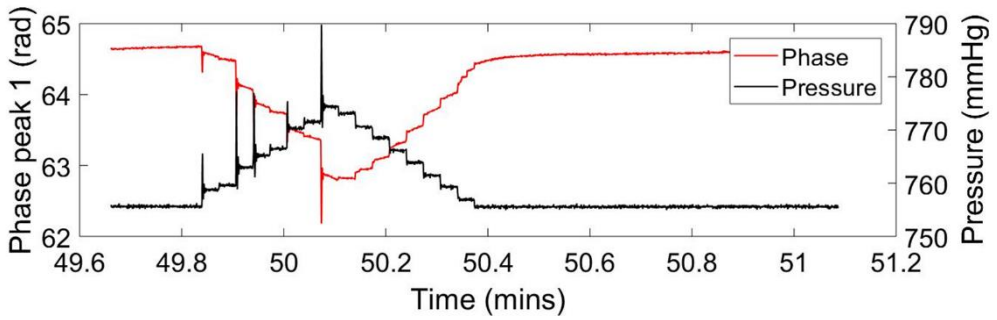

Figure 3.28 – Pressure response of concave parylene-C membrane from vacuum oil filled capillaries.

The concave shape sensors gave a reasonable phase change when exposed to varying pressure and had an average sensitivity of 0.09 radians/mmHg calculated over 3 sensors. An exemplar pressure plot from these sensors is shown in Figure 3.28. The parylene-C thickness was estimated to be ~3 µm. The change in phase manages to capture the sharp pressure spikes as the pressure is increasing in steps. The change in phase is opposite in direction to the change in pressure i.e. as the pressure increases the phase decreases. This inversion is due to the sensing mechanism. As the pressure pushes on the membrane and causes it to deform, the path length is decreasing, and the resultant phase is also decreasing.

The first attempt at curved parylene sensors using polymer sacrificial layers were coated with parylene-C ~5 µm thick. Their typical response is shown in Figure 3.29. From the figure it can be seen that the phase responds well to the changing pressure,

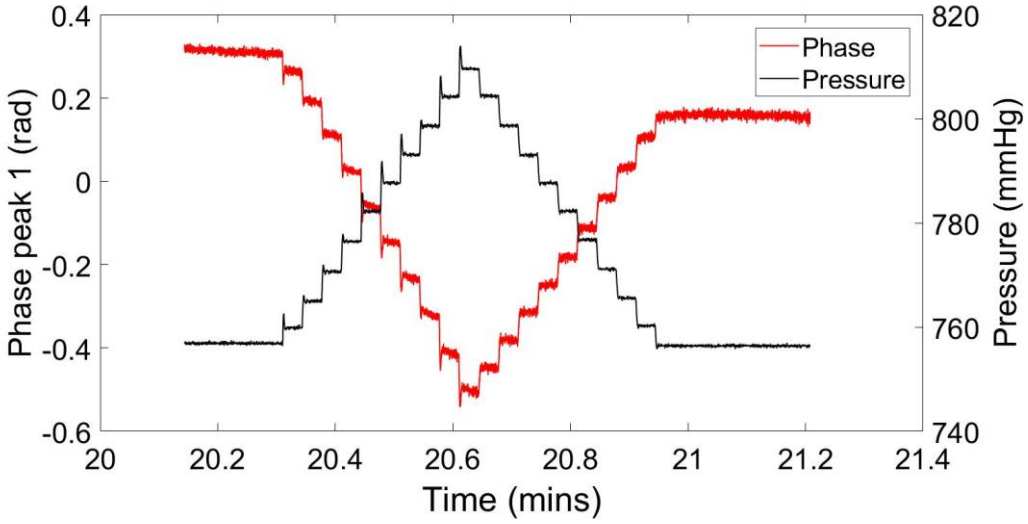

Figure 3.29 - Pressure characterisation graph for the first batch of curved parylene-C membranes. The parylene thickness was ~5 µm and the sensitivity was found to be 0.01 radians/mmHg.

capturing the sharp increases. It can also be seen that the initial and final phase measurements have shifted by ~0.2 radians due to a low frequency drift. The measured sensitivity of these sensors (0.01 radians/mmHg) was less than that of the vacuum oil filled capillaries. It was proposed that the increased thickness of the parylene could be causing the decreased sensitivity. The change of shape could also be playing a role.

To preliminarily test the theory that thickness was affecting sensitivity, the next batch of membranes were produced with a thinner parylene deposition of ~0.3-3 µm compared with the approximatley 5 µm membranes previously produced. The sensitivity of this batch was found to be an improvement on the previous batch as it increased from 0.01 to 0.5 radians/mmHg. An example pressure plot from this batch is shown in Figure 3.30. The uncertainty in the thickness of the parylene deposition is due to a variety of variables but mainly because the samples were included in the coating run as a secondary experiment, resulting in sub-optimal positioning within the coating chamber and a inhomogenious parylene deposition.

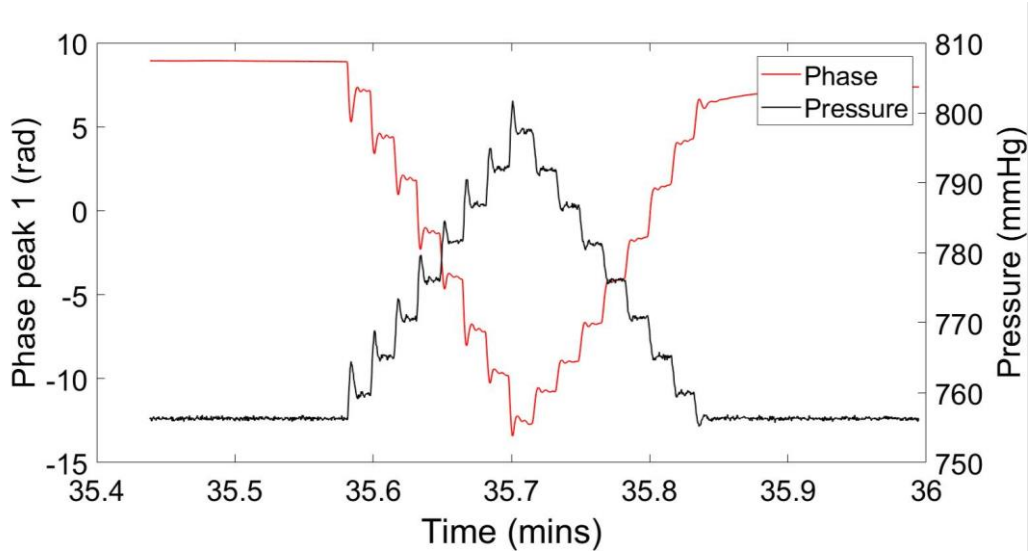

Figure 3.30 - Pressure characterisation graph for sensor with ~0.3-3 µm thick parylene-C membrane. The sensitivity was found to be 0.5 radians/mmHg.

It was noticed at this point that the spectrometer response was limiting the sensor and that sharp changes were not able to be captured, as visible in Figure 3.31. This observation indicated that a more responsive spectrometer should be used and brought about the shift from 800 nm to the use of 1550 nm optical fibre and complimentray faster LCI interogation system.

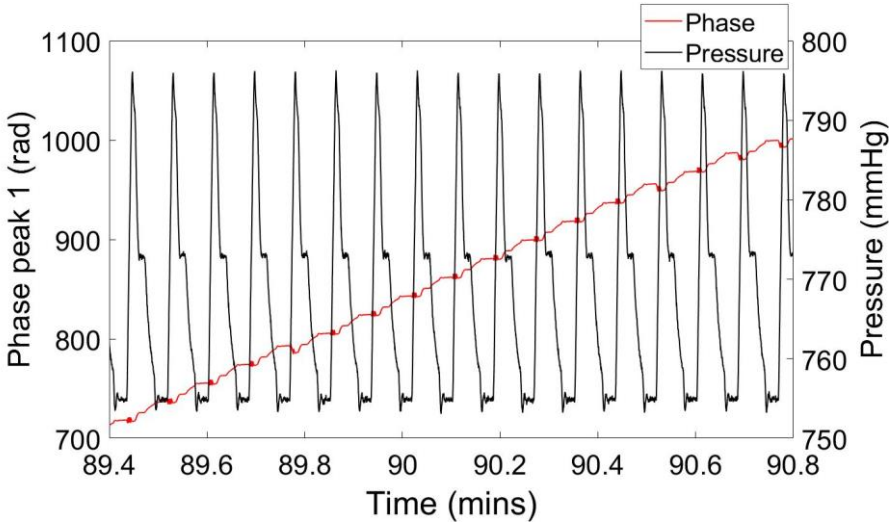

Figure 3.31 - Example of how the system was struggling to respond to sharp changes in pressure.

Post-processing of the data from the slower spectrometer showed that the sensor response was capturing the information but it was being lost due to the system lag. An improved phase unwrapping algorithm was implemented to show this. Due to the sharp pressure changes, the phase tracking was being lost. The post-processing algorithm tracked the phase better by monitoring for possible sharp phase jumps and adding 2 pi when necessary to make sure the values were correct. The updated algorithm was able to sucessfully keep track of the phase as shown be re-running the data from Figure 3.31 and generating Figure 3.32 where the phase response is in keeping with the pressure changes.

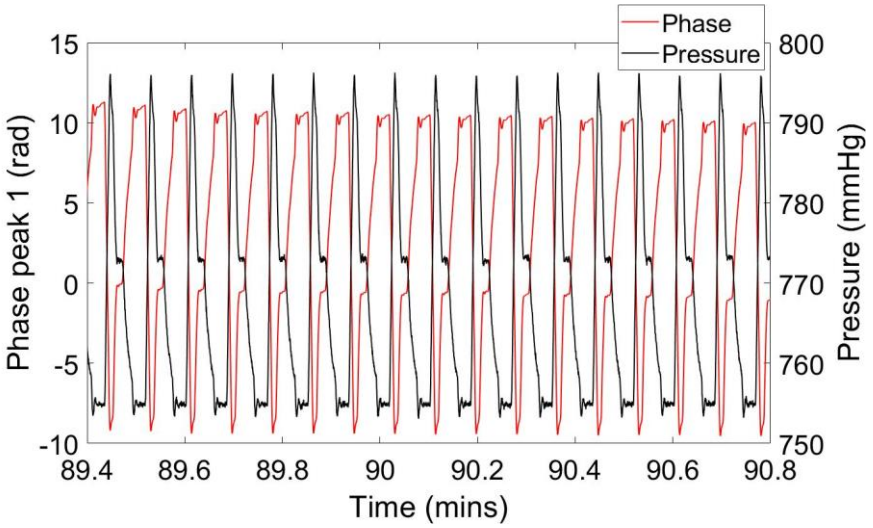

Figure 3.32 - Post-processing of the data from the spectrometer revealed that the pressure changes were being captured in the phase but hidden due to system lag.

The updated phase monitoring algorithm was effetive but was too slow to run in real time so the LCI system was switched to the faster 1550 nm Ibsen spectrometer system.

To this point, the parylene coating had been performed with an in-house parylene coater and resulted in large uncertainties in the thickness of the deposited parylene-C. To gain a better understanding of how the parylene thickness affected the sensitivity, an external coating company was used to deposit more precise thicknesses. Parylene-C coatings of 2.13 and 0.98 µm were deposited, and a third coating of 0.5 µm ±10% (precise thickness measurements of the 0.5 µm coating was not possible as it was so thin). The resultant sensitivities for each memebrane thickness are summarised in Table 3.3 and Figure 3.33.

Thickness	**Sensor**	**Sensitivity (radians/mmHg)**
2 µm	1	0.027
	2	0.005
	3	0.040
	Average	*0.024*
1 µm	1	0.050
	2	0.040
	3	0.023
	Average	*0.038*
0.5 µm	1	0.17
	2	0.063
	3	0.20
	Average	*0.14*

Table 3.3 – Pressure sensitivity results for sensors of varying parylene-C thickness.

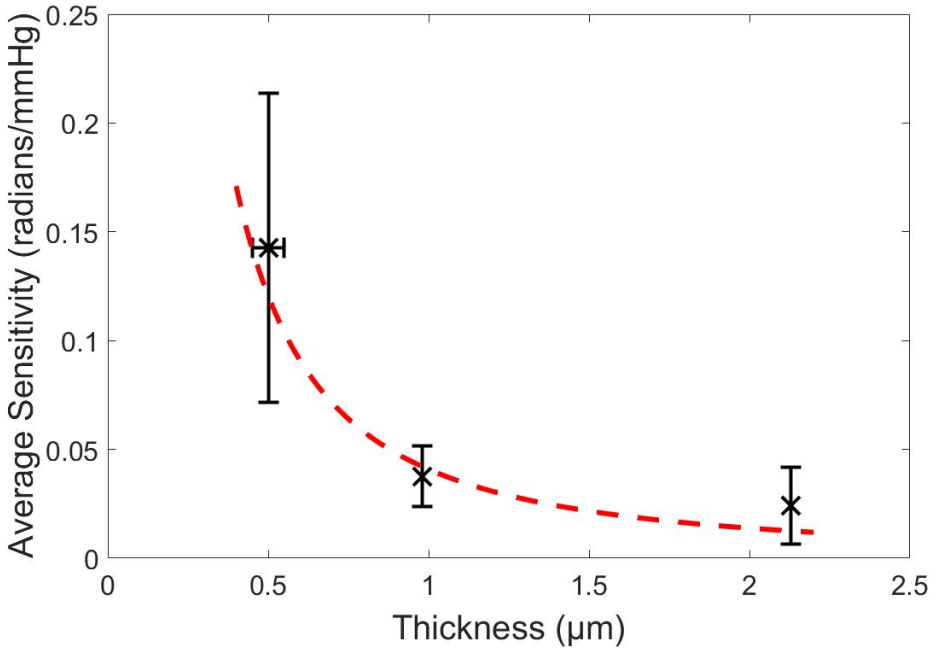

Figure 3.33 - Graph showing how the average sensor pressure sensitivity varies with parylene-C thickness.

The thickness and sensitivity data show that the average sensitivity of the sensors increases as the thickness of the parylene-C decreases, indicating that the thinner membranes are mechanically more susceptible to pressure changes and deform more, which results in larger phase changes. In Figure 3.33 a power law line of fit is included to illustrate the trend. The power law estimated from experimental data has sensitivity being proportional to thickness to the power of -1.2. This relation to the average sensitivity includes the acoustic and optical components. Equation (3.1 predicts the deformation of a flat membrane to be related to the thickness to the power of -3. This equation is purely mechanical and does not include any optical component. The difference between the 2 relations could arise due to the fact that the predicted -3 dependence is for a flat membrane not a curved one and due to the fact that an optical component is also required to couple the change in membrane deformation to obtain optical pressure sensitivity. Dome shapes mechanically vary from flat membranes and should deform less. Misalignments in the optical coupling within the F-P cavity could cause differences between the actual deformation and the optically measured changes.

The relationship between average sensitivity and membrane thickness shown in Figure 3.33 can be utilised to tune sensors for specific applications across a variety of pressures. In high pressure environments a reduced sensitivity would be preferred to prevent unnecessary damage to sensors and in other applications high sensitivity

is required to detect small pressure changes. By extrapolating the line of best fit in Figure 3.33, average sensitivities as high as 0.5 radians/mmHg are predicted for thicknesses of 0.2 µm and sensitivities as low as low as 0.007 radians/mmHg for thicknesses of 3 µm. These examples highlight the large variation in sensitivity that the sensors could potentially be tuned for, based on desired applications. Currently a thickness range of 0.5 – 2 µm has been experimentally investigated. Further work should incorporate a larger thickness range.

The samples that were coated by the external company seemed to have lower sensitivity values than the in-house coated samples. There is however a large uncertainty in the thickness of the in-house samples, with some thickness values ranging over an order of magnitude from 0.3-3 µm for a given coating. The larger sensitivity values of approximately 0.5 radians/mmHg for the in-house coated sensors indicate that perhaps the thicknesses were closer to the lower end of the estimate. The difference between in-house and external samples could also be due to differences in the parylene deposition process. The externally coated capillaries had better parylene adhesion to the glass. The external company use a blend of adhesion promoters which most likely induced this difference. There are also several other factors which can influence the quality/structure of parylene films such as the deposition pressure, annealing and oxidation effects. Some preliminary tests were carried out on annealing the membranes during this work but due to the lack of access to a nitrogen environment a vacuum oven was used instead. The initial results did not indicate stark changes in the sensor sensitivity but only a very small sample size was used as it was a preliminary study, and the process was not optimal. Annealing does however remain a promising avenue of exploration in future.

The shape of the curved membrane is another important parameter to consider. In the samples used to evaluate thickness and sensitivity the same sacrificial polymer formulation was used, and each capillary looked the same under microscope inspection. When alternative polymer blends or different polymers were used the shape of the meniscus could be varied. For example, PVA blends showed a greater affinity to the capillary walls giving more tapered sides and an almost flat top to the membranes. Despite attempts to use the same polymers and maintain the same shape, inhomogeneities in the polymer blend and variations in the capillaries could have led to slight differences in the membrane shapes. These slight differences could have resulted in the variation of sensitivity values shown in Table 3.3.

Differences in sensitivity values could also be due to the variation in optical alignment of each sensor. Though efforts were made to keep this as repeatable as possible small micrometre offsets in the alignment could result in large changes in the optical coupling and measurements between sensors.

3.9.3 Temperature results

Initial temperature tests were performed by altering the temperature of the water bath which the sensor was in. The temperature change was accelerated by adding hotter water during heating and adding cold water during cooling. As an initial test this worked (Figure 3.34) but it was not as precise as desired, so testing moved on to use a calibrated calorimeter and a focused temperature range around body temperature.

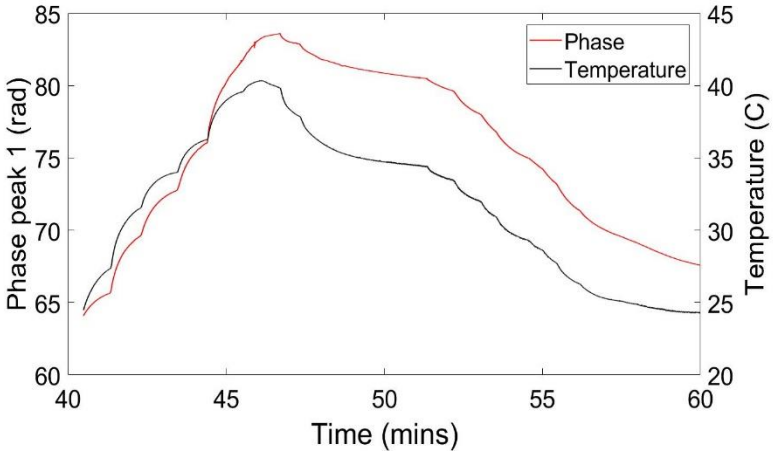

Figure 3.34 - Initial temperature characterisation graph showing heating and cooling. The sensitivity was found to be 0.99 radians/°C.

Unlike with the pressure characterisation, the change in the phase of the sensor is in line with the change in the temperature i.e. as the temperature increases so too does the phase. This relation is due to the sensing mechanism. The primary sensing mechanism is due to thermal expansion. As the temperature increases the sensor undergoes thermal expansion. The temperature increase causes the membrane to expand, increasing the distance between the fibre tip and the point of reflection on the membrane and hence the optical path. The change in optical path then results in the phase difference also increasing.

The calorimeter could be controlled to ramp to specific temperatures and hold the temperatures for fixed periods of time. An initial test found that the currents created in the calorimeter to ensure mixing for homogeneous temperature distribution disrupted the sensor. The mixing movements were quite large and led to waves which caused the sensor/fibre to detect motion/pressure changes, not just temperature. To resolve this the sensor was placed in a sealed water filled tube. The water filled tube was then positioned inside the calorimeter so it's walls were in contact with the temperature-controlled fluid. The tube protected the sensor from disruptive water currents while still allowing temperature control. This configuration reduced any water mixing effects on the sensor but delayed the speed at which the heating effects were recorded as the temperature controlled fluid in the calorimeter had to warm the tube and the water inside to impart the heat on the sensor. A thermocouple was inserted into the tube with the sensor to ensure accurate temperature readings since the calorimeter feedback control monitored the surrounding fluid, not the water in the tube in contact with the sensor.

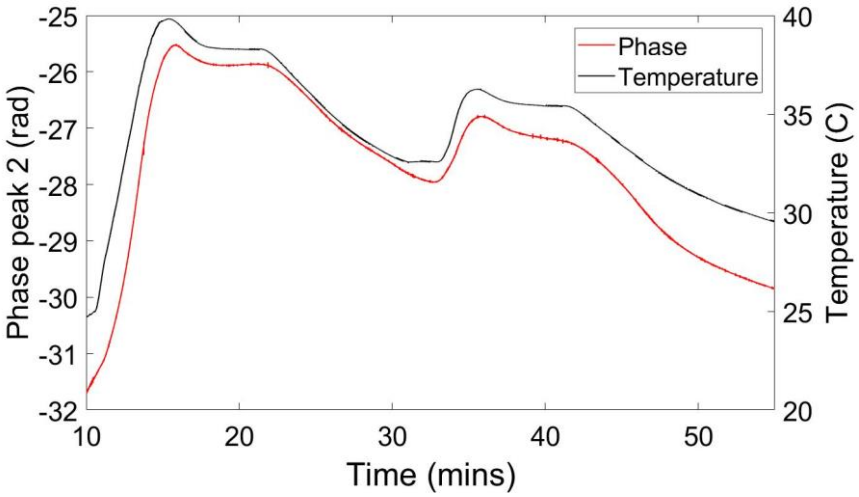

Figure 3.35 - Graph of temperature characterization using the calorimeter setup with a 1 µm curved parylene-C sensor. The sensitivity was found to be 0.47 radians/°C.

Figure 3.35 illustrates how the phase of the sensor follows the temperature changes well. The increases, dips and plateaus of the temperature curve are faithfully replicated in the phase trace.

Similar to the pressure characterisation, the temperature sensitivity was investigated for different thicknesses of parylene membranes. These results are presented in Table 3.4 and Figure 3.36.

Thickness	Sensor	Sensitivity (radians/°C)
2 µm	1	0.27
	2	0.055
	3	1.8
	Average	*0.72*
1 µm	1	1.3
	2	0.16
	3	0.28
	Average	*0.59*
0.5 µm	1	0.38
	2	0.33
	3	1.7
	Average	*0.80*

Table 3.4 - Temperature sensitivity results for sensors of varying parylene-C thickness.

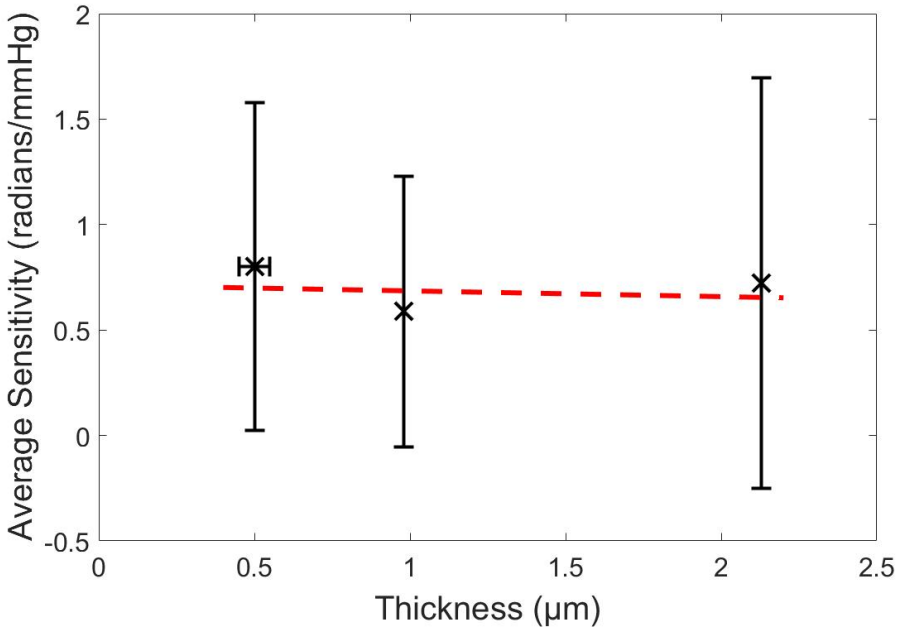

Figure 3.36 - Graph showing how the average sensor temperature sensitivity varies with parylene-C thickness.

The results suggest that the thickness of the parylene-C membrane does not affect the temperature sensitivity of the sensors. Based on linear thermal expansion, the change in length is proportional to the original length, so thicker membranes could

change more. However thinner membranes could be forced to expand more during heating as the air trapped between the parylene and the optical fibre also expands. Thinner membranes are not as mechanically stable and could be more prone to deformations due to the expanding air. In fact, the linear thermal expansion coefficient of parylene-C is 35 x 10^{-6}/°C (SCS coatings) and the volume thermal expansion coefficient of air is approximately 3400 x 10^{-6}/°C. Assuming that the linear thermal expansion of the parylene is equal in all 3 directions the volume thermal expansion can be approximated to ~100 x 10^{-6}/°C. This value implies that the expansion of the air in the sensor cavity is the dominate cause of the temperature response as the coefficient for air is an order of magnitude greater than that of the parylene-C. The differences between the temperature sensitivity results could be due to differences in cavity lengths and the amount of air trapped when sealing the sensors. The differences could also arise due to optical misalignments between the fibre and the deformable membrane so that the scale of the deformation is not conveyed efficiently to the spectrometer. Variations in the membrane's shape/structure could also lead to different deformation behaviours when the entrapped air expands into them.

3.9.4 Drift results

During the fluid pressure characterisation, the sensors were held at a constant pressure to determine how this affected their behaviour. Previous polymer-based F-P pressure sensors are known to undergo drift. Drift is a gradual change in the sensor reading despite conditions being held stable.

The curved parylene sensors exhibited a range of drift values. The average drift was 14.6 radians/hour. When the sensitivity of each sensor was included, the total drift values ranged from 44 mmHg/hour to the hundreds of mmHg/hour.

The large variation in drift values could be due to a variety of variables. One reason could be due to the sealing epoxy swelling as the sensors are submerged during testing. Water is absorbed by epoxy resin and the absorbed water can disrupt hydrogen bonds in sections of the polymer, causing swelling (Powers 2009). The sensors have epoxy between the optical fibres and the capillary walls and a larger blob at the joint between the optical fibre and the end of the capillaries to seal them. If the exposed epoxy absorbed water and began swelling this could potentially impart a force on the fibre and influence its alignment within the capillary, thus inducing a drift in the sensors.

Another potential cause of the drift could be due to optical heating of the F-P cavity by the interrogating light source. As the interrogating light is partially reflected from

the surfaces some may be absorbed and converted into heat. This gradual build-up of heat could then lead to thermal expansion of the membrane or surrounding material and cause the drift that is seen.

Or a combination of heating and swelling could be the cause. The differences in the amount of epoxy used to seal the sensors and the different amount of time the sensor has been running for and heating up could contribute to the variation that is observed.

Previous work has suggested that diffusion of molecules across the membrane from the air cavity to the surroundings and vice versa could be a source of drift. However, in this case parylene is used which is a water and gas impermeable material so should prevent this from occurring.

The overall impact of this low frequency drift is minimal when compared to the dynamic pressure and temperature changes that are occurring. However, for intravascular applications it could reduce the accuracy of measurements due to calibration changes caused by the drift. In cardiology, for FFR measurements being performed during minimally invasive procedures, a pressure drift of 5 mmHg/10 minutes is an acceptable level of drift given the clinical application and the short measurement window. Further work needs to be undertaken to fully understand the source of the drift in these sensors and minimise its effect going forwards.

3.10 Conclusion

Parylene-C polymer membranes were created at the tip of glass microcapillaries through the use of high-resolution 3D printing techniques and chemical vapour deposition. The development of suitable sacrificial layers and their removal were vital to this process. By carefully testing and optimising the elements involved in the fabrication, a scalable manufacturing process was created. If scaled up this manufacturing process could be utilised to produce large batches of extrinsic F-P sensing elements.

The resulting capillaries with membranes were integrated with single mode optical fibres to create pressure and temperature sensitive F-P probes. The F-P sensors were interrogated with an LCI setup to extract pressure and temperature information.

The assembled fibre optic sensors were characterised using *in-vitro* setups to replicate body pressures and temperatures. The sensors underwent stepped pressure increases and decreases, pressure holds at fixed pressures and pressure waveforms which replicated arterial pressure waveforms. The pressure sensitivity of the probes was found to be dependent on the thickness of the curved parylene

membrane. Thinner membranes gave increased sensitivity. Based on the experimental results, sensor sensitivity was found to be proportional to the thickness to the power of -1.2. By knowing how the thickness affects sensitivity, the sensitivity of the sensors could be tuned to make them optimised for specific pressure ranges and applications. This optimisation would enable the use of the sensors in many different medical procedures across different areas of the body where the experienced pressure ranges can vary drastically. They could also be utilised to monitor the pressure in a variety of industrial procedures.

The temperature response of the sensors was also characterised using a calorimeter. The sensors underwent heating and cooling ramps to fixed temperature values where they were held for a period of time. The temperatures were concentrated around 37 °C. It was found that the temperature sensitivity did not vary with parylene thickness. It was suggested that the air cavity inside the capillary underwent thermal expansion which exerted a force on the parylene membrane and was the main cause of the phase change which resulted in the measured temperature sensitivity. Variations in the response amongst sensors of the same batch were put down to slight differences in the membranes and differences in the cavity sizes of the assembled sensors.

During pressure and temperature measurements there was an underlying low frequency drift present. This drift varied across sensors and batches, ranging from 10's of mmHg/hour to 100's of mmHg/hour. The exact cause of the drift is not well known but has been reported in other fibre optic F-P sensors. Previous work has theorised that diffusion of molecules across the membrane from the air cavity to the surroundings and vice versa could be a source of this drift. The use of parylene-C in this work, which has extremely low gas permeability and water vapour transmission rates, suggests that this is not the source of the drift. Possible other causes are the swelling of the epoxy when submerged in fluid environments and possible self-heating effects from the interrogating light source.

Chapter 4 - Parylene based Fabry-Pérot fibre optic hydrophone for ultrasound sensing

4.1 Introduction

This chapter presents the development and characterisation of parylene-C based fibre optic hydrophones for ultrasound reception. Ultrasound has proven to be extremely useful in modern medicine. Since its introduction to the medical field in the latter half of the 20th century by H. Gohr and T. Wedekind it has found widespread use in clinics as an imaging modality due to its relatively cheap cost (as compared to MRI and CT for instance), ease of use and good safety profile. Ultrasound is non-ionising and thus does not have the potential to ionise atoms and cause ionising damage to cells. The non-ionising property of ultrasound has led to its use in areas such as fetal medicine, where cell damage can have far greater implications on developing fetuses. Outside fetal medicine ultrasound is used in many other areas of the body to image structures such as the heart and blood vessels. High intensity focused ultrasound can also be used as a treatment technique, but the focus of this chapter is sensing ultrasound by optical techniques for applications such as imaging.

As well as using ultrasound transducers externally to view inside the body, ultrasound can also be used in minimally invasive devices. Endoscopic ultrasound (EUS) makes use of *in situ* miniaturised ultrasound imaging tools. EUS has been used to diagnose oesophageal disorders and to guide minimally invasive surgeries (Das et al. 2001; Pai et al. 2015; Yoshinaga et al. 2012), highlighting the impact that minimally invasive ultrasound imaging devices can have.

In traditional ultrasound transducers piezoelectric elements are used to generate and detect ultrasound waves. When it comes to miniaturising piezoelectric elements for use in minimally invasive ultrasound imaging devices, the process is complex and strife with limitations. For minimally invasive ultrasound imaging devices, all optical ultrasound offers a more elegant solution.

As discussed in Chapter 2 ultrasound can be generated and received optically. For generating ultrasound optical laser pulses and photoacoustic materials are used. As well as this, ultrasound can be detected optically using fibre optic hydrophones (FOH). By combining fibre optic ultrasound transmitters and FOH, all optical ultrasound imaging can be performed through optical fibres. These fibres can be integrated with catheters and moved around the body to help guide medical procedures while maintaining immunity to EMI. As with traditional pulse-echo ultrasound the timing between the emission and detection is important.

Fibre optic ultrasound imaging is highly suited for use in minimally invasive surgeries due to the small dimensions of the fibres, their flexibility and biocompatibility.

4.2 Hydrophones

Ultrasound detection using hydrophones will now be examined. Ultrasound can be detected optically and piezoelectrically. Both sensing techniques can be miniaturised but the advantages of optical sensing enables the removal of long electrical cables, provide MRI compatibility and potentially lower manufacturing costs.

The term hydrophone is used to describe a device that can be used underwater to record or listen to sound waves. Since ultrasound is a sound wave the devices used to detect ultrasound are generally called hydrophones. As ultrasound waves do not propagate very far in air most applications are in fluid or soft tissue environments and experiments are generally performed in water.

4.2.1 Hydrophone properties

Some general properties of hydrophones are outlined below.

Sensitivity – For a piezoelectric hydrophone the voltage induced when an acoustic pressure is applied is known as the sensitivity. The sensitivity may be dependent on other variables such as the acoustic frequency and the response may not be linear for extremely high pressures. High sensitivity is needed to detect waves from greater penetration depths.

Bandwidth – A measure of the acoustic frequencies that can be efficiently detected. A broader bandwidth enables resolution of shorter ultrasound pulses and leads to higher image resolution. The bandwidth can be influenced by many parameters such as the sensor size. For smaller sensors diffraction effects can cause complex frequency responses.

Noise Equivalent Pressure (NEP) – As all systems have some intrinsic noise there will be a minimum measurable pressure that is above the noise level and this is the NEP. The NEP results in a signal to noise ratio (SNR) of 1. NEP is highly dependent on the hydrophone. A low NEP indicates that waves from deep penetration depths and those from weakly reflecting boundaries can be detected.

Directivity – The directivity is the angular range over which ultrasound signals can efficiently be received. Omnidirectional hydrophones can efficiently detect ultrasound signals over a large angular range. However, for applications such as M-mode imaging a highly directional sensor would be preferred so that reflections from outside the imaging plane are reduced.

4.2.2 Fibre optic hydrophones

Fibre optic hydrophones (FOH) are based on F-P interferometry sensors. As discussed in Chapter 2, F-P interferometry sensors can be used to measure many parameters such as temperature, strain, pressure, refractive index and magnetic fields. These parameters are measured by monitoring the interference between the measurand and reference light beams.

Unlike measuring physiological pressure (Chapter 3), to efficiently detect ultrasound a high finesse F-P cavity is required. The finesse of an optical cavity is essentially the number of bounces the light beam makes before escaping or being absorbed. To create a high finesse optical cavity the reflectivity of the bounding surfaces must be increased. When the reflectivity values are suitably high, the interrogating light beam will undergo multiple reflections within the F-P cavity before escaping back down the fibre. These light beams will interfere with the reference light beam depending on their relative path differences.

For ultrasound detection, if the optical length of the cavity is changed (i.e. by an ultrasound wave interacting at the deformable cavity surface) then the relative phases of the reflected beams will be shifted, and the total reflected power will be modulated. By detecting this modulation, the pressure of the wave can be determined.

4.3 Fabry-Pérot laser interferometry system

In order to maximise the total acoustic response both the optical phase sensitivity and the acoustic phase sensitivity must be addressed. The acoustic phase sensitivity is mainly dealt with in the hydrophone design. The optical phase sensitivity can be addressed in the interrogation system used. The main component of the interrogation system used is a wavelength-tuneable CW laser. A schematic overview of the system used is given in Figure 4.1. In this work a Santec TSL-550 laser with a tuning range of 1500 – 1630 nm was used. The laser was connected to the FOH via an optical circulator. Reflected light from the FOH passed back through the circulator to a photo-receiver system. The photo-receiver system had 2 outputs, a low frequency and a high frequency output. The low frequency output was digitized and used to measure the ITF of the F-P cavity. Knowing the ITF, the interrogating wavelength was adjusted to reach the optimum bias point and maximise the optical phase sensitivity. The high frequency output was also digitized and used to measure the response of the F-P sensor.

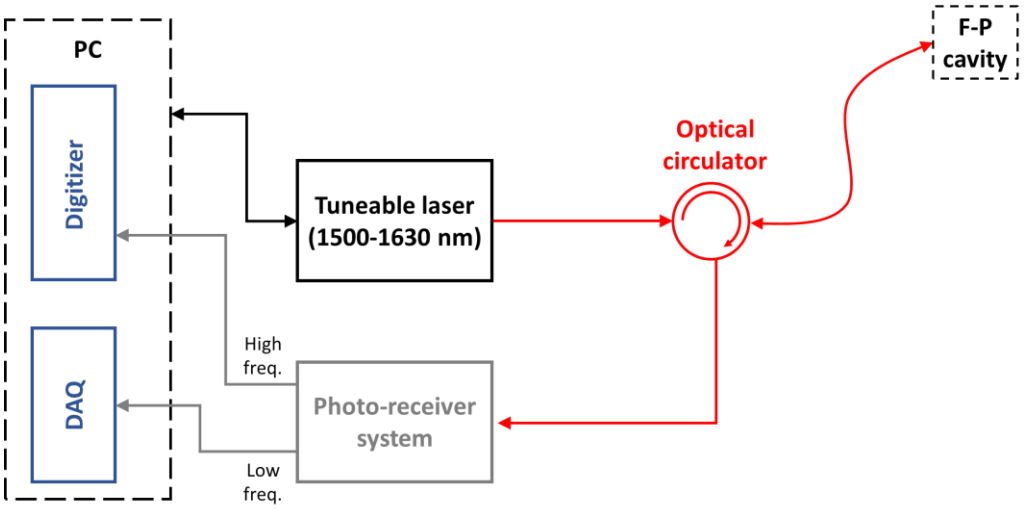

Figure 4.1 - Schematic diagram of the laser interrogation system.

4.4 Hydrophone design

The hydrophone design for this work builds upon the parylene membrane F-P cavity design utilised in Chapter 3. For F-P based hydrophones, the cavity can be composed of a solid material such as a transparent polymer film or be air or fluid filled. The ITF and hence optical phase sensitivity will be determined by things such as the materials used, the reflectivity of the surfaces and the length of the cavity.

4.4.1 Design considerations

When designing a fibre optic hydrophone there are several factors that need to be considered. Based on the literature and background information, the following considerations were proposed.

1. The FOH should be composed of a single mode fibre as the waveguide and an integrated extrinsic F-P sensing element.
2. The integrated fibre should be a single mode optical fibre, cleaved at normal incidence with a cladding diameter of 125 µm.
3. The fibre should be coated with a reflective material to create the first mirror of the F-P cavity.
4. The interrogation system will be a laser system using a wavelength-tuneable laser as a light source. The ITF should be monitored so that the wavelength can be tuned to the optimum bias point and maximise optical phase sensitivity.
5. A deformable polymer membrane should be present at the distal end of the extrinsic F-P sensing element which can respond to acoustic pressure waves.
6. The deformable polymer membrane should be highly reflective to create the second mirror of the F-P cavity.
7. A high finesse air-filled F-P cavity should be created between the deformable membrane and the cleaved single mode fibre.
8. For ultrasound sensing applications, the FOH will need to respond to acoustic pressures in the range of kPa and frequencies in the MHz range.
9. The dimensions of the FOH should be such that it can be integrated into medical catheters along with a fibre optic ultrasound transmitter so that they can be used in tandem for all-optical ultrasound imaging (FOH < 300 µm).
10. The fabrication method should be able to facilitate the production of multiple sensing elements per batch.

4.4.2 Parylene based design

Based on the design considerations it was decided to focus the hydrophone design around an extrinsic FOH. Building on the work presented in Chapter 3, creating deformable parylene-C membranes at the tip of glass micro capillaries, and integrating these with single mode optical fibres should create F-P cavities capable of detecting ultrasound. Using extrinsic F-P sensing elements and integrating with optical fibres will produce air filled F-P cavities. The air backed parylene membrane should be able to deform under small pressures resulting in a highly sensitive FOH.

From Equation (2.13) the change in length of the cavity and the change in refractive index of the cavity will determine the acoustic phase sensitivity. For an air-filled cavity changes in the refractive index due to pressure changes will be small compared to the effects from the change in cavity length from the deformable membrane. The change in length due to pressure ($\partial l/\partial p$) will be due to the deformation of the curved parylene membrane. The resultant phase shift will be dominated by the length change and will be a function of how the membrane deforms.

In order to create highly reflective surfaces (mirrors) for a high finesse F-P cavity the original parylene-C membranes as discussed in Chapter 3 need to be modified. To increase their reflectivity, they should be coated in a highly reflective material. It was decided that gold coating would provide the appropriate reflectivity values as well as being biocompatible and thin enough to not inhibit deformations. Not only would the parylene membrane need to be gold coated but the optical fibre to be integrated should also be gold coated to create complimentary optical cavity mirrors. A schematic of this design is shown in Figure 4.2.

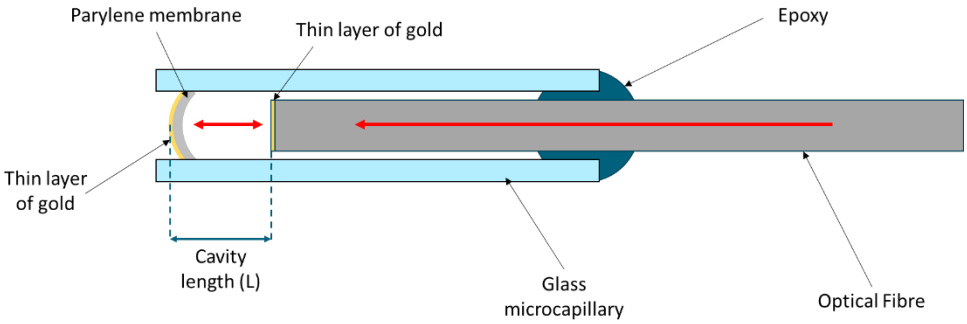

Figure 4.2 - Schematic diagram of the parylene-C based FOH design.

This design is an extension of the pressure sensor design in Chapter 3 which was shown to be successful for pressure sensing with low finesse cavities and a low coherence optical interrogation system. By incorporating highly reflective coatings the same design should also be capable of detecting ultrasound.

Many FOH designs use solid deformable material to create the F-P cavity. There are reflective coatings on the fibre and on the outer surface of the material to create a cavity. With this parylene-C based design the cavity is air filled. A thin, air-backed parylene membrane should be able to deform much more than a solid cavity under the same pressure, thus increasing acoustic phase sensitivity. The curved aspect of the design also offers improvements compared to flat surface designs. As shown by Guggenheim *et al.* (Guggenheim et al. 2017) a curved reflective surface can provide additional optical focussing and prevent beam walk-off. As the light undergoes

multiple reflections in the cavity, it will diverge. The refocussing from the curved surface will help to delay this divergence effect to enable more reflections and create higher finesse cavities.

4.5 Fabrication

The manufacturing technique used is based on the previously described process which was optimised and discussed in detail in Chapter 3, a summary is shown below in Figure 4.3.

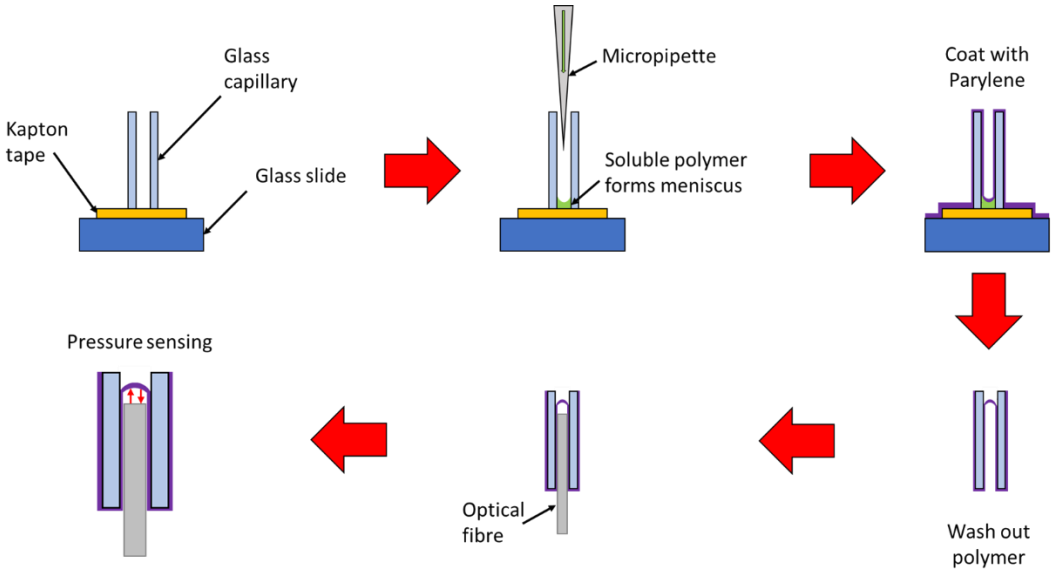

Figure 4.3 - Schematic diagram highlighting the key points of the manufacturing process.

4.5.1 Gold coating parylene membranes

Once the parylene-C membranes were created at the tip of the glass capillaries, the reflective gold coatings needed to be added. Firstly, gold was deposited onto cleaved single mode fibres (Thorlabs, SMF-800) using an electron beam evaporator gold coater (Edwards A500). After deposition, the fibres were inspected, and the reflectivity of the coating was measured by analysing the reflected light.

The next step was to deposit a gold coating on the parylene membranes. Tests were performed to determine if coating on the outside or inside surface of the membrane gave better results. The capillaries were fixed in place by adding water soluble adhesive to their outer side wall. This side mounting technique ensured that they remained unsealed, as the gold coating process requires a strong vacuum, and if the capillaries were completely sealed, pressure would build up and potentially damage the membranes. The capillaries were adhered to the side of a glass microscope slide using a water-soluble UV curable adhesive (Norland blocking adhesive 107) to ensure

that once coated they could be removed from the mounting slide. The gold was deposited on the membranes using a thermal evaporator (Edwards A306).

It was theorised that gold coating on the inside of the parylene membrane would be preferred as the gold would then be protected from the external environment as it is inside the sealed cavity. However, to achieve this the gold coating would have to penetrate all the way down the inner lumen of the capillaries and deposit on the inner parylene surface. Due to the gold coating deposition being a highly directional beam the capillaries were mounted as straight as possible under a microscope to try and ensure the gold would reach the inner membrane surface. Gold coating on the outside surface of the parylene membrane was simpler as the gold beam did not have to travel all the way through the capillary. These capillaries were also mounted as straight as possible to ensure the coatings were as uniform as possible across the membranes.

4.5.2 Sensor assembly

Once the capillaries and fibres were gold coated the FOH sensors were assembled. The assembly process was similar to that for the low finesse pressure sensors. In this case, the side mounted capillaries were kept on the mounting glass slide until the fibres were integrated as it was easier than removing all of the capillaries immediately. The glass slide was mounted to a 3-axis translational stage under a microscope and a gold coated fibre was positioned in a fibre holder and aligned to initially inspect the coatings. The fibre was connected to the LCI setup to enable quick real time feedback during the inspection phase. The gold coating on the fibre was chosen to be approximately 5 -10% thinner than that on the membranes to create a high finesse cavity. The reflective gold coatings trapped light in the optical cavity so that it

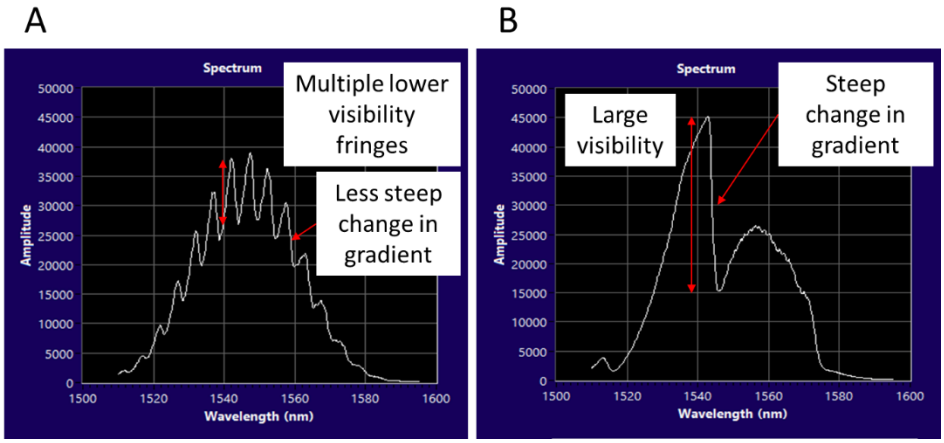

Figure 4.4 – Screenshots showing the comparison of the interference signals obtained from low finesse cavities (A) and higher finesse cavities (B) using the LCI setup.

underwent multiple reflections/round trips, while the thinner coating on the fibre allowed light to escape back into the interferometry system. When the coated fibre was inserted into the coated capillaries the real time interference signal from the LCI was closely monitored. The Fourier transformed signal was used to ensure the distance between the membrane and the fibre tip. The interference in the spectrum was used to look for Airy function shapes to indicate that an appropriate ITF was created due to proper cavity alignment and enough light being trapped. An Airy function like steep gradient can be seen in Figure 4.4B. The classic Airy function drop is superimposed onto the broadband spectrum of the LCI light source. The fibre was then removed from the capillary and used to inspect the remaining capillaries.

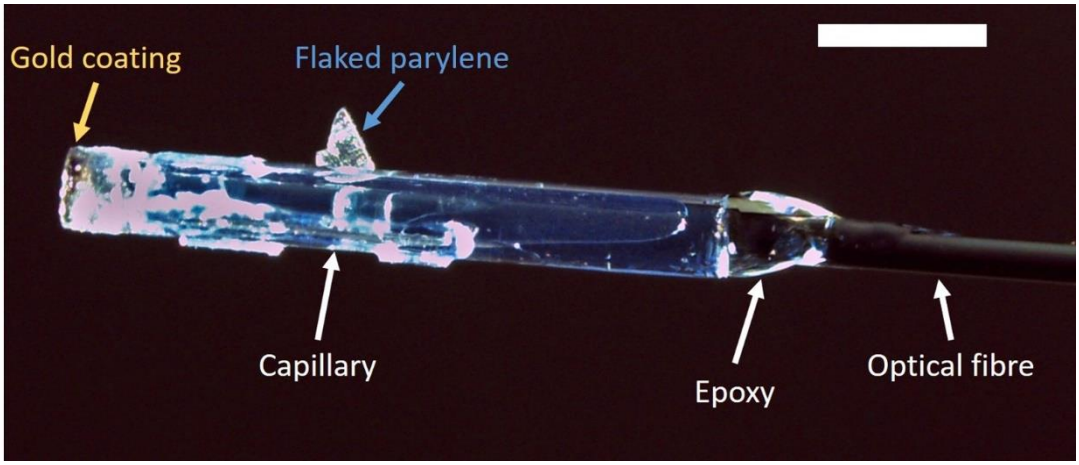

Figure 4.5 - Microscope image of an assembled FOH. Note the gold colour visible at the tip of the capillary due to the coating. Scalebar is 500 µm.

After the coated membranes were assessed with the coated fibre, the capillaries that had the appropriate gold coatings to enable high finesse cavities to be created (showed Airy function like shapes in their LCI spectra) were assembled into FOH sensors. The assembly utilised UV curable epoxy (Norland Optical Adhesive 81) to seal the cavities and hold the fibre in position within the capillaries.

Figure 4.5 shows an assembled FOH assembled with a 125 µm fibre. The membrane was coated on the outer surface with cold coating and this is visible in the image as gold colouration at the capillary tip. Part of the parylene-C coating has flaked off and is visible on the top side of the capillary.

4.6 Methods

Once assembled the FOH were connected to the laser interrogation system and a more accurate ITF was observed by conducting a wavelength sweep. Though the LCI system gave a quick real-time estimation of how the ITF would appear during

assembly, this had to be confirmed with a laser interrogation wavelength sweep. After confirming an appropriate ITF for the assembled cavity, the sensor characterisation could proceed.

4.6.1 Ultrasound detection

In order to test ultrasound detection of the FOH, an underwater ultrasound transducer was used. The FOH was mounted on a 3-axis translational stage and positioned in a water bath of DI water in alignment with the ultrasound transducer. The transducer used was a 3.5 MHz transducer (Olympus Panametrics) with a complimentary pulsar (Olympus 5072R Pulser/Receiver). An overview of the testing setup is shown in Figure 4.6. The transducer and pulsar were calibrated so that the pressures of the generated ultrasound waves were known. The calibration was done using a membrane hydrophone that has been calibrated to a standard by the national physical laboratory (NPL). Before FOH testing, the optimum bias point of the cavity was determined by the software and the wavelength was adjusted accordingly.

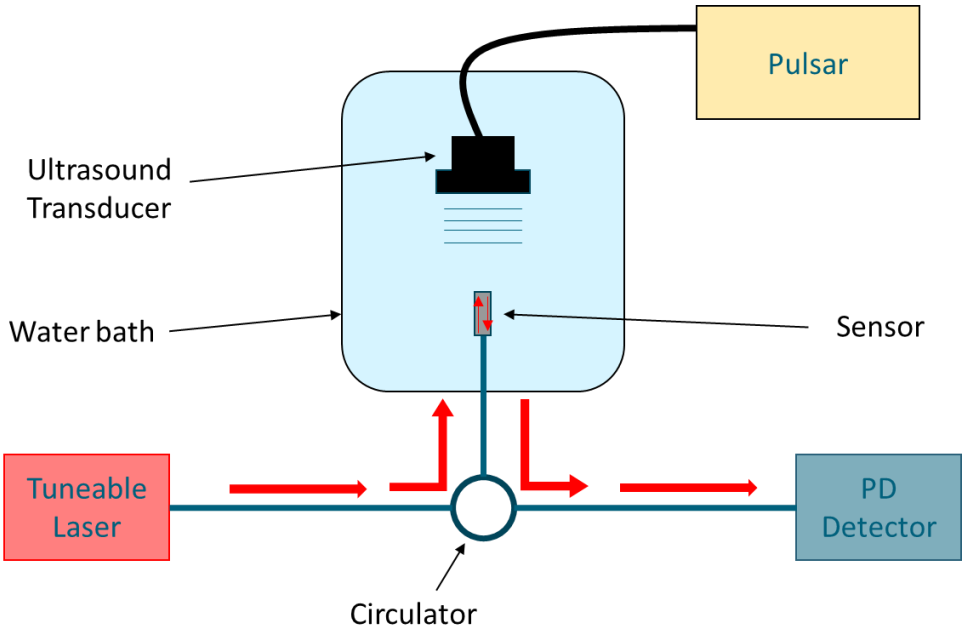

Figure 4.6 - Schematic diagram of the ultrasound detection testing setup.

Initial tests suggested that sometimes air bubbles were being trapped at the tip of the FOH. Due to the recessed membrane, a small air pocket could easily be trapped if submerged too quickly. To remedy this the FOH was angled upwards by about 30° so that when it was slowly submerged water could flow in and fill the gap between the membrane and the capillary tip. The FOH was lowered in a controlled manner using a translational stage into the water bath. Once fully submerged the angle was straightened out and the FOH position was optimised.

The FOH was then interrogated with the laser and the signal was recorded as the transducer produced ultrasound waves. The calibration of the transducer and pulsar were for specific axial distances from the front of the transducer. The FOH was moved to the calibrated distance and measurements were made. Raw signals and averaged signals were acquired for each FOH. Noise level measurements of the system were also recorded to aid with analysis and calculations of the NEP.

A commercial piezoelectric needle hydrophone was also tested in the same setup to allow for comparisons to be made.

4.6.2 Directivity measurements

To better understand the response of the FOH, directivity tests were also performed which varied the angle between the transducer and the FOH. The setup used a motorised rotational stage to vary the angle. Instead of the transducer and pulsar previously used for ultrasound detection a laser generated ultrasound source was used instead. The benefit of using a laser generated ultrasound source is that multiple frequencies of ultrasound are produced when ultrasound is optically generated. A Nd:YAG laser was combined with a 10 mm thick polymethyl methacrylate (PMMA) substrate coated on one side with highly absorbing black paint. The laser emitted 10 ns pulses at 1064 nm which were absorbed and generated ultrasound waves from 1-80 MHz. The range of frequencies produced meant that as well as testing the directivity response of the sensor, the frequency response could also be tested simultaneously. A schematic diagram of the testing system is included in Figure 4.7.

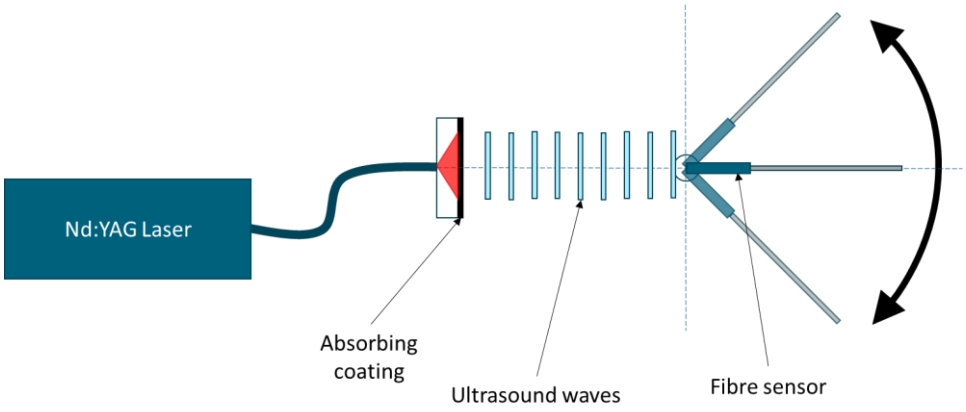

Figure 4.7 - Schematic diagram of the setup used to test directivity and frequency response of the FOH.

The directivity and frequency tests were performed in a DI water bath as previously used. The FOH was also submerged in a similar fashion in order to prevent air bubbles forming at the tip. The mount that held the FOH positioned it centrally in line

with the optical ultrasound source. The tip of the FOH was also positioned at the axis of rotation so that it remained constant as the stage rotated to vary the angles.

The laser generated ultrasound had previously been calibrated using a planar F-P sensor of known response by Zhang and Beard (Zhang and Beard 2015).

4.7 Results/discussion

The results of the fabrication process and the characterisation tests are presented and discussed below.

The initial parylene-C membranes were reproducibly manufactured following the outlined procedure which is discussed in more detail in Chapter 3. The main fabrication method explored in this section was the deposition of gold coatings onto the membranes. Using the thermal gold coater as described in section 4.5, depositing gold on the inner surface and outer surface of the membranes was investigated. The success of each method was validated by inserting a cleaved fibre coated in a 5 -10% thinner gold coating and checking if high finesse cavity interference patterns were formed. Microscope images were also used to visually inspect the membranes.

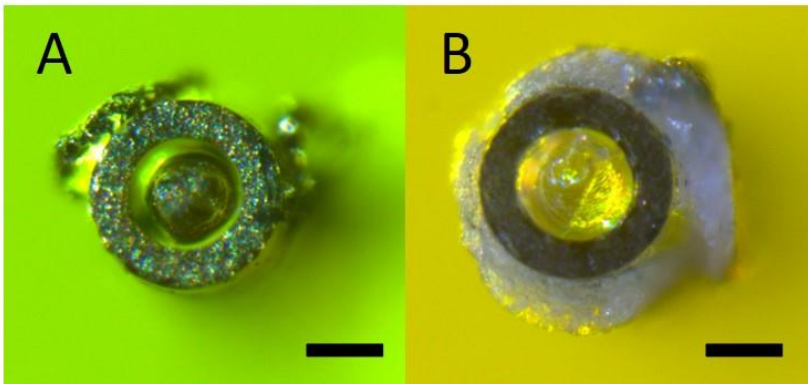

Figure 4.8 – Microscope images showing the comparison of gold coating on the outer surface of the parylene membrane (A) and the inner surface of the parylene membrane (B). Both scalebars are 100 µm.

From the microscope images and the fibre insertion checks, it was concluded that the exterior gold coating performed better than internal gold coating. The fibre insertion checks resulted in none of the internally coated membranes displaying any signs of high finesse cavity interference patterns or high reflectivity coatings. Visually, the internally coated membranes did not appear to have changed from before and after coating. Figure 4.8 highlights the difference between the two techniques. The additional material visible in the images on the outer walls of the capillaries are undissolved mounting adhesive and some remaining PDMS which did not peel off

appropriately. The additional material was located further along the capillaries, away from the tip where the membranes are located, so did not interfere with the sensing capabilities.

This result implies that the directional gold coating failed to travel through the 150 µm lumen all the way down the inside of the 2 mm capillaries and deposit on the inner parylene membrane. The slight offset of the capillaries from not being perfectly in line with the deposition beam may have caused this. The gold may also have preferentially been attracted to the glass walls of the capillaries as the beam travelled through the inner lumen, detracting from any being deposited on the membrane at the bottom. Clear gold deposition was visible around the top rim of these capillaries, but none seemed to have been deposited on the membrane at the bottom. For the capillaries coated on the outer surface of the membrane microscope images showed clear gold deposition. The fibre inspection process also showed that high finesse cavities were being formed thanks to the reflective gold coatings. It was therefore decided to proceed with coatings on the external surface of the parylene-C membranes.

While assessing the coating on the membranes by positioning a fibre inside the capillaries, it was noted that on multiple occasions the removal of the fibre caused the parylene-C coating to peel off the inner walls and be removed along with the testing fibre. The removal of parylene meant that if good reflectivity/interference was obtained, then the membrane would be damaged and could not be used. Figure 4.9

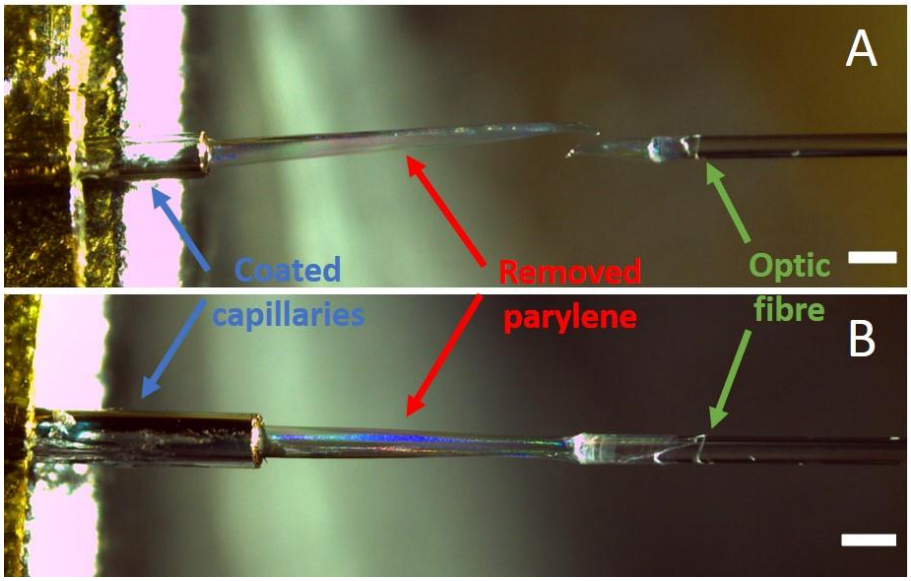

Figure 4.9 – Microscope images demonstrating how the parylene-C coating became stuck to the fibre during inspection of the reflectivity and was stripped from the capillary when the fibre was removed. Both scalebars are 250 µm.

shows how the parylene became adhered to the inspecting fibre and was stripped from the capillary as the fibre was removed. This issue was noticed when inspecting membranes fabricated using the in-house parylene coater. Once parylene coating was performed by an external company (Specialty Coating Systems, SCS) the issue became resolved. It is believed that the extra addition of adhesion promoters used by the company aided the parylene to adhere to the inner walls of the capillaries and hence was more securely held in place. Previous work in Chapter 3 also noted possible differences in material properties between the two deposition techniques.

Initial membrane gold coatings were obtained using a thermal evaporation coater. The coating did not give reflectivity values as high as hoped for. It was theorised that the deposited coatings were too thin. Despite this FOH were assembled and tested. The reflectivity was so low that the response was similar to that of a low finesse cavity. However, much was learned from testing these FOH. Firstly, the issue of submersion and trapping air bubbles was noticed and dealt with. A comparison of the ITF with and without trapped air bubbles was performed.

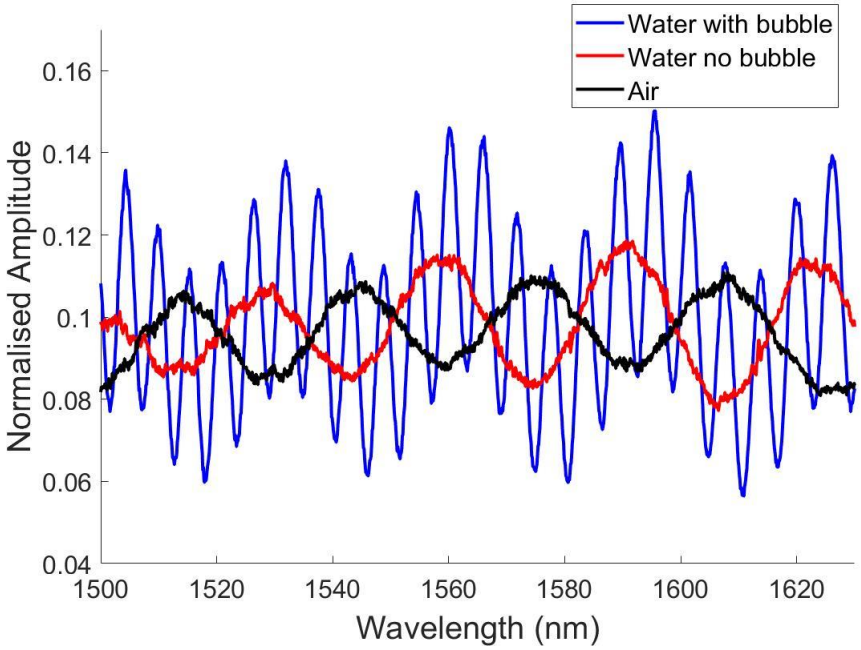

Figure 4.10 - ITF of the same sensor in air, in water and in water with an air bubble trapped at the tip.

From Figure 4.10 it can be seen that the expected Airy function shape of the ITF is not present as the sensor has a low finesse. It can also be seen that the ITF inverses when altered between air and water environments as the refractive index of the environment changes. When an air bubble is trapped at the tip a higher frequency modulation is visible. This additional modulation is possibly due to reflections

occurring at either side of the air bubble. The air bubble response also has a lower frequency component similar to the other signals.

Even though the ITF displayed low finesse, the laser interrogation system was still set to the optimum bias point and the FOH was tested with the 3.5 MHz transducer.

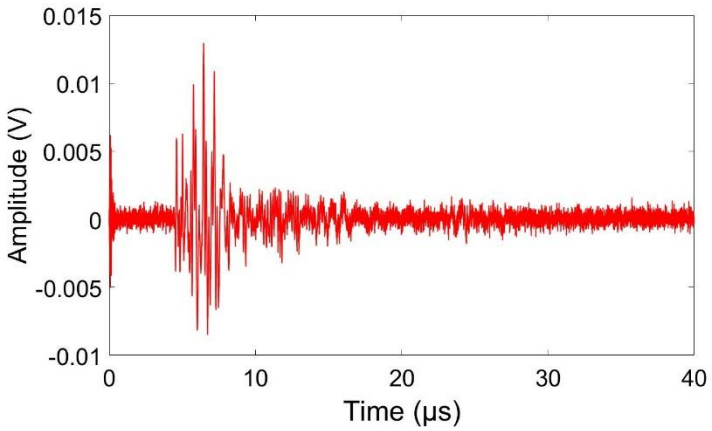

Figure 4.11 - Detected ultrasound from 3.5 MHz transducer using low finesse FOH.

Despite the lack of high reflectivity coatings, the low finesse FOH performed well and was able to detect ultrasound waves, as shown in Figure 4.11. For comparison, a commercial piezoelectric needle hydrophone was used in the same setup and their SNR were compared (Figure 4.12). The SNR of the FOH was 30 and the SNR of the piezoelectric hydrophone was 65. Both signals were filtered using a band pass filter to improve their quality.

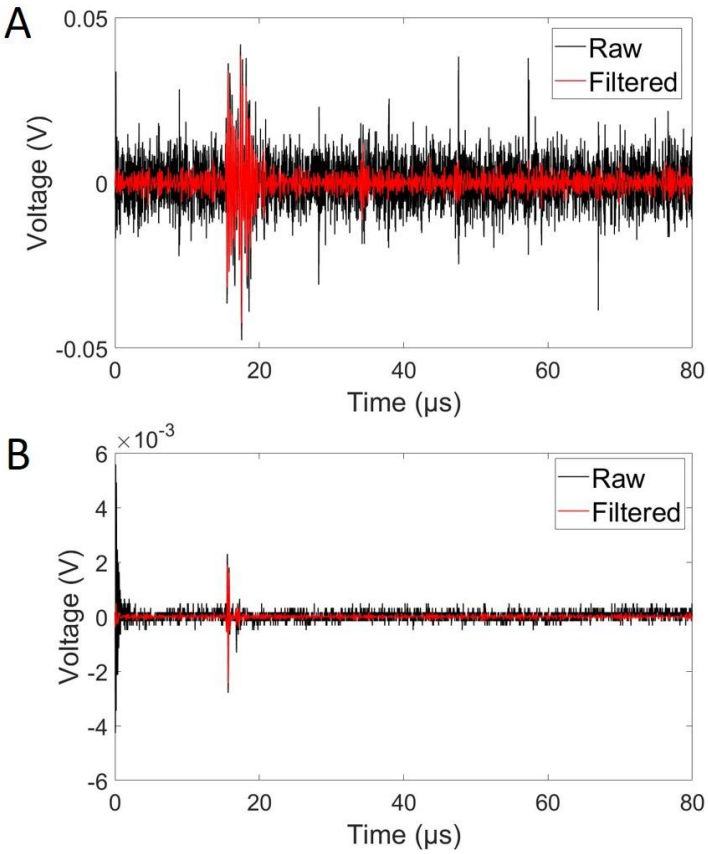

Figure 4.12 - Comparison of signals, A) from a low finesse FOH, B) from a commercial piezoelectric needle hydrophone. The SNR of the FOH was 30 and 65 for the commercial hydrophone.

From the comparison with the commercial hydrophone, it can be seen that despite low finesse the FOH has comparable SNR, this was very promising. More gold coating was performed to give a thicker gold deposition on the membranes and hence greater reflectivity. The results from this run showed estimated reflectivity values of approximately 50%. These membranes were integrated with fibres with reflectivity values of approximately 45% to create higher finesse cavities. Further coating runs were performed to obtain membrane reflectivity values of approximately 80%. Another coating run had estimated reflectivity of between 80 and 90%. These reflectivity values were estimated by including a flat cleaved fibre sample in each run. The coated fibre was then connected to a known optical system and the reflectivity of the coating was estimated by analysing the reflected light. The normalised ITF of these different reflectivity values are shown in Figure 4.13.

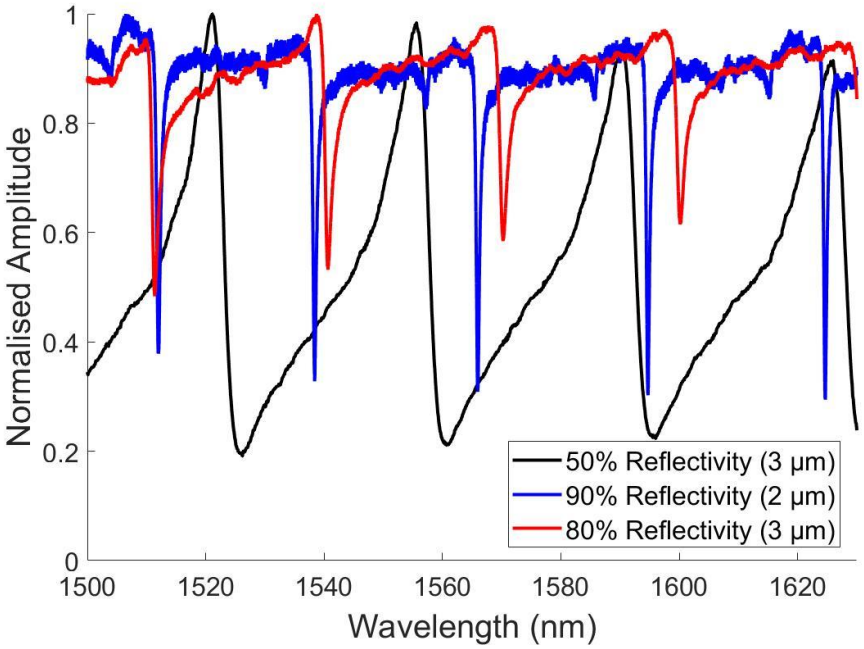

Figure 4.13 - Comparison of normalised ITFs for FOH with varying reflectivity values.

As the reflectivity increased, the sharpness of the Airy function peaks also increased. The increased sharpness indicated that higher finesse cavities were being created as the reflectivity values increased and were able to trap more light in the cavity for longer. The steeper ITF shows how the first derivative will increase and result in an increase in the optical phase sensitivity.

The assembled sensors were next characterised in the ultrasound transducer setup and their NEP was calculated. In order to calculate the NEP values, multiple raw signals from the FOH when detecting ultrasound were recorded. Using a Matlab script these signals were analysed, and the NEP was calculated. The Matlab script took the Fourier transform of the signal to check the frequency response. Based on this a band pass filter was devised to filter the signal. The maximum of the filtered signal was found and correlated to the maximum pressure from the calibrated transducer. The noise level of the signal was then estimated and used with the maximum signal and pressure information to calculate the NEP 3-sigma value of the FOH. The 3-sigma aspect relates the minimum detectable optical power to 3 times the standard deviation of the noise, a standard technique used for these types of calculations. The Matlab script is included in Appendix B for completion. Results from the NEP calculation are shown below in Table 4.1.

FOH	Estimated Reflectivity (%)	Membrane Thickness (µm)	Average NEP (Pa)	Filtered frequency range (MHz)
1	0	N/A (0.3 – 3)	2,000	0.5 – 12
2	50	N/A (0.3 – 3)	96	2 – 12
3	80	N/A (0.3 – 3)	83	0.5 – 15
4	80 – 90	2.13	370	1 – 7.5
5	80 – 90	2.13	550	0.4 – 7

Table 4.1 - Average NEP results for a variety of fabricated FOH.

The NEP results indicate that the sensors are able to measure small pressure variations in ultrasound fields less than 100 Pa. Compared to FOH and piezoelectric hydrophones in literature (Table 4.2) the NEP values here are of similar magnitudes. The FOH labelled 1 to 3 were fabricated with parylene-C membranes created with the in-house parylene coater. Their thicknesses were not precisely known but estimated to be between 0.3 and 3.0 µm. FOH labelled 4 and 5 were assembled with parylene-C membranes deposited by the external parylene company SCS with precise thicknesses. As noted previously the parylene deposited by SCS seemed to have better adhesion to the capillary walls. The two deposition processes vary and could impact on the properties of the deposited parylene membranes. Comparing FOH 2 and 3 with FOH 4 and 5 the NEP is lower for the in-house parylene membranes. The difference in NEP could be due to the thickness of the parylene being thinner and therefore able to mechanically deform more when acoustic waves interact with the membrane. It could also be due to changes in parylene properties when deposited under different conditions. Deposition temperature and pressure as well as the addition of adhesion promoters can all have an impact on the resulting parylene mechanical properties. From Figure 4.13, the FOH labelled 4 and 5 with an estimated reflectivity of 80/90% have the steepest ITF. The steep ITF shows that these FOH have the greatest optical phase sensitivity but despite this FOH 2 and 3 have lower NEP values. The lower NEP values for FOH 2 and 3 indicates that though they have a reduced optical phase sensitivity, they possess an acoustic phase sensitivity great enough to counteract this and give an overall more sensitive acoustic response. This acoustic response suggests that the membranes are much thinner than the 2.13 µm SCS parylene membranes and closer to the lower end of the 0.3 – 3 µm estimated thickness. The lower NEP could also be due to material property differences from the 2 deposition processes resulting in membranes that are easier to deform with the in house parylene-C coating process.

Hydrophone	NEP (Pa)	Measurement bandwidth (MHz)	Reference
1.0 mm piezo needle	7	100	(Hurrell and Beard 2012)
0.5 mm piezo needle	200	100	(Hurrell and Beard 2012)
0.2 mm piezo needle	1090	100	(Hurrell and Beard 2012)
0.075 mm piezo needle	6k	100	(Hurrell and Beard 2012)
Eisenmenger FOH	500k – 1000k	20	(Staudenraus and Eisenmenger 1993)
Polymer film FOH	15k	20	(Morris et al. 2009)
Rounded-tip polymer FOH	200	20	(Zhang and Beard 2015)
Plano-concave FOH	9.3	20	(Guggenheim et al. 2017)

Table 4.2 - NEP values of piezoelectric and fibre optic hydrophones from literature.

Compared with a similarly sized piezoelectric needle hydrophone (0.2 mm piezo needle hydrophone, Table 4.2) the NEP values for the FOH in this work were greatly improved,1000's Pa to 100's Pa. The NEP values of the parylene based FOH were also significantly lower than the values quoted for other FOH in literature such as the polymer film FOH reported by Morris *et al.* (Morris et al. 2009). The parylene FOH seemed most comparable with the rounded-tip polymer FOH in (Zhang and Beard 2015). The plano-concave FOH has a lower NEP than the FOH reported in this work. The plano-concave FOH has a similar design to the parylene FOH where the first reflecting surface is a flat cleaved fibre and the second reflecting surface is curved. This curvature is utilised by the rounded-tip FOH as well and helps to refocus the interrogating laser beam as it starts to expand and walk off after multiple cavity reflections. The main differences between the plano-concave FOH and the parylene FOH is that the cavity length of the plano-concave FOH is smaller (16 µm vs. 45 µm), the refractive indices of the cavities differ (polymer vs air) and greater reflectivity values in the plano-concave FOH (98 – 99.3% dielectric mirror coatings vs. 80/90% gold coatings). The optical phase sensitivity of the plano-concave FOH is superior to

that of the parylene FOH. However, the solid polymer cavity of the plano-concave FOH is less acoustically phase sensitive than the air filled parylene FOH cavity. The increased acoustic phase sensitivity of air filled cavities is highlighted by the FOH with no gold coating being able to successfully detect ultrasound and have a NEP value of 2,098 Pa, despite having poor optical phase sensitivity. By incorporating the optical phase sensitivity of the plano-concave FOH with the acoustic phase sensitivity of the parylene FOH even lower NEP values could be achieved.

Directivity measurements were also performed alongside frequency response tests to better characterise the FOH. The results of these tests are illustrated below in Figure 4.14. The plots show that the bandwidth of the FOH was quite narrow and that the FOH displays an approximately omnidirectional but complex response.

Looking at the FOH frequency response, the bandwidth was quite narrow, between 2 and 4 MHz. The bandwidth was not as large as that for other FOH reported in literature. From Table 4.2, the FOH in literature typically have a measurement bandwidth of 20 or 100 MHz for NEP calculations. There was visibly a stronger response to lower frequencies, less than 5 MHz. The frequency response of a F-P cavity is generally determined by the choice of materials and the length of the cavity, shorter cavities usually give greater bandwidth (Guggenheim et al. 2017). The cavity length of the parylene FOH was ~45 µm. With greater optical confinement the divergence/walk-off of the interrogating beam is limited. Zhang and Beard (Zhang and Beard 2015) have also shown that the shape of the cavity has a large effect on the frequency response. By rounding the edges of the fibre and cavity they showed how the frequency response could be improved to give broadband FOH.

The sharp edges of the fibre and the capillary in the parylene FOH design could be causing diffracted edge waves to propagate across the membrane surface and in the surrounding fluid. The interactions between these edge waves and the incident waves could be what is causing the low bandwidth of the FOH and the complex frequency response seen.

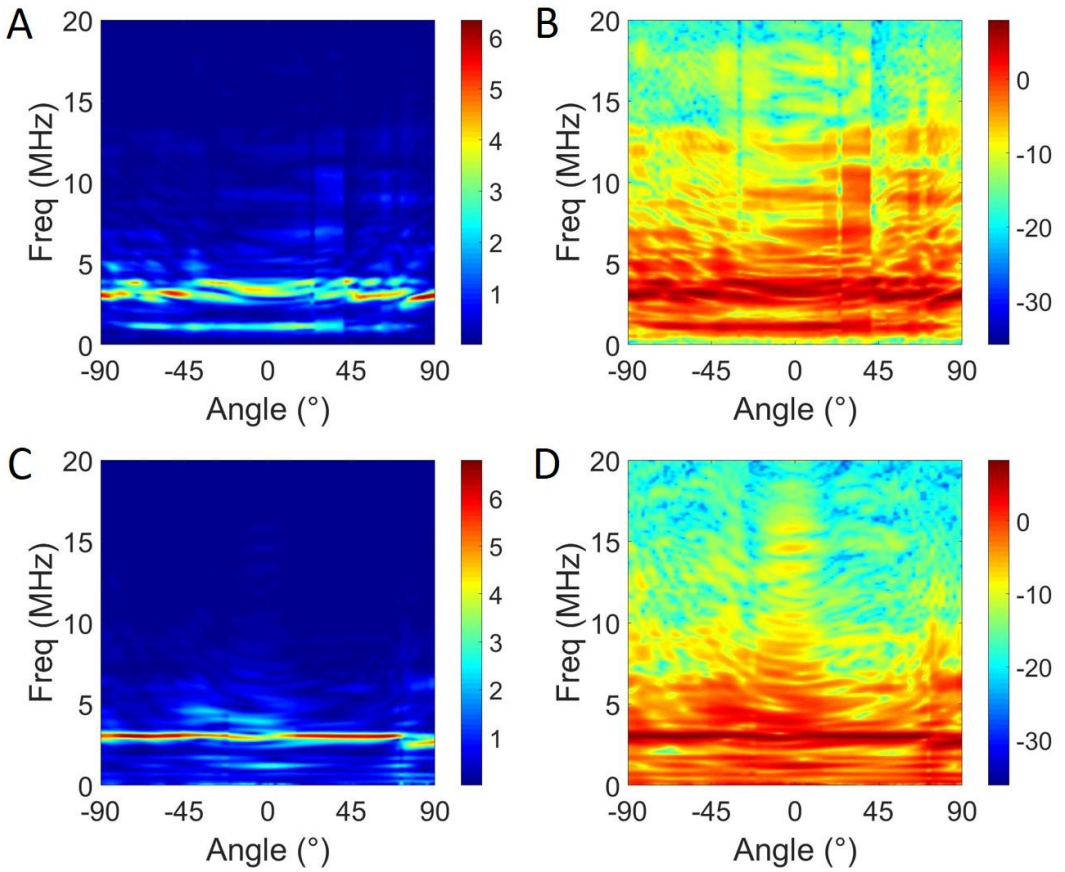

Figure 4.14 - Directivity plots. A) Linear response of 50% reflectivity FOH, B) Logarithmic response of 50% reflectivity FOH, C) Linear response of 80% reflectivity FOH, D) Logarithmic response of 80% reflectivity FOH.

Despite the low bandwidth, the directivity results show how the FOH have a substantially uniform response across a range of 180° (Figure 4.14, C and D). Within an angular range of -90° to +90° the response remains within 50% of the maximum for frequencies between 2.5 and 3.5 MHz. An omnidirectional angular response is advantageous in many applications such as photoacoustic tomography and phased array ultrasound imaging where the detection of acoustic waves from a distribution of sources is necessary to achieve high SNR images. Another application is in laser-scanning optical-resolution photoacoustic microscopy (OR-PAM) where detectors with large acoustic acceptance angles are needed to obtain an adequate field of view.

Figure 4.14 also shows that the response of the FOH was approximately symmetrical. There are some visible discrepancies which could be due to misalignments in the experimental setup or asymmetries in the parylene membranes and should be investigated further.

It was hoped to perform a study on how the thickness of the parylene membrane affected the NEP value of the FOH and probe the acoustic phase sensitivity of the

FOH, but unfortunately this was not possible. Gold coating parylene membranes less than 2 µm proved to have several issues. Parylene membranes of varying thicknesses (2, 1 and 0.5 µm) were deposited by SCS. Once returned and washed out all of the capillaries were placed in a gold coater and had a layer of gold deposited on the external surface of all the membranes. When the reflectivity values were inspected only the 2 µm membranes showed high finesse interference patterns. The thinner membranes were exposed to additional gold coating runs to try and increase their reflectivity values, but this did not improve the results. It is unclear why there would be such a difference in the reflectivity values for capillaries that were coated at the same time. Gold could be seen on the external surfaces of the membranes but when inspected by inserting fibres the interference patterns did not display any indication of high reflectivity coatings being present. Multiple fibres with varying coatings were also tried but none gave any indication of a highly reflective coating being present on the membranes. The in-house parylene membranes were able to be successfully gold coated with reflectivity values of 50 and 80%. Assuming that their lower NEP was a result of a thinner membrane then it suggests that the different deposition procedures are causing some sort of change in the parylene which is affecting the deposition of the gold on the membrane surface. Further work should be undertaken to investigate the surface interactions occurring. Potentially, SEM imaging could be performed to check if non-uniform gold deposition is occurring on the parylene-C surface.

4.8 Conclusion

High finesse parylene-C based extrinsic F-P style FOH were successfully created through the previously discussed parylene membrane fabrication method and the addition of gold deposition. This manufacturing method did not require the use of a cleanroom and has the potential to be a highly scalable procedure. It was found that the gold deposition was not always successful across different parylene batches and this aspect requires further investigation.

The FOH were characterised with an ultrasound transducer in a water bath setup and showed good ultrasound reception, even low finesse cavities with no gold coatings were capable of detecting ultrasound waves. The reflectivity of the deposited gold coating was increased to create a range of FOH with varying reflectivity values. The ITF of the optical cavities showed high finesse interference patterns (Airy function) which became more pronounced as the reflectivity values increased. The sharpening

of the Airy function peaks in turn lead to an increase in the optical phase sensitivity of the FOH.

The FOH were characterised and their NEP values were calculated. The NEP values showed how the parylene FOH could detect pressures an order of magnitude lower than similarly sized piezoelectric needle hydrophones. The NEP results also showed good comparison to other FOH found in literature. The optical phase sensitivity of the parylene based FOH was deemed to be inferior compared to some of the FOH found in literature. It was discussed that this could be due to the longer cavity lengths and lower reflectivity coatings in this work. The air filled parylene membrane cavities did however show a superior acoustic phase sensitivity when compared to FOH found in literature. Even with low optical phase sensitivity, the high acoustic phase sensitivity was able to overcome this to give a comparable overall acoustic response.

The bandwidth of the parylene FOH was low and was found to be between 2 and 4 MHz. The FOH were more receptive to lower frequencies (< 5 MHz). The cause of the reduced frequency response was thought to be due to the presence of edge waves forming and propagating in the surrounding fluid and across the membrane. The directivity response of the FOH was found to be substantially uniform despite displaying a complex response. The detected signal remained within 50% of the maximum over an angular range of -90° to +90°. Asymmetries were also noted and could be due to experimental misalignment or asymmetrical membranes.

Chapter 5 - Additional exemplar exploitations of high-resolution 3D printing for medical applications

5.1 Introduction

Most of the work outlined in this thesis utilises high-resolution 3D printing techniques for rapid manufacturing. In this chapter a more detailed view of the high-resolution 3D printing process is given and further examples of how it has been used for applications away from the parylene-C based pressure/temperature sensors and fibre optic hydrophones.

A detailed overview on high-resolution 3D printing is given in Chapter 2. To reiterate, high-resolution is being defined as that with resolution of 10 µm or less. The main printing process used in this work is direct write printing (DW). DW printing is a filament-based technique which allows many different types of materials to be printed such as hydrogels, polymers and nanoparticle composites. One of the main advantages is that it can be carried out at standard room temperatures and pressures without the need for a cleanroom environment. A schematic overview of the DW printing system used is shown in Figure 5.1.

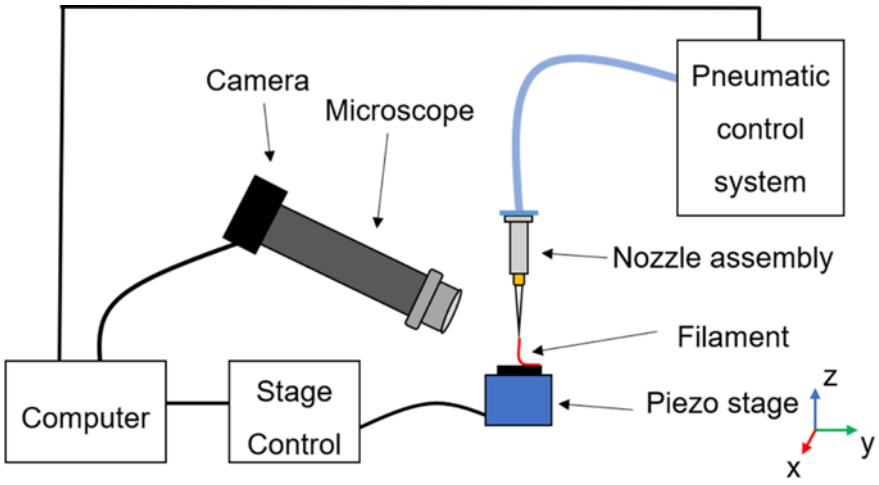

Figure 5.1 - Schematic diagram of the direct write high-resolution 3D printing system.

The bespoke DW printer used allows for precise control over each aspect of the system. Starting with the printing material/ink, these are designed in-house enabling control over material composition and solvent concentration (to modify evaporation rates if necessary). The pneumatic control system is used to extrude the chosen ink through microscale nozzles. The pneumatic control valve currently installed gives pressure control from 0.1 – 8 Bar but can easily be swapped for a valve with an alternate pressure range if necessary. The micronozzles themselves are manufactured in-house as well using a micropipette puller machine (Sutter P-1000). These can be difficult to produce repeatedly but allow control over nozzle size and nozzle taper. They can also be created with a thin filament in the lumen of the nozzle to aid with the ink wicking down to the tip. The piezoelectric stage and control modules have been integrated with a Labview script to enable computer control of the stage. The script enables printing patterns to be input as a series of x, y, z coordinates. The corresponding voltages are then applied, and the stage responds accordingly to create the printing pattern which was input.

5.1.1 Applications explored

Several different areas of high-resolution 3D printing were explored in this chapter along with their potential medical applications.

- A novel method to create microstructures of low storage modulus materials
- Printing directly onto the tip of optical fibres
- Printed photoacoustic microstructures to manipulate optically generated ultrasound fields

This work can be separated into two main parts; the development of novel fabrication printing techniques followed by investigating potential applications in the medical field.

For the development of printing techniques, a novel method to create microstructures of low storage modulus materials by using 3D printed micro moulds is presented. Using the DW printing setup and the micro moulding technique, the feasibility of printing directly onto the tip of optical fibres is then investigated.

The potential applications of these developments are then explored, in particular microscale acoustic holograms. Microscale acoustic holograms could be used to manipulate photoacoustically generated ultrasound beams and reduce the beam divergence of photoacoustic probes. The potential to print photoacoustic

microstructures directly onto optical fibres in order to manipulate optically generated ultrasound fields is discussed in the context of fetal medicine.

Based on the outlined clinical need in section 1.1.4, it was proposed to explore high-resolution 3D printing to manufacture miniaturised ultrasonic imaging probes. The high-resolution printing techniques could be used to deposit photoacoustic material directly onto the tips of optical fibres. Given the high-resolution of this manufacturing technique the material could be structured on the microscale and would not increase the diameter of the optical fibre. The paradigm of a focussed ultrasound beam was explored. Theoretically, higher resolution all optical ultrasound imaging can be achieved using a focussed beam. Typically, the generated ultrasound field diverges as the waves propagate away from the source. The angle of divergence tends to be larger for smaller sources (R. J. Colchester et al. 2019) presenting a problem for miniaturised probes. It would be interesting to reduce this divergence or achieve a focus. Possible structures for reducing this divergence are ultrasonic lenses and acoustic hologram structures.

5.2 Micro-moulding technique

A method of performing high-resolution 3D printing with low storage modulus materials was developed.

PDMS is a silicone with many uses from electrical insulation in microelectronics, to medical grade implants in the clinical field. It is also one of the most popular materials used in photoacoustic applications to improve the efficiency of generating ultrasound waves. The wide use of PDMS in photoacoustics is due to its high thermal expansion coefficient (3.1 x10^{-4}/K). Unfortunately, when it comes to 3D printing, PDMS is a difficult material to work with, and is not well suited for the requirements of the 3D printing process. The difficulty with printing with PDMS is due to the fact that PDMS has a low storage modulus (G') indicating low mechanical stiffness and rendering printed structures unstable until cured. The storage modulus of PDMS varies with temperature. As the temperature increases the polymer begins to crosslink and cure, causing G' to increase. If the PDMS can cure at room temperature, then the storage modulus will slowly increase with time as well. As the PDMS cures its viscosity increases, this in turn means that more pressure is required to extract the polymer through nozzles and clogging can easily occur. As mentioned in Chapter 2 solutions for printing low G' materials have been devised and include printing in a supportive gel-like medium or utilising sacrificial layers to embed soft materials around. These structures allow the PDMS to maintain its shape until the polymer is cured. These

solutions tend to be unable to print directly onto specific substrates and struggle to achieve high-resolution. The current solutions have only been able to structure PDMS on the millimetre/centimetre scale. To successfully print high-resolution 3D PDMS structures on the microscale, a new technique is required.

In general, to print different materials using DW high-resolution 3D printing there is a lengthy optimisation stage where the ink properties are refined in order to obtain stability and suitably high-resolution printed structures. By varying a single parameter, the whole optimisation phase must be repeated to strike the correct balance again. This re-optimisation is disadvantageous especially when 3D printing is being used to manufacture and test prototypes where parameters are often varied rapidly, and the manufacturing must keep up.

In order to overcome the limitations of printing with soft materials such as PDMS and to decouple the printing procedure from the material properties, microscale moulding was proposed. The idea is to use a soluble polymer to 3D print microscale moulds which can then be filled with the desired material, cured and the surrounding scaffold can be washed away. The main steps of this process are illustrated schematically in **Error! Reference source not found.**.

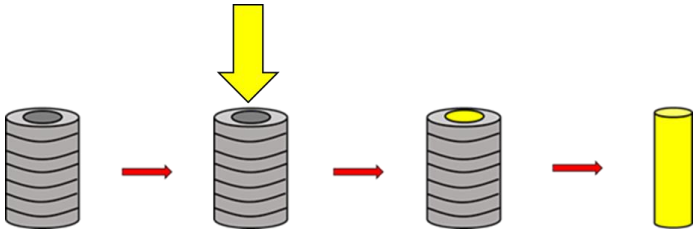

Figure 5.2 - Schematic diagram of the micro moulding technique.

The micro moulding technique reduces the amount of optimisation cycles required. Once a suitable soluble polymer ink is developed and can be printed at the desired scale then printed hollow structures can be created. These can then be filled with any material that can flow through a micro-nozzle. The filling material properties can then be adjusted and modified as needed while remaining easy to prototype microstructures with.

5.2.1 Method

This approach utilised a water-soluble polymer, polyvinylpyrrolidone (PVP), as the material for printing the hollow moulds. As PVP is soluble in water and polar solvents, the moulds could be filled with any material avoiding these. A variety of PVP was purchased from Sigma-Aldrich with different molecular weights. The molecular

weights ranged from 20,000 to 360,000. The different PVPs were initially dissolved in DI water at 30% by weight. The samples were dissolved in 20ml glass vials with PTFE caps and had approximate total volumes of 10 ml. These samples were left on a magnetic stirrer to dissolve at room temperature. Once they appeared homogeneously dissolved the samples were tested in the DW printing setup to determine the printability of each and begin to optimise for a water soluble printing material. The printability was assessed by performing a printing test. The printing test comprised of a 2D step and a 3D step. The 2D resolution of the printing was initially tested before expanding to the 3D structuring and resolution of the printing. The 2D part of the printing test was coded for to print a snaking raster pattern and the 3D part was designed to print multiple straight line passes to build up a wall structure. Combinations that showed potential were then used to try and print 3D circular column microstructures. It should be noted that since high-resolution printing was the goal, nozzle sizes of 10 µm or less were used for all printing tests. The printing tests were also carried out with a glass substrate. The substrate used were untreated glass microscope slides. The glass microscope slides provided a suitable substrate with reliable wettability and surface energy properties. In order to perform the printing tests, the PVP samples had to be loaded into the printing system. A 1ml syringe was used to extract 1ml of PVP sample from their glass vial. This was then transferred to a syringe barrel (Nordson EFD Optimum). The complementary piston was inserted into the back of the syringe barrel and pushed to move the PVP sample to the extraction tip, ensuring that no air bubbles remained in the sample. For more viscous samples, a settling period was required to eliminate all air bubbles. A suitable nozzle (manufactured in-house) was then attached to the extraction tip and the loaded barrel/nozzle system was mounted into the printing system and the pressure control connected to the back of the barrel. The pressure control was used to force the piston downwards and move the ink through the nozzle to the tip where it was extracted for printing. The pressure applied had to be carefully increased to prevent uncontrollable extraction. More viscous samples required higher pressures to be applied.

The initial tests indicated that a relatively high molecular weight of 360k was best suited for printing with. Using this molecular weight of PVP further samples were created by dissolving PVP in DI water at varying concentrations. The concentrations varied from 10 to 30% by weight. Again, each was assessed using the 2D and 3D printing tests. At this point of the process more rigorous optimisation was performed as each sample displayed varying degrees of successful printing. Many printing variables were investigated during optimisation such as the use of ethanol to alter the

evaporation rate and the addition of sucrose to try and increase the viscosity without increasing the strand formation to help with 3D structuring. It was noted that differences between batches of the same composition arose dependent on the length of time they spent stirring on the hotplates and with the age of the samples. Initially the addition of sucrose was observed to improve the printability of the ink but after further testing it was established that it in fact reduced the reproducibility of printing.

To ensure that the polymer compositions remained soluble in water, samples were initially tested on the macroscale. A droplet of polymer sample was extracted using a pipette and drop cast onto a glass microscope slide. The droplet was allowed to cure to form a polymer film. The cured sample was then submerged in DI water and at this scale it was clear if it was readily dissolvable. Any sample compositions that failed this test were removed from the optimisation process.

Due to the choice of PVP as the printing polymer PDMS could be introduced to printed structures without dissolving or damaging the printed mould. This was ensured by examining filled moulds with an optical microscope. It should be noted that adding too much PDMS so that the printed structure becomes encapsulated can occur and prevent the mould from being removed. To avoid this, a high level of control over the filling process for the micro-moulds was required. The filling process was very similar to the printing process. The 2 part PDMS was mixed in a ratio of 10:1 of monomer to crosslinker and degassed to remove air bubbles. 1ml was then loaded into a syringe barrel and a complementary piston inserted behind it. The piston and PDMS were pushed to the top of the barrel to remove air pockets and a fine nozzle of 2 to 5 µm was attached. The loaded nozzle was mounted into the printing setup and had the pneumatic pressure controller connected. The pressure controller was then used to precisely control the depositing of the PDMS into mould structures.

By decoupling the printing process and the material properties, microscale PDMS structures could be created outside a cleanroom environment while also avoiding harsh chemicals.

5.3 Printing on optical fibres

To fully utilise the micro moulding fabrication technique, the ability to print on a variety of substrates is required. Printing on optical fibres is proposed as there is great potential for further developments and integration of optic/photonic devices through 3D printing at the tip of optical fibres. The initial high-resolution 3D printing in this work was performed on a substrate of glass microscope slides. The glass slide was an

initial substrate to enable the processes to be refined before transferring the processes to printing on optical fibres.

For fibre optic sensing, many of the sensors are composed of extrinsic sensing elements located at the tip of the fibre which usually increase the overall dimensions. By 3D printing directly onto the fibre tip these types of sensing elements could be manufactured directly on the fibres without increasing the overall dimensions. A procedure such as this would also remove the need for fibre integration in the manufacturing process.

In laser generated ultrasound applications, dip coating photoacoustic materials directly onto the tips of fibres has proven to be a successful method of efficiently creating optical ultrasound emitting probes. The ability to 3D print such material directly onto the tips of fibres opens the door to manipulating the generated waves to create focussing or steering of the beam through appropriate microstructures. Such structures can induce interference patterns between the generated waves which result in the desired beam manipulations. These beam manipulating structures will be discussed in more detail later in this chapter, but examples of such structures (termed acoustic holograms) have been shown on the centimetre scale previously. Through the printing techniques outlined here acoustic holograms could be investigated on the microscale and potentially integrated directly onto optical fibres.

Manufacturing directly at the tip of optical fibres has the potential to help further miniaturise fibre optic devices and streamline the integration of fibres during manufacturing. Techniques such as lithography could potentially be used to pattern directly onto the fibre, but printing has shown the most potential. Recent work has shown that the Nanoscribe 2-photon polymerisation printing system can be used to print directly onto optical fibres (Kim et al. 2020). The limitations of using a 2-photon polymerisation system are the high associated costs and that the choice of print material is very limited. The material must be a highly IR transparent photoresist. The photoresist requirements also limit the inclusion of additional functional particles within the material. The strict material requirements limit the functional microstructures which can be created with this technique.

In order to print a large array of materials on the tip of optical fibres an alternative method is required. One solution is to implement the high-resolution micro moulding technique. Implementing this is discussed further.

5.3.1 Method

To print on optical fibres, they initially needed to be cleaved. The cleaved areas then needed to be polished to ensure the surface was suitably flat for printing on. Using varying grades of sandpaper from 30 to 0.02 µm, the surface of the fibre was gradually improved until suitably smooth surfaces were obtained for printing on. The polishing process was a time-consuming but proved to be effective, nonetheless. In order to achieve printing on the tips of fibres, the printing setup required modification. An optical fibre mount (Thorlabs) was integrated onto the piezoelectric nano positioning stage. This adaption is shown in Figure 5.3. The stage had a clearance hole in the middle of it which coupled well with the optical fibre mount to enable large sections of fibre to be securely held in place.

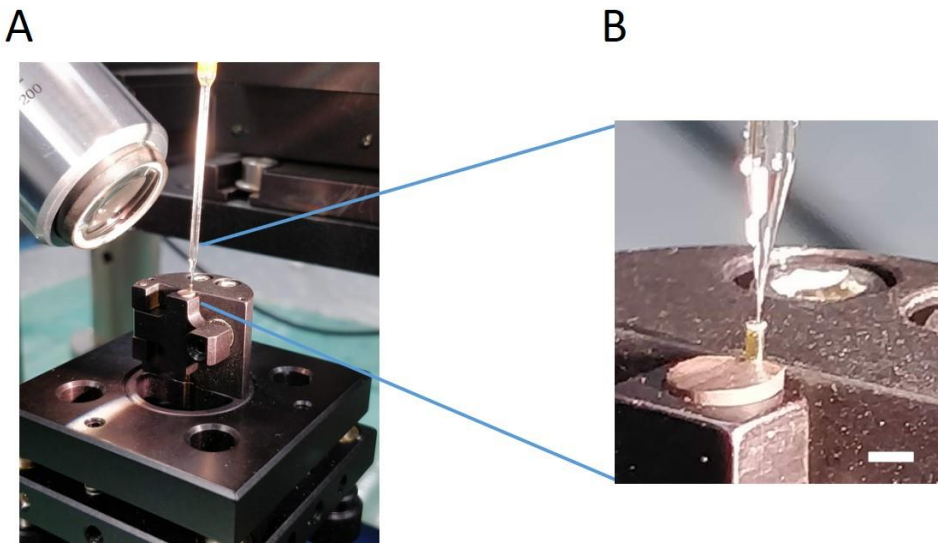

Figure 5.3 - Photographs of the printing setup with integrated optical fibre mount. A) Wide view, B) Zoom in on the fibre/nozzle alignment, scalebar is 1 mm.

Once polished and mounted into the 3D printing setup the next step was to align the printing nozzle above the fibre. This alignment required intricate manipulation of the nozzle and fibre. The alignment process had to mainly be carried out by eye as the field of view of the imaging system associated with the printer had a small field of view to achieve the appropriate magnification required for observing the printing process. It was found that the best technique was to focus the imaging system at the polished surface of the fibre and bring it into view, then raise it to a few hundred microns above the fibre surface. Then by roughly aligning the nozzle by eye, it could be lowered and translated across the field of view of the imaging system until it was identified in the imaging system field of view. Once identified in the imaging system, the nozzle was lowered in line with the microscope system until the nozzle and fibre surface were in

the same imaging frame. Once the fibre and nozzle were aligned, the start position of the printing nozzle had to be carefully chosen. With only a single viewing angle, deciding on the starting position to begin printing from was problematic. In several cases the start position was wrong and resulted in the printed structure extending off the side or not being correctly aligned with the central axis of the fibre. The most efficient way of determining the start position was to use print patterns that started on the outer edge of the fibre surface. The nozzle was then positioned so that a gap between the fibre surface and the nozzle was maintained. The nozzle tip was viewed along with its associated reflection in the polished fibre surface. A test run of the printing pattern was then be performed to see if the alignment was correct. By starting the print pattern at the outer edge/largest diameter it was possible to ensure that the alignment was appropriate to fit the entire structure on the fibre surface and using a symmetric test pattern enabled the optimum start position to be located. By performing test runs like this the relative flatness of the fibre alignment was also optimised by using the levelling knobs on the optical fibre mount to adjust the levelling. Using the imaging system lines were drawn/overlaid on the fibre and nozzle scene, and by running test programs of the printing pattern it could be seen if the gap between the fibre and nozzle remained constant over the entire print region, indicating relative flatness for printing. The method and alignment described here was initially done with large 900 µm fibres to get a feel for the system and optimise the process. After practise, it was then possible to move to smaller diameter 400 µm fibres. Despite difficulties in alignment, printing on fibres was still possible both with standard DW printing inks and with the micro moulding technique.

5.4 Photoacoustic microstructures

Photoacoustic materials are those with the appropriate combination of optical absorption and thermal expansion to generate acoustic waves when exposed to laser pulses. The principles of photoacoustics are covered in Chapter 2. In this work the photoacoustic material is structured using the micro-moulding 3D printing technique to create microstructures capable of generating acoustic waves photoacoustically when exposed to appropriate laser pulses.

For photoacoustic materials, combining the chosen optical absorber with a suitable polymer is important for efficiently generating optical ultrasound. The pressure of the generated ultrasound (p) is proportional to its optical absorption (μ_a) and its Grüneisen parameter (Γ).

$$p \propto \mu_a \Gamma, \quad \Gamma = {\beta {v_s}^2}/{C_p}$$

(5.1)

where β is the volume thermal expansion coefficient, v_s is the speed of sound in the material and C_p is the specific heat capacity at constant pressure. Polydimethylsiloxane (PDMS) has a high thermal expansion coefficient of 3.1 x10^{-4}/K compared to other polymers, such as polyurethane which as a thermal expansion coefficient of 0.57 x10^{-4}/K. Meaning that if the optical absorption remains constant, by selecting PDMS instead of polyurethane, greater pressure ultrasound waves can be generated photoacoustically. Based on this heightened thermal expansion coefficient and previous literature, PDMS was selected as the polymer of choice for this work.

Gold nanoparticles are known to be good optical absorbers. They are good optical absorbers because surface plasmons are localised around the particles which strongly absorb at a resonant wavelength (Hou et al. 2006). The wavelength dependence of the absorption leads to the concept of multiple functionalities. One wavelength which is absorbed strongly could be used to generate ultrasound waves and a second wavelength, which is away from resonance, could be passed through the absorbing layer to perform additional functions.

5.4.1 Method

As discussed in section 2.5.4, a facile method of embedding gold nanoparticles into PDMS structures is reported by Goyal *et al.* (Goyal et al. 2009). By submerging cured Sylgard PDMS into a gold salt solution the platinum curing agent in the Sylgard PDMS catalyses the chemical reduction of the gold salt *in situ* to give gold nanoparticles, which embed themselves into the PDMS structure. This technique is a promising method of creating gold nanoparticle-PDMS composites as further demonstrated by Noimark *et al.* (Noimark et al. 2018).

In this work the micro-moulding technique was utilised to create 3D printed microstructures of PDMS in acoustic hologram patterns capable of manipulating generated ultrasound fields. The cured transparent PDMS structures then had gold nanoparticles embedded in them to induce optical absorption and create photoacoustic properties.

To start, the appropriate radii for a concentric ring structure capable of focusing gnereated ultrasound were calculated according to Equation (2.10). These radii varied from 58 to 148 µm. A print code to create the required concentric ring pattern

was generated. The print code included multiple passes in order to create multiple layers and give height to the mould, so that it could contain the low storage modulus filling material. The optimised PVP solution for printing was then loaded into a syringe barrel with an accompanying 10 µm nozzle. The concentric ring acoustic hologram pattern was then printed onto a glass substrate.

The resultant 3D concentric ring structure (shown in Figure 5.5) was then allowed to fully solidify before being filled with Sylgard 184 PDMS. The monomer and the curing agent were mixed with a 10:1 ratio as instructed and then degassed in a vacuum chamber to ensure there were no air bubbles. Finer 2-5 µm nozzles were fabricated and used to precisely deposit the PDMS into the printed mould. Only every other gap between the concentric rings was filled, starting with the central area, to create a distinct pattern of PDMS and no PDMS regions in the structure. This filling pattern is illustrated in Figure 5.4**Error! Reference source not found.**. To ensure precise filling t he nozzle was aligned above the printed mould using similar alignment techniques as described in section 5.3.1. Once in position above the desired mould region the pressure was gradually increased with the pressure controller until a slow, steady and controllable flow of PDMS was achieved. This required a reduced pressure than the printing process. Care was taken to carry out the mould filling is a precise manner, but this also had to be performed quickly as the PDMS slowly begins to cure at room temperature once the 2 parts are mixed. As the PDMS cures the viscosity of the polymer increases. Therefore, the mould filling needed to be completed within this optimum viscosity window.

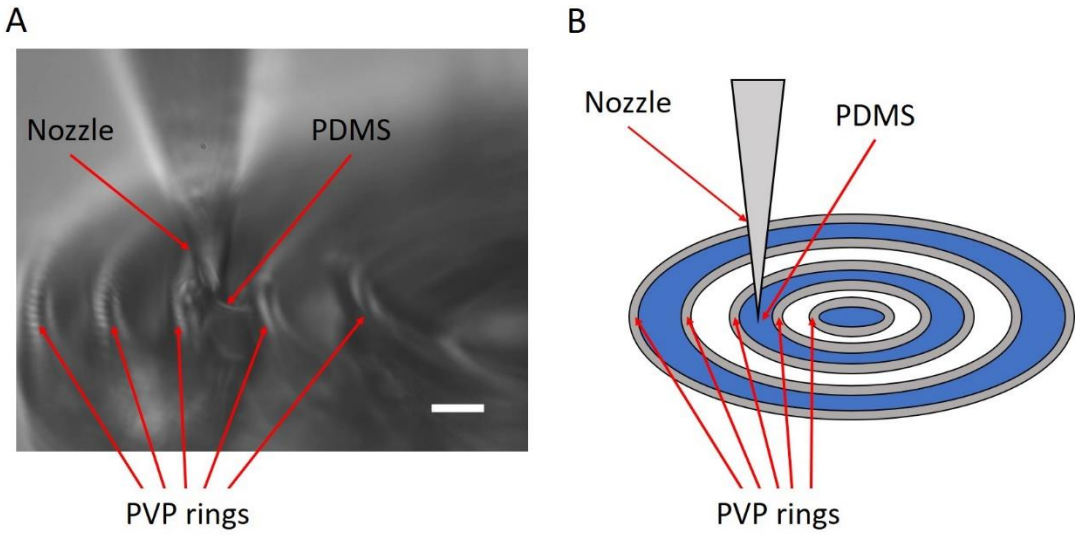

Figure 5.4 – A) microscope image of PDMS being filled into the printed concentric ring mould, B) Schematic diagram of the filling process. Scalebar is 10 µm.

Once each of the required regions of the micro mould were filled with PDMS, the mould was carefully placed in an oven at 100 °C for 35 minutes so that the PDMS completely cured. The PDMS had to be completely cured otherwise damage to the structure or complete removal would occur during the PVP dissolving stage. Once cured the surrounding PVP scaffold could be washed away. By placing a few drops of DI water onto the entire structure the PVP quickly dissolved, leaving behind only the cured PDMS microstructure rings.

Several investigations were made to try and disperse carbon black into PDMS to (create optical absorption for photoacoustic applications) before depositing it into the mould. Dispersing carbon black in PDMS had limited success as only very small percentages of carbon black could be dispersed before large agglomerates formed. These agglomerates then blocked to nozzle and prevented to flow from the nozzle required to fill the mould. Instead, gold nanoparticle-PDMS composites were used to induce photoacoustic properties into the structure. The gold nanoparticle-PDMS composite was formed by utilising the procedure outlined by Goyal *et al.* (Goyal et al. 2009).

The moulded PDMS rings (which were cured and had the PVP scaffold removed) were submerged in a gold salt solution to embed gold nanoparticles. A solution of gold salt was prepared by adding 0.5% gold(III) chloride trihydrate (Sigma Aldrich) to ethanol by weight. The solution was stirred for 12 hours to ensure full dissolution. The PDMS microstructures were then submerged in the gold salt solution for 24 hours resulting in an AuNP-PDMS composite. During this time, the gold salt is reduced to give gold nanoparticles *in situ* which penetrate into the surface of the PDMS structure and embed themselves in a top-down manner. It is believed that the platinum crosslinker specifically in the Sylgard PDMS catalyses the reduction of the gold salt resulting in the formation of gold nanoparticles (Ahmed et al. 2017; Noimark et al. 2018). After 24 hours the samples were removed from the gold salt solution. The previously transparent PDMS rings now appeared pink/purple due to the presence of gold nanoparticles.

5.5 Results/discussion

The micro moulding technique, printing on optical fibres and the resulting printed microstructures are discussed below.

Through the printing optimisation process it was determined that an ink of 20% PVP (360k) to deionised water, by weight, was the optimum ink for printing high-resolution

micro moulds with a 10 µm diameter nozzle. For larger nozzles an increased PVP concentration of 30% was necessary. It was also found that the solutions performed best when they were allowed to mix on a magnetic stirrer for 6 days at room temperature. It is believed that this extended dissolution stage ensures that the PVP is completely dissolved, and the ink is homogeneous. The lengthy stirring phase was time consuming but created good homogeneity and allowed heightened repeatability in printing results.

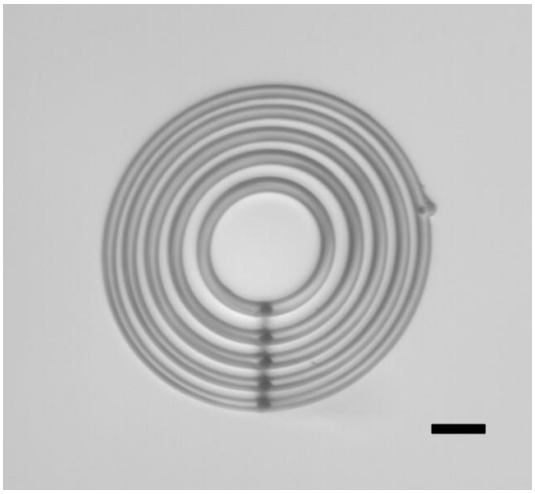

Figure 5.5 - Microscope image of concentric 3D rings printed with PVP to mould designs. Scalebar is 50 µm.

A concentric ring structure of varying radii from 58 to 148 µm was designed in keeping with the range of the printing stage (< 300 µm) and conforming to the required radii, calculated from Equation (2.10 for a focussing acoustic hologram. This structure was then coded for and printed with the 20% PVP ink and accompanying 10 µm nozzle. The rings were structured with multiple layers to give them height and enable them to contain filling materials as required for micro moulding. An image of the printed ring micro-mould structure is included in Figure 5.5.

The same 20% PVP ink and micro moulding technique was also used to create more 3D structured designs. This technique can be used to create many different 3D shapes and structures. As the PVP ink was optimised for these printing conditions it is simply dependent on generating code for the desired design. To demonstrate the capabilities of this technique a microscale hourglass shape was printed. This structure not only shows how parameters in the x-y plane can be varied, but also shows how they can be adjusted within each layer in the z-direction as well.

Figure 5.6 shows different aspects of the hourglass structure. Figure 5.6 A shows the unfilled printed PVP mould. Figure 5.6 B shows an SEM image of the final moulded PDMS microstructure from a 75° viewing angle. From this angle the smooth finish on

the top where the meniscus of the PDMS formed is seen. A steeper viewing angle was not possible with the SEM setup available. The 75° view creates the appearance that the top and bottom portions of the structure are not equal in size, but this is an artifact. Figure 5.6 C shows a closer view of the moulded PDMS microstructure. It can be seen from this how the layers of the printed mould have left a slight imprint in the moulded PDMS creating a small ribbed effect in the walls.

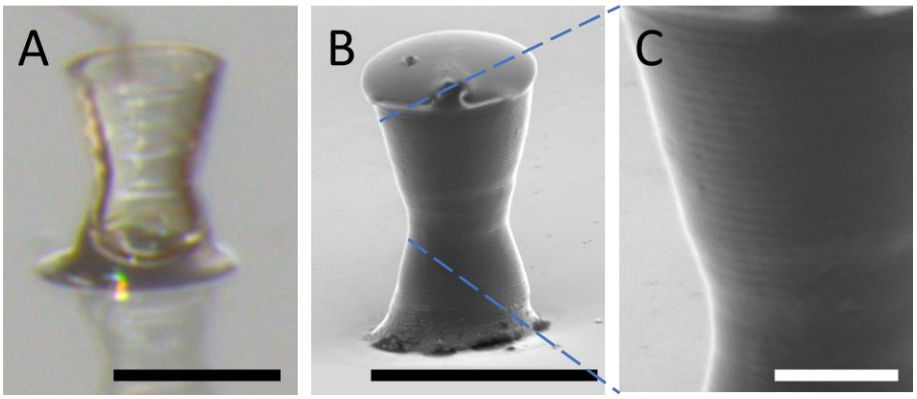

Figure 5.6 - A) Optical microscope image of a printed PVP hourglass shaped mould, scale bar 50 µm. B) SEM image of the PDMS hourglass structure resulting from the micro moulding technique. The SEM shows the structure viewed from a 75° angle, scale bar 50 µm. C) A closer view of the structure highlighting the ribbed imprint on the walls due to the layers of the mould, scale bar 10 µm.

Despite requiring optimisation of the mould printing to achieve these results, the process now enables a range of different materials to be structured on the microscale without the need to cycle through optimisation steps again. Provided the material can flow to take the shape of the printed PVP mould it can be structured into many different patterns. Some initial studies into filling micro moulds with multiple materials have also proven to be successful. Column shaped moulds were printed and partially filled with PDMS then cured. The remainder of the mould was then filled with a silver nanoparticle ink, following the same procedure as filling with PDMS, and sintered. Once the PVP supporting scaffold was washed away, PDMS columns with reflective silver tops remained. This highlights the ability of the micro mould technique to be easily used to prototype multi-material designs.

The micro-moulding printing technique was then expanded to create application driven acoustic hologram photoacoustic structures. Utilising the printed micro mould design shown in Figure 5.5, this was filled as described in section 5.4.1 with PDMS and once cured the mould was washed away using DI water. The cured concentric ring PDMS microstructure was then submerged in a gold salt solution as described in section 5.4.1 to embed gold nanoparticles, and hence optical absorption, into the microstructure. After 24 hours this process was complete, and the resulting structures

can be seen in Figure 5.7. The previously transparent PDMS rings now appeared pink/purple due to the presence of the gold nanoparticles.

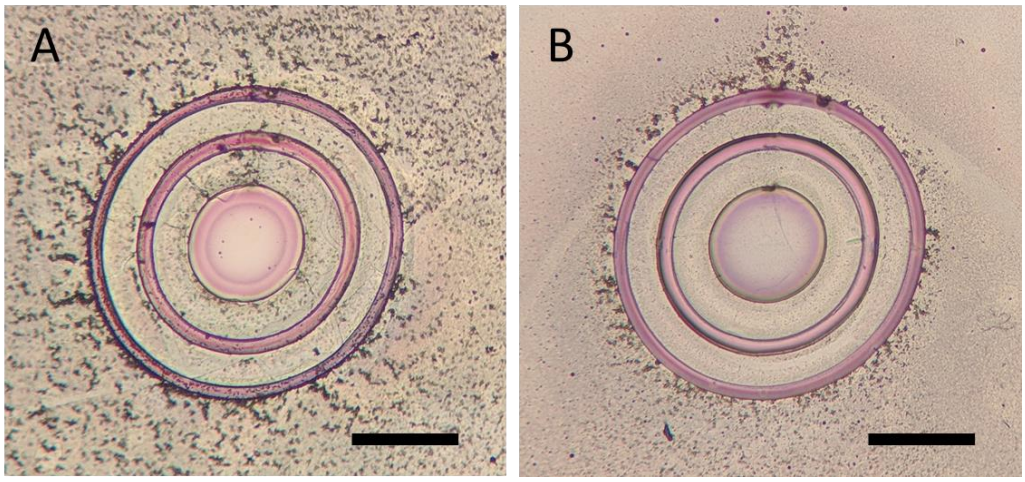

Figure 5.7 - Microscope images of the micro moulded PDMS rings after 24 hours in the gold salt solution. The colour is due to the embedded gold nanoparticles. All scale bars are 100 µm.

As visible in Figure 5.7 the micro moulding technique is able to be used to successfully print microscale designs. By embedding the gold nanoparticles, the PDMS structures have become optically absorbing. The combination of optical absorption from the gold nanoparticles and the high thermal expansion of the PDMS results in a composite material that is theoretically highly photoacoustic. Further imaging of the rings was performed using 3D microscopy to better analyse the resultant microstructures and assess the micro moulding technique. The rings were printed to have heights of approximately 15 µm. From Figure 5.8, acquired with a 3D microscope, the height of the rings is visible. The height of the rings was measured and was found to be approximately 12 µm. Care was taken not to overfill the PVP moulds as this would encapsulate the structure and prevent the wash away of the scaffold. This caution accounts for the slight deviation between printed mould and final moulded structure.

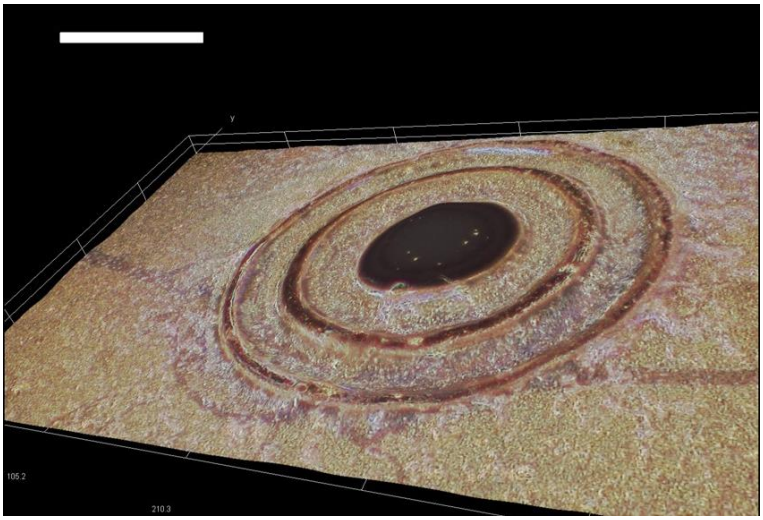

Figure 5.8 - 3D microscope image of the gold nanoparticle-PDMS composite rings. The heights of the rings are approximately 12 µm. Scalebar is 100 µm.

The design of the concentric ring microstructure was such that it conformed to the requirements outlined in Equation (2.10 to create an acoustic hologram. Theoretically the design should enable a reduction in the divergence of a generated ultrasound beam from this structure. Some basic simulations of the 3D printed gold nanoparticle-PDMS acoustic hologram structures, printed in this work, have been carried out using a Matlab toolbox called k-Wave. The preliminary test was performed to simulate the acoustic response of the printed gold nanoparticle-PDMS structures. The simulation used the same concentric ring geometry as the printed structures. Ultrasound sources were positioned at the ring locations to re-create the acoustic wave pattern of the laser generated ultrasound waves from the optically absorbing regions. When allowed to propagate the waves constructively and destructively interfered with each other as expected.

A focussing effect of the ultrasound is seen between 100 and 150 µm from the surface of the hologram structure (indicated by white dashed box) in Figure 5.9. This distance is as expected from the calculated radii of the design. The short focal length is due to the dimensional constraints of the printing setup which is optimised for printing onto the tip of optical fibres and therefore has a range of 300 µm in x, y and z directions. To ensure that the hologram design could be directly transitioned to the tip of an optical fibre once characterised the radii were kept to less than 300 µm which led to a shorter focal length due to the current print resolution. The k-wave simulation agrees with theory and highlights that even with a reduced number of concentric rings, the acoustic hologram design should still be capable of reducing the divergence of an ultrasound beam on the microscale.

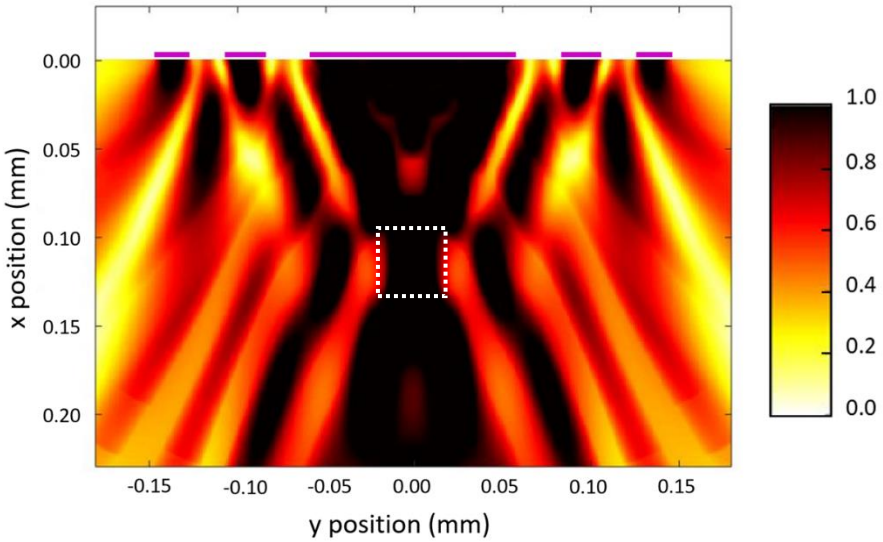

Figure 5.9 - Simulated acoustic response of the gold nanoparticle-PDMS ring structure. The shown results are for the central cut through of the structure.

Previous work has reported that gold nanoparticles synthesised in this way will strongly absorb light at a wavelength of 532 nm (Noimark et al. 2017). At wavelengths away from this resonance the light will not be as strongly absorbed and will be able to travel through the structure. In this configuration laser pulses of 532 nm could be used to generate ultrasound waves with a reduced divergence for imaging, whilst those at 1064 nm would be largely transmitted and could be used for functional photoacoustic sensing to enhance structural ultrasound images. Transmitted pulses could also be used to perform therapeutic laser treatments. To cite one example in the field of fetal medicine, in the treatment of twin-twin transfusion syndrome (TTTS) where anastomoses on the placenta need to be identified and coagulated a single multi-capability probe with such a design could be used to identify anastomoses with ultrasound imaging and coagulate them with transmitted laser pulses. In this example

the highly miniaturised size of such a probe would also be beneficial as it would reduce the risk of iPPROM since this risk is related to the size and number of operating ports.

The ability to directly print onto the tips of optical fibres has also been demonstrated in this work. Using the described printing set up, an optical fibre of diameter 900 µm was mounted to the stage and aligned with the nozzle for printing. A 2D microstructure was successfully printed onto the end of the fibre using a CB-polyurethane ink (Figure 5.10). The structure was a snaking pattern of lines and covered the majority of the piezoelectric stages range of motion, giving it dimensions of 225 x 225 µm. The fibre was cleaved by hand due to its size resulting in a visible chip. The surface was not polished post cleave but the surface was flat enough over the required range to perform printing.

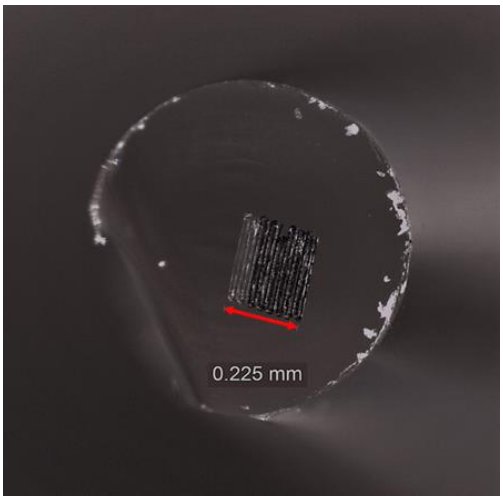

Figure 5.10 - Microscope image of a 2D microstructure printed on the tip of an optical fibre using CB-Polyurethane ink.

Some further example structures printed on fibres are shown in Figure 5.11. The fibre used in Figure 5.11 A) was not polished and the roughness can be seen in the image. Despite the unevenness of the surface, small columns with a diameter of 35 µm were possible as the surface was relatively uniform over this small range. For larger structures spanning a greater proportion of the fibre surface, polishing of the fibre surface was essential for successful prints. In Figure 5.11 D) a series of rings were printed covering a large proportion of the fibre surface. As mentioned previously correctly aligning the nozzle over the fibre with a single viewing angle sometimes resulted in a misalignment between the structures and the central axis of the fibre, as also shown in Figure 5.11 D).

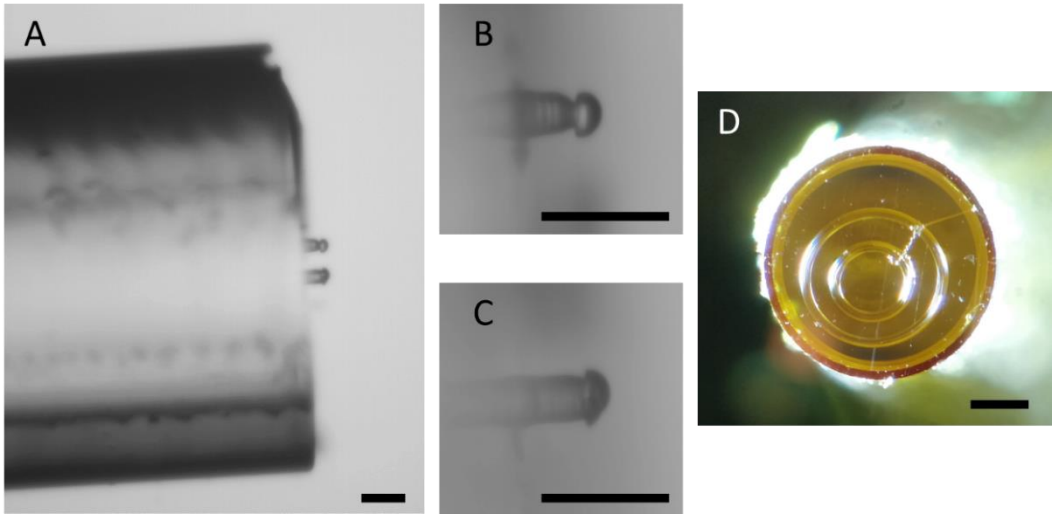

Figure 5.11 - Selection of microscope images showing structures printed on the tip of optical fibres. A), B) and C) Micro moulded columns, D) Acoustic hologram rings. All scale bars are 100 µm.

Despite the difficulties associated with alignment of the optical fibre and printing nozzle, the outlined technique has great potential for fabricating advanced all optical ultrasound probes.

5.6 Conclusions

The following conclusions can be drawn from the works outlined in this chapter. DW high-resolution 3D printing was used to deposit inks and create patterned microstructures on glass substrates and at the tip of optical fibres. This technique to directly print onto the tip of optical fibres has many potential applications for the development and integration of optic/photonic devices.

An alternative printing technique was developed to overcome the lengthy optimisation period associated with directly printing materials in a DW setup. Through this novel microscale moulding technique, the use of many more materials became possible. The material and the printing process were decoupled. Materials with a low storage modulus which could not be printed directly could now be utilised and structured on the microscale. A PVP based water soluble ink of 20% was created to 3D print high-resolution micro moulds, to be filled. These were filled with PDMS, a soft and low storage modulus material that has previously been difficult to structure on the microscale. Once filled and cured the moulds were washed away leaving only the desired PDMS inner material. It was shown how this printing technique could be used to create many shapes and patterns such as rings, columns and hourglass microstructures.

Printed PDMS microstructures were treated to create composite gold nanoparticle-PDMS microstructures. The composite material was achieved by taking advantage of a method developed by Goyal *et al.* (Goyal et al. 2009). The micro moulded PDMS microstructures were submerged in a gold salt solution where the gold salt was reduced *in situ* to give gold nanoparticles which embedded themselves into the PDMS in a top-down fashion. The high thermal expansion of the PDMS combined with the high optical absorption of the gold nanoparticles, at 532 nm, provides a theoretically efficient photoacoustic material. By utilising the micro moulding technique photoacoustic microstructures were developed. The structuring provided by this printing technique offers the ability to pattern such photoacoustic materials in a manner so as to manipulate the generated ultrasound field. By taking advantage of structures such as acoustic holograms, the divergence of a photoacoustically generated ultrasound beam could be reduced.

The skills and technologies developed through the high-resolution 3D DW printing and micro moulding techniques enable precise deposition and structuring of a wide range of materials including those with low storage modulus.

Chapter 6 - Conclusions and Future Outlook

6.1 Conclusions

During the course of my doctoral research novel imaging and sensing devices to aid minimally invasive surgery were created through the development of high-resolution 3D printing techniques. These were, miniaturised parylene based fibre optic pressure sensors for physiological measurements, miniaturised parylene based fibre optic hydrophones for ultrasound detection and microscale acoustic hologram structures for focussing optically generated ultrasound beams. The development of innovative manufacturing processes such as printing directly onto optical fibres, micro moulding and microinjection enabled the creation of such devices. The stages of fabrication, optimisation and characterisation of these microfabricated devices were detailed in this thesis.

6.1.1 Printing

A high-resolution 3D printing using a DW printing technique was demonstrated. The printing setup was adapted to include the ability to print directly onto the tips of optical fibres. Microstructures were deposited on the tips of optical fibres. Developing and optimising inks for DW printing is known to be a complex and lengthy process. Following this, a novel approach to high-resolution 3D printing soft materials was revealed in Chapter 5. The goal was to decouple the chosen material from the printing process to enable more rapid production and reduce the need for excessive optimisation steps. The development of a micro moulding technique enabled this and allowed previously unprintable materials to be deposited and structured using high-resolution 3D printing technology. The technique used a water soluble 20% PVP (360k) ink to print high-resolution hollow structures which were then filled with chosen materials. Advantages of the printing process are the lack of a required cleanroom, performed at standard temperature and pressures, and the reduced optimisation time required. The procedure was carried out on multiple substrates including printing directly onto the tips of optical fibres. Utilising the micro moulding technique, a variety of structures such as rings, columns and hourglass shapes were printed with the overarching goal of creating high-resolution 3D microstructures. The microstructures

were moulded in PDMS, a soft material which had previously been difficult to print due to its low storage modulus. As a fabrication technique, the developed micro-moulding strategy adds an additional manufacturing method to the short list of techniques for bespoke structuring low storage modulus materials on the microscale. It builds upon the previous work in the field whereby sacrificial layers and printing in supportive gel mediums have been used to structure such low storage modulus materials (Bhattacharjee, Steven M Zehnder, et al. 2015; Hinton et al. 2016; Miller et al. 2012) Additionally, by utilising the catalysing properties of the Sylgard PDMS crosslinker, gold nanoparticles could be embedded into the microstructures to create composite materials. The ability to print and shape photoacoustic microstructures enables the development of optical/photonic sensors. By printing these directly onto the tips of optical fibres these microstructure devices can easily be integrated for use across many different optical fibre based applications. The technique outlined in this work builds upon previous literature and adds a flexibility to the material choice which is a drawback to photo-polymerisation based printing on fibres (Kim et al. 2020). The micro moulding fabrication technique could be used in other fields, such as microfluidics or flexible electronics, to rapidly structure PDMS or other low storage modulus materials on the microscale.

The main contributions from this area of work are the development of a novel microfabrication technique to structure low storage modulus materials on the microscale, and the ability to perform high-resolution printing on the tips of optical fibres.

6.1.2 Parylene pressure sensors

A process for precise fabrication of free-standing parylene-C membranes at the tips of glass microcapillaries was developed. This manufacturing technique embodied components of the high-resolution 3D printing techniques and allowed for novel parylene based, extrinsic F-P fibre optic pressure sensors to be produced (Chapter 3). The fabrication process did not require the use of a cleanroom and will be highly scalable through further automation, thanks to the highly repeatable printing techniques and large batch CVD coating. The sensors were designed to be compatible with integration into medical equipment such as needles, catheters and guidewires for physiological pressure monitoring. The novel manufacturing process was deployed to create deformable curved parylene-C membranes of varying thicknesses (0.5 – 3 µm) at the tip of capillaries. The resultant membranes provided extrinsic sensing elements to be integrated with optical fibres. The constructed interferometric fibre optic sensors had an air-filled cavity which was interrogated using

an LCI setup. The performance of the sensors was tested using a bench top simulation setup of intravascular pressure conditions. The sensors showed good sensitivity (0.15 radians/mmHg for 0.5 µm thick membranes) to clinically relevant arterial pressure waveforms. It was found that the sensitivity was dependent on the thickness of the deformable parylene membrane, which was expected from the theoretical equations governing the sensing process. The sensitivity was shown to be proportional to the membrane thickness to the power of -1.2. The temperature response of the sensors (over an average body temperature range) was also investigated and was found to be uniform across the different membrane thicknesses. This temperature response suggests that the thermal expansion of the air in the cavity is causing a change far greater than that of the membrane material. This work introduces a novel method of fabricating thin polymer membranes for use in fibre optic pressure sensors and adds to the previous literature in this field (Chen et al. 2010; Coote et al. 2019; Nesson et al. 2008; Wang et al. 2016). The resultant fibre optic pressure sensors also increase the knowledge in the respective field by investigating curved membrane designs as opposed to the traditional flat membrane designs.

The key outputs from this category of work are the development of a simplified microfabrication process to create free standing parylene membranes, the design and characterisation of fibre optic parylene-C F-P physiological pressure sensors and a study of the relationship between parylene thickness and sensor sensitivity.

6.1.3 Fibre optic hydrophone (FOH) sensors

High finesse parylene-C based extrinsic F-P style fibre optic hydrophones (FOH) were successfully created through the previously discussed parylene-C membrane fabrication method and the addition of reflective gold coatings (Chapter 4). Gold coated optical fibres were integrated into extrinsic sensing elements with complimentary gold coatings on their deformable membranes to create high finesse FOH devices. The FOH were characterised in a water bath using a calibrated ultrasound transducer and showed good ultrasound reception, even with low reflectivity values. As the reflectivity values of the gold coatings increased, the optical phase sensitivity of the sensors increased. The calculated NEP values showed how the parylene FOH could detect pressures an order of magnitude lower than similarly sized piezoelectric needle hydrophones (~100 Pa vs. ~1000 Pa). The parylene based FOH also compared well with similar NEP values for FOH sensors previously reported in the literature. The bandwidth was measured to be approximately 4 MHz. The directivity response of the FOH was found to be omnidirectional, remaining within 50% of the maximum across an angular range of 180°. Such omnidirectional

behaviour is beneficial in applications such as photoacoustic tomography, phased array ultrasound imaging and laser-scanning OR-PAM. The FOH demonstrated a high acoustic phase sensitivity due to the air backed parylene membrane. The demonstration of air backed curved membrane FOH builds on previous studies, such as those by Guggenheim *et al.* (Guggenheim et al. 2017) and illustrates how air-filled cavities could be utilised to further increase the sensitivity of FOH. These thin polymer membranes pave the way for ultra-low NEP (< 10 Pa) FOH to be created by combining the high acoustic phase sensitivity seen in this work with an optimised optical phase sensitivity of the F-P cavity.

The important outcomes from this section are the development and fabrication of high finesse air backed parylene-C FOH, the characterisation and high acoustic phase sensitivity achieved, and the progress towards ultra-low NEP FOH.

6.2 Future outlook

6.2.1 Printing process

The developed micro moulding technique for printing soft materials could be used to create many different microstructures across a variety of applications both within and outside the medical field including flexible electronics, microfluidics and bioengineering. Silicones such as PDMS are a widely used soft material in many areas and the ability to rapidly create high-resolution microstructures would offer many advantages. To expand the technique to include water-based filler materials, another scaffold printing ink would be required. Polymers such as polyvinyl acetate (PVAc), polymethyl methacrylate (PMMA) and ethyl cellulose are insoluble in water and could be explored as a micro mould printing material. However, these polymers require stronger solvents such as acetone, chloroform and ethanol to dissolve them. The solvents required to remove the supporting scaffold could therefore inadvertently wash away the inner material as well, so careful consideration must be taken when choosing complimentary mould and filler materials.

An additional DW printing system with an extended range of 5x5x4 cm (x, y, z) has already been devised. I have designed a similar system to that used in this work and have created the accompanying setup to enable DW printing over a larger range. The new system has already been deployed in the lab in preparation for future work, but no results have been generated yet. The resolution of the new Aerotech stage is comparable to the piezoelectric PI stage used throughout this work. This extended range offers the opportunity to increase the size of the printed structures and allows for centimetre scale arrays of these microstructures to be produced. Potential future

work will utilise the printing processes developed in this thesis to create microstructures for sensing. Some examples that are being considered are electrochemical sensors for pH sensing and large sensor arrays for pressure sensing applications.

The possibility of printing multiple materials in a single design should also be investigated further. Through integrating multiple nozzles different materials could be deposited within a single structure in one smooth process. Multi-nozzle/multi-material printing could aid with printing complex fabrication designs by introducing multiple materials simultaneously or by printing and filling moulds in one smooth process. Multiple nozzles could also enable more complex designs of DW printing through the use of additional support structure material alongside the main printing material, as utilised in other printing techniques such as fused deposition modelling.

The ability to print microstructures directly onto the tip of optical fibres has many exciting potential applications for integrating photonic devices/sensors. By utilising this printing technique devices, such as acoustic holograms, can be integrated directly onto fibres without the need to increase dimensions through extrinsic structures.

The manufacturing process used to create parylene-C membranes at the tips of glass microcapillaries utilises highly scalable procedures. In this work batches of capillaries containing 50 to 100 at a time were easily created. Further work to automate the deposition of the sacrificial layer could speed up the process and enable larger batches to be produced. By utilising a jig or similar, the position of the capillaries can be precisely known and repeatable. With this development, complete automation of the movement of the micronozzle to deposit the sacrificial layer would be possible. The pneumatic control system is already programable to apply back pressure when needed throughout the process. With these developments, larger batches could be achieved. The main bottle neck in the sensor fabrication process is the integration of the optical fibres with the capillaries. Again, this could be improved by using jigs or mounts to position the capillaries in well known locations to enable automated motion and improve the fibre integration procedure. Through larger batch sizes, the associated fabrication costs per fibre optic pressure sensor would be reduced. Due to their intended use in the medical field the sensors and FOH should be single use/disposable to prevent infection. The benefits of monitoring pressure during procedures have been discussed and are clear but in practical applications cost is a large factor when determining procedure protocols and guidelines. Reducing the fabrication costs would open the door to using fibre optic pressure sensors in a variety

of medical procedures. The small dimensions and flexibility of the fibre optic sensors makes them well suited for integration with pre-existing medical devices to offer additional functionality.

6.2.2 Parylene pressure sensors

To truly reach its potential and achieve mass production more aspects of the parylene-C membrane manufacturing process should be automated and optimised. Using a jig to position the capillaries in repeatable well-known positions could enable more aspects to be automated. The nozzle positioning and pressure regulation could all be programmed to fill the capillaries with exact amounts of polymer. If the initial positions are well defined, then after coating with parylene-C the optical fibres could also be integrated using an automated stage. Such alterations would allow manufacturing using this process to be scaled up.

The parylene based fibre optic pressure sensors show good sensitivity in the physiological pressure regime. Going forward, the bench top pressure simulator could be replaced with an *in vivo* animal model study to further validate the sensor response to physiological conditions. An *in vivo* model would also enable the ease of use of these sensors to be evaluated in a true clinical setting. Following *in* vivo tests, the fibre optic pressure sensors could continue the translational process to be used in clinics. There are several challenges to clinical translation such as, regulatory approval and integration with existing tools/techniques. Obtaining regulatory approval for a medical device is a lengthy and costly process. Every aspect of the device design and fabrication are scrutinised to ensure complete quality assurance of the final product. Even after regulatory approval if the device does not integrate well with pre-existing surgical tools and operating procedures then it will not be taken up and used by clinicians. For the fibre optic pressure sensors outlined in this work the small dimensions and flexible design has be used to enable the sensors to be integrated with medical catheters and guidewires. By integrating the sensors with pre-existing devices, the uptake and use of the sensors is likely to be far greater.

Using the results from this work, the parylene thickness required for a specific pressure sensitivity could be estimated. As each application will have a unique pressure range this information would be useful for optimising the sensitivity of the sensors and making them application specific. Based on the experimental results documented in Chapter 3, the average sensitivity could be adjusted over an order of magnitude from ~0.015 radians/mmHg to ~0.15 radians/mmHg by varying the

parylene thickness from 2 to 0.5 µm. Further work should be performed to investigate the change in sensitivity over a larger thickness range, possibly 0.2 µm to 5 µm.

To increase the sensitivity of the sensors further, the thickness of the parylene coatings could be reduced. Below 0.5 µm difficulties might arise due to the fragility of such thin coatings but some experiments could be performed to test this. Alternatively, other deposition materials could be investigated. Some preliminary work with atomic layer deposition (ALD) of aluminium oxide coatings have already been performed during this work and are discussed in Appendix A.

Further work should also be undertaken to evaluate the effects of annealing on the sensitivity of the sensors. The annealing process is known to increase the crystallinity and affect the mechanical properties of parylene-C (for instance, it could reduce the low frequency drift) but there are conflicting reports in literature as to how the mechanical properties change (Jackson et al. 2016; Metzen and Stieglitz 2013). Jackson *et al.* report an increase in yield strength and elastic modulus along with a decrease in elongation-to-break after annealing. Conversely, Metzen and Stieglitz report a decrease in Young's modulus along with increases in the elongation-to-break, tensile strength, yield strength and yield strain. Both reports performed annealing in a nitrogen environment to avoid oxidation, up to temperatures of 300 °C, and had similar film thicknesses of 10 and 12 µm. It would be interesting to investigate how the thinner parylene-C used in these sensors would behave after annealing. A reduction in Young's modulus would result in a membrane more sensitive to deformations. An increase in yield strength would lead to an increase in membrane durability.

To address the drift, it could be beneficial to explore how different sealing methods affect this. If the drift is in fact due to epoxy swelling through water absorption, then a protective layer of material impermeable to water could be used to cover the epoxy and test this theory. If the drift is found to be due to the parylene then annealing could be investigated to alter the properties of the parylene and try to reduce the drift. To remove the need for using sealing polymers altogether the possibility of splicing the end of the capillary to the optical fibre could be explored. The heating effects from the splicing process could be detrimental to the parylene membrane due to the close proximity to the splice point. Parylene-C has a melting point of 290 °C so could remain intact after splicing depending on the proximity of the splice point. However, the heating could influence the parylene's material properties, as annealing does, but in the presence of air oxidation will occur so this should be avoided. Longer capillaries

could be investigated to increase the distance from any splice point to the parylene membrane, in an effort to reduce the heating effect. Longer capillaries will in turn require longer micronozzles for sacrificial layer deposition.

Other work could be done to develop the flat membrane design further. As discussed In Chapter 3 this was not possible to implement with the polymer blends that were tested so far in this work but should be feasible in future. A polymer blend with good film forming capabilities and good adhesion to glass upon curing is required to create polymer plugs that remain flat and in position at the tip of the capillaries despite capillary action. With this, the capillaries could be inverted and parylene could be deposited to create a flat membrane at the tip of capillaries. The sacrificial polymer plug also needs to remain easily removeable through solvent dissolving or other mechanisms.

Using a similar cleanroom free fabrication technique, large arrays of pressure sensitive membranes could be created. By depositing the membranes in a substrate with an array of holes this could be achieved. The substrate material could be explored and potentially a flexible material could be used to create a flexible array of pressure sensors for use in wearable devices. These could again be interrogated with optical fibres but would be bulky if a single fibre were used to interrogate each element of the array. Alternatively, for wearable devices a capacitive or piezoelectric method could prove useful for a larger arrayed system with deformable membrane, pressure sensors.

6.2.3 Fibre optic hydrophone (FOH) sensors

There are several avenues to explore which could lead to the improvement of the FOH sensors.

Greater membrane response could result in higher sensitivity. Despite the low NEP values reported (~100’s Pa) the sensors have the potential to reach even lower values, potentially single Pascals or sub-Pascals, and give even higher sensitivity. The acoustic phase sensitivity of the sensors is currently quite high as ultrasound signals were detected even with low reflectivity gold coatings. However, this could be increased further. Greater membrane response could be accomplished by investigating thinner parylene membranes or by increasing the radius of the membrane using a trumpet style design to increase the sensing area. The curvature of the membranes could also be investigated by altering the composition of the sacrificial layer. Flat membranes could also be investigated as a comparison to the curved designs reported here. Similar to the pressure sensors above, the parylene

membranes could be annealed to induce greater crystallinity in the material structure. The increased crystallinity could result in a reduced Young's modulus and therefore increase the membrane response.

Testing the acoustic phase sensitivity of different thicknesses of membranes should also be looked at in future work. As mentioned in Chapter 4 this was planned for in this work but proved to have too many issues to complete in the given timescale. SEM images of how the gold deposits on different membranes would be interesting to look at to determine if the gold is agglomerating on some parylene-C surfaces and explain why the expected reflectivity values are not being reached with the thinner SCS parylene membranes.

Better optical performance could also result in higher sensitivity. By maximising the optical phase sensitivity exceptionally low NEP values could be obtained. The reflectivity of the gold coated surfaces should be optimised, and finer adjustable stages could be used to aid with more precise fibre alignment. Other reflective coatings could be tested but it is feared that the increased thickness associated with reflective dielectric coatings would be detrimental to the parylene membrane response of the sensors.

Methods of increasing the bandwidth of the FOH should also be explored. As mentioned in Chapter 4, the frequency response of a F-P cavity depends on a variety of parameters. Shorter cavities usually give greater bandwidth (Guggenheim et al. 2017). Greater bandwidth due to shorter cavities could be tested by creating sensors with a variety of cavity lengths. For the work documented in this thesis the cavity length of the FOH was ~45 µm. Zhang and Beard have also shown how the shape of a cavity can also effect the frequency response of a FOH (Zhang and Beard 2015). They demonstrated that by reducing the formation of edge waves the frequency response of FOH could be improved to give broadband measurements. The sharp edges of the fibre and capillary of the parylene sensors design can induce edge waves. These edge waves can propagate across the membrane surface and interact with the incident waves creating a complex frequency response. To reduce the formation of these edge waves smoothing would need to be performed on the sharp edges of these sensors. The flat cleaved optical fibre could be replaced with a rounded tip fibre. Integrating a rounded tip fibre with the curved parylene membranes could increase the bandwidth of the sensors. Smoothing the sharp edges of the glass capillaries by polishing could be difficult due to the small dimensions and fragility of these sensing elements.

Further efforts to improve the bandwidth of the sensors could investigate using alternative materials and structures to deposit the parylene membranes into instead of the glass capillaries. Utilising high-resolution 3D printing technologies these support structures could be created out of softer polymer materials to better match the acoustic impedance of the surrounding water and reduce the strength of edge waves formed during testing. Thanks to the room temperature manufacturing process developed here even polymer structures with low melting points could have parylene membranes deposited within them and be investigated. The option to 3D print supporting structures for the membranes would also enable smoother structural designs to be created and contribute to a further reduction in edge waves and hence greater broadband response of the sensors.

Reducing the low frequency drift would enable the sensors to be more robust when deployed in physiological environments. Minimising this would also reduce the amount of compensation needed to account for it. The low frequency drift could potentially be addressed by annealing the parylene, if it were found that this is the source of the drift. Alternatively, the sealing epoxy could be causing the drift and by changing the adhesive or the sealing method this could be reduced.

Another aspect that could be improved is the fabrication yield. Currently the capillaries are batch produced with a reasonable fabrication yield. To scale up the process the yield should be improved. An increase yield could be brought about through additional automation in the manufacturing process. Much of the manipulation of the capillaries is performed by hand at present which increases the risk of such small components being dropped or damaged. The high-resolution 3D printing techniques employed and the parylene deposition used are both highly repeatable processes. The additional handling and integration surrounding these processes are the key areas to focus on to improve the overall fabrication yield.

A potential future application of the FOH is in photoacoustic tomography. Due to the substantially omnidirectional response of the current FOH they could be used as an ultrasound receiver for photoacoustic tomography applications. Investigating the effectiveness of the FOH in photoacoustic tomography could begin in photoacoustic phantoms and move towards *in vivo* studies.

6.2.4 Mechanical models for parylene membranes

The curved parylene membrane in the fibre optical pressure sensors and FOH could be modelled in simulations to better understand the mechanics of the membrane deformations as well as stresses and strains imparted during deformation. The

curvature could be investigated and compared with flat membranes before using the results to optimise the fabricated parylene membranes. Flat membranes will be easier for pressure waves to deform so should in turn create more sensitive sensors. The stability of the dome shaped membranes might see them better suited for higher pressure applications. Throughout the experimental characterisation it was noted that the degree of curvature of the membranes could be altered based on the polymer composition of the sacrificial layer. Simulations could be performed to evaluate how these different curvatures affect the sensitivity. There will likely be a trade-off between high curvature enabling beam refocussing (increasing optical phase sensitivity) and reduced curvature enabling larger deformations (increasing acoustic phase sensitivity). As well as this, slight variations and defects could be created in the membrane models. By studying the effects these have on the resultant sensitivity a greater understanding of the sensing mechanism and requirements of the manufacturing process could be established. Grid dependence studies need to be carried out on these models and a full investigation over a range of membrane thicknesses and pressure loads should be performed.

Further work should be done to better understand the mechanical aspects of the membrane under load. This information could be utilised to aid in future membrane designs for sensing applications.

6.2.5 Optical models for parylene membranes

The parylene membranes could also be investigated optically through simulated models. The curvature of the membranes has been found to have a focussing effect on the reflected light during experiments. By carrying out simulated optical models this could be better understood and adapted to increase the optical sensitivity of the FOH and fibre optic pressure sensors. Parameters such as the cavity length and the numerical aperture of the fibre could be easily explored with such a model.

Optical models could also be used to simulate the response of the FOH. A study on the curved F-P cavity where the reflectivity of the gold coatings is varied would lead to a greater understanding. With this information the optical phase sensitivity of the FOH could be optimised and therefore improve the overall response of the FOH, resulting in lower NEP measurements.

6.2.6 Multi-capability probes

The selectively absorbing materials printed in this work have the potential to enable multi-capability probes. The gold nanoparticles used in the concentric ring structure

absorb strongly at 532 nm. This selectively strong absorption means that when exposed to this wavelength of light the composite gold nanoparticle-PDMS material is photoacoustic and can generate ultrasound waves. Away from this resonant absorption wavelength, light is mainly transmitted through the material. The transmitted light could be used for additional functional PAT imaging to identify specific molecules such as lipids which absorb at 1210 nm. The transmitted light could also be utilised for performing therapeutic treatments such as laser coagulation using a wavelength of 1064 nm. Such multi-capability probes would be of interest in fetal medicine where reducing the number of operating ports required is important for reducing the risk of iatrogenic preterm premature rupture of membranes (iPPROM) during procedures. Future investigations should explore the paradigm of utilising the transmitted light for diagnostics and/or therapeutics.

6.2.7 Multimodality sensors

A single optical fibre with physiological temperature and pressure along with ultrasound sensing capabilities could be realised. Such a probe could be used during intravascular procedures and relay ultrasound images along with pressure and temperature measurements to the surgeon. Such a device could be accomplished by combining an LCI setup with a FOH laser interrogation setup with an optical switch so that light can be emitted and received by each system from a single fibre. The fibre would have an extrinsic parylene sensing element capable of measuring low frequency temperature and pressure fluctuations along with high frequency ultrasound wave detection.

6.2.8 Beam manipulation

The use of acoustic hologram designs on the microscale, and more specifically on the tip of optical fibres, has the potential to create focussed ultrasound beams and reduce beam divergence. In order to more repeatedly print onto the tip of optical fibres some improvements are required. The current method of cleaving and polishing the fibres to ensure a uniformly even surface for printing on needs optimised. The printing set up will also need to be adapted to include an additional viewing angle to help with the initial fibre-nozzle alignment. A viewing system with a larger field of view would also enable faster alignment but is not essential.

Once acoustic hologram designs are printed onto the tip of a fibre, more robust characterisation and testing of the selective absorption and beam manipulation properties can be performed. By using a 532 nm laser source ultrasound waves should be generated. An optical hydrophone should then be used to measure the

divergence of the generated acoustic field and verify if focusing/reduced divergence is achieved. Measuring the generated ultrasound field could prove difficult as the focus is close to the hologram surface and could damage the hydrophone. A small hydrophone would also be required in order to detect any focussing. Alternatively, the ultrasound waves could be detected further from the hologram and back projection techniques could be used to estimate the interactions of the waves and the shape of the beam.

Further beam focussing acoustic hologram designs could be investigated through simulated work. Optimising the ultrasound frequency, focal length and required radii for desired outcomes could be performed *in silico* before printing the designs on fibres.

The resultant beams could be used with a FOH to interrogate samples and create high-resolution images. These all optical ultrasound images could be used in clinical applications or non-clinical settings such as non-destructive material testing. If the focussing was increased, it could also be possible to cause excessive heating and cavitation to induce tissue damage with such a beam. Inducing tissue damage could be beneficial in treatments such as high intensity focussed ultrasound (HIFU). HIFU currently utilises ultrasound sources outside the body but a highly focused micro beam could be used for precise minimally invasive treatments.

Another optical ultrasound imaging probe configuration to investigate further is that of a dual material design. This design is based on a single gold nanoparticle-PDMS donut shape at the tip of the fibre. The inner section of the ring can then be filled with a carbon based PDMS composite. With this design light at 532 nm is absorbed across all sections of the structure and generates ultrasound due to the high absorption of the gold and carbon nanoparticles and the thermoelastic response of the PDMS. Away from 532 nm only the smaller inner carbon-based PDMS composite material will absorb the light and generate ultrasound waves. By switching the wavelengths, ultrasound can be generated from the whole structure or from a smaller aperture. The ultrasound beams generated by each of these sections will differ. The beam from the smaller carbon core will be more diverging and the beam from the larger area will be more directional. These could be utilised in all optical ultrasound imaging to improve tracking and image acquisition speeds. The more diverging wide angled beam could be used to establish a larger field of view initially and then the more directional beam could be used to generate higher resolution images from areas of interest.

6.3 Concluding remarks

Throughout this thesis high-resolution manufacturing techniques based on precise control at the microscale have been developed and utilised. The challenges with manufacturing at this scale have been highlighted and solutions outlined. The adaptability of these techniques have enabled a range of materials to be used, demonstrating a variety of potential applications. High-resolution 3D microstructures have been printed on an array of substrates, including optical fibres, without the requirement of a cleanroom environment. These printing techniques have also been exploited to create deformable polymer membranes for fibre optic sensing. The microscale manufacturing techniques developed here demonstrate the ability to create precise devices and microstructures utilising an assortment of different materials. With additional optimisation, the scalability of the processes could be improved; further developments could also see the expansion of this technology into many more applications across healthcare applications and beyond.

Appendix A

Atomic layer deposition coating

Atomic layer deposition coating (ALD) was preliminarily investigated during this project as an alternative coating method to chemical vapour deposited parylene. In collaboration with a colleague at Durham University it was possible to apply a layer of aluminium oxide which was approximately 1 µm thick on top of the capillaries. Two different sample preparation techniques were tested. In one case the PVP at the end of the capillary had a layer of gold sputtered on to it before ALD coating and in the other case it was left untreated. The gold was applied to incorporate a highly reflective coating on the underside of the ALD layer to create high finesse cavities. The results of the coating are shown below.

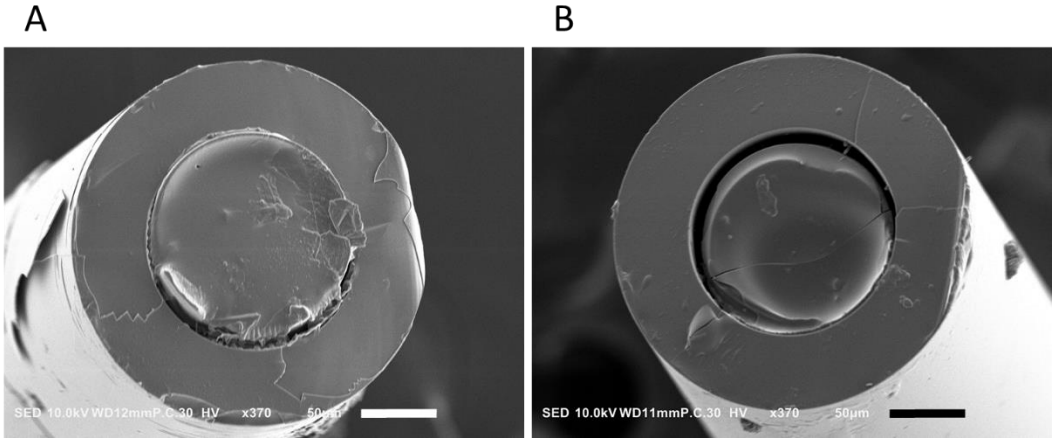

Figure A.1 – SEM images of, A) Untreated ALD sample, B) Gold treated ALD sample. All scale bars are 50 µm.

From the SEM images of the coated samples cracks and fragmentation are visible in both cases (Figure A.1). This cracking and fragmentation was seen across all of the samples. When the capillaries were submerged in DI water to dissolve the PVP plug the whole coating washed away with it. Inspection after the washing stage showed no membranes remained in any of the samples.

For ALD to be used to create free standing aluminium oxide membranes at the tip of glass microcapillaries much more work needs to be done in order to optimise the process. Potentially different polymers with poor adhesion to aluminium oxide or some other intermediate coating layer to allow the polymer to dissolve and the thin ALD coating to remain.

Appendix B

Matlab code for calculating NEP values

Presented below is the Matlab script used to calculate the NEP values from the recorded data files.

```
clear all;
close all;

% Read file from drive
% Signal data
fileID = fopen('C:\Users\rcaul\Documents\Matlab\Hydrophone\2020-02-
17\Signals\Cap5_Au-80pc_BNC-Atten-
10dB_VR_2.0V_MSR_125MHz_RL_15000_Avg_1_Int_Pow_15mW_BiasWL_1570nm_Si
gnal_4.TXT', 'r');
%fileID = fopen('C:\Users\rcaul\Documents\Matlab\Hydrophone\2019-11-
13\NEP\CPHD_No-
Au_VR_2V_MSR_125MHz_RL_10000_Avg_1_Int_Pow_21.9mW_Signal_5.TXT',
'r');
formatSpec = '%f';
sig1 = fscanf(fileID, formatSpec);
fclose(fileID);

% Noise data
fileID = fopen('C:\Users\rcaul\Documents\Matlab\Hydrophone\2020-02-
17\Signals\Cap5_Au-80pc_BNC-Atten-
10dB_VR_0.05V_MSR_125MHz_RL_15000_Avg_1_Int_Pow_15mW_BiasWL_1570nm_N
oise_2.TXT', 'r');
%fileID = fopen('C:\Users\rcaul\Documents\Matlab\Hydrophone\2019-11-
13\NEP\CPHD_No-
Au_VR_0.1V_MSR_125MHz_RL_10000_Avg_1_Int_Pow_21.9mW_Noise_1.TXT',
'r');
noise1 = fscanf(fileID, formatSpec);
fclose(fileID);

samp_rate = 125.0e6;
dt = 1/samp_rate;

no_of_samp = length(sig1);

taxis = linspace (0.00,((dt)*(no_of_samp-1)), no_of_samp);
taxis_us = taxis*1.0e6;

figure();
plot(taxis_us, sig1);
title ('Recorded signal');
ylim([-1.5 1.5]);
xlabel('Time (us)');
ylabel('Amplitude (V)');

% Calculate_fft
fft_sig1 = fft(sig1);
P2 = abs(fft_sig1/no_of_samp);
P1 = P2(1:no_of_samp/2+1);
```

```
P1(2:end-1) = 2*P1(2:end-1);

fq = samp_rate*(0:(no_of_samp/2))/no_of_samp;

fq_Mhz = fq/1e6;

figure();
plot(fq_Mhz,P1);
title ('FFT');
xlabel('f (MHz)');
ylabel('|Sig1(f)|');
xlim([0 20]);

% Apply bandpass filter
order = 4;
f_cut_low = 0.4e6;
f_cut_upp = 7e6;
f_low = (f_cut_low/(samp_rate/2));
f_upp = (f_cut_upp/(samp_rate/2));
[b,a] = butter(order,[f_low,f_upp],'bandpass');
filt_sig1 = filter(b,a, sig1);

[b,a] = butter(8,f_low,'High');
filt_sig2 = filtfilt(b,a,sig1);

[b,a]=butter(8,f_upp,'Low');
filt_sig2 = filtfilt(b,a,filt_sig2);

figure();
plot(taxis_us, filt_sig2, 'r'); %taxis_us, filt_sig1,
title ('Signal and filtered signal');

hilb_sig1 = abs(hilbert(filt_sig1));

figure();
plot(taxis_us, filt_sig1, taxis_us, hilb_sig1, 'r');
title ('Filtered signal and hilbert transform');

peak_sig1 = max(hilb_sig1);

pressure = 70.0; % Calibrated pressure value in kPa
atten = 10; % Attenuation in dB
press_atten = pressure*(10^(-atten/20));

s0 = peak_sig1/press_atten;

% Noise estimation from signal
noise_data = filt_sig1(1:500); % with the transducer at 2.2cm from
the hydrophone 200:1200

sigma = std(noise_data);

rms_n = rms(noise_data);

nep_sig = (sigma/s0)*1e3;

nep_3sig = ((sigma*3)/s0)*1e3;

nep_rms = (rms_n/s0)*1e3;

% Noise estimation from recorded noise data

% Apply bandpass filter
filt_noise1 = filter(b,a, noise1);
```

```
figure();
plot(noise1);
hold on;
plot(filt_noise1, 'r');
title ('Noise & filtered noise');

sig_noise = std(filt_noise1);

nep_3sig_from_noise = ((sig_noise*3)/s0)*1e3;
```

Appendix C

Minimally invasive fetal interventions

This section includes additional details on some minimally invasive fetal procedures gathered through literature searches and discussions with clinicians. The aim of this section is to help give a clearer understanding of the procedures and how they are performed in order to develop a greater insight into the requirements surrounding the equipment used and the key needs for future developments.

Twin-twin transfusion syndrome (TTTS) occurs in pregnancies of monochorionic twins (identical twins that share a placenta) and is present in 9-15% of these pregnancies (Apuzzio et al. 2017). The condition is an imbalance of circulating blood between the twins where one receives less (donor) and one receives an increased amount (receiver). The condition leads to adverse effects for both twins. If left untreated the overall mortality rate is 73 - 100% (Slaghekke et al. 2014). The current treatment for TTTS involves the use of lasers to coagulate the inter-twin vasculature anastomoses (connecting vessels) on the surface of the placenta to sever the vascular connection between the twins and restore equal circulation. This therapy is minimally invasive and uses external ultrasound to guide the placement of a fetoscope, which has a central lumen, through which a laser fibre can be inserted. The inter-twin vasculature anastomoses are then identified on the placenta, using optical imaging, and laser coagulated. Unfortunately, it is difficult to identify and coagulate all of the anastomoses so fine anastomoses remain in up to 33% of cases (Dhillon et al. 2015). An improved imaging technique could aid in the identification of these finer anastomoses on the placenta. The remaining anastomoses can lead to complications such as recurrent TTTS or twin anaemia-polycythaemia sequence (TAPS) (Slaghekke et al. 2014). In an effort to combat the residual anastomoses and their associated complications an alternative lasering technique was developed, the Solomon technique. As well as the selective lasering of the inter-twin anastomoses the Solomon technique has the addition of coagulating a line along the entire vascular equator so that even the very small anastomoses are coagulated. Studies have found that the Solomon technique does in fact reduce the risk of recurrent TTTS and TAPS without an increased risk of adverse effects compared to standard selective coagulation (Akkermans et al. 2015; Slaghekke et al. 2014). Despite this, selective

anastomoses coagulation is the most commonly used method in clinics globally (Akkermans et al. 2015).

Key need: improved visualisation to better identify and coagulate anastomoses. All-optical ultrasound probes could be used and would be able to identify sub-surface anastomoses as well. By utilising the developed technique of printing on fibres, beam manipulation could be possible to reduce divergence of the generated ultrasound beam and even induce a focus for higher resolution imaging. The imaging probe must remain dimensionally small in order to fit within the lumen of the fetoscope (approx. < 3 mm). The use of selectively absorbing photoacoustic materials could also enable multi-capability probes which could carry out imaging and coagulation through a single fibre or utilise PAT imaging techniques to help identify anastomoses.

Another case where minimally invasive fetal surgery is necessary is ***congenital diaphragmatic hernia (CDH)***. CDH occurs when the diaphragm does not form properly so there is a hole in it. This hole allows abdominal organs to move into the chest cavity (herniate) and prevent the lungs from developing correctly. The treatment for CDH is fetoscopic endoluminal tracheal occlusion (FETO) (Apuzzio et al. 2017). FETO is a minimally invasive fetal surgical procedure where a small balloon is inflated in the trachea of the fetus to block it. By obstructing the trachea improved lung development is promoted (Deprest, Gratacos, and Nicolaides 2004). The balloon traps the fluid secreted by the fetal lungs and prevents it from being drained out to the amniotic cavity. This build-up of fluid causes the lung tissue to stretch and sparks lung growth (Jani et al. 2009). Usually the balloon is placed at 26-28 weeks into the pregnancy and removed at 34 weeks when the lungs are better developed (Apuzzio et al. 2017). The placement of the balloon is a very precise procedure and is currently executed using a fetoscope, through which the balloon is inserted using a catheter. Navigating the fetoscope through the amniotic fluid, into the fetuses mouth and down its trachea requires clear, high-resolution imaging which can be problematic if the amniotic fluid is cloudy and restricts the surgeon's field of view. In utero ultrasonic imaging is a possible solution to improve clarity and aid in the intricate placement of the balloon.

Key need: improved visualisation and haptic feedback. Through better visualisation, navigating to the placement site for the balloon could be made easier. Utilising an *in utero* ultrasonic visualisation modality would circumnavigate the issue of cloudy fluid disrupting the view. All optical ultrasound imaging probes with printed hologram structures could provide a suitable imaging modality. A haptic or tactile sensor to

provide feedback to the surgeon during the placement and removal of the balloon would enable greater safety profiles. An extension of the printing work on fibres could enable the integration of tactile sensors directly on to the tips of optical fibres. Using interferometric monitoring techniques, the sensors could be optically interrogated and provide measurements while remaining highly miniaturised.

Lower urinary track obstruction (LUTO) is another fetal abnormality that requires minimally invasive intervention. LUTO is a blockage that prevents the fetus from passing urine. If left untreated it could lead to life threatening complications (Morris et al. 2013). The treatment requires the placement of a shunt (a hollow tube) to bypass the blocked urinary track, vesicoamniotic shunting. The shunt is usually placed through the abdominal wall into the bladder, thus connecting the bladder to the amniotic fluid and allowing urine to be drained away (Haeri 2015). The shunting procedure is performed under external ultrasound guidance and has associated fetal morbidity risks due to infection or bleeding. Trials assessing the effectiveness of the shunting treatment have been unable to draw certain conclusions. However, the results from the randomised Percutaneous shunting in Lower Urinary Tract Obstruction (PLUTO) trial have indicated towards greater fetal survival compared to conservative treatments after 28 days and after 1 year (Morris et al. 2013).

Key need: improved visualisation and haptic feedback. This procedure is another that could benefit from the development of a highly miniaturised ultrasound imaging probe to better guide the placement of the shunt and hopefully lead to improved fetal outcome. The addition of haptic feedback would also be useful for monitoring the applied forces throughout the procedure.

Finally, ***spina bifida*** is a debilitating defect of the central nervous system that can also be treated with minimally invasive fetal surgery. Spina bifida is a defect in the development of the neural tubes. The most common and most severe type of spina bifida is ***myelomeningocele (MMC)*** (Kabagambe et al. 2017). MMC is when the neural tubes do not close properly leaving a gap through which the spinal cord and meninges (layers of protective tissue) protrude creating a cyst filled with spinal cord, meninges, spinal fluid and nerves (Adzick 2012). If untreated MMC will cause lifetime paralysis. Previous treatment involved corrective operations to remove the cyst and close the neural tubes postnatally. A study known as the Management of Myelomeningocele Study (MOMS) found that prenatal repair reduced the risk of death, decreased the need for shunting and improved mental and motor function compared to postnatal repair (Adzick et al. 2011). The reason is believed to be due

to the “two-hit hypothesis”. This hypothesis states that the first “hit” is the defect in the neural tubes preventing them to close. The second “hit” is then when healthy spinal cord tissue becomes damaged due to factors such as exposure to amniotic fluid, trauma and hydrodynamic pressure (Adzick 2012). In utero intervention reduces the impact of the secondary damage. MOMS compared prenatal open fetal surgery to postnatal procedures. Debate still surrounds the comparison of open fetal surgery and minimally invasive fetal surgery when treating MMC. Those in favour of the minimally invasive approach say that it reduces obstetrical complications, whereas those in favour of open surgery argue that minimally invasive techniques increase the risk of ruptured membrane and preterm birth (Kabagambe et al. 2017). Kabagambe *et al.* found comparable outcomes from both methods of fetal intervention. An alternative technique was developed by Belfort *et al.* this involves the removal of the uterus from the mother’s abdomen by maternal laparotomy followed by minimally invasive surgery in utero (Belfort et al. 2017). Belfort’s technique also utilises carbon dioxide gas to insufflate small gas pockets inside the uterus to enable better optical imaging. The use of carbon dioxide gas in utero is still being debated as it could cause fetal acidosis (high levels of acid in the blood) (Moise Jr and Flake 2017). Belfort’s technique resulted in better obstetrical outcomes than either open surgery or percutaneous (through the skin) minimally invasive surgery and enabled the possibility of vaginal delivery (Kabagambe et al. 2017). Despite Belfort *et al.* having a small sample size and no long-term data their results are promising.

Key need: improved intraoperative visualisation. The use of carbon dioxide in Belfort’s operating technique highlights the need for better imaging. A device such as a miniaturised optical ultrasound probe could address this issue and provide improvements to the MMC repair treatments.

References

Achenbach, Stephan, Tanja Rudolph, Johannes Rieber, Holger Eggebrecht, Gert Richardt, Thomas Schmitz, Nikos Werner, Florian Boenner, and Helge Möllmann. 2017. “Performing and Interpreting Fractional Flow Reserve Measurements in Clinical Practice: An Expert Consensus Document.” *Interventional Cardiology Review* 12(2):97–109.

ACIST Medical. 2017. “Navvus Rapid Exchange FFR MicroCatheter.”

Adzick, N. Scott. 2012. “Fetal Surgery for Myelomeningocele: Trials and Tribulations. Isabella Forshall Lecture.” *Journal of Pediatric Surgery* 47(2):273–81.

Adzick, N. Scott, Elizabeth A. Thom, D. Ph, Catherine Y. Spong, John W. Brock, Pamela K. Burrows, Mark P. Johnson, Lori J. Howell, A. Farrell, Mary E. Dabrowiak, and Leslie N. Sutton. 2011. “A Randomized Trial of Prenatal versus Postnatal Repair of Myelomeningocele.” *N Engl J Med* 364(11):993–1004.

Agarwal, Abhinav, Aubrey Shapero, Damien Rodger, Mark Humayun, Yu Chong Tai, and Azita Emami. 2018. “A Wireless, Low-Drift, Implantable Intraocular Pressure Sensor with Parylene-on-Oil Encapsulation.” *2018 IEEE Custom Integrated Circuits Conference, CICC 2018* 1–4.

Ahmed, Syed Rahin, Jeonghyo Kim, Van Tan Tran, Tetsuro Suzuki, Suresh Neethirajan, Jaebeom Lee, and Enoch Y. Park. 2017. “In Situ Self-Assembly of Gold Nanoparticles on Hydrophilic and Hydrophobic Substrates for Influenza Virus-Sensing Platform.” *Scientific Reports* 7:44495.

Ahn, Bok Yeop, Eric B. Duoss, Michael J. Motala, Xiaoying Guo, S. I. Park, Yujie Xiong, Jongseung Yoon, Ralph G. Nuzzo, John A. Rogers, and Jennifer A. Lewis. 2009. “Omnidirectional Printing of Flexible, Stretchable, and Spanning Silver Microelectrodes.” *Science* 323(5921):1590–93.

Akkermans, J., S. H. P. Peeters, J. M. Middeldorp, F. J. Klumper, E. Lopriore, G. Ryan, and D. Oepkes. 2015. “A Worldwide Survey of Laser Surgery for Twin-Twin Transfusion Syndrome.” *Ultrasound in Obstetrics & Gynecology* 45(2):168–74.

Ansari, R., E. Zhang, A. E. Desjardins, and P. C. Beard. 2017. “All-Optical Endoscopic Probe for High Resolution 3D Photoacoustic Tomography.” *Photons Plus*

Ultrasound: Imaging and Sensing 2017 10064:100641W.

Apuzzio, Joseph J., Anthony M. Vintzileos, Vincenzo Berghella, and Jesus R. Alvarez-Perez. 2017. *Operative Obstetrics*. 4th ed. CRC Press.

Arias, Irene and Jan D. Achenbach. 2003. “Thermoelastic Generation of Ultrasound by Line-Focused Laser Irradiation.” *International Journal of Solids and Structures* 40(25):6917–35.

Ashitate, Yoshitomo, Eiichi Tanaka, Alan Stockdale, Hak Soo Choi, and John V. Frangioni. 2011. “Near-Infrared Fluorescence Imaging of Thoracic Duct Anatomy and Function in Open Surgery and Video-Assisted Thoracic Surgery.” *The Journal of Thoracic and Cardiovascular Surgery* 142(1):31-38.e2.

Baac, Hyoung Won, Jong G. Ok, Taehwa Lee, and L. Jay Guo. 2015. “Nano-Structural Characteristics of Carbon Nanotube-Polymer Composite Films for High-Amplitude Optoacoustic Generation.” *Nanoscale* 7(34):14460–68.

Baac, Hyoung Won, Jong G. Ok, Adam Maxwell, Kyu Tae Lee, Yu Chih Chen, A. John Hart, Zhen Xu, Euisik Yoon, and L. Jay Guo. 2012. “Carbon-Nanotube Optoacoustic Lens for Focused Ultrasound Generation and High-Precision Targeted Therapy.” *Scientific Reports* 2.

Bae, H. and M. Yu. 2012. “Miniature Fabry-Perot Pressure Sensor Created by Using UV-Molding Process with an Optical Fiber Based Mold.” *Optics Express* 20(13):14573.

Baim, Donald S., ed. 2006. *Grossman’s Cardiac Catheterization, Angiography, and Intervention*. 7th ed. Lippincott Williams & Wilkins.

Basaran, Osman A. 2002. “Small-Scale Free Surface Flows with Breakup: Drop Formation and Emerging Applications.” *AIChE Journal* 48(9):1842–48.

Batchelor, GK. 2000. *An Introduction to Fluid Dynamics*.

Beard, P. C. 1998. “Optical Fiber Photoacoustic – Photothermal Probe.” 23(15):1235–37.

Beard, Paul. 2011. “Biomedical Photoacoustic Imaging.” *Interface Focus* 1(4):602–31.

Beck, Veronika, Paul Lewi, Leonardo Gucciardo, and Roland Devlieger. 2012. “Preterm Prelabor Rupture of Membranes and Fetal Survival after Minimally Invasive Fetal Surgery: A Systematic Review of the Literature.” *Fetal Diagnosis*

and Therapy 31(1):1–9.

Belfort, Michael A., William E. Whitehead, Alireza A. Shamshirsaz, Zhoobin H. Bateni, Oluyinka O. Olutoye, Olutoyin A. Olutoye, David G. Mann, Jimmy Espinoza, Erin Williams, Timothy C. Lee, Sundeep G. Keswani, Nancy Ayres, Christopher I. Cassady, Amy R. Mehollin-Ray, Magdalena Sanz Cortes, Elena Carreras, Jose L. Peiro, Rodrigo Ruano, and Darrell L. Cass. 2017. “Fetoscopic Open Neural Tube Defect Repair: Development and Refinement of a Two-Port, Carbon Dioxide Insufflation Technique.” *Obstetrics and Gynecology* 129(4):734–43.

Bhattacharjee, Tapomoy, Steven M. Zehnder, Kyle G. Rowe, Suhani Jain, Ryan M. Nixon, W. Gregory Sawyer, and Thomas E. Angelini. 2015. “Writing in the Granular Gel Medium.” *Science Advances* 1(8).

Bhattacharjee, Tapomoy, Steven M Zehnder, Kyle G. Rowe, Suhani Jain, Ryan M. Nixon, W. Gregory Sawyer, and Thomas E. Angelini. 2015. “Writing in the Granular Gel Medium.” *Science Advances* 1(8):e1500655–e1500655.

Biagi, E., S. Cerbai, L. Masotti, L. Belsito, A. Roncaglia, G. Masetti, and N. Speciale. 2009. “Fiber Optic Broadband Ultrasonic Probe for Virtual Biopsy: Technological Solutions.” in *Proceedings - IEEE Ultrasonics Symposium*.

Biagi, Elena, Fabrizio Margheri, and David Menichelli. 2001. “Efficient Laser-Ultrasound Generation by Using Heavily Absorbing Films as Targets.” *IEEE Transactions on Ultrasonics, Ferroelectrics, and Frequency Control* 48(6):1669–80.

Boonsuk, Phetdaphat, Kaewta Kaewtatip, Sirinya Chantarak, Antonios Kelarakis, and Chiraphon Chaibundit. 2018. “Super-Tough Biodegradable Poly(Vinyl Alcohol)/Poly(Vinyl Pyrrolidone) Blends Plasticized by Glycerol and Sorbitol.” *Journal of Applied Polymer Science* 135(26):1–8.

Bostwick, J. B. and P. H. Steen. 2015. “Stability of Constrained Capillary Surfaces.” *Annual Review of Fluid Mechanics* 47(1):539–68.

British Heart Foundation. 2019. “UK Factsheet.” *British Heart Foundation* (August).

Brown, Jeremy A., Christine E. M. Démoré, and Geoffrey R. Lockwood. 2004. “Design and Fabrication of Annular Arrays for High-Frequency Ultrasound.” *IEEE Transactions on Ultrasonics, Ferroelectrics, and Frequency Control* 51(8):1010–17.

Brown, M. D., D. I. Nikitichev, B. E. Treeby, and B. T. Cox. 2017. “Generating Arbitrary Ultrasound Fields with Tailored Optoacoustic Surface Profiles.” *Applied Physics Letters* 110(9):094102.

Brown, Michael D., Thomas J. Allen, Ben T. Cox, and Bradley E. Treeby. 2014. “Control of Optically Generated Ultrasound Fields Using Binary Amplitude Holograms.” Pp. 1037–40 in *IEEE International Ultrasonics Symposium, IUS*.

Brown, Michael D, Ben T. Cox, and Bradley E. Treeby. 2017. “Design of Multi-Frequency Acoustic Kinoforms.” *Citation: Appl. Phys. Lett* 111.

De Bruyne, Bernard, William F. Fearon, Nico H. J. Pijls, Emanuele Barbato, Pim Tonino, Zsolt Piroth, Nikola Jagic, Sven Mobius-Winckler, Gilles Rioufol, Nils Witt, Petr Kala, Philip MacCarthy, Thomas Engström, Keith Oldroyd, Kreton Mavromatis, Ganesh Manoharan, Peter Verlee, Ole Frobert, Nick Curzen, Jane B. Johnson, Andreas Limacher, Eveline Nüesch, and Peter Jüni. 2014. “Fractional Flow Reserve–Guided PCI for Stable Coronary Artery Disease.” *New England Journal of Medicine* 371(13):1208–17.

Buma, T., M. Spisar, and M. O’Donnell. 2001. “High-Frequency Ultrasound Array Element Using Thermoelastic Expansion in an Elastomeric Film.” *Applied Physics Letters* 79(4):548–50.

Carlson, Andrew, Audrey M. Bowen, Yonggang Huang, Ralph G. Nuzzo, and John A. Rogers. 2012. “Transfer Printing Techniques for Materials Assembly and Micro/Nanodevice Fabrication.” *Advanced Materials* 24(39):5284–5318.

Caulfield, Richard, Feihuang Fang, and Manish K. Tiwari. 2018. “Drops, Jets and High-Resolution 3D Printing: Fundamentals and Applications.” Pp. 123–62 in *Applications Paradigms of Droplet and Spray Transport: Paradigms and Applications*. Springer, Singapore.

Chang, Wei Yi, Wenbin Huang, Jinwook Kim, Sibo Li, and Xiaoning Jiang. 2015. “Candle Soot Nanoparticles-Polydimethylsiloxane Composites for Laser Ultrasound Transducers.” *Applied Physics Letters* 107(16).

Chen, L. H., C. C. Chan, W. Yuan, S. K. Goh, and J. Sun. 2010. “High Performance Chitosan Diaphragm-Based Fiber-Optic Acoustic Sensor.” *Sensors and Actuators, A: Physical* 163(1):42–47.

Chen, Sung-Liang and Sung-Liang. 2016. “Review of Laser-Generated Ultrasound Transmitters and Their Applications to All-Optical Ultrasound Transducers and

Imaging.” *Applied Sciences* 7(1):25.

Chen, Xiangfan, Wenzhong Liu, Biqin Dong, Jongwoo Lee, Henry Oliver T. Ware, Hao F. Zhang, and Cheng Sun. 2018. “High-Speed 3D Printing of Millimeter-Size Customized Aspheric Imaging Lenses with Sub 7 Nm Surface Roughness.” *Advanced Materials* 30(18):1–8.

Citerio, Giuseppe, Ian Piper, Iain R. Chambers, Davide Galli, Per Enblad, Karl Kiening, Arminas Ragauskas, Juan Sahuquillo, and Barbara Gregson. 2008. “Multicenter Clinical Assessment of the Raumedic Neurovent-P Intracranial Pressure Sensor: A Report by the BrainIT Group.” *Neurosurgery* 63(6):1152–58.

Clausen, Ingelin and Thomas Glott. 2014. “Development of Clinically Relevant Implantable Pressure Sensors: Perspectives and Challenges.” *Sensors (Switzerland)* 14(9):17686–702.

Colchester, R. J., E. J. Alles, and A. E. Desjardins. 2019. “A Directional Fibre Optic Ultrasound Transmitter Based on a Reduced Graphene Oxide and Polydimethylsiloxane Composite.” *Applied Physics Letters* 114(11).

Colchester, Richard J., Callum Little, George Dwyer, Sacha Noimark, Erwin J. Alles, Edward Z. Zhang, Christopher D. Loder, Ivan P. Parkin, Ioannis Papakonstantinou, Paul C. Beard, Malcolm C. Finlay, Roby D. Rakhit, and Adrien E. Desjardins. 2019. “All-Optical Rotational Ultrasound Imaging.” *Scientific Reports* 9(1):5576.

Colchester, Richard J., Charles A. Mosse, Davinder S. Bhachu, Joseph C. Bear, Claire J. Carmalt, Ivan P. Parkin, Bradley E. Treeby, Ioannis Papakonstantinou, and Adrien E. Desjardins. 2014. “Laser-Generated Ultrasound with Optical Fibres Using Functionalised Carbon Nanotube Composite Coatings.” *Applied Physics Letters* 104(17).

Colchester, Richard J., Edward Z. Zhang, Charles A. Mosse, Paul C. Beard, Ioannis Papakonstantinou, and Adrien E. Desjardins. 2015. “Broadband Miniature Optical Ultrasound Probe for High Resolution Vascular Tissue Imaging.” *Biomedical Optics Express* 6(4):1502.

Collins, Robert T., Jeremy J. Jones, Michael T. Harris, and Osman a. Basaran. 2008. “Electrohydrodynamic Tip Streaming and Emission of Charged Drops from Liquid Cones.” *Nature Physics* 4(2):149–54.

Coote, J. M., E. J. Alles, S. Noimark, C. A. Mosse, C. D. Little, C. D. Loder, A. L.

David, R. D. Rakhit, M. C. Finlay, and A. E. Desjardins. 2019. “Dynamic Physiological Temperature and Pressure Sensing with Phase-Resolved Low-Coherence Interferometry.” *Optics Express* 27(4):5641.

Correia, R., S. James, S. W. Lee, S. P. Morgan, and S. Korposh. 2018. “Biomedical Application of Optical Fibre Sensors.” *Journal of Optics (United Kingdom)* 20(7).

Dankelman, Jenny, John J. Van Den Dobbelsteen, and Paul Breedveld. 2011. “Current Technology on Minimally Invasive Surgery and Interventional Techniques.” *Proceedings of 2011 2nd International Conference on Instrumentation Control and Automation, ICA 2011* (November):12–15.

Das, A., M. V. Sivak, A. Chak, R. C. Wong, V. Westphal, A. M. Rollins, J. Willis, G. Isenberg, and J. A. Izatt. 2001. “High-Resolution Endoscopic Imaging of the GI Tract: A Comparative Study of Optical Coherence Tomography versus High-Frequency Catheter Probe EUS.” *Gastrointestinal Endoscopy* 54(2):219–24.

Dausch, David E., Kristin H. Gilchrist, James B. Carlson, Stephen D. Hall, John B. Castellucci, and Olaf T. Von Ramm. 2014. “In Vivo Real-Time 3-D Intracardiac Echo Using PMUT Arrays.” *IEEE Transactions on Ultrasonics, Ferroelectrics, and Frequency Control* 61(10):1754–64.

Deegan, Robert D., Olgica Bakajin, Todd F. Dupont, Greb Huber, Sidney R. Nagel, and Thomas A. Witten. 1997. “Capillary Flow as the Cause of Ring Stains from Dried Liquid Drops.” *Nature* 389(6653):827–29.

Deprest, J., E. Gratacos, and K. H. Nicolaides. 2004. “Fetoscopic Tracheal Occlusion (FETO) for Severe Congenital Diaphragmatic Hernia: Evolution of a Technique and Preliminary Results.” *Ultrasound in Obstetrics and Gynecology* 24(2):121–26.

Destino, Joel F., Nikola A. Dudukovic, Michael A. Johnson, Du T. Nguyen, Timothy D. Yee, Garth C. Egan, April M. Sawvel, William A. Steele, Theodore F. Baumann, Eric B. Duoss, Tayyab Suratwala, and Rebecca Dylla-Spears. 2018. “3D Printed Optical Quality Silica and Silica–Titania Glasses from Sol–Gel Feedstocks.” *Advanced Materials Technologies* 3(6):1–10.

Dhillon, R. K., S. C. Hillman, R. Pounds, R. K. Morris, and M. D. Kilby. 2015. “Comparison of Solomon Technique with Selective Laser Ablation for Twin-Twin Transfusion Syndrome: A Systematic Review.” *Ultrasound in Obstetrics & Gynecology* 46(5):526–533.

Diletti, Roberto, Nicolas M. Van Mieghem, Marco Valgimigli, Antonis Karanasos, Bert R. C. Everaert, Joost Daemen, Robert Jan Van Geuns, Peter P. De Jaegere, Felix Zijlstra, and Evelyn Regar. 2015. “Rapid Exchange Ultra-Thin Microcatheter Using Fibre-Optic Sensing Technology for Measurement of Intracoronary Fractional Flow Reserve.” *EuroIntervention* 11(4):428–32.

Dominguez-Flores, Carmen E., David Monzon-Hernandez, Vladimir P. Minkovich, J. A. Rayas, and Daniel Lopez-Cortes. 2019. “In-Fiber Capillary-Based Micro Fabry-Perot Interferometer Strain Sensor.” *IEEE Sensors Journal* 1–1.

Dong, Zhichao, Jie Ma, and Lei Jiang. 2013. “Manipulating and Dispensing Micro/Nanoliter Droplets by Superhydrophobic Needle Nozzles.” *ACS Nano* 7(11):10371–79.

Drexler, Wolfgang and James G. Fujimoto. 2008. *Optical Coherence Tomography Technology and Applications*.

Dunklin, Jeremy R., Gregory T. Forcherio, Keith R. Berry, and D. Keith Roper. 2013. “Asymmetric Reduction of Gold Nanoparticles into Thermoplasmonic Polydimethylsiloxane Thin Films.” *ACS Applied Materials and Interfaces* 5(17):8457–66.

Duoss, Eric B., Todd H. Weisgraber, Keith Hearon, Cheng Zhu, Ward Small, Thomas R. Metz, John J. Vericella, Holly D. Barth, Joshua D. Kuntz, Robert S. Maxwell, Christopher M. Spadaccini, and Thomas S. Wilson. 2014. “Three-Dimensional Printing of Elastomeric, Cellular Architectures with Negative Stiffness.” *Advanced Functional Materials* 24(31):4905–13.

Earley, Mark J. 2009. “How to Perform a Transseptal Puncture.” *Heart* 95(1):85–92.

Eaton, W. P. and J. H. Smith. 1997. “Micromachined Pressure Sensors: Review and Recent Developments.” *Smart Materials and Structures* 6(5):530–39.

Einstein, Albert. 1926. *Investigations on the Theory of Brownian Movement*. edited by R. Furth and A. . Cowper. Dover Publications Inc.

Eom, Jonghyun, Chang Ju Park, Byeong Ha Lee, Jong Hyun Lee, Il Bum Kwon, and Euiheon Chung. 2015. “Fiber Optic Fabry-Perot Pressure Sensor Based on Lensed Fiber and Polymeric Diaphragm.” *Sensors and Actuators, A: Physical* 225:25–32.

Epstein, Max. 1982. “Fiber Optics in Medicine.” *Critical Reviews in Biomedical*

Engineering 7(2):79–120.

Fang, Feihuang, Saja Aabith, Shervanthi Homer-Vanniasinkam, and Manish K. Tiwari. 2017. “High-Resolution 3D Printing for Healthcare Underpinned by Small-Scale Fluidics.” Pp. 167–206 in *3D Printing in Medicine*. Elsevier.

Ferraro, P., S. Coppola, S. Grilli, M. Paturzo, and V. Vespini. 2010. “Dispensing Nano-Pico Droplets and Liquid Patterning by Pyroelectrodynamic Shooting.” *Nature Nanotechnology* 5(6):429–35.

Fiorillo, A. S., C. D. Critello, and S. A. Pullano. 2018. “Theory, Technology and Applications of Piezoresistive Sensors: A Review.” *Sensors and Actuators A: Physical* 281:156–75.

FISO Medical. 2020. “Medical | Fiso.” Retrieved February 26, 2020 (https://fiso.com/en/service/medical/).

FISO Technologies. 2019a. *Medical Pressure Sensor - Datasheet*.

FISO Technologies. 2019b. *Medical Temperature Sensor - Datasheet*.

Fowler, Steven F., Roman M. Sydorak, Craig T. Albanese, Diana L. Farmer, Michael R. Harrison, and Hanmin Lee. 2002. “Fetal Endoscopic Surgery: Lessons Learned and Trends Reviewed.” *Journal of Pediatric Surgery* 37(12):1700–1702.

Fraden, Jacob. 2004. *Handbook of Modern Sensors : Physics, Designs, and Applications*. AIP Press/Springer.

Fu, Dongying, Xiujuan Liu, Jianyu Shang, Weimin Sun, and Yongjun Liu. 2020. “A Simple, Highly Sensitive Fiber Sensor for Simultaneous Measurement of Pressure and Temperature.” *IEEE Photonics Technology Letters* 1–1.

Fu, Xin, Ping Lu, Wenjun Ni, Hao Liao, Deming Liu, and Jiangshan Zhang. 2017. “Phase Demodulation of Interferometric Fiber Sensor Based on Fast Fourier Analysis.” *Optics Express* 25(18):21094.

Gawedzinski, John, Michal E. Pawlowski, and Tomasz S. Tkaczyk. 2017. “Quantitative Evaluation of Performance of Three-Dimensional Printed Lenses.” *Optical Engineering* 56(08):1.

Ge, Yixian, Kaijie Cai, Tingting Wang, and Jiahong Zhang. 2018. “MEMS Pressure Sensor Based on Optical Fabry–Perot Interference.” *Optik* 165:35–40.

de Gennes, Pierre-Gilles, Françoise Brochard-Wyart, and David Quéré. 2004.

Capillarity and Wetting Phenomena. Springer, New York.

Goyal, Anubha, Ashavani Kumar, Prabir K. Patra, Shaily Mahendra, Salomeh Tabatabaei, Pedro J. J. Alvarez, George John, and Pulickel M. Ajayan. 2009. “In Situ Synthesis of Metal Nanoparticle Embedded Free Standing Multifunctional PDMS Films.” *Macromolecular Rapid Communications* 30(13):1116–22.

Griggio, Flavio, Christine E. M. Demore, Hyunsoo Kim, James Gigliotti, Yongqiang Qiu, Thomas N. Jackson, Kyusun Choi, Rick L. Tutwiler, Sandy Cochran, and Susan Trolier-Mckinstry. 2012. “Micromachined Diaphragm Transducers for Miniaturised Ultrasound Arrays.” *IEEE International Ultrasonics Symposium, IUS* 4–7.

Guggenheim, James A., Jing Li, Thomas J. Allen, Richard J. Colchester, Sacha Noimark, Olumide Ogunlade, Ivan P. Parkin, Ioannis Papakonstantinou, Adrien E. Desjardins, Edward Z. Zhang, and Paul C. Beard. 2017. “Ultrasensitive Plano-Concave Optical Microresonators for Ultrasound Sensing.” *Nature Photonics* 11(11).

Guo, Rui, Shizhou Xiao, Xiaomin Zhai, Jiawen Li, Andong Xia, and Wenhao Huang. 2006. “Micro Lens Fabrication by Means of Femtosecond Two Photon Photopolymerization.” *Optics Express* 14(2):810.

Guo, Yunbo, Hyoung Won Baac, Sung-Liang Chen, Theodore B. Norris, and L. Jay Guo. 2011. “Broad-Band High-Efficiency Optoacoustic Generation Using a Novel Photonic Crystal-Metallic Structure.” *Photons Plus Ultrasound: Imaging and Sensing 2011* 7899(February 2011):78992C.

Von Gutfeld, R. J. and H. F. Budd. 1979. “Laser-Generated MHz Elastic Waves from Metallic-Liquid Interfaces.” *Applied Physics Letters* 34(10):617–19.

Haeri, Sina. 2015. “Fetal Lower Urinary Tract Obstruction (LUTO): A Practical Review for Providers.” *Maternal Health, Neonatology and Perinatology* 1(1):26.

Hernaez, Miguel, Carlos Zamarreño, Sonia Melendi-Espina, Liam Bird, Andrew Mayes, and Francisco Arregui. 2017. “Optical Fibre Sensors Using Graphene-Based Materials: A Review.” *Sensors* 17(1):155.

Hernández-Vaquero, D., M. Fernández-Fairen, A. Torres-Perez, and A. Santamaría. 2012. “Minimally Invasive Surgery versus Conventional Surgery. A Review of the Scientific Evidence.” *Revista Española de Cirugía Ortopédica y Traumatología (English Edition)* 56(6):444–58.

Hett, J. .. and L. .. Curtis. 1961. “Fiber Optics Duodenoscope and Ureterscope.” *Journal of the Optical Society of America* 51(5):581–82.

Hill, G. C., R. Melamud, F. E. Declercq, A. A. Davenport, I. H. Chan, P. G. Hartwell, and B. L. Pruitt. 2007. “SU-8 MEMS Fabry-Perot Pressure Sensor.” *Sensors and Actuators, A: Physical* 138(1):52–62.

Hinton, Thomas J., Andrew Hudson, Kira Pusch, Andrew Lee, and Adam W. Feinberg. 2016. “3D Printing PDMS Elastomer in a Hydrophilic Support Bath via Freeform Reversible Embedding.” *ACS Biomaterials Science and Engineering* 2(10):1781–86.

Hinton, Thomas J., Quentin Jallerat, Rachelle N. Palchesko, Joon Hyung Park, Martin S. Grodzicki, H. J. Shue, Mohamed H. Ramadan, Andrew R. Hudson, and Adam W. Feinberg. 2015. “Three-Dimensional Printing of Complex Biological Structures by Freeform Reversible Embedding of Suspended Hydrogels.” *Science Advances* 1(9):e1500758–e1500758.

Hirsch, Marzena, Daria Majchrowicz, Paweł Wierzba, Matthieu Weber, Mikhael Bechelany, and Małgorzata Jędrzejewska-Szczerska. 2017. “Low-Coherence Interferometric Fiber-Optic Sensors with Potential Applications as Biosensors.” *Sensors* 17(2):261.

Hirt, Luca, Alain Reiser, Ralph Spolenak, and Tomaso Zambelli. 2017. “Additive Manufacturing of Metal Structures at the Micrometer Scale.” *Advanced Materials* 29(17).

Van De Hoef, Tim P., Martijn Meuwissen, Javier Escaned, Justin E. Davies, Maria Siebes, Jos A. E. Spaan, and Jan J. Piek. 2013. “Fractional Flow Reserve as a Surrogate for Inducible Myocardial Ischaemia.” *Nature Reviews Cardiology* 10(8):439–52.

Hong, Seunghun, Ray Eby, Sung Myung, Byung Yang Lee, Saleem G. Rao, and Joonkyung Jang. 2006. “Dip-Pen Nanolithography.” Pp. 141–74 in *Scanning Probe Microscopies Beyond Imaging*. Weinheim, FRG: Wiley-VCH Verlag GmbH & Co. KGaA.

Hou, Yang, Shai Ashkenazi, Sheng Wen Huang, and Matthew O’Donnell. 2007. “Improvements in Optical Generation of High-Frequency Ultrasound.” *IEEE Transactions on Ultrasonics, Ferroelectrics, and Frequency Control* 54(3):682–86.

Hou, Yang, Jin-Sung Kim, Shai Ashkenazi, Matthew O'Donnell, and L. Jay Guo. 2006. "Optical Generation of High Frequency Ultrasound Using Two-Dimensional Gold Nanostructure." *Applied Physics Letters* 89(9):093901.

Hsieh, Bao Yu, Jinwook Kim, Jiadeng Zhu, Sibo Li, Xiangwu Zhang, and Xiaoning Jiang. 2015. "A Laser Ultrasound Transducer Using Carbon Nanofibers-Polydimethylsiloxane Composite Thin Film." *Applied Physics Letters* 106(2).

Hsu, J. M., Loren Rieth, Sascha Kammer, Mike Orthner, and Florian Solzbacher. 2008. "Effect of Thermal and Deposition Processes on the Surface Morphology, Crystallinity, and Adhesion of Parylene-C." *Sensors & Materials* 20(2):87–102.

Hu, Hua and Ronald G. Larson. 2006. "Marangoni Effect Reverses Coffee-Ring Depositions." *Journal of Physical Chemistry B* 110(14):7090–94.

Huff, Michael. 2002. *Tutorial: MEMS Fabrication*. Vol. 22.

Hurrell, A. and P. C. Beard. 2012. "Piezoelectric and Fibre-Optic Hydrophones." Pp. 619–76 in *Ultrasonic Transducers: Materials and design for sensors, actuators and medical applications*. Woodhead Publishing Ltd.

Hwan Lee, Seok, Mi Ae Park, Jack J. Yoh, Hyelynn Song, Eui Yun Jang, Yong Hyup Kim, Sungchan Kang, and Yong Seop Yoon. 2012. "Reduced Graphene Oxide Coated Thin Aluminum Film as an Optoacoustic Transmitter for High Pressure and High Frequency Ultrasound Generation." *Applied Physics Letters* 101(24).

Islam, Md., Muhammad Ali, Man-Hong Lai, Kok-Sing Lim, and Harith Ahmad. 2014. "Chronology of Fabry-Perot Interferometer Fiber-Optic Sensors and Their Applications: A Review." *Sensors* 14(4):7451–88.

Israelachvili, Jacob N. 2011. *Contrasts between Intermolecular, Interparticle, and Intersurface Forces*.

Iwasaki, Kohichiro and Shozo Kusachi. 2010. "Coronary Pressure Measurement Based Decision Making for Percutaneous Coronary Intervention." *Current Cardiology Reviews* 5(4):323–33.

Jackson, Nathan, Frank Stam, Joe O'Brien, Lekshmi Kailas, Alan Mathewson, and Cian O'Murchu. 2016. "Crystallinity and Mechanical Effects from Annealing Parylene Thin Films." *Thin Solid Films* 603(March):371–76.

Jang, Jae-Won, Zijian Zheng, One-Sun Lee, Wooyoung Shim, Gengfeng Zheng, George C. Schatz, and Chad A. Mirkin. 2010. "Arrays of Nanoscale Lenses for

Subwavelength Optical Lithography.” 10:27.

Jani, J. C., K. H. Nicolaides, E. Gratacós, C. M. Valencia, E. Doné, J. M. Martinez, L. Gucciardo, R. Cruz, and J. A. Deprest. 2009. “Severe Diaphragmatic Hernia Treated by Fetal Endoscopic Tracheal Occlusion.” *Ultrasound in Obstetrics and Gynecology* 34(3):304–10.

Jaworek, A. and A. Krupa. 1999. “Classification of the Modes of EHD Spraying.” *Journal of Aerosol Science* 30(7):873–93.

Jeong, Jae Won, Woon Ik Park, Lee Mi Do, Jong Hyun Park, Tae Heon Kim, Geesung Chae, and Yeon Sik Jung. 2012. “Nanotransfer Printing with Sub-10 Nm Resolution Realized Using Directed Self-Assembly.” *Advanced Materials* 24(26):3526–31.

Johnson, K. L., K. Kendall, and A. D. Roberts. 1971. “Surface Energy and the Contact of Elastic Solids.” *Proceedings of the Royal Society A: Mathematical, Physical and Engineering Sciences* 324(1558):301–13.

Judy, J. W. 2001. “Microelectromechanical Systems (MEMS): Fabrication, Design and Applications.” *Smart Materials and Structures* 10(6):1115–34.

Jung, Joontaek, Wonjun Lee, Woojin Kang, Eunjung Shin, Jungho Ryu, and Hongsoo Choi. 2017. “Review of Piezoelectric Micromachined Ultrasonic Transducers and Their Applications.” *Journal of Micromechanics and Microengineering* 27(11).

Kabagambe, Sandra K., Guy W. Jensen, Yue Julia Chen, Melissa A. Vanover, and Diana L. Farmer. 2017. “Fetal Surgery for Myelomeningocele: A Systematic Review and Meta-Analysis of Outcomes in Fetoscopic versus Open Repair.” *Fetal Diagnosis and Therapy* 95817.

Kim, Jang Ah, Dominic J. Wales, Alex J. Thompson, and Guang-Zhong Yang. 2020. “Fiber-Optic SERS Probes Fabricated Using Two-Photon Polymerization For Rapid Detection of Bacteria.” *Advanced Optical Materials* 1901934:1901934.

Kirby, Brian J. 2010. *Micro- and Nanoscale: Fluid Transport in Microfluidic Devices*. Cambridge University Press.

Klocke, F., A. McClung, and C. Ader. 2004. *Direct Laser Sintering of Borosilicate Glass*.

Kochergin, Vladimir, Kevin Flanagan, Zhong Shi, Michael Pedrick, Blake Baldwin, Thomas Plaisted, Balakishore Yellampelle, Eugene Kochergin, and Larry Vicari.

2009. “All-Fiber Optic Ultrasonic Structural Health Monitoring System.” *Sensors and Smart Structures Technologies for Civil, Mechanical, and Aerospace Systems 2009* 7292(March 2009):72923D.

Korolev, V. A. and V. T. Potapov. 2012. “Biomedical Fiber-Optic Temperature and Pressure Sensors.” *Meditsinskaia Tekhnika* 46(2):38–42.

Kotz, Frederik, Karl Arnold, Werner Bauer, Dieter Schild, Nico Keller, Kai Sachsenheimer, Tobias M. Nargang, Christiane Richter, Dorothea Helmer, and Bastian E. Rapp. 2017. “Three-Dimensional Printing of Transparent Fused Silica Glass.” *Nature Publishing Group* 544.

Kukkonen, Esa, Elmeri Lahtinen, Pasi Myllyperkiö, Jari Konu, and Matti Haukka. 2018. “Three-Dimensional Printing of Nonlinear Optical Lenses.”

Kumar, Satish. 2015. “Liquid Transfer in Printing Processes: Liquid Bridges with Moving Contact Lines.” *Annual Review of Fluid Mechanics* 47(1):67–94.

Kyriacou, P. A. 2010. “Temperature Sensor Technology.” P. 9781606500569 in *Biomedical Sensors*, edited by D. P. Jones. New York: Momentum Press.

L.D. Landau and E.M. Lifshitz. 1986. *Theory of Elasticity*. 3rd Edition. Elsevier.

Lee, C. E., A. M. Markus, E. Udd, and H. F. Taylor. 1989. “Optical-Fiber Fabry–Perot Embedded Sensor.” *Optics Letters* 14(21):1225.

Levine, Jeffrey M. 2010. “Peripheral Arterial Disease Is Underdiagnosed in the Elderly.” Retrieved March 17, 2020 (http://jmlevinemd.com/peripheral-arterial-disease-is-underdiagnosed/).

Lewis, Jennifer A. 2006. “Direct Ink Writing of 3D Functional Materials.” *Advanced Functional Materials* 16(17):2193–2204.

Li, Cheng, Xiangyang Gao, Tingting Guo, Jun Xiao, Shangchun Fan, and Wei Jin. 2015. “Analyzing the Applicability of Miniature Ultra-High Sensitivity Fabry-Perot Acoustic Sensor Using a Nanothick Graphene Diaphragm.” *Measurement Science and Technology* 26(8).

Li, Cheng, Qianwen Liu, Xiaobin Peng, and Shangchun Fan. 2015. “Analyzing the Temperature Sensitivity of Fabry-Perot Sensor Using Multilayer Graphene Diaphragm.” *Optics Express* 23(21):27494.

Li, K., D. W. Zeng, K. C. Yung, H. L. W. Chan, and C. L. Choy. 2002. “Study on Ceramic/Polymer Composite Fabricated by Laser Cutting.” Pp. 147–50 in

Materials Chemistry and Physics. Vol. 75. Elsevier.

Li, Zhuoyan, Jin H. Shen, John A. Kozub, Ratna Prasad, Pengcheng Lu, and Karen M. Joos. 2014. “Miniature Forward-Imaging B-Scan Optical Coherence Tomography Probe to Guide Real-Time Laser Ablation.” *Lasers in Surgery and Medicine* 46(3):193–202.

Limbert and Amiri. 2019. “Intra-Aortic Balloon Pump for Patients with Cardiac Conditions: An Update on Available Techniques and Clinical Applications.” *Reports* 2(3):19.

Liu, Chang, Bin Qian, Rongping Ni, Xiaofeng Liu, and Jianrong Qiu. 2018. “3D Printing of Multicolor Luminescent Glass.” *RSC Advances* 8(55):31564–67.

Liu, Xiaobo, Tingting Gang, Rongxin Tong, Xueguang Qiao, Chi Zuo, Xiaohong Bai, Ce Bian, and Manli Hu. 2018. “Air-Coupled Fiber Fabry-Perot Ultrasonic Sensor Formed by Diaphragm for Seismic Physical Model Imaging.” *Optik* 168:794–99.

Liu, Xuan, Iulian I. Iordachita, Xingchi He, Russell H. Taylor, and Jin U. Kang. 2012. “Miniature Fiber-Optic Force Sensor Based on Low-Coherence Fabry-Pérot Interferometry for Vitreoretinal Microsurgery.” *Biomedical Optics Express* 3(5):1062.

Liu, Yueying, Zhenguo Jing, Rui Li, Yang Zhang, Qiang Liu, Ang Li, Chao Zhang, and Wei Peng. 2020. “Miniature Fiber-Optic Tip Pressure Sensor Assembled by Hydroxide Catalysis Bonding Technology.”

Luo, Junjie, Luke J. Gilbert, Chuang Qu, Robert G. Landers, Douglas A. Bristow, and Edward C. Kinzel. 2017. “Additive Manufacturing of Transparent Soda-Lime Glass Using a Filament-Fed Process.” *Journal of Manufacturing Science and Engineering, Transactions of the ASME* 139(6).

Ma, Weiyi, Jiang Yi, Jie Hu, and Lan Jiang. 2019. “Microelectromechanical System-Based, High-Finesse, Optical Fiber Fabry–Perot Interferometric Pressure Sensors.” *Sensors and Actuators A: Physical* 111795.

Maciak, Erwin. 2019. “Low-Coherence Interferometric Fiber Optic Sensor for Humidity Monitoring Based on Nafion® Thin Film.” *Sensors* 19(3):629.

Mansouri, Kaweh and Tarek Shaarawy. 2011. “Continuous Intraocular Pressure Monitoring with a Wireless Ocular Telemetry Sensor: Initial Clinical Experience in Patients with Open Angle Glaucoma.” *British Journal of Ophthalmology*

95(5):627–29.

Maquet Getinge Group. 2019. *SENSATION ® and CS300 ™ IABP System Smaller Meets Faster*.

Marescaux, Jacques and Michele Diana. 2015. “Inventing the Future of Surgery.” *World Journal of Surgery* 39(3):615–22.

Markets and Markets. 2017. “Optical Sensing Market by Industry & Application - Global Forecast 2023 | MarketsandMarkets.” Retrieved February 26, 2020 (https://www.marketsandmarkets.com/Market-Reports/optical-sensing-market-197592599.html).

Marshall, V. F. 1964. *Fiber Optics in Urology*. Vol. 91.

Martínez-Mañas, Rosa M., David Santamarta, José M. De Campos, and Enric Ferrer. 2000. “Camino® Intracranial Pressure Monitor: Prospective Study of Accuracy and Complications.” *J Neurol Neurosurg Psychiatry* 69:82–86.

Matern, U. and P. Waller. 1999. “Instruments for Minimally Invasive Surgery.” *Surgical Endoscopy* 13(2):174–82.

McHale, G., S. M. Rowan, M. I. Newton, and M. K. Banerjee. 1998. “Evaporation and the Wetting of a Low-Energy Solid Surface.” *Journal of Physical Chemistry B* 102(11):1964–67.

Meitl, Matthew a., Zheng-Tao Zhu, Vipan Kumar, Keon Jae Lee, Xue Feng, Yonggang Y. Huang, Ilesanmi Adesida, Ralph G. Nuzzo, and John a. Rogers. 2006. “Transfer Printing by Kinetic Control of Adhesion to an Elastomeric Stamp.” *Nature Materials* 5(1):33–38.

Melde, Kai, Andrew G. Mark, Tian Qiu, and Peer Fischer. 2016. “Holograms for Acoustics.” *Nature* 537(7621):518–22.

Melki, Samir, Amit Todani, and George Cherfan. 2014. “An Implantable Intraocular Pressure Transducer Initial Safety Outcomes.” *JAMA Ophthalmology* 132(10):1221–25.

Metzen, Rene Patrick Von and Thomas Stieglitz. 2013. “The Effects of Annealing on Mechanical , Chemical , and Physical Properties and Structural Stability of Parylene C.” 727–35.

Meyers, Marc André, Krishan Kumar Chawla, and Marc Andre Meyers. 2009. *Mechanical Behavior of Materials*. Second Edi. Cambridge University Press.

Michel, Bruno, André Bernard, Alexander Bietsch, Emmanuel Delamarche, Mattias Geissler, David Juncker, Hannes Kind, Jean-Philippe Renault, Hugo Rothuizen, Heinz Schmid, Patrick Schmidt-Winkel, Richard Stutz, and Heiko Wolf. 2002. "Printing Meets Lithography: Soft Approaches to High-Resolution Patterning." *CHIMIA International Journal for Chemistry* 56(10):527–42.

Van Mieghem, Tim, David Baud, Roland Devlieger, Fetal Medicine, Liesbeth Lewi, Luc De Catte, and Jan Deprest. 2012. "Minimally Invasive Fetal Therapy." *Best Practice & Research Clinical Obstetrics & Gynaecology* 26:711–25.

Miller, Jordan S., Kelly R. Stevens, Michael T. Yang, Brendon M. Baker, Duc Huy T. Nguyen, Daniel M. Cohen, Esteban Toro, Alice A. Chen, Peter A. Galie, Xiang Yu, Ritika Chaturvedi, Sangeeta N. Bhatia, and Christopher S. Chen. 2012. "Rapid Casting of Patterned Vascular Networks for Perfusable Engineered Three-Dimensional Tissues." *Nature Materials* 11(9):768–74.

Mishra, Manish Kumar, Vikas Dubey, P. M. Mishra, and Isharat Khan. 2019. "MEMS Technology: A Review." *Journal of Engineering Research and Reports* 4(1):1–24.

Moise Jr, Kenneth J. and Alan Flake. 2017. "Fetoscopic Open Neural Tube Defect Repair : Development and Refinement of a Two-Port , Carbon Dioxide Insufflation Technique." *Obstertics and Gynecology* 130(3):648.

Morita, Takeshi. 2003. "Miniature Piezoelectric Motors." *Sensors and Actuators, A: Physical* 103(3):291–300.

Morris, Paul, Andrew Hurrell, Adam Shaw, Edward Zhang, and Paul Beard. 2009. "A Fabry–Pérot Fiber-Optic Ultrasonic Hydrophone for the Simultaneous Measurement of Temperature and Acoustic Pressure." *The Journal of the Acoustical Society of America* 125(6):3611–22.

Morris, R. K., G. L. Malin, E. Quinlan-Jones, L. J. Middleton, L. Diwakar, K. Hemming, D. Burke, J. Daniels, E. Denny, P. Barton, T. E. Roberts, K. S. Khan, J. J. Deeks, and M. D. Kilby. 2013. "The Percutaneous Shunting in Lower Urinary Tract Obstruction (PLUTO) Study and Randomised Controlled Trial: Evaluation of the Effectiveness, Cost-Effectiveness and Acceptability of Percutaneous Vesicoamniotic Shunting for Lower Urinary Tract Obstruction." *Health Technology Assessment* 17(59).

Nakayama, Don K., Michael R. Harrison, Maria Seron-Ferre, and Robin L. Villa. 1984.

"Fetal Surgery in the Primate II. Uterine Electromyographic Response to Operative Procedures and Pharmacologic Agents." *Journal of Pediatric Surgery* 19(4):333–39.

National Health Service. 2018. "Cardiovascular Disease - NHS." Retrieved November 28, 2019 (https://www.nhs.uk/conditions/cardiovascular-disease/).

National Institute for Health and Care Excellence. 2014. "The PressureWire Fractional Flow Reserve Measurement System for Coronary Artery Disease." Retrieved March 3, 2020 (https://www.nice.org.uk/advice/mib2/resources/the-pressurewire-fractional-flow-reserve-measurement-system-for-coronary-artery-disease-pdf-1763862133957).

Neoptix. 2017. "Neoptix T1 Model Fiber Optic Temperature Probe." Retrieved February 27, 2020 (https://www.neoptix.com/t1-sensor.asp).

Nesson, Silas, Miao Yu, Xuming Zhang, and Adam H. Hsieh. 2008. "Miniature Fiber Optic Pressure Sensor with Composite Polymer-Metal Diaphragm for Intradiscal Pressure Measurements." *Journal of Biomedical Optics* 13(4):044040.

Noimark, S., R. J. Colchester, R. K. Poduval, E. Maneas, E. J. Alles, T. Zhao, E. Z. Zhang, M. Ashworth, E. Tsolaki, A. H. Chester, N. Latif, S. Bertazzo, A. L. David, S. Ourselin, P. C. Beard, I. P. Parkin, I. Papakonstantinou, and A. E. Desjardins. 2018. "Polydimethylsiloxane Composites for Optical Ultrasound Generation and Multimodality Imaging." *Advanced Functional Materials*.

Noimark, Sacha, Richard J. Colchester, Ben J. Blackburn, Edward Z. Zhang, Erwin J. Alles, Sebastien Ourselin, Paul C. Beard, Ioannis Papakonstantinou, Ivan P. Parkin, and Adrien E. Desjardins. 2016. "Carbon-Nanotube–PDMS Composite Coatings on Optical Fibers for All-Optical Ultrasound Imaging." *Advanced Functional Materials* 26(46).

Noimark, Sacha, Richard J. Colchester, Radhika K. Poduval, Efthymios Maneas, Erwin J. Alles, Tianrui Zhao, Edward Z. Zhang, Michael Ashworth, Elena Tsolaki, Adrian H. Chester, Najma Latif, Sergio Bertazzo, Anna L. David, S. Ourselin, Paul C. Beard, Ivan P. Parkin, Ioannis Papakonstantinou, and Adrien E. Desjardins. 2017. "Polydimethylsiloxane (PDMS) Composites for Optical Ultrasound Generation and Multi-Modality Imaging." *Advanced Functional Materials*.

O'Neill, Jim. 2016. "Tackling Drug-Resistant Infections Globally: Final Report and

Recommendations the Review on Antimicrobial Resistance." *Review on Antimcrobial Resistance*.

O'Toole, John E., Kurt M. Eichholz, and Richard G. Fessler. 2009. "Surgical Site Infection Rates after Minimally Invasive Spinal Surgery." *Journal of Neurosurgery. Spine* 11(December 2007):471–76.

Oesterle, Adair. 2018. *Pipette Cookbook 2018, P-97 & P-1000 Micropipette Pullers*. Sutter Instrument Company.

Ohara, Yoshinobu, Masaru Miyayama, Kunihito Koumoto, and Hiroaki Yanagida. 1994. "PZT-Polymer Composites Fabricated with YAG Laser Cutter." *Sensors and Actuators: A. Physical* 40(3):187–90.

Onses, M. Serdar, Erick Sutanto, Placid M. Ferreira, Andrew G. Alleyne, and John A. Rogers. 2015. "Mechanisms, Capabilities, and Applications of High-Resolution Electrohydrodynamic Jet Printing." *Small* 11(34):4237–66.

Opsens. 2019. *Opsens Medical OptoWire ™ Brochure*.

Pai, Madhava, Nagy Habib, Hakan Senturk, Sundeep Lakhtakia, Nageshwar Reddy, Vito R. Cicinnati, Iyad Kaba, Susanne Beckebaum, Panagiotis Drymousis, Michel Kahaleh, and William Brugge. 2015. "Endoscopic Ultrasound Guided Radiofrequency Ablation, for Pancreatic Cystic Neoplasms and Neuroendocrine Tumors." *World Journal of Gastrointestinal Surgery* 7(4):52–59.

Park, Jang-Ung, Matt Hardy, Seong Jun Kang, Kira Barton, Kurt Adair, Deep kishore Mukhopadhyay, Chang Young Lee, Michael S. Strano, Andrew G. Alleyne, John G. Georgiadis, Placid M. Ferreira, and John A. Rogers. 2007. "High-Resolution Electrohydrodynamic Jet Printing." *Nature Materials* 6(10):782–89.

Perçin, Gökhan, Abdullah Atalar, F. Levent Degertekin, and Butrus T. Khuri-Yakub. 1998. "Micromachined Two-Dimensional Array Piezoelectrically Actuated Transducers." *Applied Physics Letters* 72(11):1397–99.

Pevec, Simon and Denis Donlagić. 2019. "Multiparameter Fiber-Optic Sensors: A Review." *Optical Engineering* 58(07):1.

Phithakwatchara, Nisarat, Katika Nawapun, Tacharee Panchalee, Sommai Viboonchart, Nadda Mongkolchat, and Tuangsit Wataganara. 2017. "Current Strategy of Fetal Therapy I: Principles of In-Utero Treatment, Pharmacologic Intervention, Stem Cell Transplantation and Gene Therapy." *Journal of Fetal*

Medicine 4:131–38.

Pijls, Nico H. J., Bernard de Bruyne, Kathinka Peels, Pepijn H. van der Voort, Hans J. R. M. Bonnier, Jozef Bartunek, and Jacques J. Koolen. 1996. “Measurement of Fractional Flow Reserve to Assess the Functional Severity of Coronary-Artery Stenoses.” *New England Journal of Medicine* 334(26):1703–8.

Piner, Richard D., Jin Zhu, Feng Xu, Seunghun Hong, and Chad A. Mirkin. 1999. “‘Dip-Pen’ Nanolithography.” *Science* 283(5402):661–63.

Pinet, Éric, Edvard Cibula, and Denis Đonlagić. 2007. “Ultra-Miniature All-Glass Fabry-Pérot Pressure Sensor Manufactured at the Tip of a Multimode Optical Fiber.” P. 67700U in *Fiber Optic Sensors and Applications V*. Vol. 6770, edited by E. Udd. SPIE.

Piqué, Alberto, Raymond C. Y. Auyeung, Heungsoo Kim, Nicholas A. Charipar, and Scott A. Mathews. 2016. “Laser 3D Micro-Manufacturing.” *Journal of Physics D: Applied Physics* 49(22):223001.

Podoleanu, A. Gh. 2012. “Optical Coherence Tomography.” *Journal of Microscopy* 247(3):209–19.

Poduval, Radhika K., Sacha Noimark, Richard J. Colchester, Thomas J. Macdonald, Ivan P. Parkin, Adrien E. Desjardins, and Ioannis Papakonstantinou. 2017. “Optical Fiber Ultrasound Transmitter with Electrospun Carbon Nanotube-Polymer Composite.” *Citation: Appl. Phys. Lett* 110.

Poeggel, Sven, Dineshbabu Duraibabu, Kyriacos Kalli, Gabriel Leen, Gerard Dooly, Elfed Lewis, Jimmy Kelly, and Maria Munroe. 2015. “Recent Improvement of Medical Optical Fibre Pressure and Temperature Sensors.” *Biosensors* 5(3):432–49.

Poeggel, Sven, Daniele Tosi, Dineshbabu Duraibabu, Gabriel Leen, Deirdre Mcgrath, and Elfed Lewis. 2015. “Optical Fibre Pressure Sensors in Medical Applications.” *Sensors* 15:17115–48.

Polla, Dennis L., Arthur G. Erdman, William P. Robbins, David T. Markus, Jorge Diaz-Diaz, Raed Rizq, Yunwoo Nam, Hui Tao Brickner, Amy Wang, and Peter Krulevitch. 2000. “Microdevices in Medicine.” *Annual Review of Biomedical Engineering* 2(1):551–76.

Popov, Yuri O. 2005. “Evaporative Deposition Patterns: Spatial Dimensions of the

Deposit." *Physical Review E - Statistical, Nonlinear, and Soft Matter Physics* 71(3).

Powers, Dana. 2009. *Interaction of Water with Epoxy*.

Psarski, Maciej, Jacek Marczak, Grzegorz Celichowski, Grzegorz B. Sobieraj, Konrad Gumowski, Feng Zhou, and Weimin Liu. 2012. "Hydrophobization of Epoxy Nanocomposite Surface with 1H,1H,2H,2H-Perfluorooctyltrichlorosilane for Superhydrophobic Properties." *Central European Journal of Physics* 10(5):1197–1201.

Qiu, Yongqiang, James V. Gigliotti, Margeaux Wallace, Flavio Griggio, Christine E. M. Demore, Sandy Cochran, and Susan Trolier-McKinstry. 2015. "Piezoelectric Micromachined Ultrasound Transducer (PMUT) Arrays for Integrated Sensing, Actuation and Imaging." *Sensors (Switzerland)* 15(4):8020–41.

Rajan, G. 2015. *Optical Fiber Sensors: Advanced Techniques and Applications*. CRC Press, Taylor & Francis Group.

Rajibul Islam, Md, Muhammad Mahmood Ali, Man Hong Lai, Kok Sing Lim, and Harith Ahmad. 2014. "Chronology of Fabry-Perot Interferometer Fiber-Optic Sensors and Their Applications: A Review." *Sensors (Switzerland)* 14(4):7451–88.

Ran, Z. L., Y. J. Rao, W. J. Liu, X. Liao, and K. S. Chiang. 2008. "Laser-Micromachined Fabry-Perot Optical Fiber Tip Sensor for High-Resolution Temperature-Independent Measurement of Refractive Index." *Optics Express* 16(3):2252.

Rao, Yun Jiang. 1997. "In-Fibre Bragg Grating Sensors." *Measurement Science and Technology* 8(4):355–75.

RJC Enterprises. 2020. "RJC Enterprises, LLC - Current Fiber Optic Sensor Users." Retrieved February 26, 2020 (http://rjcenterprises.net/users.html).

Rogers, John A. and Ungyu Paik. 2010. "Nanofabrication: Nanoscale Printing Simplified." *Nature Nanotechnology* 5(6):385–86.

Roriz, Paulo, Orlando Frazão, António B. Lobo-Ribeiro, José L. Santos, and José A. Simões. 2013. "Review of Fiber-Optic Pressure Sensors for Biomedical and Biomechanical Applications." *Journal of Biomedical Optics* 18(5):050903.

Rose, L. R. F. 1984. "Point-Source Representation for Laser-Generated Ultrasound." *Journal of the Acoustical Society of America* 75(3):723–32.

Ru, Changhai, Jun Luo, Shaorong Xie, and Yu Sun. 2014. “A Review of Non-Contact Micro- and Nano-Printing Technologies.” *Journal of Micromechanics and Microengineering* 24(5):053001.

SadAbadi, Hamid, Simona Badilescu, Muthukumaran Packirisamy, and Rolf Wuẗhrich. 2012. “PDMS-Gold Nanocomposite Platforms with Enhanced Sensing Properties.” *Journal of Biomedical Nanotechnology* 8(4):539–49.

Salaita, K., Y. Wang, and C. A. Mirkin. 2007. “Applications of Dip-Pen Nanolithography.” *Nature Nanotechnology* 2(3):145–55.

Santander, Cecilio, Elena Perea, María Caldas, and Pere Clave. 2017. “Catheter-Based High-Frequency Intraluminal Ultrasound Imaging Is a Powerful Tool to Study Esophageal Dysmotility Patients.” *Annals of the New York Academy of Sciences* 1395(1):60–66.

Schena, Emiliano, Daniele Tosi, Paola Saccomandi, Elfed Lewis, and Taesung Kim. 2016. “Fiber Optic Sensors for Temperature Monitoring during Thermal Treatments: An Overview.” *Sensors (Switzerland)* 16(7).

Schirmer, Niklas C., Carmen Kullmann, Martin S. Schmid, Brian R. Burg, Timo Schwamb, and Dimos Poulikakos. 2010. “On Ejecting Colloids against Capillarity from Sub-Micrometer Openings: On-Demand Dielectrophoretic Nanoprinting.” *Advanced Materials* 22(42):4701–5.

Schirmer, Niklas C., Stefan Ströhle, Manish K. Tiwari, and Dimos Poulikakos. 2011. “On the Principles of Printing Sub-Micrometer 3D Structures from Dielectric-Liquid-Based Colloids.” *Advanced Functional Materials* 21(2):388–95.

Schols, Rutger M., Nicole D. Bouvy, Ronald M. van Dam, and Laurents P. S. Stassen. 2013. “Advanced Intraoperative Imaging Methods for Laparoscopic Anatomy Navigation: An Overview.” *Surgical Endoscopy* 27(6):1851–59.

Schols, Rutger M., Niels J. Connell, and Laurents P. S. Stassen. 2015. “Near-Infrared Fluorescence Imaging for Real-Time Intraoperative Anatomical Guidance in Minimally Invasive Surgery: A Systematic Review of the Literature.” *World Journal of Surgery* 39(5):1069–79.

Schreuder, Jan J., Alessandro Castiglioni, Andrea Donelli, Francesco Maisano, Jos R. C. Jansen, Ramzi Hanania, Pat Hanlon, Jan Bovelander, and Ottavio Alfieri. 2005. “Automatic Intraaortic Balloon Pump Timing Using an Intrabeat Dicrotic Notch Prediction Algorithm.” *Annals of Thoracic Surgery* 79(3):1017–22.

Schubert, Carl, Mark C. van Langeveld, and Larry A. Donoso. 2014. “Innovations in 3D Printing: A 3D Overview from Optics to Organs.” *The British Journal of Ophthalmology* 98(2):159–61.

Scruby, C. B. 1989. “Some Applications of Laser Ultrasound.” *Ultrasonics* 27(4):195–209.

Scruby, C. B., R. J. Dewhurst, D. A. Hutchins, and S. B. Palmer. 1980. “Quantitative Studies of Thermally Generated Elastic Waves in Laser-Irradiated Metals.” *Journal of Applied Physics* 51:6210.

Shao, Guangbin, Rihan Hai, and Cheng Sun. 2020. “3D Printing Customized Optical Lens in Minutes.” *Advanced Optical Materials* 8(4):1–7.

Shen, Shi, Huanhuan Liu, Fufei Pang, Ziming Guo, Junfeng Yang, Zhenyi Chen, and Tingyun Wang. 2019. “Fiber-Optic Water Pressure Sensor Fabricated by a 3D Printing Technique.” P. 26 in *Advanced Sensor Systems and Applications IX*, edited by T. Liu, G.-D. Peng, and Z. He. SPIE.

Shen, Xiaoying, Chih Ming Ho, and Tak Sing Wong. 2010. “Minimal Size of Coffee Ring Structure.” *Journal of Physical Chemistry B* 114(16):5269–74.

Shung, K. Kirk., Michael. Smith, and Benjamin M. W. Tsui. 1992. *Principles of Medical Imaging.* Elsevier Science.

Shutilov, Vladimir Aleksandrovich. 1988. *Fundamental Physics of Ultrasound*. Gordon and Breach Science Publishers.

Sigel, Andre, Markus Merkel, and Andreas Heinrich. 2017. “Miniaturization of an Optical 3D Sensor by Additive Manufacture of Metallic Mirrors.” P. 103290Q in *Optical Measurement Systems for Industrial Inspection X*. Vol. 10329, edited by P. Lehmann, W. Osten, and A. Albertazzi Gonçalves. SPIE.

Skogås, J. , Myhre, H. , Ødegård, A. and Kiss, G. 2016. “Imaging for Minimally Invasive Surgery.” *Surgical Science* 7(8):334–41.

Slaghekke, Femke, Enrico Lopriore, Liesbeth Lewi, Johanna M. Middeldorp, Erik W. Van Zwet, Anne Sophie Weingertner, Frans J. Klumper, Philip DeKoninck, Roland Devlieger, Mark D. Kilby, Maria Angela Rustico, Jan Deprest, Romain Favre, and Dick Oepkes. 2014. “Fetoscopic Laser Coagulation of the Vascular Equator versus Selective Coagulation for Twin-to-Twin Transfusion Syndrome: An Open-Label Randomised Controlled Trial.” *The Lancet* 383(9935):2144–51.

van Soest, Gijs, Evelyn Regar, and Antonius F. W. van der Steen. 2015. “Photonics in Cardiovascular Medicine.” *Nature Photonics* 9(10):626–29.

Song, Peishuai, Zhe Ma, Jing Ma, Liangliang Yang, Jiangtao Wei, and Yongmei Zhao. 2020. “Recent Progress of Miniature MEMS Pressure Sensors.” 1–38.

Spaan, Jos A. E., Jan J. Piek, Julien I. E. Hoffman, and Maria Siebes. 2006. “Physiological Basis of Clinically Used Coronary Hemodynamic Indices.” *Circulation* 113(3):446–55.

Spicer, James B. and David H. Hurley. 1996. “Epicentral and near Epicenter Surface Displacements on Pulsed Laser Irradiated Metallic Surfaces.” *Cite as: Appl. Phys. Lett* 68:3561.

Stahl, T., T. Allen, and P. Beard. 2014. “Characterization of the Thermalisation Efficiency and Photostability of Photoacoustic Contrast Agents.” *Photons Plus Ultrasound: Imaging and Sensing 2014* 8943(March 2014):89435H.

Staudenraus, J. and W. Eisenmenger. 1993. *Fibre-Optic Probe Hydrophone for Ultrasonic and Shock-Wave Measurements in Water*. Vol. 31.

Sutanto, Erick, Yafang Tan, M. Serdar Onses, Brian T. Cunningham, and Andrew Alleyne. 2014. “Electrohydrodynamic Jet Printing of Micro-Optical Devices.” *Manufacturing Letters* 2(1):4–7.

Tam, Andrew C. 1986. *Applications of Photoacoustic Sensing Techniques*. Vol. 58.

Tarkin, Jason M., Marc R. Dweck, Nicholas R. Evans, Richard A. P. Takx, Adam J. Brown, Ahmed Tawakol, Zahi A. Fayad, and James H. F. Rudd. 2016. “Imaging Atherosclerosis.” *Circulation Research* 118(4):750–69.

Tateishi, R., S. Kimura, T. Kawakami, N. Kanehama, S. Tachibana, H. Arai, K. Hayasaka, S. Hara, J. Hiroki, K. Yoshioka, S. Kuroda, R. Iwatsuka, A. Mizukami, T. Hayashi, and A. Matsumura. 2018. “P5502Comparison of Accuracy of Fractional Flow Reserve Using Optical Sensor Wire to Conventional Pressure Wire.” *European Heart Journal* 39(suppl_1).

Tian, Ye, Nan Wu, Xiaotian Zou, Haitham Felemban, Chengyu Cao, and Xingwei Wang. 2013. “Fiber-Optic Ultrasound Generator Using Periodic Gold Nanopores Fabricated by a Focused Ion Beam.” *Optical Engineering* 52(6):065005.

Tiwari, Manish K., Ilker S. Bayer, Gregory M. Jursich, Thomas M. Schutzius, and Constantine M. Megaridis. 2010. “Highly Liquid-Repellent, Large-Area,

Nanostructured Poly(Vinylidene Fluoride)/Poly(Ethyl 2-Cyanoacrylate) Composite Coatings: Particle Filler Effects." *ACS Applied Materials and Interfaces* 2(4):1114–19.

Truong, Thanh Chung, Ayalsew Dagnew Abetew, Jung-Ryul Lee, and Jeong-Beom Ihn. 2018. "Thermo-Elastic Model of Epicenter Displacement by Laser Pulse Irradiated on Metallic Surfaces." *Journal of Nondestructive Evaluation, Diagnostics and Prognostics of Engineering Systems* 1(2).

Urban, Frantisek, Jaroslav Kadlec, Radek Vlach, and Radek Kuchta. 2010. "Design of a Pressure Sensor Based on Optical Fiber Bragg Grating Lateral Deformation." *Sensors* 10(12):11212–25.

Vaezi, Mohammad, Hermann Seitz, and Shoufeng Yang. 2013. "A Review on 3D Micro-Additive Manufacturing Technologies." *International Journal of Advanced Manufacturing Technology* 67(5–8):1721–54.

Vieira, Melissa Gurgel Adeodato, Mariana Altenhofen Da Silva, Lucielen Oliveira Dos Santos, and Marisa Masumi Beppu. 2011. "Natural-Based Plasticizers and Biopolymer Films: A Review." *European Polymer Journal* 47(3):254–63.

Voldman, Joel, Martha L. Gray, and Martin A. Schmidt. 1999. "Microfabrication in Biology and Medicine." *Annual Review of Biomedical Engineering* 1(1):401–25.

Wang, Fuyin, Zhengzheng Shao, Jiehui Xie, Zhengliang Hu, Hong Luo, and Yongming Hu. 2014. "Extrinsic Fabry-Pérot Underwater Acoustic Sensor Based on Micromachined Center-Embossed Diaphragm." *Journal of Lightwave Technology* 32(23):4026–34.

Wang, Haoran, Yuanyuan Yu, Zhenfang Chen, Hao Yang, Huabei Jiang, and Huikai Xie. 2018. "Design and Fabrication of a Piezoelectric Micromachined Ultrasonic Transducer Array Based on Ceramic PZT." in *Proceedings of IEEE Sensors*. Vols. 2018-October. Institute of Electrical and Electronics Engineers Inc.

Wang, Jijun, Zhonghua Shen, Baiqiang Xu, Xiaowu Ni, Jianfei Guan, and Jian Lu. 2007. "Numerical Simulation of Laser-Generated Ultrasound in Non-Metallic Material by the Finite Element Method." *Optics and Laser Technology* 39(4):806–13.

Wang, Lihong V. and Hsin-I. Wu. 2007. "Photoacoustic Tomography." in *Biomedical Optics: Principles and Imaging*. John Wiley & Sons, Inc.

Wang, Qiaoyun, Wenhua Wang, Xinsheng Jiang, and Qingxu Yu. 2010. “Diaphragm-Based Extrinsic Fabry-Perot Interferometric Optical Fiber Pressure Sensor.” P. 76564V in *5th International Symposium on Advanced Optical Manufacturing and Testing Technologies: Optical Test and Measurement Technology and Equipment*. Vol. 7656, edited by Y. Zhang, J. Sasián, L. Xiang, and S. To. International Society for Optics and Photonics.

Wang, Shun, Ping Lu, Li Liu, Hao Liao, Yuan Sun, Wenjun Ni, Xin Fu, Xinyue Jiang, Deming Liu, Jiangshan Zhang, Hao Xu, Qiuping Yao, and Yanming Chen. 2016. “An Infrasound Sensor Based on Extrinsic Fiber-Optic Fabry-Perot Interferometer Structure.” *IEEE Photonics Technology Letters* 28(11):1264–67.

Weeks, B. L., A. Noy, A. E. Miller, and J. J. De Yoreo. 2002. “Effect of Dissolution Kinetics on Feature Size in Dip-Pen Nanolithography.” *Physical Review Letters* 88:255505.

White, R. M. 1963. “Generation of Elastic Waves by Transient Surface Heating.” *Journal of Applied Physics* 34(12):3559–67.

Wolthuis, Roger A., Gordon L. Mitchell, Elric Saaski, James C. Hartl, and Martin A. Afromowitz. 1991. “Development of Medical Pressure and Temperature Sensors Employing Optical Spectrum Modulation.” *IEEE Transactions on Biomedical Engineering* 38(10):974–81.

Won Baac, Hyoung, Jong G. Ok, Hui Joon Park, Tao Ling, Sung Liang Chen, A. John Hart, and L. Jay Guo. 2010. “Carbon Nanotube Composite Optoacoustic Transmitters for Strong and High Frequency Ultrasound Generation.” *Applied Physics Letters* 97(23).

Wong, Kaufui V. and Aldo Hernandez. 2012. “A Review of Additive Manufacturing.” *ISRN Mechanical Engineering* 2012:1–10.

World Health Organization. 2019. “Cardiovascular Diseases.” 127. Retrieved November 28, 2019 (https://www.who.int/news-room/fact-sheets/detail/cardiovascular-diseases-(cvds)).

Wu, Nan, Kai Sun, and Xingwei Wang. 2011. “Fiber Optics Photoacoustic Generation Using Gold Nanoparticles as Target.” *Sensors and Smart Structures Technologies for Civil, Mechanical, and Aerospace Systems 2011* 7981(April 2011):798118.

Wu, Nan, Ye Tian, Xiaotian Zou, Vinicius Silva, Armand Chery, and Xingwei Wang.

2012. “High-Efficiency Optical Ultrasound Generation Using One-Pot Synthesized Polydimethylsiloxane-Gold Nanoparticle Nanocomposite.” *Journal of the Optical Society of America B* 29(8):2016.

Yan, Lu, Zhiguo Gui, Guanjun Wang, Yongquan An, Jinyu Gu, Meiqin Zhang, Xinglin Liu, Zhibin Wang, Gao Wang, and Pinggang Jia. 2017. “A Micro Bubble Structure Based Fabry–Perot Optical Fiber Strain Sensor with High Sensitivity and Low-Cost Characteristics.” *Sensors* 17(3):555.

Yang, Yi, He Tian, Yu Feng Wang, Yi Shu, Chang Jian Zhou, Hui Sun, Cang Hai Zhang, Hao Chen, and Tian Ling Ren. 2013. “An Ultra-High Element Density PMUT Array with Low Crosstalk for 3-D Medical Imaging.” *Sensors (Switzerland)* 13(8):9624–34.

Yoo, Geonwook, Youngseo Park, Pilgyu Sang, Hyoung Won Baac, and Junseok Heo. 2016. “High-Frequency Optoacoustic Transmitter Based on Nanostructured Germanium via Metal-Assisted Chemical Etching.” *Optical Materials Express* 6(8):2567.

Yoshinaga, Shigetaka, Ichiro Oda, Satoru Nonaka, Ryoji Kushima, and Yutaka Saito. 2012. “Endoscopic Ultrasound Using Ultrasound Probes for the Diagnosis of Early Esophageal and Gastric Cancers.” *World Journal of Gastrointestinal Endoscopy* 4(6):218–26.

Yu, Feifan, Qianwen Liu, Xin Gan, Mingxiang Hu, Tianyi Zhang, Cheng Li, Feiyu Kang, Mauricio Terrones, and Ruitao Lv. 2017. “Ultrasensitive Pressure Detection of Few-Layer MoS2.” *Advanced Materials* 29(4).

Yunker, Peter J., Tim Still, Matthew A. Lohr, and A. G. Yodh. 2011. “Suppression of the Coffee-Ring Effect by Shape-Dependent Capillary Interactions SI.” *Nature* 476(7360):308–11.

Zaumseil, Jana, Matthew A. Meitl, Julia W. P. Hsu, Bharat R. Acharya, Kirk W. Baldwin, Yueh-Lin Loo, and John A. Rogers. 2003. “Three-Dimensional and Multilayer Nanostructures Formed by Nanotransfer Printing.” *Nano Letters* 3(9):1223–27.

Zhang, Dao, Xiaofeng Liu, and Jianrong Qiu. 2020. “3D Printing of Glass by Additive Manufacturing Techniques: A Review.”

Zhang, Edward Z. and Paul C. Beard. 2015. “Characteristics of Optimized Fibre-Optic Ultrasound Receivers for Minimally Invasive Photoacoustic Detection.” *Photons*

Plus Ultrasound: Imaging and Sensing 2015 9323:932311.

Zhang, Qi, Jincheng Lei, Yizheng Chen, Yongji Wu, Chuan Chen, and Hai Xiao. 2019. "3D Printing of All-Glass Fiber-Optic Pressure Sensor for High Temperature Applications." *IEEE Sensors Journal* PP(c):1–1.

Zhang, Qing, Jing Juan Xu, Yan Liu, and Hong Yuan Chen. 2008. "In-Situ Synthesis of Poly(Dimethylsiloxane)-Gold Nanoparticles Composite Films and Its Application in Microfluidic Systems." *Lab on a Chip* 8(2):352–57.

Zhang, Wen, Hui Zhang, Fei Du, Jianchao Shi, Shijiu Jin, and Zhoumo Zeng. 2015. "Pull-In Analysis of the Flat Circular CMUT Cell Featuring Sealed Cavity." *Mathematical Problems in Engineering* 2015(February).

Zhao, Yong, Mao qing Chen, Feng Xia, and Ri qing Lv. 2018. "Small In-Fiber Fabry-Perot Low-Frequency Acoustic Pressure Sensor with PDMS Diaphragm Embedded in Hollow-Core Fiber." *Sensors and Actuators, A: Physical* 270:162–69.

Zhou, Jingcheng, Cong Du, and Xingwei Wang. 2019. "Ultrasound Beam Steering Using Fiber Optic Ultrasound Phased Array." *Optics Letters*.

Zhou, Jingcheng, Nan Wu, and Xingwei Wang. 2019. "The Enhancement of the Photoacoustic Generation Efficiency Based on Fiber Optic Ultrasound Phased Array." *Measurement*.

Zhou, Peilin, Haibo Yu, Wuhao Zou, Ya Zhong, Xiaoduo Wang, Zhidong Wang, and Lianqing Liu. 2020. "Cross-Scale Additive Direct-Writing Fabrication of Micro/Nano Lens Arrays by Electrohydrodynamic Jet Printing." *Optics Express* 28(5):6336.

Zhu, Cheng and James E. Smay. 2012. "Catenary Shape Evolution of Spanning Structures in Direct-Write Assembly of Colloidal Gels." *Journal of Materials Processing Technology* 212(3):727–33.

Zolfaghari, Abolfazl, Tiantong Chen, and Allen Y. Yi. 2019. "Additive Manufacturing of Precision Optics at Micro and Nanoscale." *International Journal of Extreme Manufacturing* 1(1).

Zou, Xiaotian, Nan Wu, Ye Tian, and Xingwei Wang. 2014. "Broadband Miniature Fiber Optic Ultrasound Generator." *Optics Express* 22(15):18119.

Zywietz, Urs, Andrey B. Evlyukhin, Carsten Reinhardt, and Boris N. Chichkov. 2014.

“Laser Printing of Silicon Nanoparticles with Resonant Optical Electric and Magnetic Responses.” *Nature Communications* 5.